Tungsten nanostructure formation in a magnetron sputtering device

by

TJ Petty

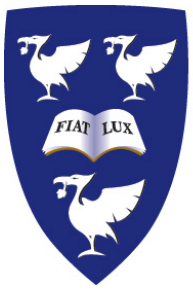

UNIVERSITY OF LIVERPOOL

Department of Electrical Engineering and Electronics

Thesis submitted in accordance with the requirements of the University of Liverpool for the degree of Doctor of Philosophy

September 2015

Declaration

I hereby declare that this thesis is my own work and no further sources of information have been used other than the references cited. Neither this thesis nor any part of it have been submitted to any other university or institution for the application of another degree or qualification.

Signed: _____(TJ Petty)

Date: _____

Abstract

Fuzzy tungsten is a phenomena that could potentially occur in future fusion reactors. There are three conditions for fuzz to form, the existence of He ions impinging on a tungsten sample for a sufficient amount of time, that these ions be of sufficient energy, and that the surface temperature of the tungsten is hot enough. These conditions will likely be fulfilled in ITER, the future flagship fusion reactor. Therefore efforts to understand and characterise the fuzz formation are of importance.

A thorough literature review has been provided, bringing together for the first time works from over 100 papers on the area. The history of its discovery is explained and the characteristics of the structure are detailed. The potential for fuzz to occur in ITER is shown, and positive and negative aspects of fuzz for fusion operation are discussed. The current accepted growth mechanisms are explained and a brief summary of the current work on simulating the phenomena is given. Fuzz appearing on other metals is introduced, and evidence of creating fuzz in a tokamak is shown. Methods for removing fuzz are presented should it be deemed necessary to do so in ITER.

Results are compiled from many fuzz samples created in the literature spanning four orders of magnitude of fluence. This provided the foundation for a collaboration with the UC San Diego, and lab time at their facilities. Several samples were created to complement the dataset. The compilation provides new insights into the growth equation surrounding fuzz formation. A new addition to the equation is introduced in the form of an incubation fluence, a minimum fluence required before fuzz can develop. The growth model is expanded to fuzz grown in erosive regimes, and a new equation is proposed that encompasses the competition between growth and erosion, giving good predictions for the resulting equilibrium thickness.

A new method for creating fuzz has been developed in a cheap and simple way. Conventional methods involve using large scale expensive devices, only available in a select few places worldwide. Magnetrons are apparent in many laboratories around the world and a technique for making fuzz in them has been developed. The three parameters controlling fuzz formation have been studied in the magnetron by making samples at many different conditions. The results provide new insight into early fuzz formation, providing results in a fluence range often over-looked. A cross-over fluence is noted from pre-fuzz to fully formed fuzz, overlapping with the predicted incubation fluence. The results differ slightly from fuzz created in other devices at similar fluence. The most probable cause is due to the unique existence of deposition of metallic particles in a magnetron incident on the samples during the growth of fuzz.

Acknowledgements

Thanks must be given first and foremost to my PhD supervisor, Prof. James Bradley, who took a chance on me, to whom I am forever indebted for this great opportunity, and for all the guidance and support he provided me. I would especially like to thank Nu for originally teaching me how to work the rig, Big Mike for being a constant inspiration both inside and out of work, Fred for making my time at Liverpool highly enjoyable (bien qu'il n'est pas très rigolo), and Mo for teaching me so much about the world (and physics). Thanks must go to Alan Roby who built many contraptions for me and was a real pleasure to work with. Larry Barnes, for making me feel welcome at Liverpool from day one. Jill (and Phil) for their constant cheery support. Lindsey Clarke, Hannah Fosh, and Jane Gallagher who provided me with a lot of behind the scenes support. I also wish to thank Michael John, Francis, Zaenab, Steve, Carl, Ni, Tom Farley, Mark, James Walsh, Tom Hardiment, Paul, Jun-Seok, Ali, Liu, Danhua, Zeng, and Kirsty, for their joyful company and support throughout my PhD at Liverpool.

From UC San Diego I wish to thank Matthew Baldwin, the Grand Master of fuzz, for giving me the incredible opportunity to work with him. To Michael Simmonds for making my stay in San Diego enjoyable, and to Ionut Jepu, Russell Doerner, and Tyler Lynch for helping out with the experiments.

I would also like to thank people who helped me out with my work along the way, Kerry Abrams provided great initial SEM images and inspiration, Tim Joyce put up with many hours teaching me how to work many devices. Aneeqa Khan, fellow fuzz buddy, provided me with lots of support throughout my PhD. David Sawtell was a great help throughout, providing me with many resources. Tobias Heil gave me some beautiful results I struggled for 2 years to achieve. Ruben Weise who was an enjoyable and unique experience. Also thanks must be extended to John Lynch, Charles Clavering, Simon Romani, and Terry Whitmore, for their help along the way.

I wish to thank my fantastic friends and family for their support throughout my time at Liverpool. You are my raison d'être.

Lastly, I would like to thank the University of Liverpool for funding my studentship.

Publications

The research carried out during the course of this study has, thus far, led to the following publications

- **T. J. Petty**, M. J. Baldwin, M. I. Hasan, R. P. Doerner, and J. W. Bradley, "Tungsten 'fuzz' growth re-examined: the dependence on ion fluence in non-erosive and erosive helium plasma", *Nuclear Fusion* **55**, 093033 (2015).
- **T. J. Petty** and J. W. Bradley, "Tungsten nanostructure formation in a magnetron sputtering device", *Journal of Nuclear Materials* **453**, 320-322 (2014).
- P. Poolcharuansin, M. Bowes, **T. J. Petty**, J. W. Bradley, "Ionized metal flux fraction measurements in HiPIMS discharges", *Journal of Physics D: Applied Physics* **45**, 322001 (2012).

Conferences

- Surface Science Day **(Poster presentation)** - University of Central Lancashire, UK, 22nd June 2015.
- Plasmas, Surfaces and Thin Films : Early Career Researchers Meeting **(Oral presentation)** - Loughborough University, UK, 17th June 2015.
- 15th International Conference on Plasma-Facing Materials and Components for Fusion Applications **(Poster presentation)** - Aix-en-Provence, France, 18-22nd May 2015.
- 42nd IOP Plasma Physics Conference **(Oral presentation)** - Milton Keynes, UK, 30th March - 2nd April 2015.
- Culham PhD Showcase Event **(Oral presentation)** - Culham, UK, 12-13th June 2014.
- 14th International Conference on Plasma-Facing Materials and Components for Fusion Applications - Jülich, Germany, 13-17th May 2013.
- 40th IOP Plasma Physics Conference **(Poster presentation)** - York, UK, 25-28th March 2013.
- FuseNet PhD Event in Fusion Science and Engineering **(Poster presentation)** - Pont-à-Mousson, France, 22-25th October 2012.

Nomenclature

Provided here is a list of commonly used abbreviations and notations

Abbreviations

ITER formerly this stood for International Thermonuclear Experimental Reactor, although it is said to no longer stand for that due to the use of unpopular words. It is also Latin for 'the way' or 'the road', this is the future fusion reactor being built in France, the first to potentially provide more energy out than is put in.

JET Joint European Tokamak, the current largest operational fusion reactor located in Oxfordshire in the UK.

DEMO a DEMOnstration plant, the proposed next step after ITER, expected to be the first attempt to get usable energy out of a fusion reactor, this is not just one device but is expected to be many devices in different parts of the world.

CFC Carbon Fibre Composite

PFM Plasma Facing Material

LPD Linear Plasma Device

DC Direct Current

MSD Magnetron Sputtering Device

D deuterium, an isotope of hydrogen, used in fusion reactions, formed of one neutron and one proton.

T tritium, another isotope of hydrogen, also used in fusion reactions, formed of two neutrons and one proton.

DT Deuterium-tritium, a DT plasma is a plasma generated in a deuterium and tritium mixed gas. This is the most promising mixture to generate fusion in tokamaks.

ELM Edge-Localised Mode, an instability in tokamak operation which generates excess heating at the divertor

SEM Scanning Electron Microscope

TEM Transmission Electron Microscope

IR Infra-Red

MD Molecular Dynamics

MC [kinetic] Monte Carlo

QCM Quartz Crystal Microbalance

SE Secondary Electron

BSE BackScattered Electron

CFM ConFocal Microscope

AFM Atomic Force Microscope

FIB Focused Ion Beam

UoL University of Liverpool

UC San Diego University of California at San Diego

PISCES the plasma surface interaction experimental facility, located at UC San Diego.

TC ThermoCouple

RGA Residual Gas Analysis

ATP Active Thermal Probe

PTP Passive Thermal Probe

Notation

t time, usually of sample exposure to conditions necessary for fuzz to form, (s)

Γ flux, the number of particles (mostly He ions) incident on a surface per second, ($m^{-2}\,s^{-1}$)

Φ fluence, being flux × time, in other words the 'dose' of particles throughout the exposure, (m^{-2})

Φ_0 incubation fluence, a fluence necessary before fuzz can begin to grow (m^{-2})

k_B the Boltzmann constant, ($1.38{\times}10^{-23}\ m^2\,kg\,s^{-2}\,K^{-1}$)

T temperature, (K)

T_e the electron temperature, the mean temperature of the electrons, (eV)

T_i the ion temperature, the mean temperature of the ions, (eV)

n plasma density, the number of ions per m^{-3}, (m^{-3})

e the charge on a single electron, (1.6×10^{-19} C)

V_p plasma potential, the potential of the bulk plasma, (V)

V_f floating potential, the potential an electrically isolated object will be at in a plasma, (V)

V_B sample bias, the potential applied to the samples during growth, (V)

I_{is} ion saturation current, the ion current which Langmuir probes saturate to at large negative potentials, (V)

m_i ion mass, (kg)

A note on pressure units

The SI units of pressure are Pascals (Pa), however, the pressure gauges used in all the experiments here measured the pressure in millitorr (mTorr). Throughout this thesis the units used varies depending on the context. The conversion from mTorr to Pa is provided below:

$$1\,\text{mTorr} = \frac{101\,325}{760}\,\text{Pa}$$
$$1\,\text{mTorr} \approx 133.3\,\text{Pa}$$

$$1\,\text{Pa} = \frac{760}{101\,325}\,\text{mTorr}$$
$$1\,\text{Pa} \approx 7.5 \times 10^{-3}\,\text{mTorr}$$

Contents

List of Figures

List of Tables

Chapter 1

Introduction

Fusion power has the potential to be one of the main energy sources for future generations. It is the method by which the sun generates energy, and scientists and engineers have been trying to recreate it on the Earth for almost 100 years. When two atomic nuclei have enough energy to overcome the electrostatic repulsion between them, they can fuse together. The sum of the initial masses is more than the sum of the combined mass, this excess mass is converted into energy in the form of Einstein's famous equation, $E = mc^2$. The most promising fusion reaction to reproduce on Earth is the fusion of a deuterium ion and a tritium ion into helium[1]. The sun's core is around 15,000,000 $^{\circ}$C yet the rate at which it generates energy from fusion reactions is very slow, generating only 270 $\mathrm{W\,cm^{-3}}$, as opposed to ~$\mathrm{MW\,cm^{-3}}$ necessary for commercial power plants [1]. In fusion experiments on Earth, temperatures of ~200,000,000 $^{\circ}$C are required to provide enough energy for fusion reactions to occur with a frequency to be worthwhile [1]. Such a high temperature gas is highly ionised, in that the electrons are completely removed from the atoms, leaving a mixture of electrons and ions. Such a mixture is no longer called a gas, but instead is called a *plasma*.

Efforts to confine such high temperature plasmas have led to the design of a fusion reactor called a tokamak, which holds the plasma in a doughnut-like shape known as a torus, preventing the plasma from touching the walls except for in a controlled region known as the divertor. The largest tokamak to date is the Joint European Tokamak (JET), built in 1982 in Oxfordshire, UK. In 1991 it demonstrated the first controlled release of fusion power [2]. This paved the way for ITER[2], the next generation fusion reactor currently being built in Cadarache, on the south coast of France. This is a global endeavour with most of the developed world actively financing it and is planned to be fully operational before 2030[3]. ITER will be the largest tokamak to date, and is aimed to give ten times more energy output than is put into the system [3]. The inside of

[1] Deuterium and tritium are both isotopes of hydrogen, with 1 and 2 extra neutrons, respectively.
[2] ITER is the name, and is no longer an acronym, it is Latin for 'the way' or 'the road'.
[3] When this PhD commenced the expected date was 2020.

the tokamak will reach incredibly high temperatures (~200,000,000 °C), and although the plasma is confined, the temperature of the materials lining the wall will also be very high (~1000 °C). In addition to this, when there are disruptions in the plasma this increases the surface temperatures to heights where very few materials in the world can withstand it. The main candidate for the materials lining tokamaks to date has been carbon fibre composites (CFCs) which can withstand very high temperatures, as it does not melt but sublimes [3]. CFC is a very capable plasma facing material (PFM) as it can withstand high heat loads, and will remain standing during many disruptions. However, CFCs retain unacceptable levels of tritium, which is one of the main fuels for the fusion reaction. Tritium retention in CFC weakens the CFC tiles, it is a rare fuel, and it is highly volatile in air, and were there to be a vacuum breach (hypothetically), there could be a dangerous explosion [4, 5]. As such, for ITER, there has been a safety limit set in place for the amount of tritium allowed in the vacuum vessel at any one time, about 350 g [6]. If CFC tiles were to line the inside of ITER, this limit would be exceeded in about 100 full performance pulses [6] (with about 10 pulses planned daily [7]).

The second best material to be used is tungsten due to it having the highest melting point of any element at ~3400 °C, it also erodes much less than CFC [8], and most importantly, it retains much less tritium, only exceeding the tritium safety limit in ~3000 full performance pulses [9]. Therefore, tungsten has been chosen to be the main replacement of CFC in ITER, and will line the majority of the divertor region of the tokamak, and possibly cover the entire vacuum vessel for the next generation of reactors after ITER (namely DEMO[4]) [10].

In a tokamak, the fusion reaction will involve deuterium and tritium, these combine to make a helium ion, a neutron, and 17.6 MeV of energy. If a tungsten sample is raised to a high enough temperature, and bombarded by helium ions, the surface layer will deform into a 'fuzzy-like' structure on the nanometre scale, sometimes reaching micrometres in layer thickness. This deformation is known as 'fuzzy tungsten' [11]. This has been confirmed multiple times in laboratory-scale plasma devices, and the first paper mentioning it appears to be by Takamura et al. in 2006 [12]. As there will be helium present due to the fusion reaction taking place, and as there will be sufficient heating of the wall in a tokamak, there is a high possibility that this will occur in ITER. If so, the degree to which it could be a negative or positive effect must be understood to better predict the operation of ITER. For example, tungsten tiles could erode more easily with fuzz developed on it, and if tungsten atoms get into the bulk plasma, it can quickly cease the fusion reaction by radiating away all the energy input to the plasma [7]. Thus research must be conducted to understand the nature of his phenomenon and it's attributes.

To date, most of the research on fuzzy tungsten has been performed using linear plasma devices (LPDs) [11]. Presented here, for the first time, is the formation of fuzzy tungsten

[4]DEMO stands for DEMOnstration plant.

in a DC magnetron sputtering device. The bulk of the work presented in this thesis is a study of the formation conditions of fuzzy tungsten in a magnetron sputtering device. The fuzz created here is compared with fuzz created by other devices, and a compilation of many results of fuzz covering several parameters sheds some new light on the formation of fuzz.

This thesis begins with chapter 2 providing a background on fuzzy tungsten, setting the scene for the nature of this research. In chapter 3 details of the experimental set-up are given. The initial calibration of the rig using various diagnostic techniques is explained in chapter 4. Chapter 5 describes the research into fuzz as a whole, and looks at compilations of a large dataset of fuzz whilst incorporating newly created data, providing new insight into the underlying growth mechanisms. In chapter 6 the results of the fuzz created in the magnetron device are presented and discussed. Finally in chapter 7 a conclusion of this thesis is provided, with a look to future work that could be explored.

Chapter 2

Literature Review

In this chapter a thorough background to fuzzy tungsten will be provided, highlighting key works from the literature and the current knowledge surrounding this field of research. At the end of this chapter a brief introduction to plasmas will also be provided putting them in the context necessary for this thesis.

2.1 Fuzzy tungsten

Tungsten fibreform nanostructure formation, often known as fuzzy tungsten, or simply 'fuzz', is a phenomenon whereby a tungsten (W) surface can be deformed by bombardment by helium (He) ions at elevated temperatures. In this section a background of the research thus far conducted on fuzzy tungsten will be described.

2.1.1 Visual description

First, a description of fuzzy tungsten should be provided. It owes its name to the structure, in that it looks fluffy or fuzzy. Fully grown fuzz, (that of several μm's) is a dense forest of tendrils, and has been visually compared to coral [13] and cotton [14]. An example of fuzz is shown in figure 2.1. Overall layer thicknesses can grow from around 100 nm to several μm's. The individual tendrils are around 20-50 nm thick. Fuzzy tungsten cannot be seen with the naked eye. However, as fuzz grows on a sample, the surface becomes optically black, decreasing in reflectivity as the thickness of the layer grows. Ueda *et al.* noted that after about 500 nm layer thickness, the samples are optically black, as is shown in figure 2.2 [15]. This can be used as a simple indicator for whether or not fuzz has formed, however, the early stages of fuzz may have formed on a sample with very little darkening occurring.

The structure is a growth process, the tendrils grow upward from the surface, rather than being an erosion process, as is shown in figure 2.3 [18]. The growth upwards also removes a little of the original surface below the original surface layer. Measurements

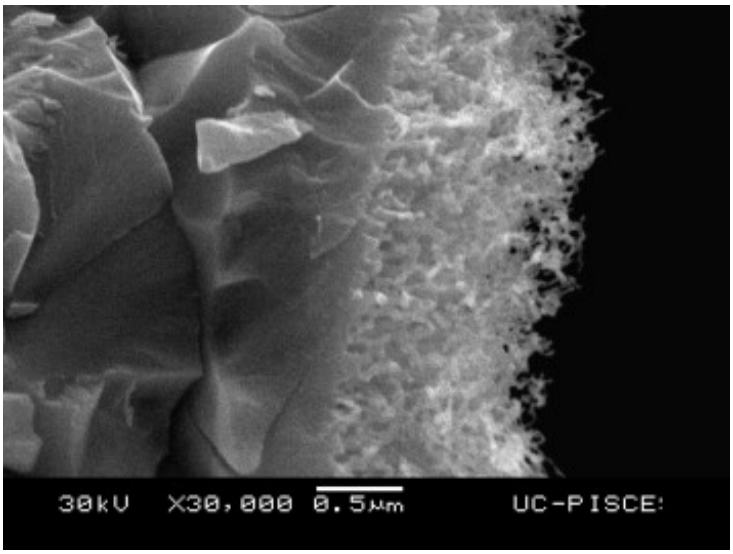

Figure 2.1. An example SEM image of a fuzzy W sample. Image taken from [16].

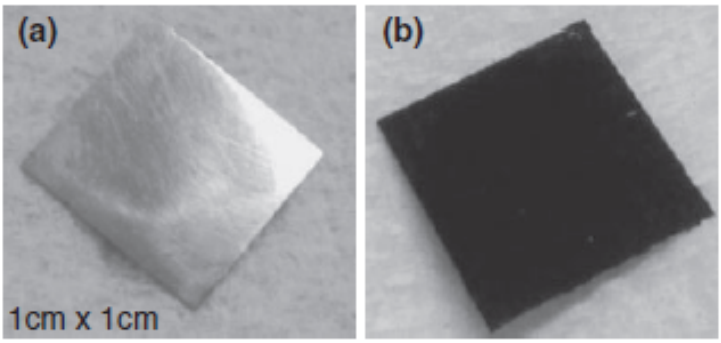

Figure 2.2. A photo of a W sample before and after fuzz growth, showing the blackness after fuzz growth. Image taken from [17].

were taken of the porosity of the fuzz layer, and it was calculated that in the images of figure 2.3, 94% of the fuzz layer is unoccupied space [18]. The dense structure seen in the cross-sections is due to the background fuzz being observable through the 94% unoccupied space, hence it seems like one dense layer. It is in fact lots of thin tendrils. Transmission electron microscopy (TEM) images of fuzz reveal the gaps in between the tendrils more clearly [19].

Upon inspection via TEM, bubbles can be seen inside the tendrils, giving rise to the idea that He ions upon impact with the surface coalesce as bubbles, see figure 2.4 [19]. Possible growth mechanisms of the fuzz will be discussed in section 2.1.5.

To confirm that the fuzzy structure is indeed tungsten, the compositional information was obtained using energy dispersive X-ray (EDX) analysis. In figure 2.5 it can be seen that the fuzz layer is indeed tungsten not a layer of deposition, with the impurities coming from the plasma chamber (in the case of carbon and molybdenum), and from possible oxidisation in moving the sample from the plasma chamber to the SEM [20].

Fuzz layers are easily removed from a sample with light abrasion, a simple scratch

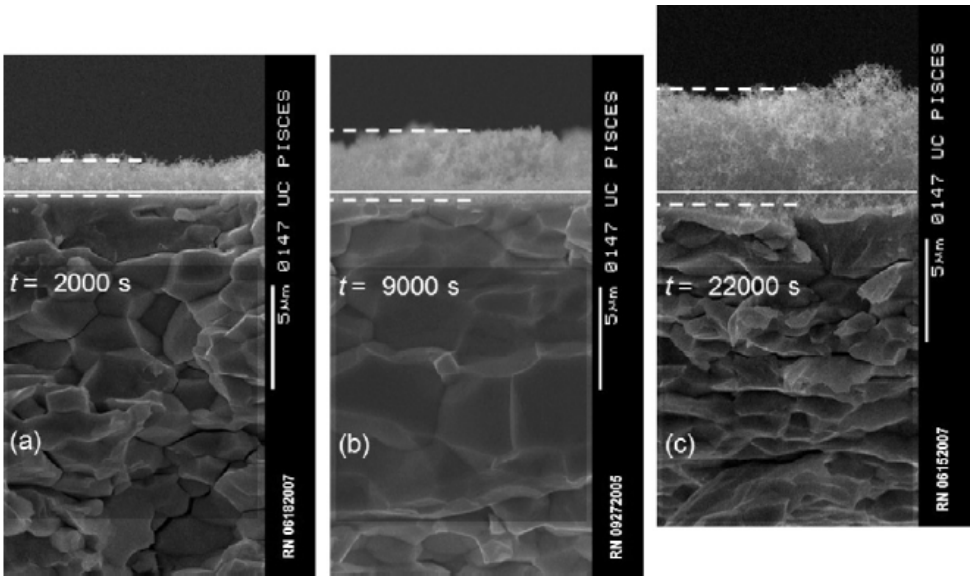

Figure 2.3. SEM images of fuzz grown for different lengths of time, showing that fuzz grows upwards from the original surface, whilst also removing a little of the original surface. Image taken from [18].

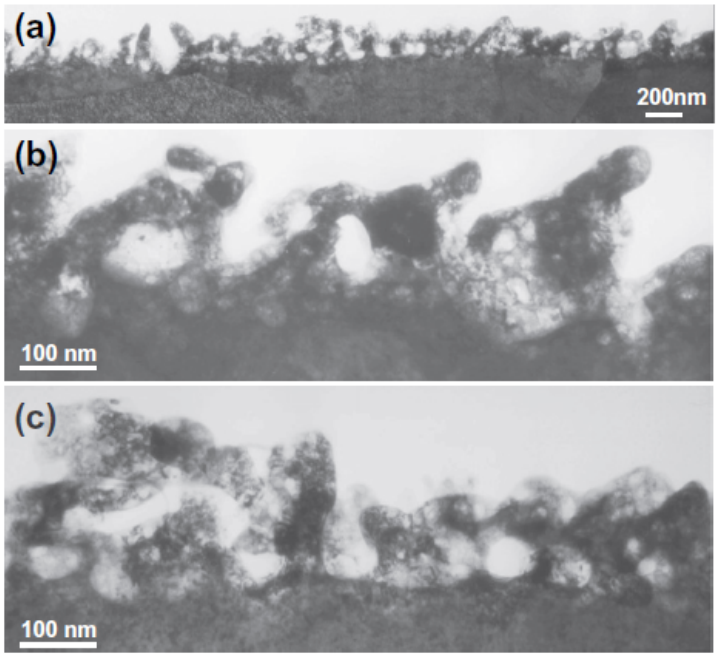

Figure 2.4. TEM images of fuzz close up, showing the existence of bubbles within the tendrils and the top of the surface. Image taken from [19].

with tweezers or even a wooden toothpick will remove the black layer, revealing the shiny metal surface underneath [18]. This has cast concern over fuzz potentially forming in future fusion tokamaks, as tungsten atoms are very efficient at converting energy input to the plasma into radiation, thereby wasting the energy that should otherwise be going to the D and T ions in order to cause fusion [21].

Fuzz is uniquely caused by helium, it has not been seen by exposure to any other atoms, although hydrogen and its isotopes do cause surface modifications, this is in the

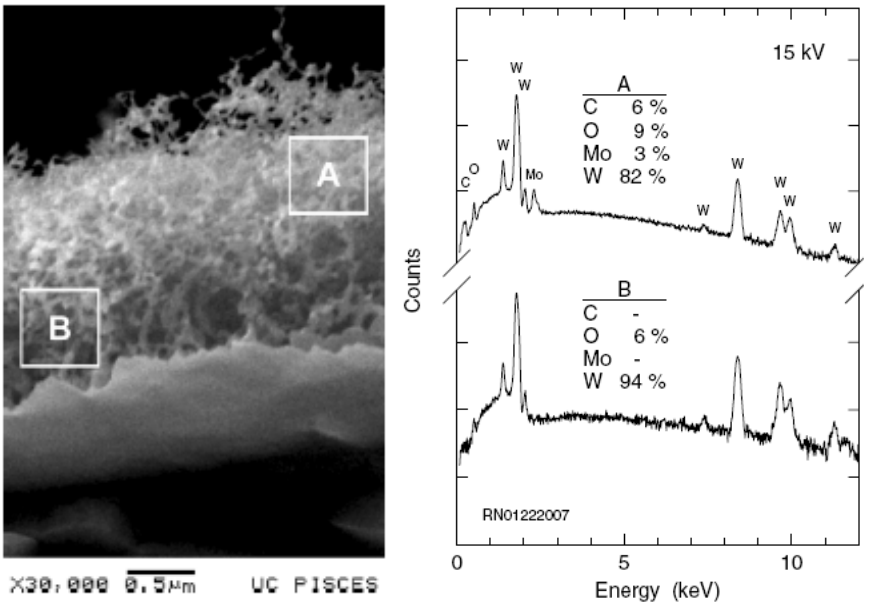

(a) (b)

Figure 2.5. EDX was performed on a fuzz layer, on the left the SEM image of the sample shows two highlighted areas, labelled A and B, which correspond to the two EDX spectra in (b). Small amounts of C and Mo are due to impurities from the vacuum chamber, and O could be due to surface oxidation before SEM imaging. Image taken from [20].

form of bubbles and blisters [22]. However, this is not unique to tungsten, and has been found on other metals, although tungsten has had the most research surrounding it due to it being a primary choice for plasma facing materials in future tokamaks. Fuzz on other metals will be discussed a little later in section 2.1.10, at this initial stage only fuzz on tungsten will be exclusively discussed.

2.1.2 The history of fuzzy tungsten

Damage of metals by bombardment from He ions has been known about and studied for several decades [23–29]. If He ions are incident on a metal, they form bubbles which can coalesce and burst leaving pinholes on the surface, as shown in figure 2.6. The damage caused by the He bubbles appears to have a temperature [29], and an energy dependence [28]. Fuzz on the other hand is a more recent discovery. The first case of making fuzz is believed to be by Ye *et al.* [30] in 2000. In [30], although the fuzz has not been confirmed by SEM imaging, the conditions to form it were fulfilled, and they reported darkening of the surface, a tell-tale sign of fuzz formation. In 2003 Tokunaga *et al.* reported in [31] seeing tiny morphological changes, fine structure, and the sample going black. The conditions were again fulfilled for fuzz to form, and thus it is quite likely they made fuzz. However, images of the tendrils were possibly beyond the capabilities of the SEMs and no image was provided. Thus it cannot be said for sure whether fuzz was formed in this work. The first SEM image of fuzz was brought to light in 2006 by

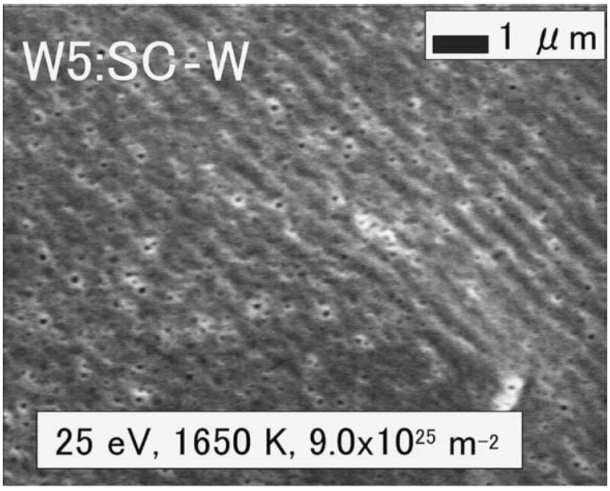

Figure 2.6. An SEM image showing He damage on a W sample in the form of hole formation. Image taken from [28].

Takamura *et al.* in [12]. This is the first occasion that tendril formation can be seen, sparking the community to research this new nanostructure formation. It is interesting to note that fuzz may have very well been created many times before hand, however, no-one attempted to look at such samples in the SEM, often dismissing the black appearance of samples as some impurity deposition or contamination [32]. The use of the name 'fuzz' was first used in 2010 by Baldwin and Doerner in [18] and has since been relatively universally adopted, however some authors still refer to it as 'nanostructure formation'.

2.1.3 Formation conditions

There are three main parameters surrounding fuzz growth, these are the temperature of the W surface; the energy of the bombarding He ions; and time. Kajita *et al.* in [33] performed a compilation of a number of experiments with He exposure to W samples charting each experiment in terms of the energy of the bombarding He ions and the surface temperature of the W sample. In the chart they marked whether fuzz formed, bubbles formed, or nothing appeared. An outline of the necessary requirements for each of these parameters will be discussed, working from Kajita *et al.*'s chart of [33] and work from other papers.

Surface temperature

Kajita *et al.*'s chart is shown in figure 2.7. From this chart and from most papers, a lower boundary has been put at 900 K, with some papers putting this a bit closer to 1000 K [33–35]. Some papers, including the chart of Kajita *et al.*'s chart, have placed an upper boundary on the temperature at 2000 K [11, 33], though there has been some similar structure found at higher temperatures, for example Nishijima *et al.* at 2300 K produced some tendril-like formation, only with tendrils several hundred nm's wide [36].

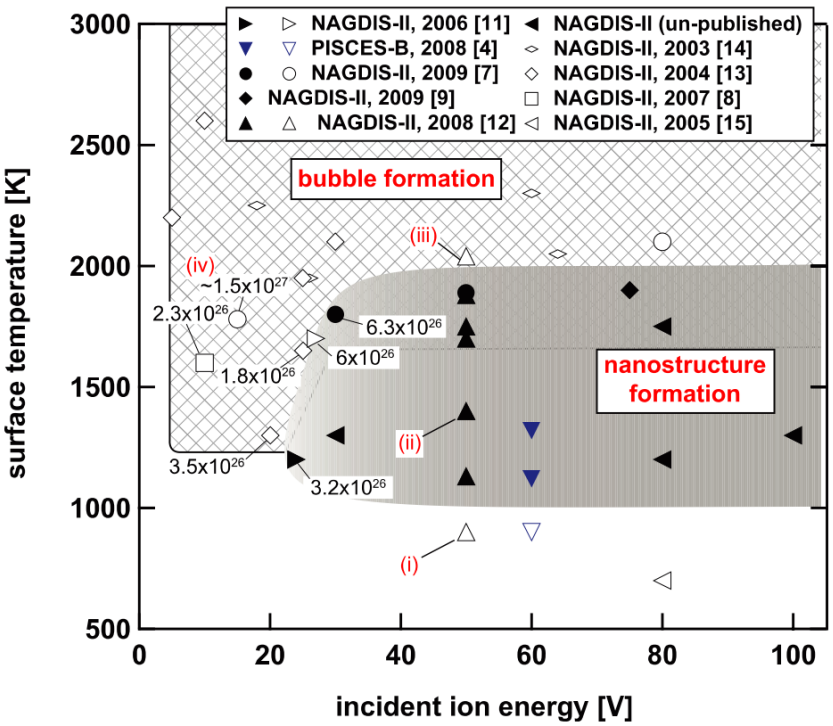

Figure 2.7. A compilation of experiments with He ions bombarding W samples, charting the He ion energy and the W surface temperature. Samples were marked whether fuzz was formed (filled-in shapes), bubbles formed (crosshatch grid), or nothing changed (open shapes at the bottom). Image taken from [33].

Also, at 2900 K, Tokunaga *et al.* found similar thick tendrils, although in this experiment the He ions were of 19 keV as opposed to the usual 10-100 eV used to generate fuzz [37].

Bombarding He ion energy

In terms of the energy of the bombarding He ions, papers have set a range of lower limits for fuzz formation, with the lowest being at 12 eV [12], however, Baldwin *et al.* found no change at 20 or 27 eV [38]. Kajita *et al.* also stated they found a minimum energy of 20 eV [33]. Many plasma devices are limited in their lowest energy possible being defined by the floating potential of the particular device. However, the discrepancies in lowest energy of fuzz formation has not been fully investigated, and perhaps other parameters, such as temperature, have an effect on this.

There does not seem to be a maximum on the energy required to form fuzz, with some reports seeing fuzz at 12 keV (at 1400 K) [39] and 19 keV (the 2900 K case) [37], though the tendrils in these high energy cases are much thicker than typical low energy fuzz. Of course, at energies above the sputter threshold energy for W (~108 eV) He begins to erode the growing fuzz sample, becoming a larger factor at higher energies. Thus at higher energies there will be a competition between growth and erosion. But there seems to be no upper bound on the energy for fuzz to form, and this is the least strict, and hence least investigated, requirement. Baldwin *et al.* in [38] reported that fuzz forms readily at

57 eV and therefore this will form a starting point for experiments within this thesis.

Exposure time/fluence

Baldwin *et al.* noted a square root of time ($t^{1/2}$) dependence of the layer thickness [20], this has been confirmed by many other authors who have also noticed a $t^{1/2}$ dependence [14, 19, 33, 40–45]. When considering the time of exposure, it is better to introduce the notion of fluence, which is the flux of He ions onto the W sample, multiplied by the time of exposure. Fluence takes into account the comparison between short exposures in high power plasma devices, and long exposures in low power plasma devices. In Baldwin *et al.*'s original paper, they say that fuzz can grow directly from $t = 0$ ($\Phi = 0$), whereas other authors have hinted that growth does not start at $t = 0$ but at some later t_0 (or Φ_0). Kajita *et al.* in [19] proposed a minimum fluence of $4{\times}10^{24}$ m^{-2} before fuzz can form.

2.1.4 ITER conditions

With ITER changing the divertor region to be fully W, one of the biggest concerns with fuzzy tungsten is whether it will occur in ITER, and if so, will it be an issue? To address the first question, the predicted conditions for ITER will be compared against the conditions necessary for fuzz to form, as just discussed in section 2.1.3.

Temperature

In ITER, the predicted temperature for a W divertor tile has most recently been presented by Pitts *et al.*, with the results shown in figure 2.8 [46]. With the minimum temperature for fuzz to form, of 900 K (627 °C), this is exceeded in every case. Looking particularly at the profile for the deuterium-tritium (DT) case[1], the length of this part is only ~7 cm, however this is expected all the way around the tokamak, and therefore is quite a large area of potential fuzz production[2].

Energy

It is necessary to discuss two possible plasma regimes in ITER, an attached plasma, or a detached plasma. An attached plasma is a regular plasma that is the default operation within tokamaks and plasma devices. A detached plasma is produced by injecting gas into the divertor region which reduces the energy of the particles colliding with the divertor tiles [48]. In an attached plasma the expected incident energies of the ions in the divertor region are >30 eV [7]. In such a regime, the energy is sufficient enough for fuzz to form. However, for a detached regime, the energy of the incident ions will be reduced to a few

[1] The operation of a DT plasma is currently the optimal route to creating fusion in tokamaks.

[2] The radius of the outer target is 5.5 m, thus the area of potential fuzz formation is ~2.4 m^2 [47].

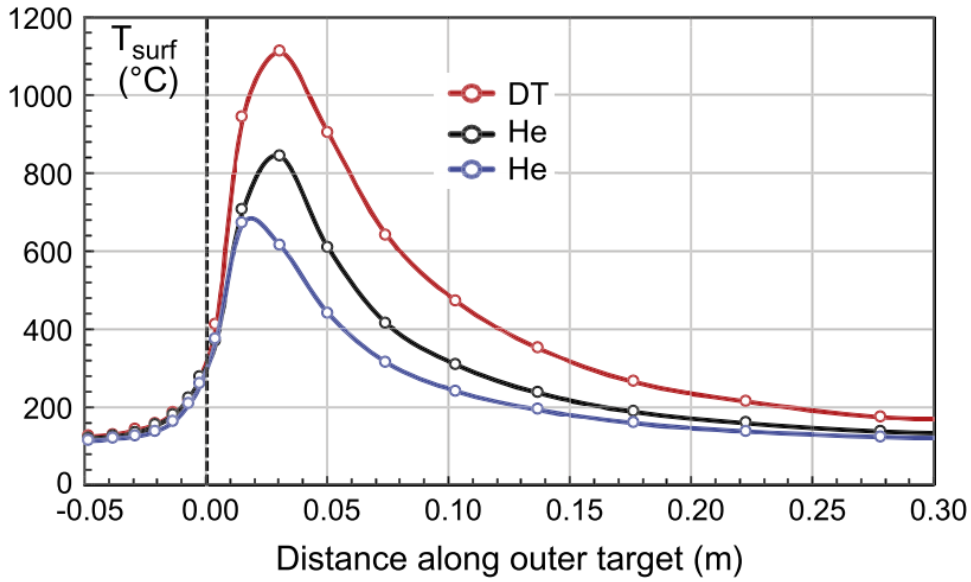

Figure 2.8. The predicted temperature profile of a ITER W divertor tile. Temperature profiles are simulated for different He and DT plasmas. Image reproduced from [46].

eV, possibly as high as 8 eV [49, 50]. In such a scenario the energy is most likely too low to form fuzz. Although until ITER is actually up and running it is hard to predict the energy of the incoming ions to the divertor.

Time/fluence

According to Brook *et al.* in [51], they predict the D-T flux to the divertor to be ~4×10^{23} $m^{-2}\,s^{-1}$, and as they assume that 5-10% of this flux is He, this will give the He flux of ~2×10^{22} $m^{-2}\,s^{-1}$, which will provide the predicted minimum fluence of 4×10^{24} m^{-2} in 400 s, which is precisely the predicted time for one full performance pulse of ITER [7].

2.1.5 Growth mechanisms

The first model proposed was by Kajita *et al.* and resulted from noticing the bubbles forming in the tendrils and below the surface in low fluence fuzz samples under inspection by TEM (see figure 2.4) [19]. The formation mechanism has been presented in a diagram, reproduced in figure 2.9. The idea is that upon exposing a He plasma to a W sample, nanometre sized He bubbles form just under the surface, as shown in figure 2.9a. These bubbles migrate and coalesce to form larger bubbles which begin to push up the surface causing blisters (fig. 2.9b). With more He irradiation some of these bubbles burst, which leads to the protrusions that eventually, with more bursting, resemble the fuzz structure (fig. 2.9c). Additional He bubbles begin to form inside these protrusions, and as these grow and burst the protrusions get longer and finer (fig. 2.9d). This model is a very simplistic model, and is more hypothetical, requiring more evidence. However it does introduce the idea of bursting He bubbles being a precursor to fuzz formation.

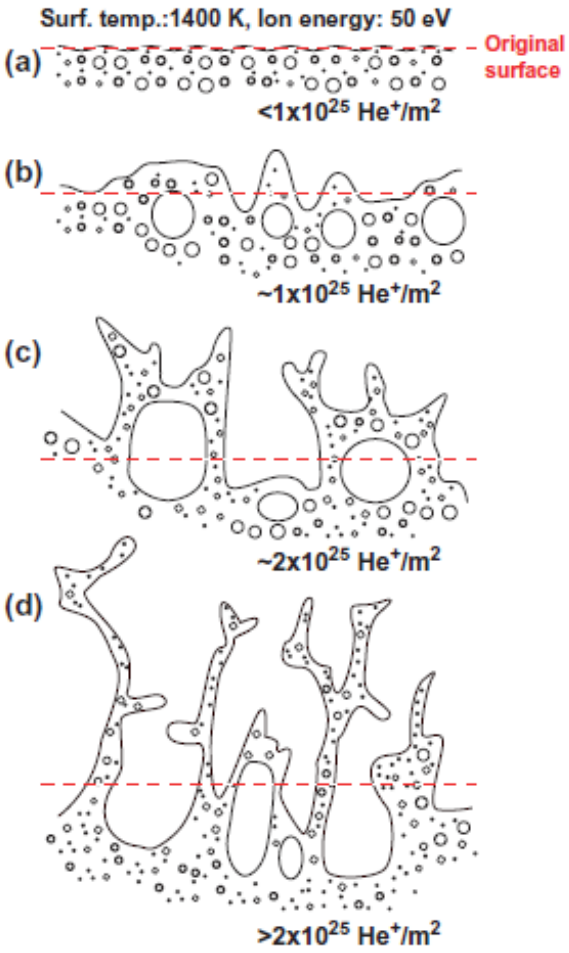

Figure 2.9. A diagram showing a possible growth mechanism of fuzz caused by growing and bursting He bubbles. Image taken from [19].

An alternative approach, with equations to support it, was proposed by Krasheninnikov [52]. The underlying principle here is based on the viscous flow of W atoms. A diagram of the theory is reproduced in figure 2.10. Again the initial stage is He ions penetrating the surface and forming bubbles, which coalesce to form bigger bubbles. Taking the surface W atoms into account, adjacent W atoms exert a force on each other. The W atoms near the surface will have an asymmetrical force exerted on them, in that on the surface side there are a few atoms, and on the bulk side there are the bulk atoms (essentially infinite). This forms a pressure difference either side of the W atoms near the surface, hence there is a net upward force on the W atoms. This force is also apparent on the bubbles that form, so the bubbles are forced upwards too. At high enough surface temperatures the effective viscosity of the W becomes low enough such that creep becomes important. This allows the W atoms to flow upwards around the bubbles (fig. 2.10a). As the protrusions grow, new bubbles form above the old ones and allow the W atoms to continue to flow upwards, leading to the formation of tendrils (fig. 2.10b). This model predicts the $t^{1/2}$ dependence of fuzz growth, it also predicts a strong temperature dependence of the growth rate, and the saturation of fuzz growth at ~2000 K, all consistent

with the literature (see section 2.1.3).

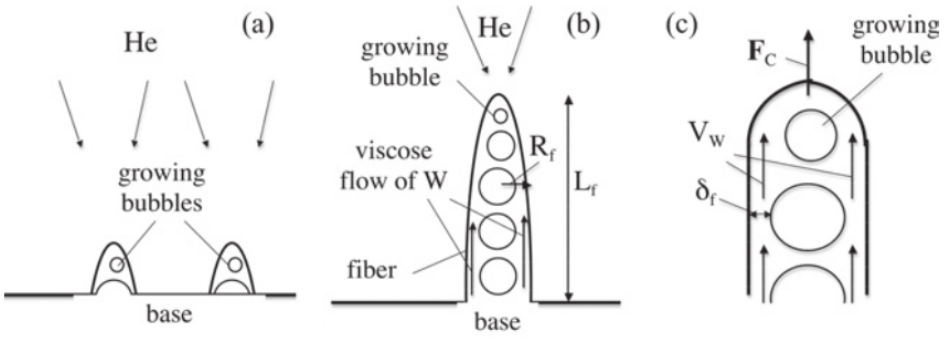

Figure 2.10. An alternative growth mechanism based on the viscous flow of W atoms. Image taken from [52].

Martynenko and Nagel propose another mechanism via adatom formation [44]. Adatoms appear on the surface upon being ejected from a surface layer. These adatoms form preferentially around unopened He bubbles. This proposed model gives the same $t^{1/2}$ dependence, arising from the kinetics of the adatom diffusion over the surface. In addition to a reason for the observed energy dependence ($\gtrsim$20 eV), due to the threshold energy for adatom formation.

Lasa *et al.* propose an alternative approach based on He bubbles causing the surface above to grow via loop-punching [45]. As the surface grows, the surface roughness increases. This increased roughness increases the surface area. The area of W atoms surrounding He bubbles is therefore increased, and bubble rupture is more likely, hence He retention rate decreases as the fuzz layer grows. As the retention rate lowers, therefore so to does the rate of loop-punching, and hence the growth rate of the fuzz. This proposed mechanism also gives rise to the $t^{1/2}$ observed dependence.

2.1.6 Possible concerns

There is some concern for fuzz in that the tendrils could be eroded in a tokamak environment, in addition, getting W atoms into the bulk plasma is very detrimental to the plasma [7]. During steady-state operation in ITER, fuzz may remain intact, however, disruptions and instabilities called '*edge-localised modes*' (ELMs) are a concern for ITER operation. ELMs are a type of instability characterised by periodic disturbances at the edge of the tokamak plasma which leads to expulsion of the edge plasma's energy and particles which reduces the confinement of the plasma [53, 54]. They can deposit energy on the divertor plate leading to high levels of erosion, being a concern for ITER regardless of the existence of fuzz [53]. The efforts to suppress them and mitigate their effects are on-going and are an active area of research.

For fuzz there is an additional concern due to the thermal conductivity of a fuzz sample being reduced by two orders of magnitude when compared to a clean W tile [55]. Kajita

et al. irradiated fuzzy samples with ELM-like laser pulses and found areas of melting, even though the temperature should have been below the melting point for W [55]. They proposed that this is due to the poor thermal conductivity of the tendrils. This could be detrimental for a PFM in ITER where ELMs are expected to be unavoidable at present. A follow up paper discussed the impact of fuzz in ITER during ELMs, suggesting that it could be a concern due to parts of the fuzz boiling and being ejected into the plasma [56]. The estimations of [57] show erosion on the order 0.01 mm over a 24 hour period due to ELMs.

Fuzz has also been shown to be more prone to the formation of arcs on the surface. Arcs were easily initiated with low energy laser pulses, which can also erode the W surface [58, 59]. Arcs could not be seen on a clean W sample, whereas for a fuzzy sample the probability of ignition of arcing was greater than 90% when He fluence was more than $2{\times}10^{24}$ m^{-2} [60]. Aussems *et al.* in studying arc ignition on fuzz suggested that fuzz prevention may need to be investigated due to the ease of arcing and mass loss involved [61]. Aussems *et al.* suggest that the mass loss for a W tile with fuzz on could be double the expected mass loss for a clean tile during steady-state operation [61].

Concerns for ELMs and arc ignition mentioned above do not take into account the potential swift re-deposition of W atoms. Brooks *et al.* suggest that there could be ~100% re-deposition due to the short mean free paths for ionisation of W atoms and the strong flow of the W ions back to the divertor due to collisions with the incoming plasma and the existence of the electric field [51]. Therefore W fuzz may not be a concern after all, as any eroded material will swiftly be re-deposited.

2.1.7 Positive features

There are some positive aspects of fuzz for tokamak operation. W was chosen to be the material of choice due to its much lower retention of T over CFC tiles [4, 5]. As such the amount of T retained is an important measurement. Due to T being a rare and expensive gas, laboratory studies of T use D gas. In measuring the retention of D in clean W samples and pre-fuzzed samples after exposure to D plasma, it was found that fuzzy samples retained much less D than clean samples [62, 63]. It was proposed that perhaps the He bubbles form a permeation barrier preventing the D from penetrating the bulk [62].

Nishijima *et al.* in [16] investigated the sputter yield of fuzzy samples and actually measured a decrease in the sputter yield with increasing fuzz thickness. They measured that the sputter yield drops to 0.15 that of a clean sample. They proposed this was due to sputtered particles from lower down in the fuzz getting trapped by the tendrils and hence not escaping the surface. This has also been confirmed in further studies by Takamura *et al.* [64], where the sputter yield became ~0.2 of a clean sample.

It has been shown that the existence of fuzz can prevent cracks forming in heated samples. For a mirror-finish W sample cracks were observed after one plasma pulse of ~0.7 MJ m^2, whereas fuzz samples with thicknesses between 1-3 μm did not show signs of cracking after 10 of these shots [65]. This is speculated to be due to the increase of effective surface area due to the porous structure of the fuzz dissipating the energy further around.

Further to this, there are some experiments that seem to show that fuzz increases cooling for a W sample. In [66], Takamura *et al.* showed that the surface temperature of a fuzzy sample decreased much more over time than a clean sample when exposed to a constant plasma. A follow-up paper was recently published which investigated the temperature of surfaces exposed to two different heat sources, measuring the temperature by thermocouples and by IR pyrometers, Takamura showed that the temperature of fuzzy samples was almost 400 degrees lower than a clean sample [67]. This is proposed to be due to the blackening of the surface and it becoming more black body-like with fuzz formation.

Lastly, it has been reported that the secondary electron emission (SEE) of fuzzy samples is decreased as compared with clean samples [68]. Takamura *et al.* measured a decrease in the floating potential of W surfaces over time, as fuzz was grown. They propose this reduction in floating potential may be due to the reduction of effective SEE due to the fuzz preventing the emission of the electrons from the bulk to the sheath region.

2.1.8 Other aspects

There is some potential interest for the generation of fuzz outside that of fusion research. When fuzz grows the samples go from a shiny metal finish to a deep dark black, with very little reflectivity. Kajita *et al.* measured the reflectivity of clean and fuzzy samples and showed that it was nearly zero [69]. Kajita *et al.* summarised, in relation to previous research and understanding, that this is the darkest man-made metal ever. They proposed that this could potentially have a place as a medium in solar thermophotovoltaic (TPV) cells in that it absorbs approximately 98% of the solar spectrum and emits in the infra-red.

Another possible use for fuzz is in the photoelectrochemical (PEC) splitting of water molecules. Photo-emitted current can split water into hydrogen and oxygen gas. The hydrogen can be used as a fuel and hence is a way to store solar energy. De Respinis *et al.* showed that if you oxidise a fuzzy surface into WO_3 it has a much higher photon-to-current efficiency than WO_3 created by other methods [70].

There is also cause to believe that due to the high surface area of fuzz samples they could be used as catalysts [69, 71]. This has yet to be proven though.

2.1.9 Simulations of fuzzy tungsten

There have been several attempts to model the growth of fuzz although the growth mechanisms are not fully understood. Various approaches have been used, including molecular dynamics (MD) simulations [41, 72–79] , density functional theory (DFT) [80, 81], binary collision approximation (BCA) [82], and kinetic Monte Carlo (MC) [83]. Simulations have shown some underlying principles occurring with W irradiated by He ions. Firstly, He atoms strongly favour clustering together as bubbles in W vacancies [72, 73, 76, 80, 83]. The cluster size seems to be able to support 9 He atoms [80]. Larger bubbles have been shown to be favoured by higher temperatures [41]. Clusters with >8 He atoms can cause Frenkel pairs (a vacancy and a displaced interstitial W atom) [72]. The displaced W atoms can migrate to the surface as adatoms [75], leading to surface roughening [72]. The He bubbles have been shown to migrate creating dislocation loops as it moves causing new clusters to form [78, 79]. He bubble rupture has been shown to occur as the surface above the bubbles thin to the point of rupture, providing early stages of fuzz growth [72, 74]. The $t^{1/2}$ relation has also been shown to occur in some simulations [41, 84].

The uniqueness of He (over other noble gasses) causing fuzz has been shown to perhaps be due to He ions having greater penetration depths at below sputter threshold energies [82]. Also, H-H clusters are shown to be unstable, whereas He-He clusters form strong bonds [83]. The reduced D retention as described in section 2.1.7 has been supported by a simulation showing that He bubbles can trap H and interrupts or disturbs the H diffusion in W [85]. An attempt to simulate the reduced sputtering yield of He irradiated W (as shown in section 2.1.7) showed no reduction with He fluence. The authors do note, however, that they need to look to larger fluences [77].

A recent simulation by Ito *et al.* explained the drawbacks of separate simulation methods [84], describing how MD simulations incorporate large fluxes, but operate on very short time-scales, this does not give the He atoms time to diffuse and so cannot fully portray what is happening. However, Ito *et al.* have created a hybrid simulation which uses MC to simulate the diffusion of atoms, and MD to simulate the deformation, with each step passing information between the two codes [84]. The images produced from Ito *et al.*'s hybrid simulation seem to be the most promising yet, showing early stages of fuzz formation with small tendrils appearing due to bubbles rupturing. Fluences in this simulation are still very low compared to experiments, being on the order of 10^{21} m^{-2}. There is still no simulation that recreates the long tendril formation seen in experiments on a scale closer to the experimental seen fluences of 10^{24} m^{-2}.

2.1.10 Fuzzy structure on other metals

Fuzz formation is not unique to W, it was found first on W, and research is mainly involved with W due to its use in ITER. It has, however, been found on other materials, such as

molybdenum (Mo) [33], nickel (Ni) [71], iron (Fe) [71,86], and titanium (Ti) [57,71]. Each of these has shown similar fuzz, as shown in figure 2.11. However, the authors of these papers note the difficulty in forming the fuzz in a repeatable manner, as they are dealing with lower temperatures which are harder to achieve in linear plasma devices and with He ion energies above the sputter threshold [57].

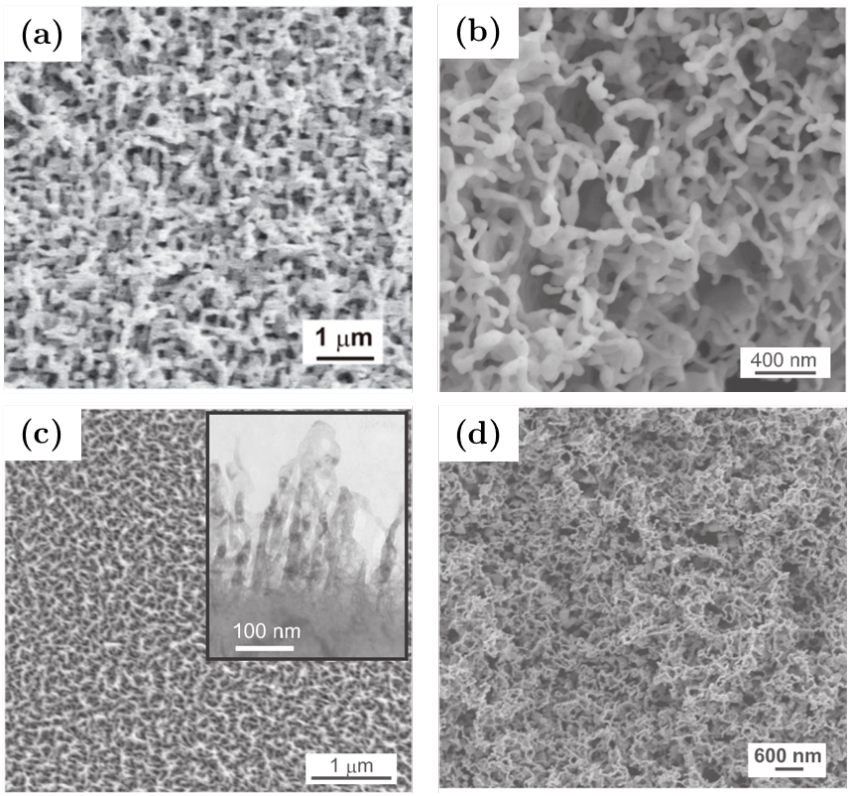

Figure 2.11. SEM images of fuzz formed on metals other than tungsten, where (a) is molybdenum [33], (b) titanium [71], (c) nickel [71], and (d) iron [71].

Attempts with other metals are harder to find, as the conditions for each metal have not been studied yet. Kajita *et al.* propose that the temperature window for fuzz formation is a function of the melting point, T_m, of the subject metal, such that some studies try to keep T/T_m constant for each metal [41]. For W, with T_m = 3695 K, the temperature window as discussed in section 2.1.3 is 900 - 2000 K, such that the window of opportunity for other metals should be 0.25 - 0.55 T/T_m. The He fluence necessary to create fuzz on other metals appears to be in the same region as for tungsten with most attempts quoting a fluence on the order of 10^{26} m^{-2}, although it is noted that the thicknesses of fuzz created at such fluences is much less than that created with W [71]. The energy requirement for fuzz formation on W is not a strict requirement, however, with lower threshold energies the competition between sputtering and growth becomes more important. In table 2.1 the potential temperature windows are provided for a few materials, as well as the sputter threshold energies for ease of reference when deeming whether an attempt to make fuzz on other materials is relevant.

Metal	T_m (K)	0.25-0.55 T_m (K)	E_{th} (eV)
Tungsten	3695	900-2000	104
Molybdenum	2896	720-1590	45
Rhodium	2236	560-1230	40
Titanium	1941	485-1070	17
Nickel	1726	430-950	19
Copper	1357	340-750	16
Aluminium	934	230-510	7.6

Table 2.1. Potential temperature windows for fuzz to form on other metals. Threshold energies calculated from equation 2.1 using values from [87, 88].

Potentially fuzz could also be made on copper (Cu), with images looking similar to fuzz. Attempts have also been made on aluminium (Al) but the result is not fuzz-like, this could be due to the temperature for Al studies at T = 0.56 T_m [89]. An attempt was made on rhodium (Rh), with no fuzz formed, however, the fluence was only 3.7×10^{25} m^{-2}, also the He ion energy was slightly above the sputter threshold [90]. However, the reflectivity of the Rh samples was measured to be decreased, hinting at early stages of fuzz formation, perhaps with longer fluences this will be possible. Nanocones, also seen in Ti, have been made on stainless steel [71], however, due to this being an alloy, it is harder to determine formation conditions and was hence omitted from table 2.1.

2.1.11 Devices for making fuzzy structures

To date, most of the research on fuzzy tungsten has been performed using LPDs. There are 5 major LPDs in operation working on fuzzy tungsten, they are the PISCES-A and PISCES-B devices at the University of California at San Diego, USA [91,92], the NAGDIS-II at Nagoya University, Japan [93], and the Pilot-PSI and Magnum-PSI located at the DIFFER institute in the Netherlands [94, 95]. LPDs are long metal columns (1-5 m) in which a vacuum is maintained via pumping systems. At one end a plasma is generated, either by a heated LaB_6 cathode (as is the case for PISCES-A, PISCES-B, and NAGDIS-II) or by a cascaded arc source (as is the case for Pilot-PSI and Magnum-PSI). The plasma then travels down the main chamber and is confined by a magnetic field generated by large coils surrounding the chamber. LPDs provide high fluxes of ions and one of their main research avenues is in simulating the divertor region of tokamaks such as ITER or DEMO. Typical fluxes are on the order of 10^{22}-10^{24} $m^{-2}\,s^{-1}$, with ITER divertor fluxes expected to be $>10^{23}$ $m^{-2}\,s^{-1}$, and 10^{23}-10^{24} $m^{-2}\,s^{-1}$ for DEMO. Other devices have been used to generate He ions, and theoretically any device that can i) create a sufficient He fluence of $\sim10^{24}$ m^{-2}, ii) free from serious impurities, and iii) can simultaneously have the W sample held at temperatures between 900-2000 K whilst iv) biasing the sample with at least -30 V (if not lower), could create fuzz.

2.1.12 Evidence of growth in a tokamak

Although fuzz can be made in the laboratory with relative ease, especially in LPDs, it is predicted that it could potentially occur in ITER, but current tokamaks simply do not reach the temperatures for fuzz growth under normal operation (disruption temperatures are high enough, but create quite erosive conditions [96,97]). Also, most tokamaks did not have tungsten tiles until quite recently. More importantly, tokamaks do not often operate with He or tritium, for ITER the He is expected to come about due to the deuterium (D) + tritium (T) reaction. Only two tokamaks have ever operated with tritium, being JET and the TFTR during the D-T campaigns in the 90's [2,98]. However, at the time, these tokamaks did not have any W tiles installed. Tritium is a very rare radioactive isotope, and is hence rarely used. However, even if there was He and the temperature was hot enough there is speculation as to whether the conditions are too harsh for fuzz to grow.

Laboratory plasmas differ from tokamaks for many reasons as pointed out by Ueda *et al.* in [14,15] and by Wright *et al.* in [99]. For example, the angle of incidence of the ions, in LPDs you have normal incidences, whilst in tokamaks it is glancing [14,99]. In tokamaks ions are not 'cold' by definition, which they are in LPDs [99]. The parallel heat flux, (parallel to the W tile) is much higher in tokamaks, also the sheath distances are much smaller in tokamaks too [99]. There are other differences too, and these point at the possibility that perhaps when it comes to ITER, fuzz actually may not grow. But despite the differences, Wright *et al.* showed in 2012 that fuzz can grow and survive in a tokamak [99]. The experiment was conducted in the Alcator C-mod tokamak at MIT, USA [100]. As surface temperatures do not get to sufficient temperatures under normal operation Alcator C-mod has a section of the divertor specifically designed to be further into the plasma than one would want, in order to study heat loads. A W Langmuir probe was placed on these ramped tiles with the surfaces angled 11° into the parallel heat flux and were scanned from -150 V to 50 V in a triangle wave at 100 Hz. With 14 He discharges it was deemed that there was 12.7 s of exposure time, with a fluence on the order of 10^{25} m^{-2}. With such a small exposure time fuzz was apparent after observing the sample under SEM. The fuzz was measured to be 600±150 nm. This result makes it much more plausible that fuzz could occur in ITER.

An interesting presentation at the 14th PFMC conference in Jülich, Germany 2013, by CPC Wong, showed work on an experiment where they pre-made some fuzz, then placed it in the DIII-D tokamak at General Atomics, San Diego, USA, and purposely encouraged disruptions to see what effect it would have on the samples [101]. The fuzz was exposed to 3 vertical displacement events (VDEs) with a heat load of ~20 MW m^{-2} for ~4 ms. Surprisingly, the fuzz remained entirely intact apart from a few arc trails where the fuzz was removed. This result hints that fuzz may be able to survive some disruptions in a tokamak, implying that it may not lead to enhanced erosion of the W tiles.

2.1.13 Removing fuzzy structure

In the scenario that fuzz is deemed a problem for tokamak operation and it is required to be removed, experiments have shown that if a fuzzy sample is annealed at high temperatures the fuzz simply re-integrates back to a clean sample, with no mass loss. The annealing in these papers is carried out separately after growth of fuzz is established. Baldwin and Doerner showed that annealing up to 1900 K produced reintegration of fuzz [18]. Kajita *et al.* studied the competition between annealing out and growth of the fuzz, and noted that fuzz started to be annealed out at 1400 K, with almost all fuzz removed after 10 minutes [102]. Recent work by Meyer *et al.* showed that with 30 minutes of annealing at 1300 K the fuzz was almost entirely re-integrated back into the bulk [103][3]. It is possible that fuzz can be annealed at lower temperatures if maintained for a longer time. These hint that whilst growing fuzz at high temperature there must be a competition between the growth and the annealing-out of fuzz.

For fuzz studies at temperatures at >1400 K, it is therefore necessary to consider that fuzz layer thickness may be lower than that created at the same fluence but a lower temperature.

It has also been noted that small levels of Be or C impurities can prevent fuzz from growing, favouring instead the formation of a Be-W alloy or C film on the surface preventing fuzz from forming [104–106]. Al-Ajlony *et al.* found that with only 0.01% C atoms present in the flux of He ions incident on a W sample the fuzz is almost non-existent, only apparent in small isolated 'islands', with the majority of the surface showing a smooth finish of a tungsten carbide film [106].

2.2 Introduction to basic plasma concepts

As plasmas are used as a source of He ions in almost all cases of making fuzz and for the work presented in this thesis, it is fitting to provide a brief introduction to them.

Plasmas are considered by many to be the fourth state of matter. Although some purists dislike the definition, it serves as a simple way to introduce the concept. In a gas the neutral particles are free from other particles and consist of atoms with a positive nucleus of neutrons and protons and a negative cloud of electrons surrounding it. If these electrons gain enough energy, through collisions or excitation, they can be removed from the confines of the nucleus, thus ionising the atom. This leaves the positive nucleus in the form of an ion, and one or more electrons. In a plasma, the atoms have been ionised such that it is now a collection of ions and electrons which exhibit collective behaviour. As the positive and negative charges cancel each other out, it is defined as being *quasi-neutral*,

[3] This is strange fuzz formation, being formed at very high energies (0.2-12 keV), the tendrils were much wider than usual, being ~200 nm wide. As such, this result is viewed with an air of caution.

meaning on large enough length scales the net charge is zero. Plasma can also screen out any applied charge by surrounding it with the opposite charged species. This can be achieved on sizes on the order of Debye lengths, λ_{De} (typically ~10 μm), and within time-scales on the order of the inverse of the plasma frequency, ω_p (typically ~40 μs) [107]. This ensures that the overall quasi-neutrality of the plasma is maintained.

Plasmas can be classed into two forms of plasma, thermal and non-thermal. In a thermal plasma the temperature of the electrons, T_e, and the temperature of the ions, T_i, are the same. Such plasmas are usually very high energy plasmas, as is the case in fusion tokamaks, arc welders, and arc cutters. On the other hand, in non-thermal plasmas, the electron temperature is usually much higher than the ion temperature ($T_e \gg T_i$). The ions in this case, being originally low temperature neutral particles, are ionised by high energy electrons colliding with them. These plasmas tend to be found in laboratories and industries and are known as technological plasmas. In such plasmas there are relatively few ionised particles compared to the number of neutral particles still remaining (~0.01-1%) and as such the charged particles can often interact with the neutrals. This thesis involves the use of technological plasmas.

The basic generation of a technological plasma can begin by taking a grounded vacuum chamber and filling it with a gas. Typically noble gasses are used, such as argon or helium, as these are easy to ionise, however, plasmas can be generated in other gases. A target, often being a metal disc, placed inside the vacuum chamber in contact with the gas, is then biased to a negative voltage on the order of several hundred volts (depending on the neutral gas). In the neutral gas, there are some naturally occurring free electrons, this could be due to collisions with other neutrals, or ionised by cosmic rays. These free electrons are accelerated by the negative bias of the target and collide with neutral atoms in the gas. This can cause ionisations of the neutral particles, leading to the generation of an ion and an additional electron. This new electron is again accelerated by the bias, and goes on to cause more collisions, and hence an avalanche effect occurs. This leads to the generation of positively charged ions and electrons, i.e. a plasma.

2.2.1 Sputtering

The positively charged ions created in the gas are attracted to the negatively biased target. Upon hitting the metal target, if the ion energy, E_i, is high enough, then the collision can lead to a metal target atom being ejected. This effect is called sputtering and depends on the species of gas and metal target used. The energy necessary for this is called the sputter threshold energy, E_{th}, such that sputtering occurs if $E_i \geq E_{th}$. The threshold energy for sputtering to occur is given by [88],

$$E_{th} = \frac{(M_i + M_t)^2}{4 M_i M_t} E_s \tag{2.1}$$

where M_i and M_t are the ion and target atomic mass, respectively, and E_s is the surface binding energy. The ejected target atom is usually a neutral particle that is free to float through the chamber and be deposited on the chamber walls. This is the method by which many thin films are made in industry. A useful measure for the rate of removal by sputtering is the sputter yield, Y, given simply as,

$$Y = \frac{\text{flux of ejected atoms}}{\text{flux of incident ions}} \tag{2.2}$$

Typical values for Y are >0.4 for a range of metallic targets using argon gas at usual operating conditions [108].

As technological plasmas are weakly ionised, the mean free path must be taken into account to ensure that the sputtered particles can make it to the substrate, being the area where the depositing film is being grown (conventionally facing the target). The mean free path, λ_m, is given by [107],

$$\lambda_m = 1/n_n\sigma \tag{2.3}$$

where n_n is the density of neutral atoms per m^3, and σ is the cross-sectional area of the neutral atoms.

2.2.2 The sheath

In plasmas, any potential placed inside of it will be surrounded by a cloud of charge, screening the potential from the bulk plasma. At the edge of the cloud the thermal energy of the particles can be sufficient to escape this electrostatic potential well, thus the actual edge of the cloud is where the thermal energy of the particles is approximately equal to the potential energy of the well,

$$eV = k_B T \tag{2.4}$$

where e is the electron charge, V is the potential placed in the plasma, k_B the Boltzmann constant, and T the particle temperature. Following through some math, as done in Chen's book [107], one can arrive at the distance of the edge of this screening cloud, λ_{De}, the Debye length, given by,

$$\lambda_{De} = \left(\frac{\epsilon_0 k_B T_e}{ne^2}\right)^{1/2} \tag{2.5}$$

where ϵ_0 is the permittivity of free space, and n is the density of the bulk plasma. The number of particles in such a cloud, known as a 'Debye sphere' can be easily calculated as,

$$N_{De} = \frac{4}{3}\pi n \lambda_{De}^3 \tag{2.6}$$

Plasmas have three requirements in their definition, i) that $\lambda_{De} \ll L$, where L is the

length of the chamber the plasma is in, and ii) $N_{De} \ggg 1$ [107]. The third and final criteria for a plasma requires that there are not too many collisions of the ionised particles with the neutral gas. If ω is the frequency of typical plasma oscillations, and τ the average time between collisions of the ions with the neutral gas, the third requirement is iii) that $\omega\tau > 1$, ensuring that the behaviour of the plasma is not governed by collisions with the neutral gas.

Any surface in contact with a chamber will have a sheath surrounding it, therefore whenever fuzz is being grown via He ions in a plasma, a sheath will surround the W sample. The potential drop from the ions in the plasma across the sheath to the sample is given by,

$$V_i = V_p - V_B \tag{2.7}$$

where V_i is the potential drop of the ion, V_p is the potential of the bulk plasma, and V_B is the bias on the W sample. Therefore the ion energy bombarding the sample, E_i, will be given simply by $E_i = V_i$ in electron volts (eV). This is sufficient as long as the sheath can be considered collision-less, in the sense that the ions do not collide with the neutral atoms through the sheath before hitting the sample, lowering their energy in doing so. This requirement is expressed by needing $\lambda_m > \lambda_{De}$.

2.2.3 Magnetron sputtering devices

Originally plasma devices were simply metal plates separated by a dielectric material, usually a gas, however the magnetron incorporates a ring of magnets behind the metal target causing the electrons to remain in a dense halo close to the target. This dense region of electrons generates a more dense plasma than was previously possible without magnets, and allows operation at much lower pressures. They were developed originally for the deposition of functional thin films in industry, with the films being deposited by the sputtered neutral target atoms [109]. For the purposes of growing fuzz they provide a good source of ions which can be drawn to a negatively biased sample. The experimental process in this thesis used a magnetron in a non-conventional way, by using a W target and a He gas the deposition is very low, with a sputter yield of ~0.003 atoms/ion (with ion energies of 300 eV) (compare with typical values of >0.4 for argon ions on a typical metal target) [108].

LPDs provide a high flux of ions, and as a by-product of this high flux the bombarded samples attain sufficient temperatures for fuzz to occur without the need for additional heating. However, this limits the control over the temperature as it is coupled to the plasma parameters. In order to change the temperature the plasma conditions have to be changed. This makes it difficult to correctly analyse a temperature range whilst keeping either a constant He^+ ion fluence or constant ion bombardment energy. Magnetron sputtering plasma sources produce a much lower incident ion flux on the W sample compared

with typical LPDs, thereby preventing excessive heating by the ion bombardment, and hence decoupling the surface temperature from the plasma properties, making it possible to control the temperature of the sample by utilising a separate heating method. This enables the study of the temperature requirements of fuzzy tungsten whilst keeping other parameters constant.

The lower fluxes found in magnetron sputtering devices (MSDs) imply that for equivalent fluences an MSD would have to be run for much longer times, though this can still be used as a tool to study the fuzz formation in the early stages, an area fairly overlooked. MSDs offer other benefits over LPDs as comparatively, MSDs are much smaller in scale, and they are also cheaper and simpler to set-up, thus if fuzzy tungsten can be produced in such a device, possibilities are opened for much more research to be conducted on the phenomenon.

Chapter 3

Experimental Setup

In this section the experimental apparatus used throughout this research will be explained. It will begin with an overview of the experimental rig, as it stood for the majority of the experiments, including an explanation of the vacuum chamber, the pumping system, the magnetron sputtering source, the sample heater, and the temperature sensors. The plasma diagnostic techniques used are also explained in this section. A brief description of the devices used at the University of California at San Diego (UC San Diego) will also be provided.

3.1 The apparatus

All of the experiments based at the University of Liverpool were carried out in a cylindrical, stainless steel vessel supplied by Gencoa Ltd, 600 mm in length, and 388 mm internal diameter. A photo of the rig and a schematic for the most common set-up are shown in figures 3.1 and 3.2, respectively. This set-up was used for chapter 6, but only differs slightly from the other sections. Where it does differ, the changes to the set-up will be explained. The chamber was pumped using both a rotary pump (Edwards E2M40), and a turbomolecular pump (LEYBOLD Vacuum Turbovac 1000) in series. The base pressure that could be achieved was of the order of 10^{-4} Pa. Helium gas of 99.9995% purity (supplied by BOC) was fed into the chamber through a needle valve and the pressure monitored using three pressure gauges. A Pirani gauge (BOX Edwards APG100) monitored the pressure from atmosphere down to 10^{-2} Pa, an inverted magnetron gauge (BOC Edwards) monitored pressures in the range $10^{-2} - 10^{-4}$ Pa, and lastly a capacitance monometer (MKS Baratron® Type 627) monitored the working pressure with a typical range of $1 - 6$ Pa. The pressure gauges are shown in figure 3.2 labelled as P1, P2, and P3, respectively.

A V-Tech™ 150 magnetron sputtering source (Gencoa Ltd.) mounted on one side of the chamber was used to generate the plasma. The axial position could be varied by ~50 mm. The sample holder and heater was situated facing the magnetron on the same

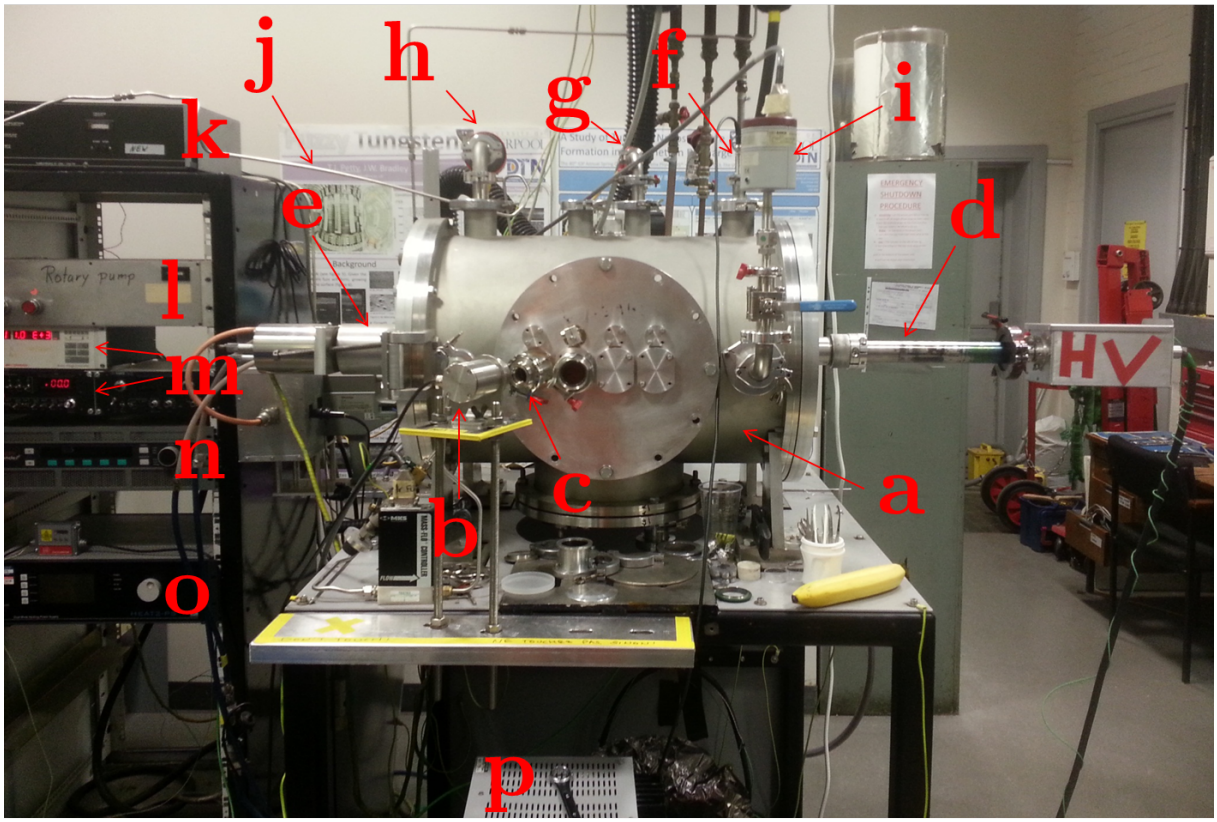

Figure 3.1. A photo of the experimental apparatus used for the majority of this thesis. Labelled parts are: a, the vacuum chamber, b, the IR pyrometer, c, the sapphire window, d, the feedthrough for the heating cables and the rod that held the sample holder, e, the magnetron, f, the feedthrough for the sample bias, g, the pirani gauge, h, the inverted magnetron gauge, i, the Baratron gauge, j, the He gas input line, k, the turbo controller, l, the rotary pump controller, m, the pressure gauge displays, n, the magnetron power supply, o, the sample heater power supply, and p, the sample bias power supply. The pumping system is behind the rig in this picture.

axis, mounted on a long cylindrical pipe allowing the wires to pass through the back of the chamber. The temperature of the samples were either monitored by an IR Pyrometer (CTLM-3H1CF4-C3, Micro-Epsilon UK Ltd.) through a sapphire window, or by type-k thermocouples. A HEAT-2PS power supply (PREVAC) connected to a filament behind the samples was used to heat the samples to the required temperature.

3.1.1 The magnetron sputtering device

The V-Tech^{TM} 150 magnetron used in this study is an unbalanced, circular planar magnetron. It was equipped with a tungsten target disc of 150 mm diameter and 6.35 mm thick. Behind the target is an array of permanent magnets in a ring formation creating a magnetic field around the target. The target is held down by a stainless ring which protrudes from the target by about 5 mm, keeping it in contact with the water-cooling

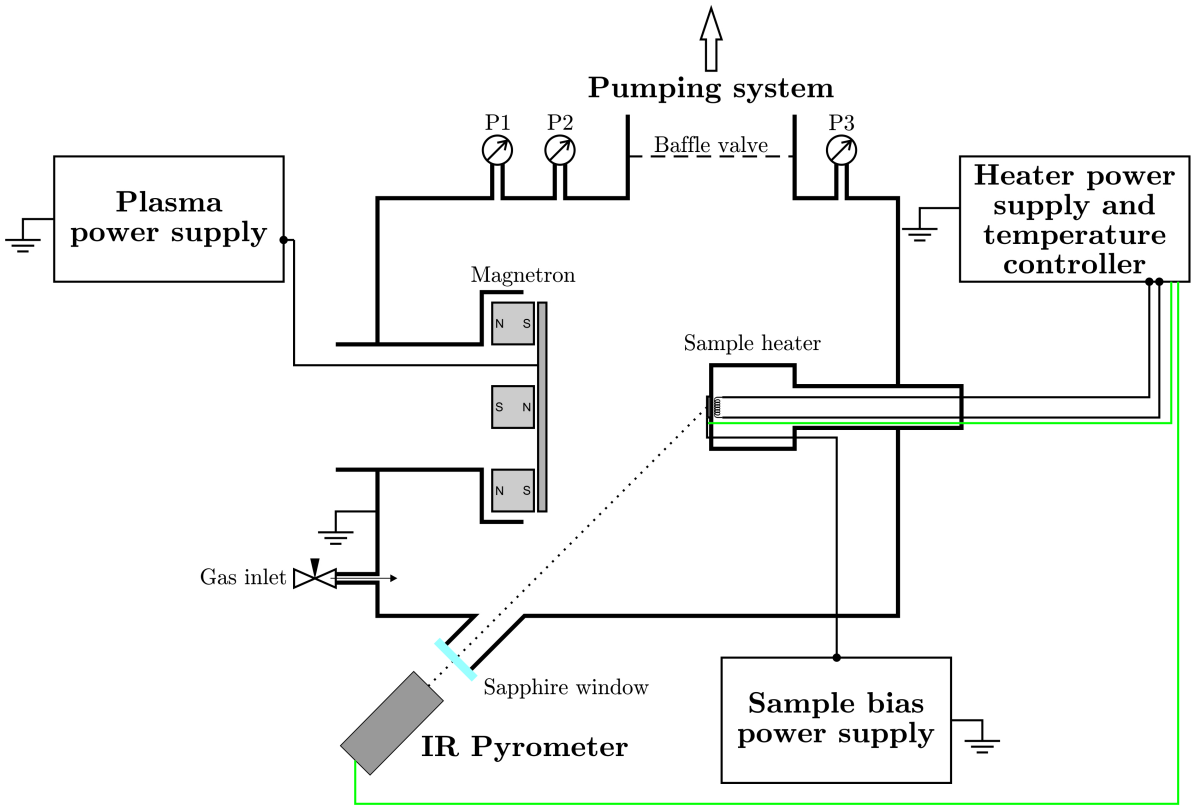

Figure 3.2. A schematic showing the rig in its most common usage, that intended for creating samples of fuzz. The magnetron source used a tungsten target. The helium gas was fed into the chamber by a needle valve. The pressure gauges are a Pirani gauge, an inverted magnetron gauge, and a Baratron® gauge at positions P1, P2, and P3, respectively.

system to prevent it from overheating. Surrounding the target, and sitting flush with the stainless steel ring is a grounded aluminium ring, serving as the anode.

3.1.2 The substrate heater

To heat the samples to the required temperature required involves several parts. A power supply, a substrate holder, and a temperature sensor. The HEAT2-PS power supply powers a filament held just behind the sample in the substrate holder. A diagram showing how the heater works is shown in figure 3.3. The heating is due to electron bombardment, the basic principle is that a (cathode) current, I_c, is passed through a tungsten filament, of $1-2$ A due to a (cathode) potential, U_c, of $2.8-3.5$ V. With such a current, a tungsten filament (of 0.8 mm thickness) will emit electrons due to thermionic emission. An (emission) potential, U_e, is applied between the filament and the tungsten sample causing an (emission) current, I_e, from the filament to the back of the sample, heating occurs due to these electrons colliding with the surface. Although the values for these parameters varied between different samples and different filaments, typical operating values are shown in table 3.1. The HEAT2-PS unit operated in a feedback loop with the measured

temperature of the sample, via a type-k thermocouple input. The temperatures of the samples were either measured by thermocouples, or by an IR pyrometer (as explained in section 3.1.4.2) with a thermocouple emulation output. The heater was always operated in automatic heating mode. In such a mode, a value of I_c is set, giving rise to a certain U_c, then a temperature set point, T_{sp}, is chosen and U_e is varied automatically, I_e is a function of U_e, and as I_e rises, so to will the temperature of the sample. The T_{sp} rises at a rate of 1 Ks^{-1}, therefore to get to 1100 K it typically takes ~14 minutes.

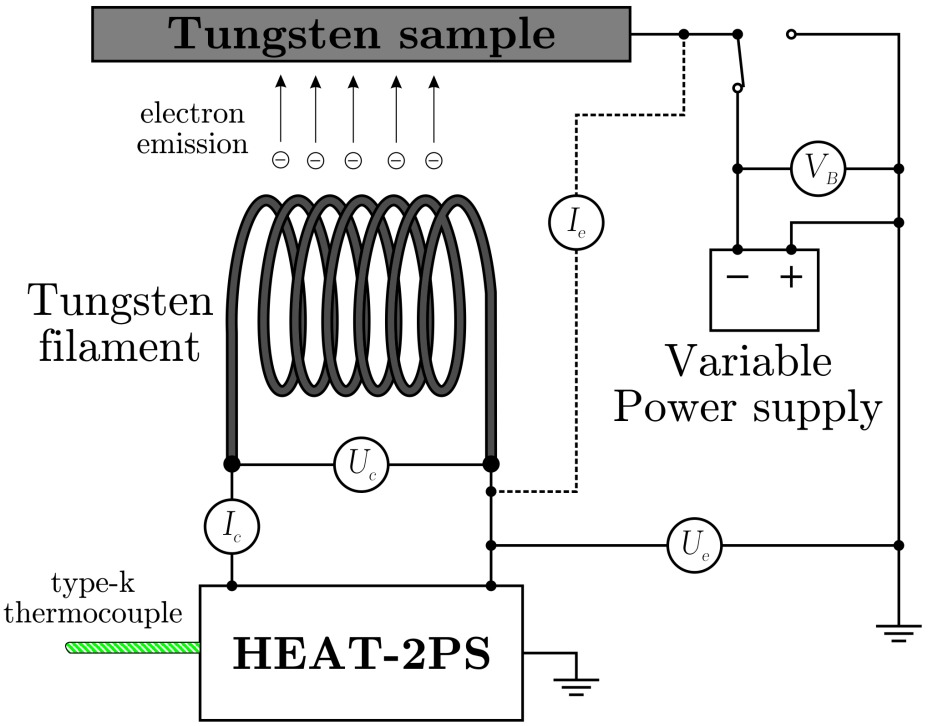

Figure 3.3. A diagram to show how the heating of the samples works, where I_c is the cathode current, U_c is the cathode potential, I_e is the emission current, U_e is the emission potential, and V_B is the sample bias.

Parameter	Symbol	Value	Units
Cathode current	I_c	1.3	A
Cathode potential	U_c	2.9	V
Emission potential	U_e	230	V
Emission current	I_e	24	mA

Table 3.1. Typical operating values of the HEAT-2PS heater. These values are for a typical situation (see chapter 6) heating a sample to ~1100 K, 1 hour after reaching temperature, and with a sample bias, V_B of -63.5 V.

3.1.3 The sample holder

The original sample holder was a PTS-1200 EB (Henniker-Scientific), it houses the filament used to heat the sample, a thermocouple to read the sample temperature, and holds

the sample in place via 3 metal clips. The thermocouple was sandwiched under one of the holder clips, allowing it to be in contact with the sample. A photo of the sample holder is shown in figure 3.4. This sample holder has the capability to attain temperatures of 1570 K, limited by the materials used in the construction.

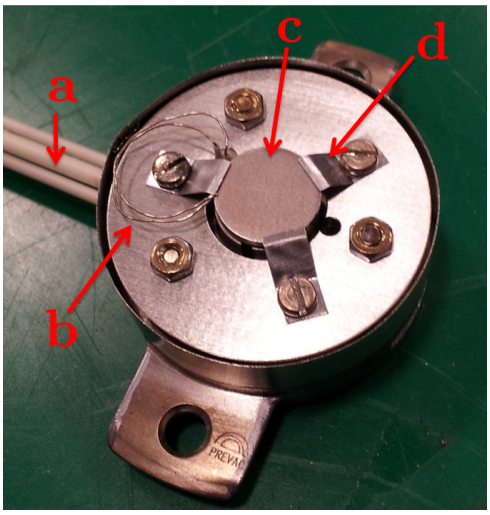

Figure 3.4. A photo of the original sample holder, where a is the cables that power the heating filament, b is the thermocouple, c is the sample, and d is the sample clips. For the scale, note that the sample (c) has a diameter of 10 mm.

Experiments were carried out on this holder, however, issues quickly arose in its use. The main issue was that the filament and the power cables attached to the filament were quite exposed to the plasma. As such this cause lots of arcing, and hence issue with maintaining a constant temperature. Therefore, a new sample holder was designed based on backwards engineering of the original one, and built on similar design principles but shielding the heating components from the plasma as is shown in figure 3.5. The heating power supply can supposedly heat to 2370 K, however the materials used in the custom built sample heater limit this. The Macor shield around the filament is the lowest limiting factor, with a recommended continuous operating temperature of 1170 K and a maximum temperature of 1270 K. Therefore it was deemed that the sample would not exceed 1270 K. No tests were done higher than 1250 K, however, because the Macor shield is not directly in contact with the sample but touches through the medium of a sapphire ring, which has a melting point of 2310 K, therefore there could be room to push this sample limit at some point. However, for the present purposes the risk of damaging the sample heater did not outweigh the desire of obtaining data at higher temperatures. A custom box was also built to house the heating components and prevent the plasma from getting in contact with them. The majority of the experiments in chapter 6 used this sample holder. Several photos showing the new sample holder and box are presented in figure 3.5.

The filaments used in the original sample holder were also supplied by Henniker Scien-

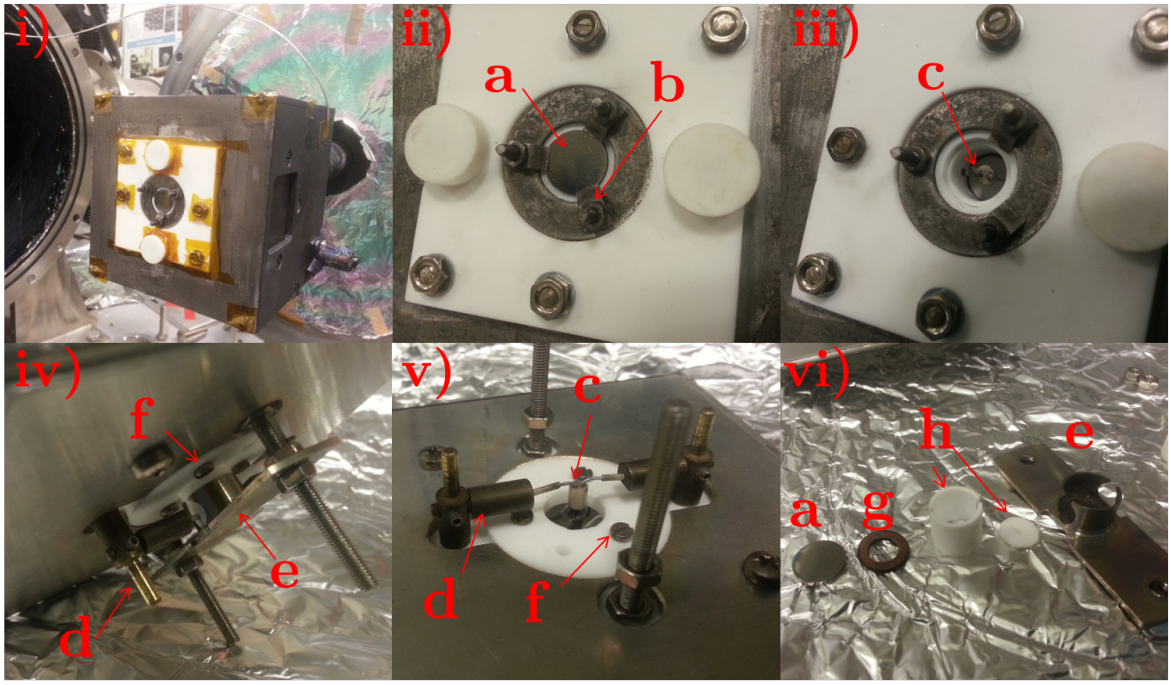

Figure 3.5. Several photos of the custom-built sample holder. In i) the sample holder attached to the box which houses the heating cables can be seen, in this image Kapton (Polyamide) tape has been used to protect certain parts from being coated. The wire carrying the sample bias can be seen going in to the box on the right hand side. In ii) the sample can be seen labelled as a, with b being the sample clips holding the sample in place. In iii) the sample has been removed to reveal the custom-made filament underneath, labelled c. In iv) the reverse of the sample holder is shown, with d pointing out where the heating cables are connected to the filament, e the shield support, and f points out the screw which the sample bias was connected to. In v) the shield support has been removed to show how the filament is held in place. In vi) the various components in the shield support are shown, with a, the sample (10 mm diameter) sitting on top of g, a sapphire ring, which sits on top of h, a Macor™ shield which surrounds the filament (with the small alumina disc going underneath it).

tific, however their longevity was not great. As the filaments become brittle after use, even the slightest touch can break them. As replacing them became costly, in-house filaments were created, which could last as long, if not longer, than the original filaments. The filament shown in figure 3.5iii and v is one of the custom-made filaments. These involved a 0.8 mm tungsten wire bent into a coil of ~1 mm diameter, with either end wrapped around tinned copper wires. The filament was insulated at several points by alumina.

3.1.4 Temperature sensing

3.1.4.1 Thermocouples

For the original sample holder, and early uses of the new sample holder, type-k thermocouples were used to record the temperature. These are useful over a wide range of temperatures from room temperature up to ~1520 K, suiting the present needs. How-

ever, they proved to be very unreliable. A second thermocouple was added to see if the temperatures would agree with one another. However, it seemed that as the plasma was turned on, the readings would often become erroneous. This was thought to be possibly due to the biasing of the sample. As the thermocouples were in direct contact with the sample, and as they rely on a potential difference across the two metal wires, if only one side was touching the sample, this would cause erroneous temperature recordings. Also, when the plasma was ignited, the readings would often become highly inaccurate, this is probably due to the thermocouples pulling current, and becoming charged from the plasma. This is also seen in other laboratories [32]. As such, it was deemed necessary to try an alternative approach to measure the temperature of the samples.

3.1.4.2 IR pyrometer

In the literature, to record the temperatures of fuzzy samples, they mostly use IR pyrometers. An IR pyrometer was used for all of the experiments in chapter 6. This IR pyrometer is capable of recording temperatures between 420−1270 K, it is situated approximately 450 mm away from the sample, as this gives the smallest spot size of 1.4 mm. The samples are 10 mm in diameter so this is sufficient. The IR pyrometer has two guiding lasers to aid the positioning of the IR pyrometer on the centre of the samples. The IR pyrometer operates at a wavelength of 2.3 μm. As such, a sapphire window (Kurt J. Lesker) was used which, according to the specification, has ~87% transmittance at 2.3 μm. This was experimentally checked later on, in section 4.4. The IR pyrometer additionally requires inputting the emissivity of the sample, this was also done in section 4.4. The IR pyrometer has the ability to output an emulation of a type-k thermocouple. This allows the output of the IR pyrometer to be a direct input to the HEAT-2PS heater unit, forming a feedback loop with the heater monitoring the temperature and automatically adjusting U_e to maintain the temperature.

3.2 Diagnostic equipment

A description of the diagnostic equipments used throughout the thesis will be described here.

3.2.1 Langmuir probe

The Langmuir probe is a very simple but versatile tool invented in the 1920's by Nobel prize winning Irvin Langmuir and Harold Mott-Smith [110]. The basic principle is that the current of a biased probe is measured as a function of the bias voltage. When inserted into a plasma it can be used to gather many plasma parameters, such as the electron temperature, the floating potential, the plasma potential, the plasma density, the electron

energy distribution, the negative ion density and temperature, and other things. There are many variants on the original probe design, such at the double, triple, emissive, spherical, and Mach probes. The simplest form is the cylindrical Langmuir probe, being a small length (typically ~10 mm) of bare metal wire (usually tungsten due to its high melting point) isolated from the probe stem, attached to a power supply with the current being monitored. This results in an I-V curve from which various plasma parameters can be derived. Today, fast automatic Langmuir probe acquisition systems exist which can sweep the voltage and record the current in matters of seconds. The acquisition system used for Langmuir probe measurements in this thesis is an ALP-150 (Impedans), but the probe used varied.

If a Langmuir probe is placed in a plasma unbiased, a voltage reading on the probe will give the floating potential, V_f. A probe that is floating receives no net current from the plasma, so the potential is negative such that it repels the more mobile species in the plasma, being the electrons, causing the current to the wire to be zero. If the bias on the sample is swept the ideal I-V curve would look like figure 3.6.

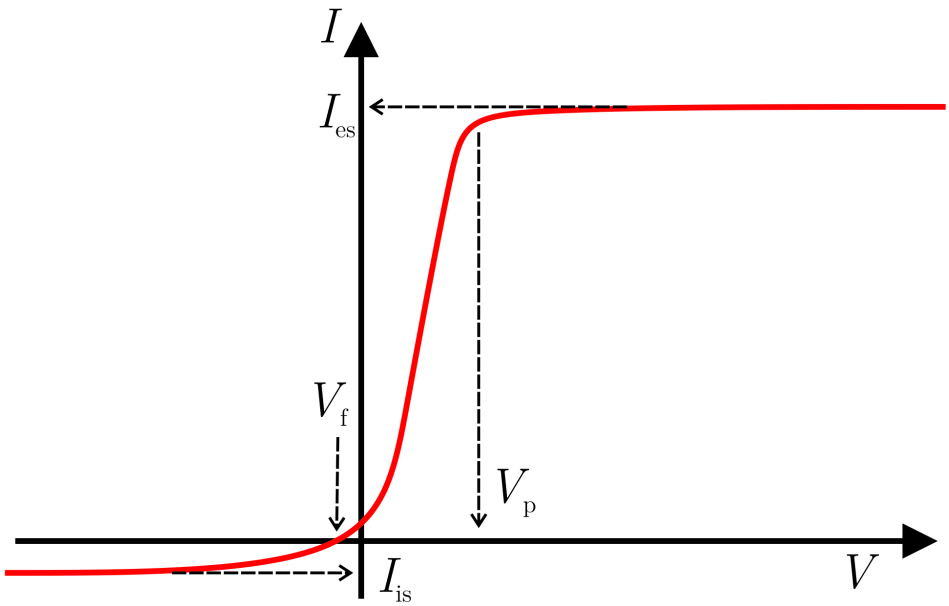

Figure 3.6. The ideal I-V curve obtained from a Langmuir probe. Indicated values are the floating potential, V_f, the plasma potential, V_p, and the ion and electron saturation current, I_is and I_es, respectively.

By convention, Langmuir probe I-V curves are inverted with the ion current being negative. If a Langmuir probe is biased strongly negatively, then all the electrons will be repelled and only the ions will be collected, the value of the current drawn at large negative potentials is called the ions saturation current, I_is. As the bias is raised towards 0 V energetic electrons will be able to overcome the repulsion and the drawn current begins to rise. At a certain point the current drawn from the ions and the electrons will be equal, and hence there will be no net current drawn by the probe. The bias at which

point this occurs will therefore be the floating potential, V_f. As the bias is raised past 0 V the energetic ions will begin to be repelled until only the electrons are collected, giving rise to the electron saturation current, I_{es}. The transition to a purely electron collecting regime gives rise to the plasma potential, V_p, at the so-called 'knee' of the curve, this is the energy which the ions in the bulk plasma have.

For I-V curves in practice it is not simply a case of reading the values from the graphs, some manipulation has to be performed. Shown in figure 3.7 is an actual Langmuir probe curve obtained during experiments. As can be seen from a real curve, the position of the 'knee' is much harder to define and neither the electron or ion current saturates. This lack of saturation is because as the bias is increased (either negatively or positively) the sheath expands. The effective area for particle collection is the sheath area and not the geometric probe area, hence as the bias sheath increases more particles will be collected. If, however, the logarithm of the current is plotted against the voltage, as is done in figure 3.8a, V_p can be seen more easily, with still some given error. The slope of the downward portion of the semilog plot gives the electron temperature, T_e. From the plot of figure 3.8b I_{is} can be obtained by extrapolating the flat region to V_p.

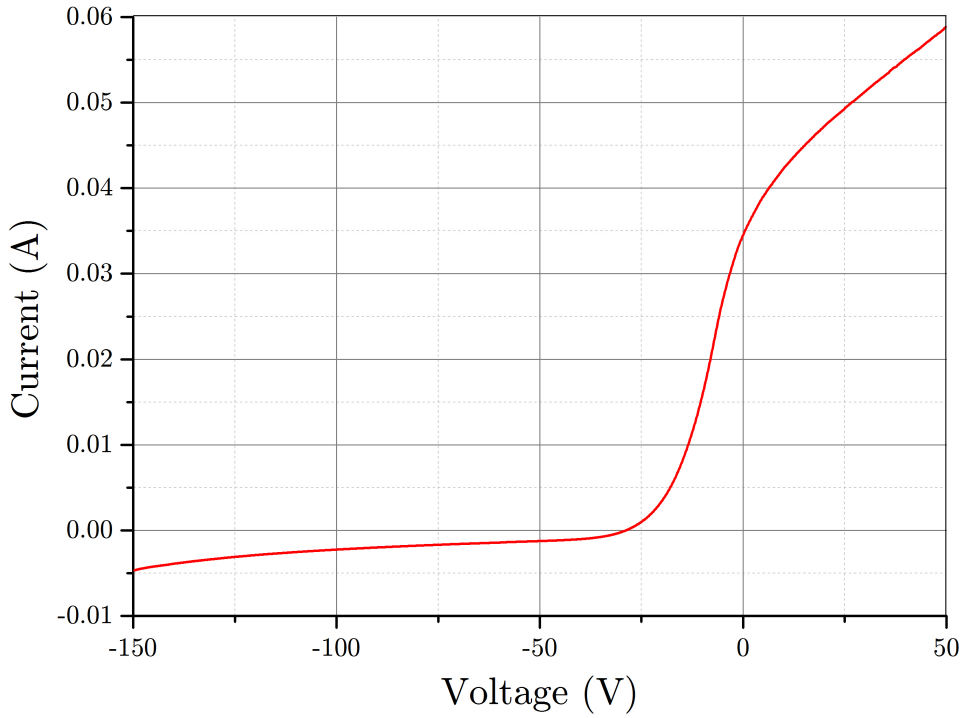

Figure 3.7. A real I-V curve obtained from a He plasma of 40 mTorr and 700 W plasma power using a flat probe.

For technological plasmas, where $T_e \gg T_i$ the ion saturation is given by the Bohm Ion current [111],

$$I_{is} = I_{Bohm} = 0.6 e n_i \sqrt{\frac{k_B T_e}{m_i}} A \tag{3.1}$$

where e is the charge on a electron, n_i is the ion density, k_B is the Boltzmann constant,

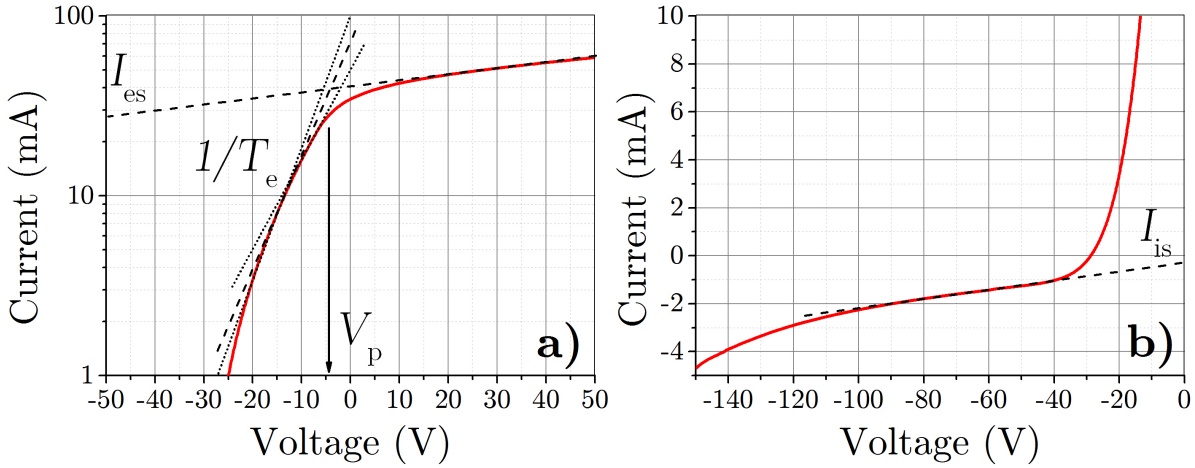

Figure 3.8. Real IV characteristics obtained from Langmuir probes, showing how to obtain certain values. To obtain the plasma potential, in a) the current has been plotted on a logarithmic scale to make the 'knee' more apparent. In b) the ion saturation is obtained from a linear fit of the ion current region and extrapolated to V_p.

m_i is the mass of the ions, and A is the area of the probe. In this equation, the only unknown is n_i, hence this can be calculated. Note that, if the plasma is assumed to be quasi-neutral, then $n_i \approx n_e \approx n$, where n_e is the electron density, and n the plasma density.

Lastly for the growth of fuzz, the flux, Γ, is a parameter that is very important. This can be easily calculated from the current at a particular bias and given by,

$$\Gamma = \frac{I}{eA} \tag{3.2}$$

However, for low negative biases, the energetic electrons will begin to be collected, such that the measured current, I_m, will be a combination of both the electron and the ion current,

$$I_m = I_e - I_i \tag{3.3}$$

From Lieberman [112], an expression for the electron component of the ion current is given as,

$$I_e = \frac{1}{4} e n_0 \bar{v}_e A \exp\left(\frac{V_B - V_p}{T_e}\right) \tag{3.4}$$

where V_B is the bias voltage and $\bar{v}_e$ is the mean electron speed, given by

$$\bar{v}_e = \left(\frac{8eT_e}{\pi m_e}\right)^{1/2} \tag{3.5}$$

where m_e is the mass of the electron. We can therefore get an expression for the ion flux as

$$\Gamma_i = \frac{1}{eA}(I_e - I_m) \tag{3.6}$$

and substituting in equation 3.4 for I_e gives,

$$\Gamma_i = \frac{1}{4} n_0 \bar{v}_e \exp\left(\frac{V_B - V_p}{T_e}\right) - \frac{I_m}{eA} \tag{3.7}$$

So by taking an I-V curve, and obtaining T_e from the semi-log plot as shown in figure 3.8a, then obtaining the density from the ion saturation region, as shown in figure 3.8b, Γ_i can be computed. It can be seen that for large negative values of V_B, as is this case in the ion saturation region, the exponential term will tend to zero, and the electron contribution will go to zero, and the measured current will be just the ion current.

3.2.2 Sample probe

To get accurate recordings of the flux of He ions to the samples, a probe was made from a steel sample. A 10 mm disc, 1 mm thick, was made, matching the exact size of the W samples. In to the side of it, a small 0.5 mm diameter hole was drilled, 2 mm deep. A wire was inserted into this, with the wire folded back on itself to make a tight fit. The wire was shielded mostly by its own Kapton shielding, but a ceramic tube was put over the end near the connection with the sample. Kapton tape was also placed around the whole edge of the sample, to prevent current being drawn from the sides. The sample clips which hold it in place were also wrapped in Kapton tape to prevent current being drawn from them. A photo of the sample probe is shown in figure 3.9. The probe was operated with the Langmuir probe acquisition system used to get I-V curves from Langmuir probes.

3.2.3 Mass spectrometer

The quadrupole mass spectrometer used in section 4.5 was a EQP300 (Hiden Analytical Limited). In figure 3.2, the mass spectrometer replaces the sample heater unit and is positioned on the same axis as the target, in the exact same position that the sample would sit for the majority of the experiments (as in chapter 6), being 93 mm away from the target.

3.2.4 Thermal probe

Two thermal probes were used, an active and a passive thermal probe. Both were inserted through a feedthrough and the magnetron moved such that the distance between the head of the thermal probes and the target is the same as the working distance of the target and the growing fuzz samples in chapter 6. The active thermal probe was a recent invention by Dr. Ruben Weise, as described in [113]. It works on the principle of a heating a cell to a specific temperature (typically ~ 520 K) at the end of a manipulator arm. Upon stabilisation of the cell temperature, the heating source is then applied (in the present

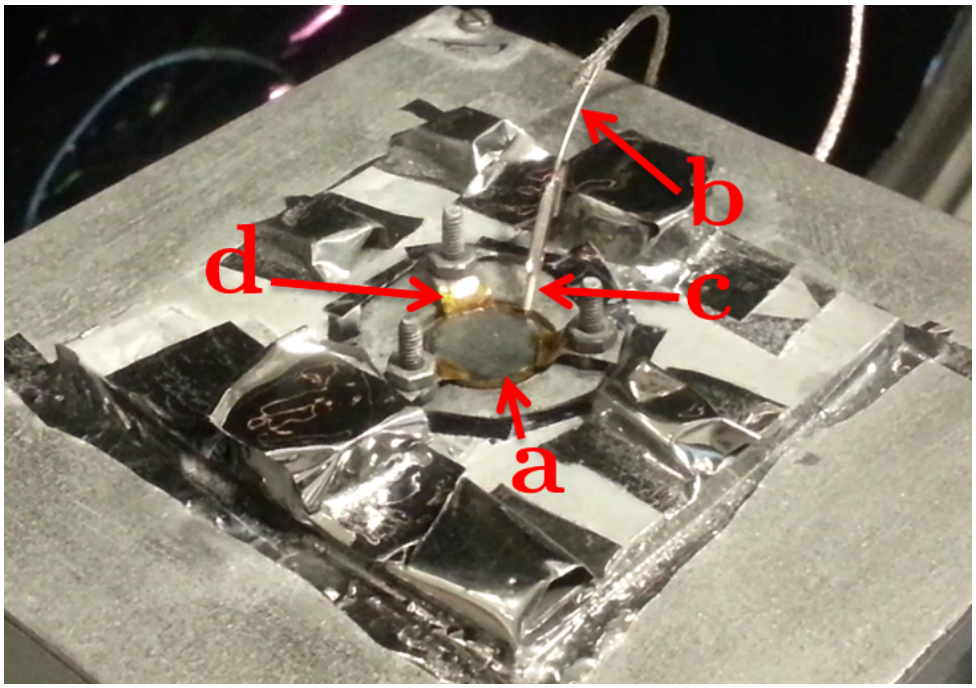

Figure 3.9. A photo of the sample probe. The label 'a' is the sample (10 mm diameter), b is the wire connected to the sample, c is the ceramic tube shielding the wire, and d shows the Kapton tape on the sample clips.

case the plasma is switched on). The temperature of the cell will increase, and in order to keep the cell at the set temperature the heating power provided by the probe is reduced. This reduction in heating power of the probe therefore can be inferred as the heating power of the plasma.

Figure 3.10. A photo of the active thermal probe, invented by Dr. Ruben Weise. The length of the probe is 130 mm with 6 mm diameter. Image taken from [113].

The active thermal probe has the benefit of being able to have live measurements of the energy flux. However, it was not possible to bias the probe. Hence a custom bias-able passive thermal probe was designed and created. This involved an isolated disc of aluminium, to the back of which was spot-welded a type-k thermocouple and a wire which is connected via a feedthrough to a power supply, enabling a bias to be applied to the disc.

The passive thermal probe was calibrated to readings from the active thermal probe.

3.2.5 Quartz crystal microbalance

Due to the nature of the magnetron device, the sputtered atoms from the target will be deposited on the walls of the chamber, and hence on the growing fuzz sample. For this reason W was chosen as the target, because it has a low sputter yield, and because impurities are known to reduce fuzz growth. In this situation, it will only be tungsten being deposited on tungsten. To measure the deposition rate a quartz crystal microbalance (QCM) was used. A quartz crystal is oscillated at a resonant frequency of several MHz, this frequency will vary with the mass of the crystal. As particles are deposited on the crystal, the frequency will change. From this change in frequency, and knowing the mass of the depositing atoms, the deposited thickness can be measured, and the deposition rate implied.

The QCM instrument consists of a quartz crystal coated with gold electrodes and mounted on a water-cooled stainless steel holder, keeping it at the operating temperature (0 to 50 °C). The electrodes of the crystal are connected to a microbalance monitor (Inficon Maxtek TM-400) which drives the electrodes and displays real-time measurements of the film thickness and deposition rate. It was necessary to calibrate the QCM with the density of the depositing atoms, in the present case always being tungsten, with a density of 19.25 $\mathrm{g\,cm^{-2}}$.

3.3 Sample preparation

An outline of the sample preparation for the samples created in the magnetron will be provided here. For samples created in the devices at UC San Diego, the sample preparation is described later on in the relevant results section of chapter 5.

3.3.1 Sandpaper polishing

For initial experiments in the magnetron device the samples were prepared by mechanical polishing by hand using wet and dry sandpaper (P1000). Polishing times varied, being between 30 - 120 minutes, and was deemed finished when no more polishing seemed to make a difference and a vague smudge of a reflection could be seen. An example of a finish is shown in figure 3.11. One can see that there is very little reflectivity, and there are still many scratches on the surface. This is certainly not a mirror finish. After polishing in this way, the samples were cleaned via first placing in a sonic bath of isopropanol for 3 minutes, followed by acetone for 3 minutes.

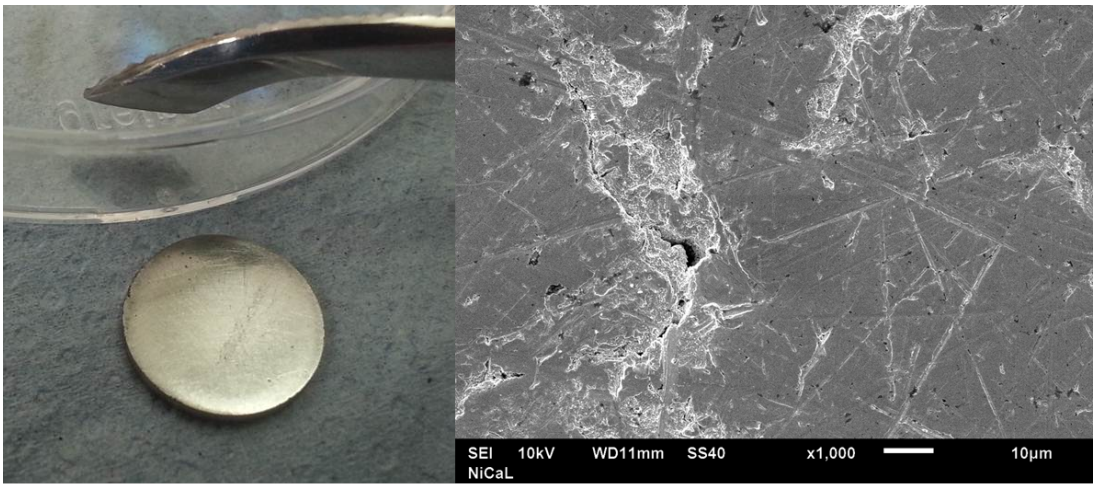

(a) (b)

Figure 3.11. A photo of a sample (10 mm diameter) prepared by mechanical polishing by hand using wet and dry sandpaper (P1000). In (a) the tweezers are shown to display the degree of reflection, as compared to electro-polishing in figure 3.13. In (b) an SEM image at 1000× magnification is shown.

3.3.2 Electro-polishing

Although fuzz could be made on such a rough sample, as the temperature sensor was changed from thermocouples to an IR pyrometer, the surface roughness plays a part on the value of the emissivity. Due to some inconsistencies during experiments with the IR pyrometer, it was deemed necessary to have a more consistent emissivity value between samples, and hence a defined finish, i.e. a mirror finish. The technique used to achieve such a finish was electro-polishing. Electro-polishing works by submerging the specimen, serving as an anode, in an electrolyte solution then running a current between the specimen and a cathode. The metal atoms on the surface are oxidised and then dissolved in the electrolyte. This erosion takes place preferentially on parts protruding into the solution, hence protrusions are eroded down to provide a uniform finish. A diagram of the circuit is shown in figure 3.12 as well as a photo of the electro-polishing setup.

The setup used for electropolishing consisted of a basic power supply, with the negative terminal attached to a steel rod (via an ammeter), and the positive terminal attached to steel tweezers holding the sample. The positive terminal is driven with ~12 V, giving rise to ~2 A as recorded by the ammeter. The electrolyte solution is 2% by weight of potassium hydroxide (KOH) dissolved in a glass beaker containing water that has been passed through a purifier (Purite DC7). Using 150 ml of water implies 2% by weight of KOH is 3 g. The KOH solution is placed on a magnetic stirring plate with a magnetic stirrer placed in the glass beaker. It was found that applying the bias for too long periods of time ($\gtrsim$40 s) leads to warping of the sample, and as such the bias was operated in a DC

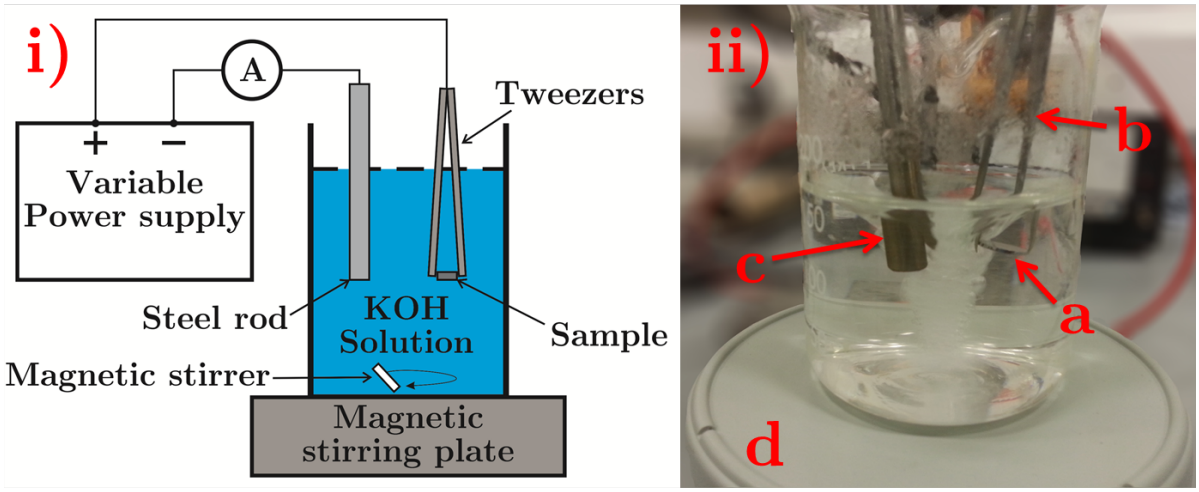

Figure 3.12. The electro-polishing setup, with i) showing a diagram of the experimental setup, with a variable power supply attached to a steel rod and tweezers holding a sample, submerged in KOH solution, and stationed on a magnetic stirring plate. In ii) a photo of the glass beaker during polishing, with 'a' labelling the sample, b, the tweezers holding the sample (10 mm diameter), c the steel rod, and d the magnetic stirring plate.

pulse with 20 seconds on time, and 20 seconds cooling time. It was also found that the tweezers would cause indentations on the samples if kept in the same position for more than ~4 minutes of this pulsing. As such, every 3 minutes the sample was rotated in the tweezers. Before being electro-polished, samples were mechanically polished as before to as best a finish as possible by hand, now working through the grades of sandpaper, from coarse to fine (P400, 360, 240, and 150). Overall time of electro-polishing per sample varied from sample to sample, depending on the finish the sample had before being electro-polished. Typical total times were 15-20 minutes per sample. In each 3 minute interval, whilst rotating the sample, the finish was inspected, and it was decided whether to continue polishing or if the sample was done. Samples were defined as finished when they perfectly showed a mirror image of tweezers in focus only 10 mm away from the sample. A photo of the finish achieved with this image is shown in figure 3.13 , compare this against figure 3.11 of the mechanical polishing. Note, the small pits appearing in figure 3.11 are a by-product of the electro-polishing process, rather than from He damage, as the samples shown has not yet been exposed to He [114].

After electro-polishing, samples were placed in a sonic bath of acetone for 3 minutes, then isopropanol for 3 minutes, before being deemed ready.

3.4 Scanning electron microscope

A scanning electron microscope (SEM) was used to image the surfaces of samples of fuzz made. The particular models used were a JEOL 6610 and 7001. SEMs allow surface

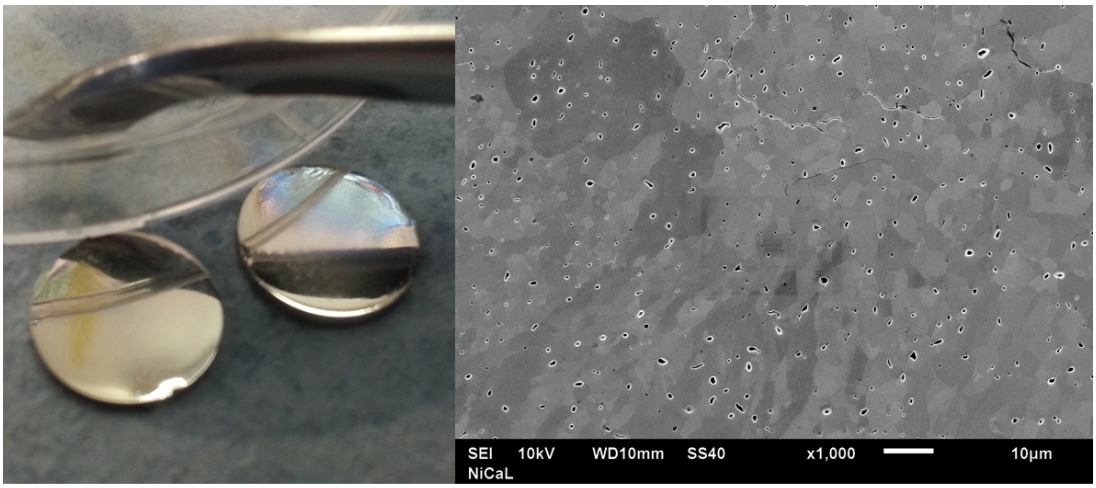

(a) (b)

Figure 3.13. Samples (10 mm diameter) after electro-polishing. In (a) the purpose of the tweezers in the photo is to show the reflection, in (b) an SEM image at 1000× magnification is shown. Compare these images with the mechanically polished samples of figure 3.11.

imaging with nanoscale resolution. The particular SEMs used allowed in-focus images to be taken with at least 100,000× magnification. Typical tendrils are around 50 nm wide, so at 100,000× magnification a 50 nm tendril would appear on the monitor as 5 mm. So the imaging of fuzz is well within the capabilities of these SEMs, with fuzz being apparent in practice from about 5,000× magnification.

A schematic of an SEM is shown in figure 3.14. In an SEM, the electron gun generates close to mono-energetic electrons. The main types of electron gun are the field emission gun (FEG), the Shottky electron gun, and the tungsten or lanthanum hexaboride hairpin. In the JEOL 6610 a tungsten hairpin is used, and in the 7001 a Shottky electron gun. The tungsten hairpin works on the principle of heating the tungsten hairpin filament causing thermionic emission to occur. With the Shottky electron gun, a strong electric field is applied while heating a zirconium oxide tip, the energy barrier for the electrons is lowered, via Shottky effect and electrons are emitted. In either case electrons are emitted and then extracted and accelerated by two electrodes. The second electrode is grounded, and the potential difference between this and the filament defines the acceleration voltage, which controls the degree of penetration of the electrons into the samples. In both cases of guns, the tip must be free of contaminants, and thus must be held under ultra high vacuum conditions (typically 10^{-10} to 10^{-11} Torr). A series of lenses are used to focus the beam on the sample, namely the condenser and objective lenses. Apertures are placed along the beam path to reduce the beam size, and reduces defocused electrons. Deflector coils are used to raster the beam across the sample to attain the images on the computer screen. The sample sits on a stage which can be manipulated in the x, y, and z planes, as well as rotated and tilted to a maximum of 70°.

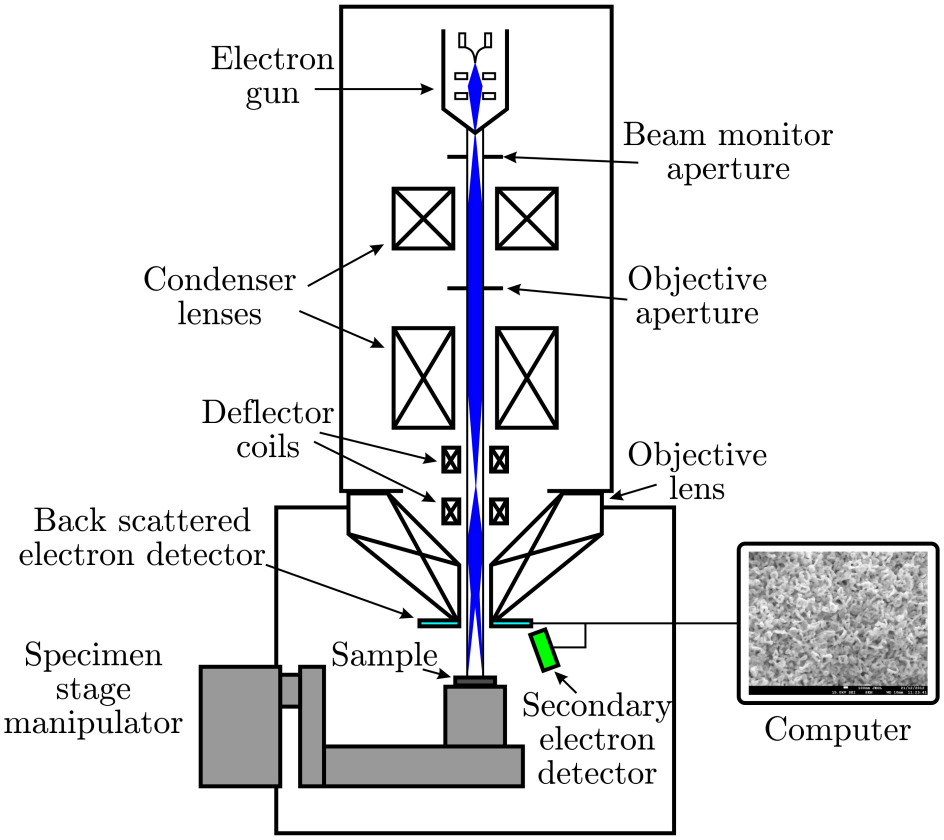

Figure 3.14. A schematic of an SEM, showing the main components to generate the image The electron gun shown is a tungsten hairpin filament, as is the case in the JEOL 6610.

When an electron beam interacts with a specimen, several different interactions can occur, resulting in a range of signal types coming off of the specimen. Such signals are Auger electrons, X-rays, cathadoluminescence, backscattered electrons, and secondary electrons. For SEMs the signals of interest are from backscattered and secondary electrons. An incoming electron can undergo an inelastic collision with an electron in the nucleus of an atom in the specimen. This can liberate the electron, with the liberated electron being called a secondary electron (SE). SEs by definition have less than 50 eV energy. If an electron from a higher energy level falls down to this vacancy, a characteristic X-ray for the atom is emitted. Backscattered electrons (BSEs) are created when an incoming electron travels close enough to a nucleus of a specimen atom, causing the path to be deflected. If this happens a sufficient amount of times the electron can make it back out of the specimen, and is labelled a BSE. Such a change in the path of the beam does not significantly affect the energy of the electron, and as such their energies can range from 50 eV to almost the incident beam energy. However, most BSEs keep at least 50% of the incident beam energy. The generation of SEs and BSEs are shown in diagrams in figures 3.15a and b, respectively.

The different signals given off when the electron beam interacts with a specimen can arrive to the detector from different depths in the specimen. This is shown in a diagram

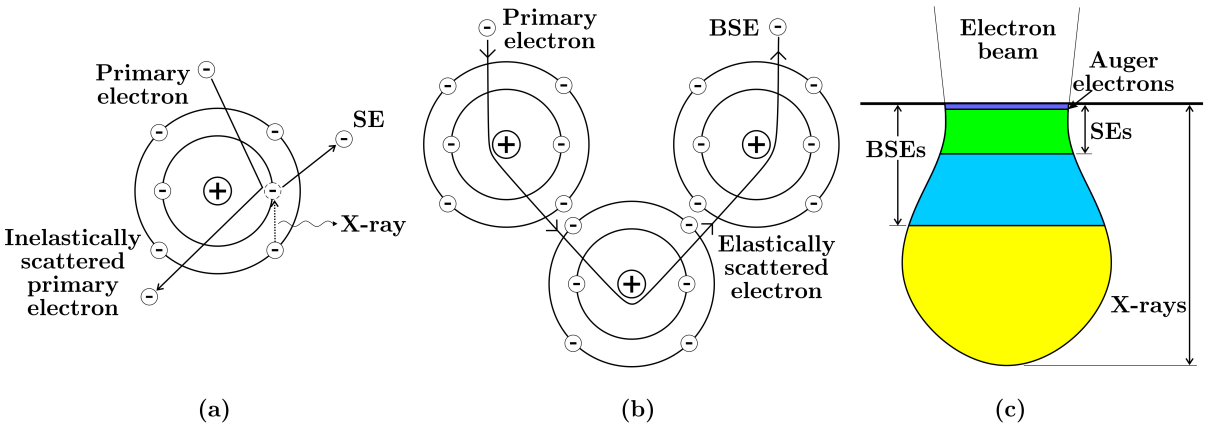

Figure 3.15. Two of the possible interactions of electrons with an atom. With (a) showing the generation of a secondary electron (SE), and as a by product a possible X-ray, and (b) showing how a backscattered electron (BSE) can come about by its path being deflected. In (c) the interaction depth is shown in a diagram, these depths are not to scale.

in figure 3.15c. For SEs their escape depth is approximately 5-50 nm, whereas BSEs can escape from a depth 100× greater than this, and X-rays even further. The chosen technique of imaging can therefore give rise to different levels of resolution. As images of fuzz will need to be taken at very high resolution, the detected signal used was from SEs.

3.5 Reflectivity

The reflectivity of samples was measured using a USB2000+ spectrometer (Ocean Optics) using a DH-2000-BAL balanced deuterium halogen light source reflecting off the sample before being collected by the spectrometer. A special fibre optic cable was held in position above the samples which split into two cables, one going to the light source, the other to the spectrometer. The spectrometer was capable of measuring wavelengths of light between 400 - 1000 nm.

3.6 Depth measurements

Here, different approaches used to attempt to get thickness measurements will be described.

3.6.1 SEM

The SEM, as just described in section 3.4, is the literature standard for obtaining thicknesses. To do so, the sample must first be broken in half. The approach to doing this is not in anyway elegant, and usually involves placing the sample in a vice and gently hitting it with a hammer. Tungsten is quite brittle, and with sufficient force will break,

hopefully giving a clean cut. An example of a cross-sectional image taken in an SEM is shown in figure 3.16. The boundary where the bulk tungsten ends, and the fuzz starts is quite obvious for thick fuzzy samples. This is great for samples such as those made in PISCES-B or NAGDIS-II where the thicknesses of samples are several microns. However, for the thicknesses created in a magnetron (50 - 500 nm), it is harder to define where the transition from fuzz to bulk is.

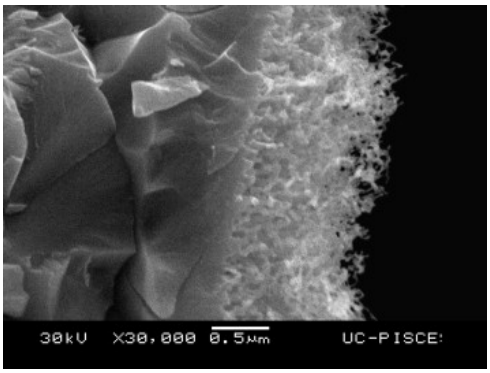

Figure 3.16. An example of the SEM technique used to measure the thickness of samples. Image taken from [16].

3.6.2 Confocal microscope

Laser confocal microscopes (CFM) can also be used to get depth measurements. The particular models used were a LEXT OLS4100 (Olympus) at UC San Diego, and a VK-X210 (Keyence) at the University of Manchester. They both operate under the same principles being a small modification to a regular optical microscope by the addition of the confocal pinhole. A diagram is shown in figure 3.17; if one was to remove the confocal pinhole it would simply be a regular optical microscope. The light comes from a source, in the case of a CFM a point light source is used, it arrives at a beam splitter and is reflected to the sample, the light reflects off the sample and passes through the beam splitter and ends up at a light detector. In regular optical microscopes all the light is collected, both the focused and the unfocused light. However, with the addition of a confocal pinhole, the unfocused light is blocked out, thus only the light in focus is collected. The laser CFM uses a specific wavelength of light (405 nm for the OLS4100, 408 nm for the VK-X210) which travels in a very straight line as the point light source. Using such a monochromatic laser reduces unnecessary scattered light and improves contrast over regular optical microscopes. Depth measurements can be attained from CFMs by moving the sample in the z direction, thus collecting light from different heights. Due to the unfocused light not making it past the pinhole, only light in focus at each z value is collected, the surface structure can therefore be regenerated by a computer.

To get thicknesses of fuzz layers from a CFM the fuzz must be removed in a certain area. This is done by scratching the surface. Due to the hardness of tungsten the scratch

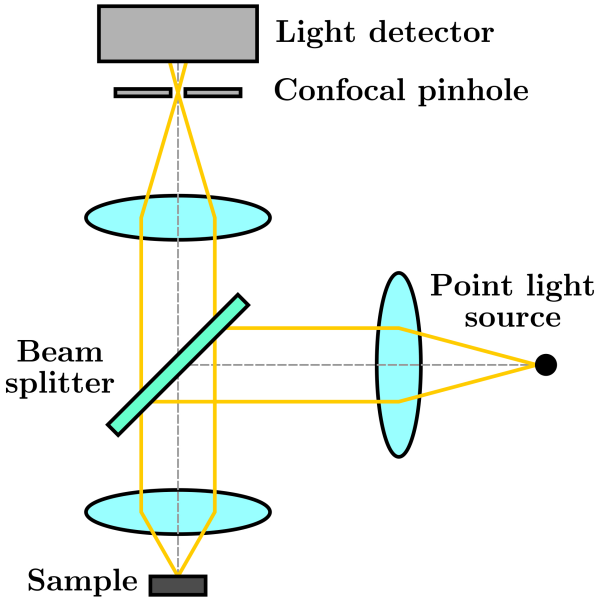

Figure 3.17. A diagram showing how a confocal microscope works.

should not penetrate the bulk, whereas the fuzz is easily removed. A small scratch, approximately 3 mm long, is made on samples, thus causing a trench to appear on the surface. The trench can then be imaged in a CFM and the depth of the trench can be measured, giving the thickness of the fuzz layer grown. The benefit of this technique over the SEM technique is that the sample is not entirely destroyed, only a very small area has to be removed to get a measurement from this technique.

3.6.3 Atomic force microscope

Atomic force microscopes (AFM) can in principle be used to get thickness measurements using the same technique as for CFMs, whereby a scratch is made on the surface and the depth of the trench measured. The AFM used was a CPII AFM (Veeco). The principle of how an AFM works is that a nano sized tip is placed at the end of a silicon spring and is either directly in contact with the specimen surface or close enough to maintain a fixed attraction by van der Waals forces. A laser beam is focused on to the back of the tip and as the tip passes the surface of the sample the tip will move up and down. The laser beam is reflected off the tip and to a photodiode, and the displacement is calculated as a change in height on the surface. A diagram of an AFM is shown in figure 3.18. The whole configuration of laser, cantilever, mirror, and photodiode move over the surface of the sample and record the displacement of the tip across the surface. The information is then digitally recreated on a computer screen.

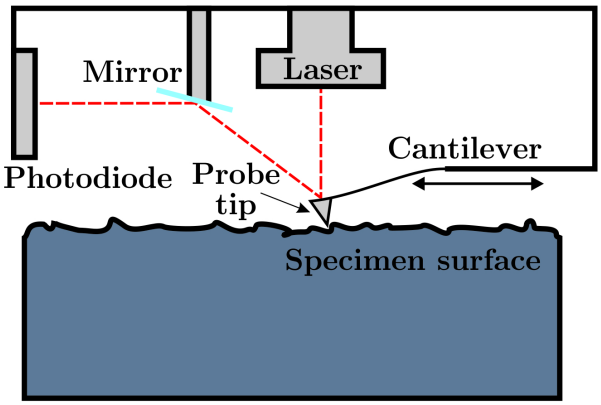

Figure 3.18. A diagram showing how atomic force microscopes work.

3.6.4 Profilometer

A Dektak IIA profilometer was used to attempt to measure the thicknesses of the fuzz layers. Profilometers can be used to measure the height of a trench. Therefore, following the same method as for CFM, the scratch made into the surface was attempted to be measured by the Dektak machine. The measurement of height is done by a diamond-tipped stylus, lowered onto the sample. In a similar way as the AFM, this tip is moved along the surface, and the displacement is measured, and converted into a digital format.

3.6.5 Interferometer

A ZeGage (Zygo) white light interferometer, otherwise known as an optical profilometer was used in a very similar manner to the CFM, by using light to get a profile of the surface with a scratch made through the fuzz. A beam of light is split into a reference beam and a measurement beam. The reference beam goes to a mirror then to the camera, whilst the measurement beam hits the surface of the sample before going to the camera. The vertical position of the sample is varied which brings the measurement beam in and out of phase with the reference beam depending on the height of the surface structure. This causes fringe patterns to appear, which is digitally converted into a height profile for the surface.

3.6.6 Focussed ion beam milling

An advanced technique involving the use of a focussed ion beam (FIB) and SEM imaging can be used to get thickness measurements of thin films. The process involves milling out a trench and observing the cross-section, a diagram of the process is shown in figure 3.19. As milling out a trench using a FIB causes a curve on the upper edge (fig. 3.19b), first a protection layer is deposited on top of the tendrils in order to protect them (fig. 3.19c). This protection layer is a mix of platinum and gallium ions, and is deposited using the

aid of a precursor gas [115]. There are four stages to the process, as shown in figure 3.20. The first stage is to mount the sample in an SEM and tilt the camera to 52° (in line with the FIB) (see fig. 3.20a). Then a layer of platinum is deposited on top of the fuzz such that the tendrils are protected (fig. 3.20b and 3.19c). Next a FIB of gallium ions is used at higher energies in order to mill out a trench, exposing the cross-section of the tendrils (fig. 3.20c and fig. 3.19d). The SEM can be tilted back to 45° in order to take a close-up image of the cross-section of the fuzz, and a measurement of the thickness can easily be obtained (fig. 3.20d and fig. 3.19e).

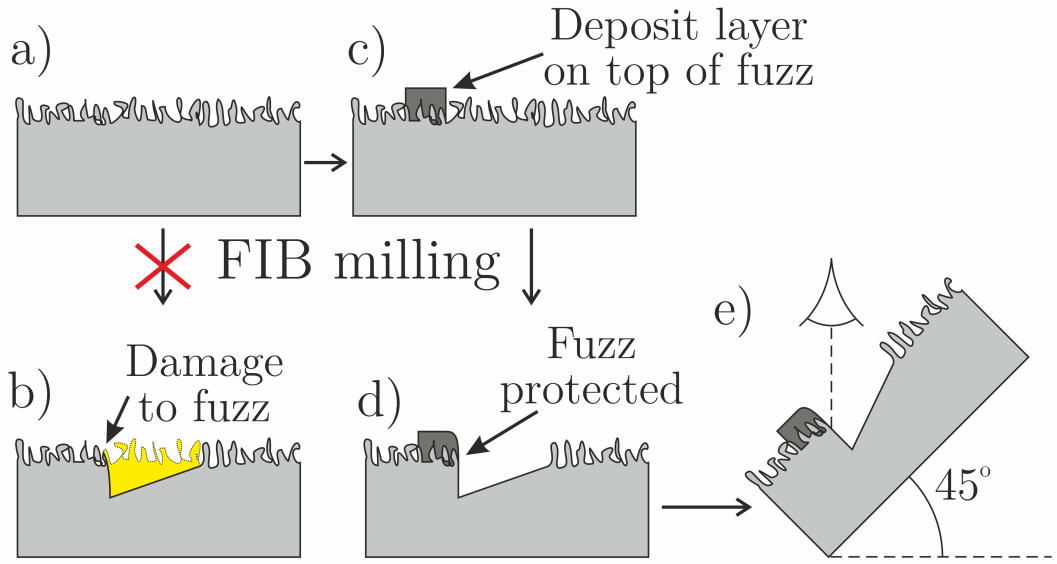

Figure 3.19. The FIB milling technique shown in diagrams. In a) there is the starting fuzzy sample, b) shows why a protection layer must be added before milling, c) shows the deposited protection layer, d) shows the result of milling after deposition, and e) shows how the cross-section is imaged.

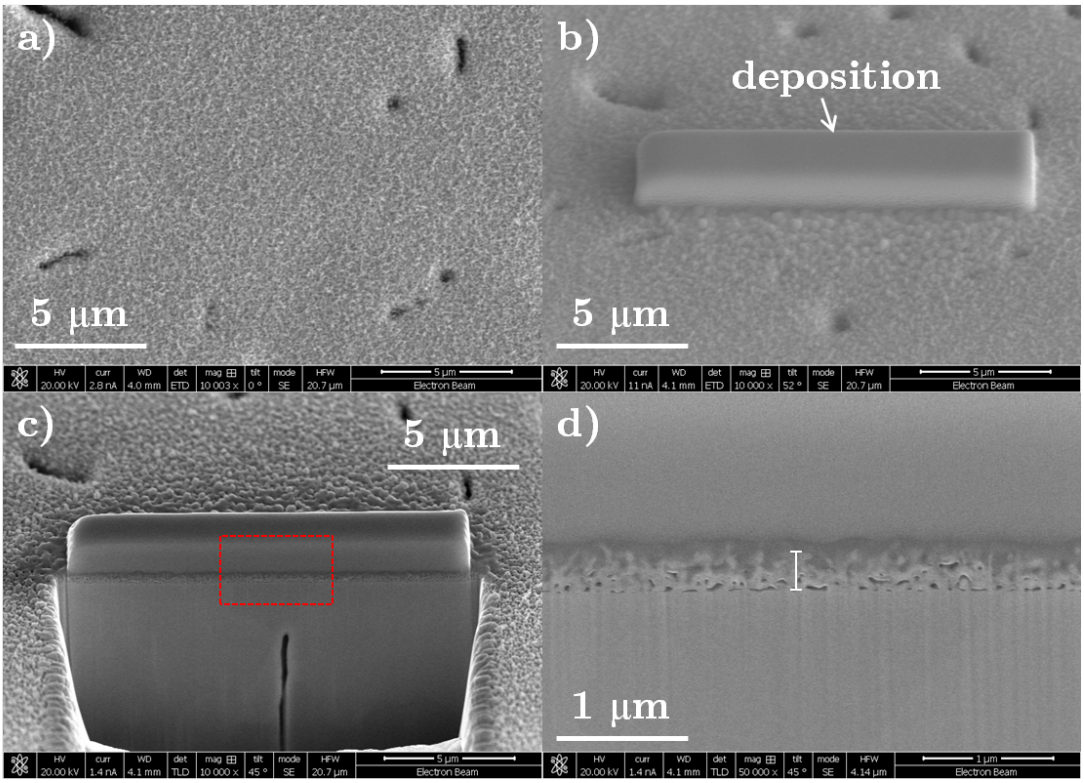

Figure 3.20. The four stage process for getting thickness measurements of fuzz layers using FIB milling and SEM imaging. A surface image of the fuzz is shown in a) with no tilt on the sample. In b) a layer is deposited on top of the fuzz to protect it, this image, as well as c) and d), are taken at 52°. In c) a trench is milled out and the red square shows where the magnified image of d) is taken from, allowing thickness measurements to be taken. An example measurement is shown in d). The scale bar for each image is displayed overlaid. Lengths in the titled images (b-d) must be multiplied by sin(52°).

3.7 Measurements of the surface roughness

The CFM could also be used to get measurements of the surface roughness from profiles of the fuzz areas. The technique to get roughness values is shown in figure 3.21. First, a profile of an area of the fuzz was taken, then a polynomial fit of the data was made in order to account for the underlying surface finish (fig. 3.21a). Next, an absolute value of the thickness minus the fit was attained at each point (fig. 3.21c). Lastly, these values were integrated with respect to their x-position and divided by the distance of the profile as,

$$R_a = \frac{1}{L}\int_0^L |R_x| \mathrm{d}x \tag{3.8}$$

where R_a is the arithmetic mean roughness, L the reference length, and R_x the value of the roughness at each x position; these are all labelled in figure 3.21c. Ten profiles are attained for each sample, giving ten values of R_a are attained and then averaged over to provide a final value of R_a for that sample.

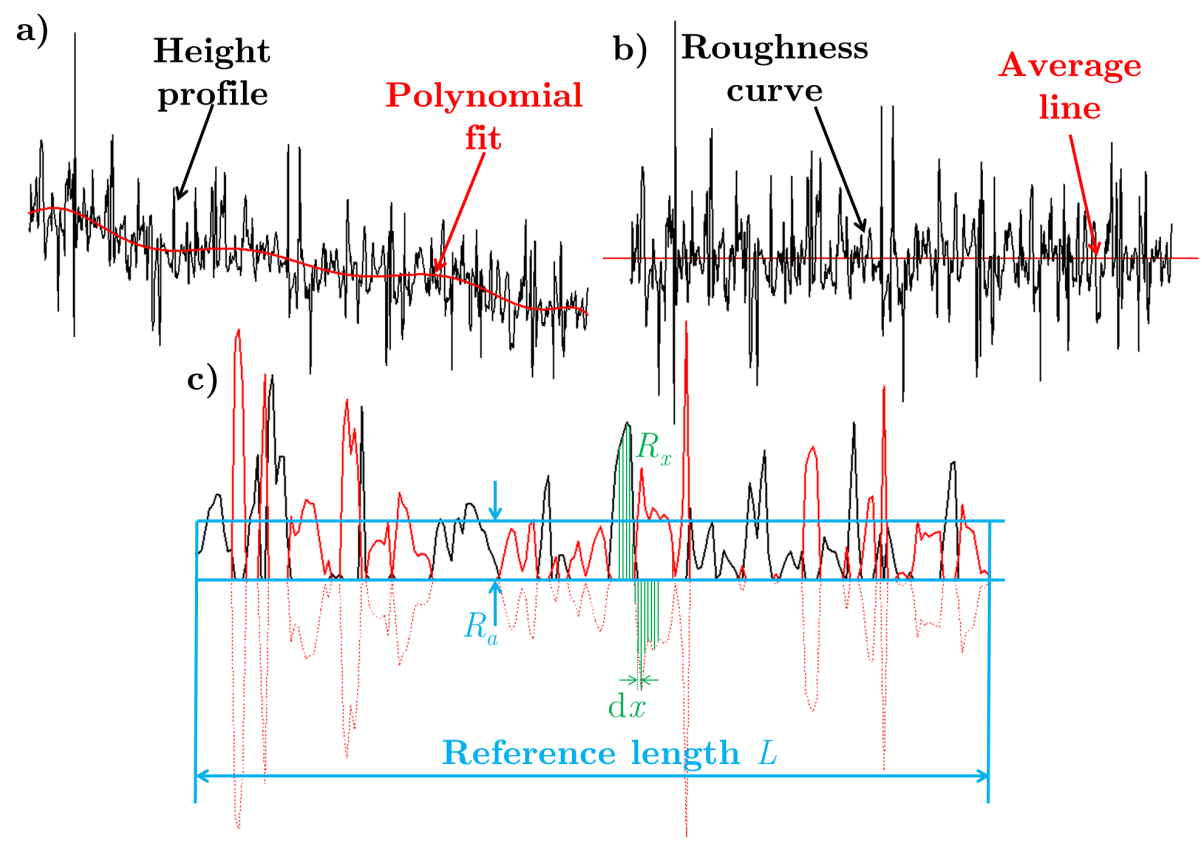

Figure 3.21. The technique used to find the roughness of each sample from a profile measurement using the CFM. In a) the height profile is obtained and a polynomial fit overlaid. In b) the fit is subtracted from the height profile. In c) the absolute value of the average roughness is attained, as shown for a magnified section.

3.8 Alternative devices

In chapter 5, some experiments were performed on devices at UC San Diego, these devices will be explained here.

3.8.1 PISCES-E

The PISCES-E device is well described in [116–118], but a brief description will be provided here. PISCES-E is an inductively coupled plasma modified from the commercially available plasma source M⌀RI^{TM} (PMT). A schematic of the device is shown in figure 3.22. The source has the capability to operate as a helicon wave plasma source by using magnetic field coils around the helicon, however, for the present purposes these coils were not used and the source was operated in an unmagnetised inductively coupled mode. The source consists of a 100 mm diameter Pyrex bell jar which is surrounded by a double loop antenna driven at 13.56 MHz. The antenna loops are 110 mm in diameter and 150 mm apart, they are designed such that the radio-frequency (RF) currents in the loops are 180° out of phase. The bell jar sits on top of an aluminium chamber 350 mm in diameter and 400 mm high. The RF power is coupled to the antenna through a feedback controlled matching network which is capable of driving the antenna over a large range of process gasses and RF powers. A gas injection ring is located at the top of the chamber at a radius of 93 mm which injects gas into the chamber from 4 equally spaced injection ports.

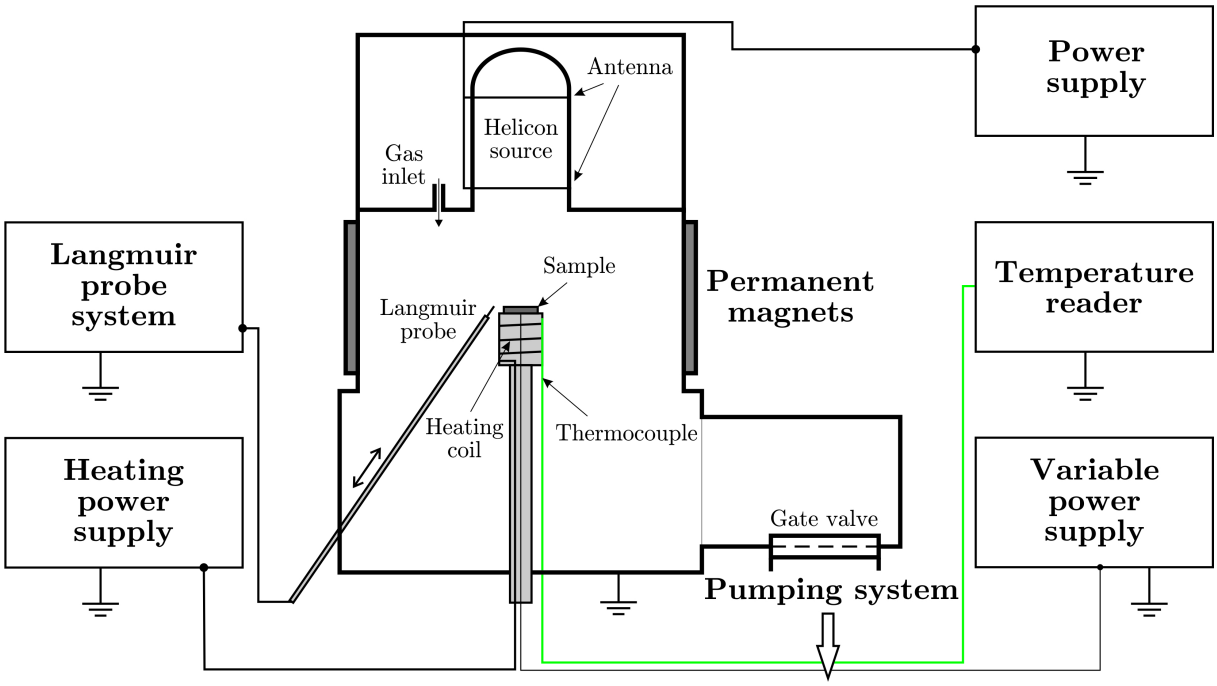

Figure 3.22. A schematic of PISCES-E. A schematic of PISCES-E. The plasma source is an inductively coupled RF helicon source. The sample is mounted on a heating stage 100 mm away from the bottom of the helicon bell jar. Pressure is monitored by an ion gauge.

The Langmuir probe measurements can be made via a retractable cylindrical Langmuir

probe that had RF compensation built into the circuitry. The probe can be inserted into the plasma at a distance of 10 mm from the sample edge giving an approximation of the conditions of the sample. The sample is placed on the top of a heating stage which consists of a molybdenum cylinder, with a heating coil inside. The sample is situated on the axis of the helicon device, and 100 mm away from the bottom of the bell jar. The sample is heated by simply passing a current through this coil, and resistively heating the molybdenum cylinder. This heating current is driven by a power supply, with typical values of 8.15 V and 13.4 A. A type-k thermocouple was inserted into the side of the Mo cylinder less than 5 mm from the surface and 5 mm away in the radial direction, an error on the temperature reading of ±50 K is assumed due to the distance of the thermocouple to the sample. However the glow from the sample at operating temperatures is consistent with the glow of samples in other devices with better temperature sensors, and consistent with the temperature being above the minimum temperature for fuzz to form (as detailed in section 2.1.3). He ion bombardment is achieved by biasing the sample and heater stage using a variable power supply.

3.8.2 PISCES-A

The PISCES-A device is well described in [91], but a brief description will be provided here. A schematic of the PISCES-A device is provided in figure 3.23. The device consists of a 2.5 m long 200 mm diameter stainless steel cylindrical vacuum chamber that is differentially pumped by cold trapped diffusion pumps which control the gas pressure along the system. A base pressure of $1{\times}10^{-4}$ Pa can be achieved. The vacuum vessel is actively cooled via copper water lines soldered to the chamber walls. The plasma is produced by a reflex arc discharge from a 70 mm diameter lanthanum molybdenum (La-Mo) disc cathode to a water-cooled cylindrical anode surrounding it. The plasma generated is $90-100$ mm in diameter being confined by a $0.2-0.4$ T solenoidal magnetic field. The He gas is fed into the chamber just in front of the La-Mo disc, and the pressure is monitored via various pressure gauges along the chamber.

Langmuir probe measurements can be made by an actively cooled retractable Langmuir probe situated about 400 mm upstream of the sample position. The probe can be triggered to be automatically inserted into the plasma and record data before retracting to a safe position out of the plasma beam, all within 2 seconds. The sample is placed on a mounting stage on the axis of the plasma beam 1 m away from the plasma source. The sample is heated by the plasma and air cooling behind the sample controlled manually by a needle valve allows temperature control. A type-k thermocouple is placed behind the sample to constantly record the temperature. The sample can be biased by a variable power supply.

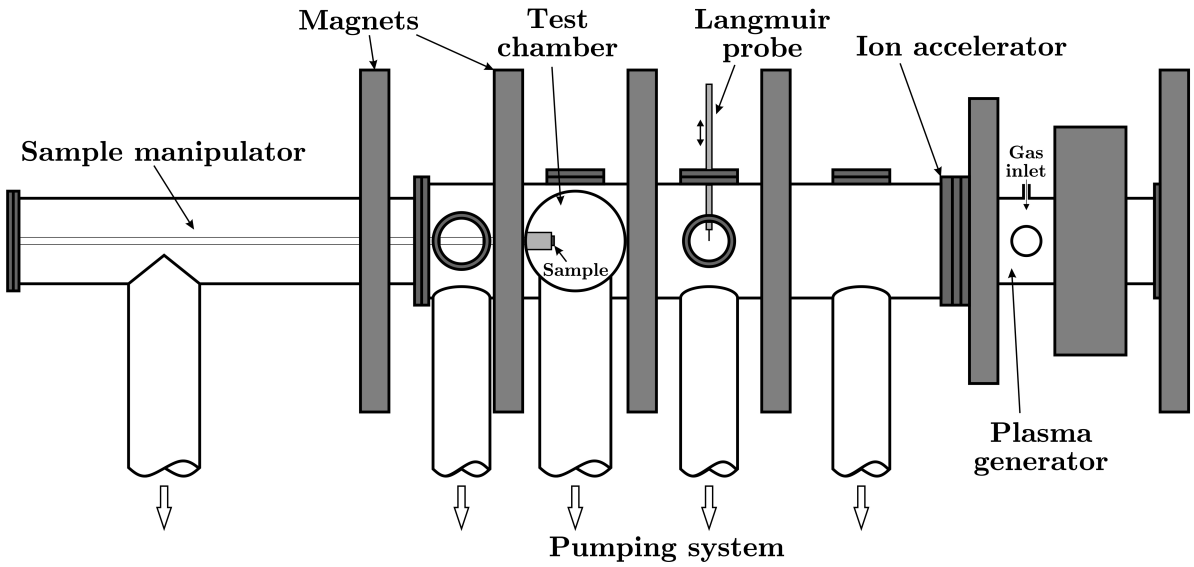

Figure 3.23. A schematic of PISCES-A. The device is a 2.5 m long stainless steel chamber 200 mm in diameter. The sample is 1 m from the source placed on the same axis as the plasma beam. The sample is heated by the plasma and actively cooled by an air flow to the back of the sample.

3.8.3 PISCES-B

The PISCES-B device is of similar design to PISCES-A, and is well explained in detail in [92]. As the device was only used once, only a very brief description will be provided here. PISCES-B was intended to be an evolution of PISCES-A, built upon similar design principals, they are both linear plasma devices, and are operated in the same way. However PISCES-B has several enhancements over PISCES-A apart from just being able to achieve a higher flux plasma. PISCES-B has *in-situ* analysis capabilities by Auger electron spectroscopy (AES), X-ray induced photoelectron spectroscopy (XPS), and secondary ion mas spectroscopy (SIMS). A lower base pressure can be achieved of $1{\times}10^{-6}$ Pa. PISCES-B has a Langmuir probe attached in order to attain plasma parameters in the same way as the other devices. The sample can also be biased and the temperature controlled using the same method as PISCES-A by heating from the plasma and air-cooling behind the sample. PISCES-B is also housed in a special clean room, with a decontamination room in between the clean room and the rest of the laboratory, allowing beryllium to be used in PISCES-B. Therefore, PISCES-B is fully controllable from outside the clean room.

Chapter 4

Preliminary Results

In this chapter the initial calibration of the rig and the results of the plasma diagnostics will be shown.

4.1 Langmuir probe data

Throughout this thesis, many Langmuir probe curves were acquired, using a variety of probes, and covering many parameter-spaces. The main probes used were a cylindrical probe, a flat planar probe, and a dummy probe. Initially, it was necessary to know where the best position to place the W sample was, and the optimal plasma conditions to make fuzz. The best conditions will primarily be those that give the highest flux of He ions to the W sample, whilst not jeopardising the magnetron device, by, for example, melting the target by overheating due to using too much power.

Initially a cylindrical probe was constructed using a tungsten wire of 0.1 mm diameter with 4.42 mm exposed. An example of a cylindrical Langmuir probe after being used in a chamber is shown in figure 4.1. For the initial stages, three parameters were varied in turn: the distance of the probe from the target, the pressure of the He gas, and the power of the plasma discharge. For these initial scans, the cylindrical probe was connected to an ALP-150 (Impedans) data acquisition box, which sweeps the voltage whilst collecting the current. Baldwin *et al.* in [38] reported that at a He ion energy of 57 eV fuzz readily formed, this will therefore be the starting target energy. As the plasma potential was not yet known, it was assumed, based on data from previous work on the rig, to be 2 eV. As such, the resulting current at a bias of -55 V was selected, giving a He ion energy of ~57 eV.

Firstly, the distance of the probe from the target was varied along the axis of the target. The probe was kept at a fixed position whilst the target was moved in and out of the chamber in step sizes of 5 mm, with a maximum range of 50 mm. The probe was then moved to another port and the target position varied again. A plasma power of 200 W and a He gas pressure of 30 mTorr were kept constant. These were chosen fairly

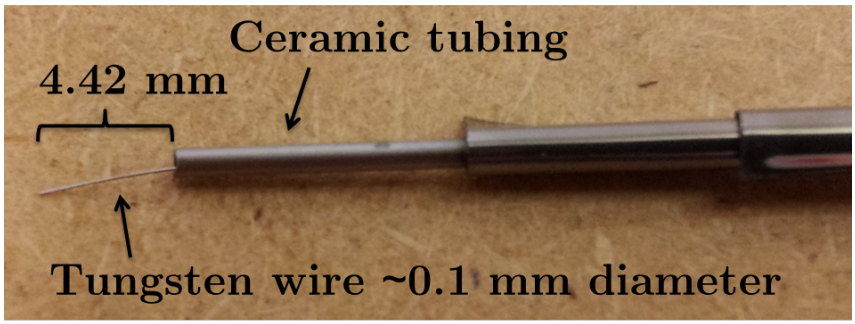

Figure 4.1. A photo of a cylindrical Langmuir probe showing the metal tungsten tip, with 4.42 mm exposed and of 0.1 mm diameter. The probe is held in position by ceramic tubing, which isolates the wire from the metal rod which supports the probe in the chamber. The ceramic tubing appears metallic because of the deposition occurring inside the chamber.

arbitrarily at this point, as initial forays into using He in the vacuum chamber showed that a minimum gas pressure of ~8 mTorr was necessary for the plasma to ignite, and 200 W produced a sufficient glow without being too high to jeopardise the system. From the scan, the current at -55 V was recorded, and converted to flux via,

$$\Gamma = \frac{I}{eA} \tag{4.1}$$

where Γ is the flux of He ions, I is the current, e is the electron charge, and A is the area of the probe. The area of the probe, being a cylinder, is given by ,

$$A = \pi dl + \pi \left(\frac{d}{2}\right)^2 \tag{4.2}$$

where d is the diameter of the probe (0.1 mm), and l is the length of the probe (4.42 mm). This gives $A = 1.4{\times}10^{-6}$ m^2. The flux scan at -55 V is shown in figure 4.2a. Due to the geometry of the rig, there was a small distance where the flux could not be measured. However, from the result, it appears that the position giving the highest He flux is at 103 mm from the target.

Next, the He gas pressure in the chamber was varied, keeping the probe at the fixed position of 103 mm away from the target, and a plasma power of 200 W again. The results can be seen in figure 4.2(b), showing an exponential decay. At pressures lower than 10 mTorr it was hard to ignite the plasma, whereas higher pressures could not be achieved using the current setup as the needle valve was fully opened. Also, there is concern with higher pressures that the mean free path will become less than the sheath thickness. As there was little change beyond 40 mTorr, this pressure was chosen to be the operational pressure, serving as a stable medium.

Lastly, the plasma power was varied, keeping the He gas pressure at 40 mTorr, and the position at 103 mm. The power was varied from 100 W to 800 W, as it was recommended

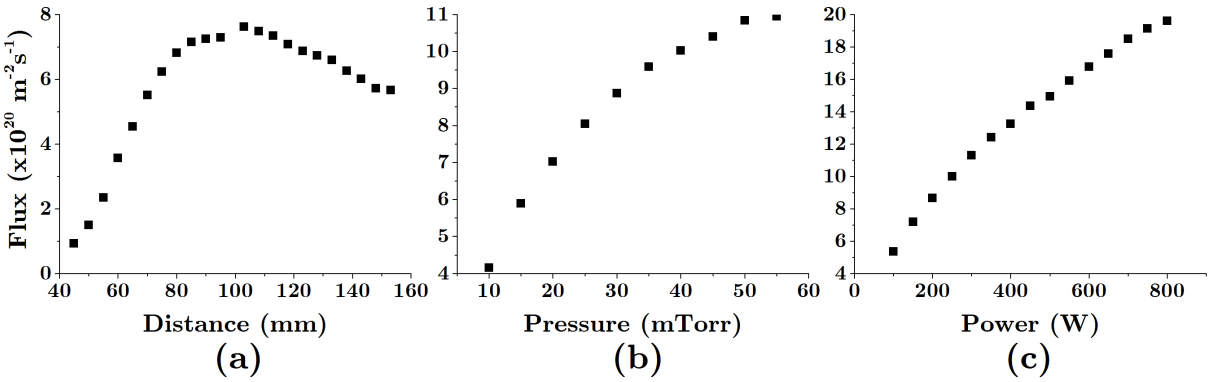

Figure 4.2. The measured He ion flux whilst varying the parameters to find the optimal conditions for fuzz growth, using a cylindrical Langmuir probe. Whilst varying one parameter the other parameters were kept at 103 mm, 30 mTorr, and 200 W, for the distance between the probe and the target, the He gas pressure, and the plasma power, respectively. In (a) the distance alone is varied, in (b) the He gas pressure, and in (c) the plasma power.

not to go higher than 800 W with the existing cooling capability. The results are shown in figure 4.2(c). In the end, a power of 700 W was chosen, as it was a compromise between a high flux and not risking melting the target.

As such, the chosen parameters to initially attempt to grow fuzz involved placing the sample a distance of 103 mm from the target, keeping the He gas pressure at 40 mTorr, and the plasma power at 700 W. These provide a starting point for making fuzz, however, the actual flux values from these measurements cannot be used to estimate the growth. Principally because a cylindrical probe was used. Cylindrical probes collect current from every direction, whereas the W sample, upon which fuzz will be grown, will only be collecting He ions from the front facing surface, as the back side is not exposed to the plasma. Also, the existence of the sample heater will influence the plasma in the chamber, and hence affect the results. As such, these flux values are an overestimate of the actual flux values.

4.2 Dummy probe

For more accurate measurements of the flux, a probe was made that recreates the situation of the W sample in the sample holder. A photo of this dummy probe is shown in figure 4.3. The probe was designed to emulate the sample clips shielding part of the sample face from exposure to the plasma. The probe holder was made from PTFE with the dummy sample made from aluminium. The sample holder allows an insulated wire to take the current from the sample through the metal stem and out of the vacuum chamber. This can then be connected to the Langmuir probe acquisition box. This time, fuller Langmuir probe sweeps were taken, going form -60 V to 20 V, allowing the plasma potential to be measured. The distance of the probe face from the target was again varied in the same way

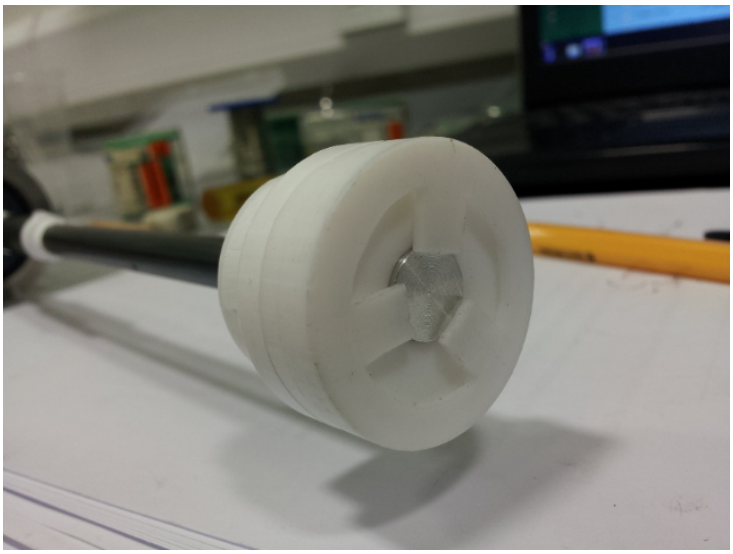

Figure 4.3. A photo of the dummy probe, aimed to emulate the conditions for the sample on the sample heater. The dummy sample exposed is 10 mm in diameter.

as before, by moving the target back. Due to the geometry of this probe the distances could be overlapped for different ports into the chamber. The probe was operated at two He gas pressures of 30 mTorr and 40 mTorr. Lastly, the construction of the probe allowed measurements to be taken with the probe facing the target, or perpendicularly (as is the case in figure 4.3). It is possible to have the sample growing fuzz positioned perpendicularly to the target generating the plasma. This may be done in order to reduce the deposition to the growing sample, but at a cost of a reduced He ion flux. Thus Langmuir probe measurements in this direction were also sought after.

This was done in order to have flux information if the sample was placed facing perpendicularly to the target, in order to reduce sputtering, but at the cost of reduced He ion flux.

The plasma potential was calculated first, and is shown in figure 4.4, showing both the results for the probe positioned face-on to the target, and facing perpendicular to the target. The plasma potentials were calculated by locating the position of the 'knee' of the Langmuir curve, aided by plotting $\ln I$ against the voltage, as is shown in figure 3.8. It can be seen that at a distance of ~100 mm from the target the plasma potential for the probe facing the target is ~0.5±0.3 eV.

The flux to the probe is calculated again using equation 4.1. For the area of the probe the chords covered up by the clips must be accounted for. The area of the circle is simply $\pi r^2 = \pi(0.005)^2 = 7.85\times10^{-5}$ m^2. The area of the segment, as shown in figure 4.5 by the yellow-coloured segment, is given by the area of the wedge minus the area of the isosceles triangular portion, given by,

$$A = \frac{1}{2}r^2\theta - \frac{1}{2}r^2\sin\theta \tag{4.3}$$

where r is the radius of the circle, θ the angle of the wedge (in radians), and c the length

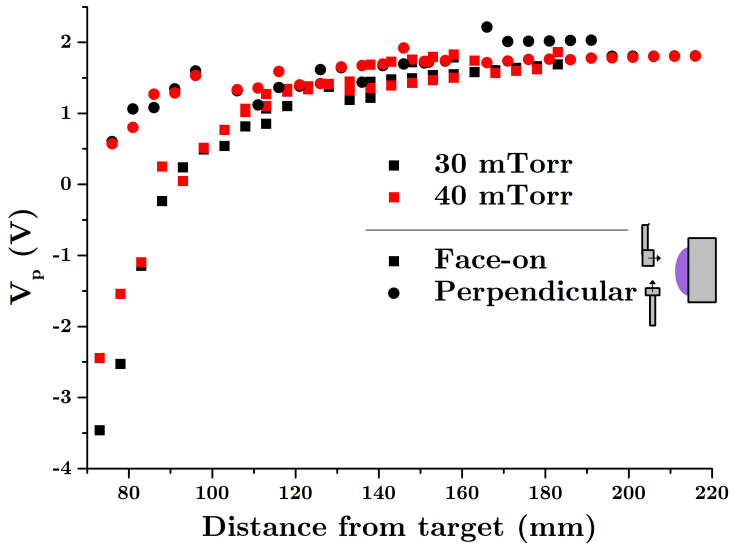

Figure 4.4. Plasma potential measurements as measured by the dummy probe.

of the chord, as shown in figure 4.5. The clips covering the sample give $c \approx 3.5$ mm, and since the chord length can be given by,

$$c = 2r \sin\left(\frac{\theta}{2}\right) \tag{4.4}$$

θ is attained by re-arranging this as c and r are known, giving,

$$\theta = 2 \sin^{-1}\left(\frac{c}{2r}\right) \tag{4.5}$$

resulting in $\theta = 0.72$ rad. Plugging this into equation 4.3 gives $A = 7.68{\times}10^{-7}$ m^2. Therefore the area of the sample exposed to the plasma is the area of the circle minus 3 $\times$ $7.68{\times}10^{-7}$ m^2 $\Rightarrow$ $7.63{\times}10^{-5}$ m^2.

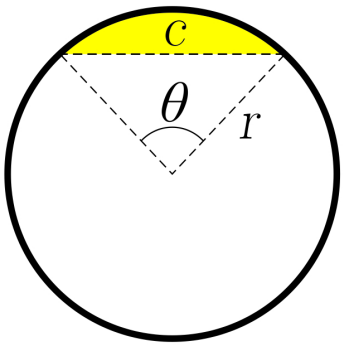

Figure 4.5. A sketch of the probe surface, used to calculate the area of a segment of a circle.

Given the area of the exposed surface it is possible to calculate the fluxes at a fixed bias of -53.5 V resulting in an ion energy of ~54 eV. The fluxes are calculated at various positions and at He gas pressures of 30 and 40 mTorr, both for the probe face-on to the target, and perpendicular. The results are shown in figure 4.6. It can be seen that the

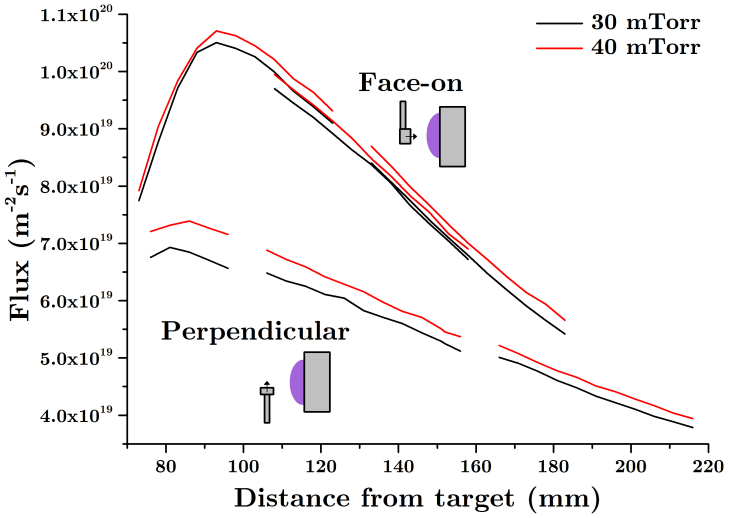

Figure 4.6. Flux vs. distance of the probe from the target, for a dummy probe face-on to the target and perpendicular to it. The black lines indicate readings at 30 mTorr and the red lines at 40 mTorr.

perpendicular fluxes are about 2/3 that of the face-on fluxes, and the drop in flux from the pressure difference is not much, and possibly within the error. Due to the geometry of the probe, measurements could overlap with one another, as can be seen in the middle of the face-on probe results, showing that there is some error in trying to repeat results, similar to the drop in flux for changing pressure. The optimal flux in this figure was shown to be 1.07×10^{20} m^{-2} at 93 mm from the target. After this result was achieved, samples were moved to this position, which, according to figure 4.4 has a plasma potential of 0.05 eV.

4.3 Sample probe

For even more accurate measurements of the flux, a dummy sample was made, as is described in section 3.2.2, which was connected to the Langmuir probe acquisition system. This enabled the most accurate recreation of the conditions that will be apparent whilst growing fuzz. For these results an even larger scan was taken at much smaller voltage steps, spanning -150 V to 50 V, in intervals of 0.1 V. Firstly, the floating potential, V_f, was measured, being the easiest to record as it is simply the point where the Langmuir probe IV curve crosses the x-axis. The recorded V_f's are shown in figure 4.7a. Next, from plotting $\ln I$ against V, as discussed in section 3.2.1, the plasma potential, V_p, and the electron temperature, T_e, are attained, as is shown in figure 4.7b and c, respectively. It seems from these results that the actual position of the samples (at 93 mm decided by the previous results using the dummy probe) is inside the magnetic null, with the null being at approximately 98 mm from the target. This is evident by V_f being at a local maximum (least negative), and T_e being at a local minimum. It may be that the addition

of the large grounded sample holder so close to the target (93 mm) disturbs the plasma significantly. Previous work on this rig has found the magnetic null to be located at 95 mm away from the target on the axis, which fits in with the observed trends in the plasma parameters of figure 4.7.

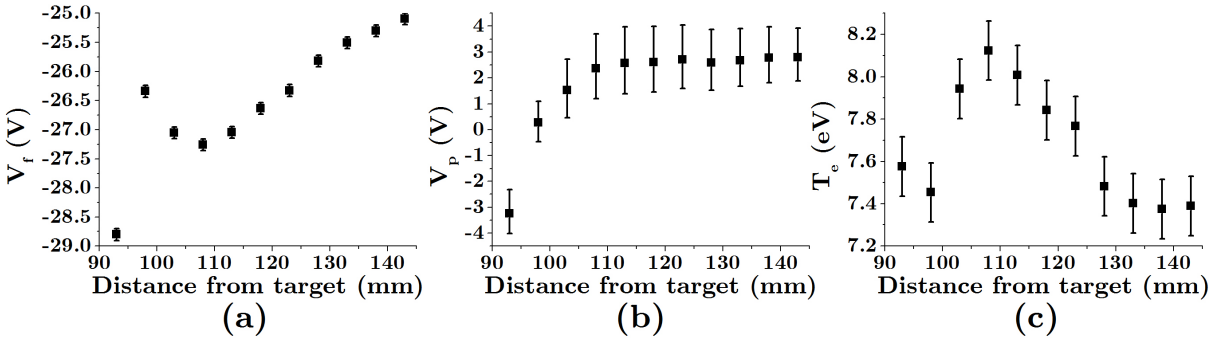

Figure 4.7. Plasma parameters using the sample probe, obtained whilst varying the distance from the target, where (a) shows the floating potential, (b) the plasma potential, and (c) the electron temperature.

The measurement of V_p shows a more negative value than the last results, being -3.2 eV, as opposed to 0.05 eV with the dummy probe. This is perhaps due to the distortion of the plasma by the bulky grounded sample heater being so close to the target, thereby distorting the plasma much more than a PTFE insulated sample holder as was the case for the dummy probe.

The ion saturation, I_{is}, can be calculated by extrapolating the ion current region to V_p, as displayed in figure 3.8a. The values of I_{is} were of the order of 0.1 mA. The area of the sample was calculated in the same way for the dummy probe. From the values of I_{is} for each position, using equation 3.1, substituting in the values of T_e shown in figure 4.7, values of the ion density, n_i, can be attained. The values of n_i were of the order of $1{\times}10^{15}$ m^{-3}. Knowing this, the electron contribution to the current in the ion current region (below V_f) can be removed, giving the true ion current, and hence the most accurate calculation of He ion flux to the W sample. This is done via equation 3.7, and the results of which are shown in figure 4.8. The flux is seen to decrease as the sample bias becomes more positive, as the electrons begin to be collected and hence ions repelled. This is in line with previous work on ion fluxes to biased substrates [119,120]. Figure 4.8(b) shows the fluxes at a sample bias of -60.2 V, which would cause a He ion energy of 57 eV (V_p = -3.2 eV), the energy specified for optimal growth by Baldwin [38]. This also shows that 93 mm is not the optimal position, but 98 mm is. However, the majority of experiments were performed at the position of 93 mm for consistency with earlier experiments. The flux here was measured to be $1.15{\times}10^{20}$ $m^{-2}\,s^{-1}$.

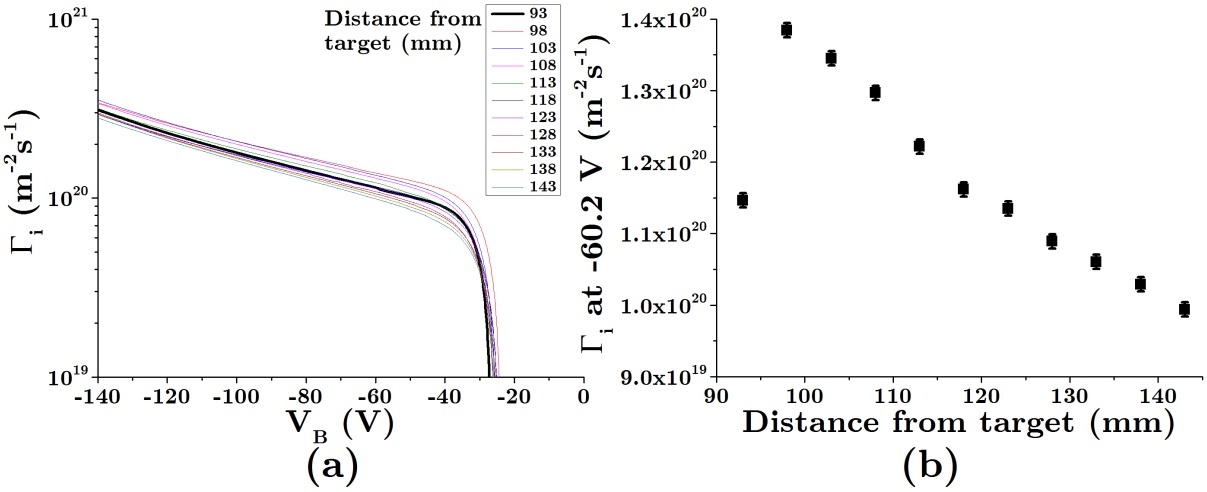

Figure 4.8. Results from the sample probe, showing (a) the flux versus sample bias for different distances, with the thick black line showing where the growing sample was placed, in (b) the flux at -60.2 V is shown, with a He ion energy of 57 eV, plotted against the distance of the probe from the target.

4.4 IR pyrometer

Upon changing to the use of an IR pyrometer over thermocouples to measure the sample temperature, as described in section 3.1.4.2, it was necessary to calibrate the pyrometer. The pyrometer has two values that need calibrating, the emissivity and the transmittance. The transmittance was the easier of the two to calibrate, and relied on the medium through which the IR pyrometer views the sample. The IR pyrometer views the sample through a sapphire window, which reportedly has ~87% transmittance at 2.3 μm, the spectral range of the IR pyrometer. However, it was necessary to experimentally verify this, to get an accurate recording for our experiment.

A rig was made to perform the calibration, involving an aluminium plate, to which two type-k thermocouples were attached. The aim was to heat the metal plate to a temperature above the minimum observable temperature of the IR pyrometer, of 150 ˚C. The two thermocouples were very close to one another, about 1 mm apart, held down by washers and screws. In the middle of these two thermocouples the IR pyrometer was pointed, the alignment aided by laser guides on the pyrometer. The plan was to heat the metal plate with no obstruction between the plate and the pyrometer, calibrate the emissivity until the temperatures on the thermocouples and on the pyrometer agree, then place the sapphire window in the path of the pyrometer and change the transmittance until the temperatures again agree. Thus setting the transmittance of the sapphire window. As such it was necessary to heat the metal plate in atmosphere, as the window of the rig would be open. To do so, two soldering irons were used, both held in position touching the metal plate ~10 mm away from where the pyrometer was aligned. A photo of the experimental setup is shown in figure 4.9. The temperature attained was ~169 ˚C. The

thermocouples agreed with each other within 2 degrees, and the transmittance was found to be optimal at 0.80±0.01.

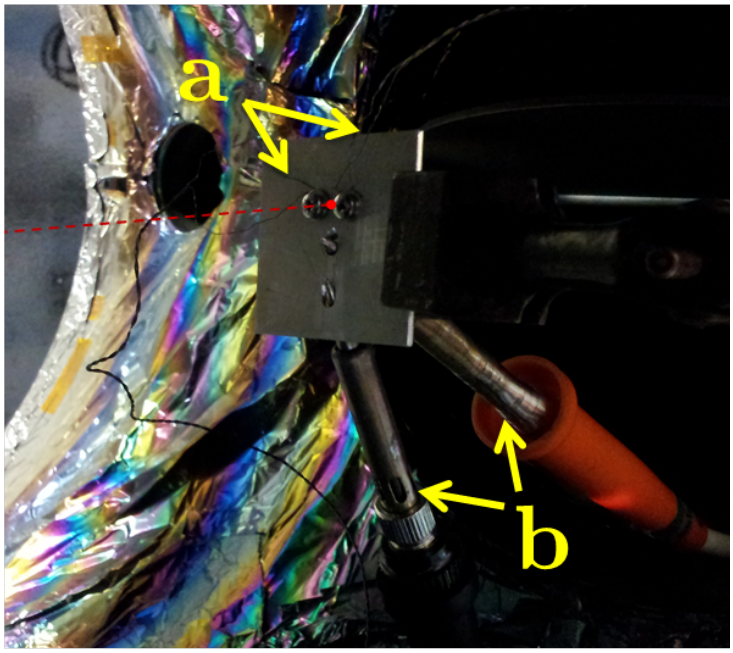

Figure 4.9. A photo of the rig made to calibrate the transmittance of the IR pyrometer. The two type-k thermocouples are pointed out by a, and b points out the two soldering irons used to heat the metal plate. The line of the IR pyrometer camera has been drawn over the photo to show where it was aligned between the two thermocouples, which were held in place under the washers under the screws, as can be seen either side of the alignment point.

The calibration of the emissivity required heating the tungsten samples. This was done with samples that had been electro-polished to a mirror finish, as described in section 3.3.2. The chamber was set up for normal operation, only with two type-k thermocouples (TCs) placed on the sample, held down by the sample clips. The IR pyrometer was aligned to be at the same distance from the filament to the sample as the two TCs, as can be seen in the diagram of figure 4.10. The sample was heated up using the sample heater as will be used during fuzz growth. The sample heater works by controlling the temperature on a feedback loop, such that it will reduce or increase the potential on the filament depending on the difference between the recorded and the set temperature. As such, one of the TCs is set as the primary, and one as the secondary, whereby the primary controls the feedback loop, with the secondary separate from this. During the calibration, the transmittance was set to 0.80 and the emissivity set to 0.70, however the emissivity set here is arbitrary, as will later be shown.

The temperature of the primary TC was at first raised to 227 °C (500 K), then held here for five minutes while the temperature stabilised, after which the temperatures were recorded on all 3 devices, the two TCs and the IR pyrometer. The temperature was then sequentially raised by 50 degrees all the way to 977 °C (1250 K), the operational safety limit of the heater. This was done for 5 different samples.

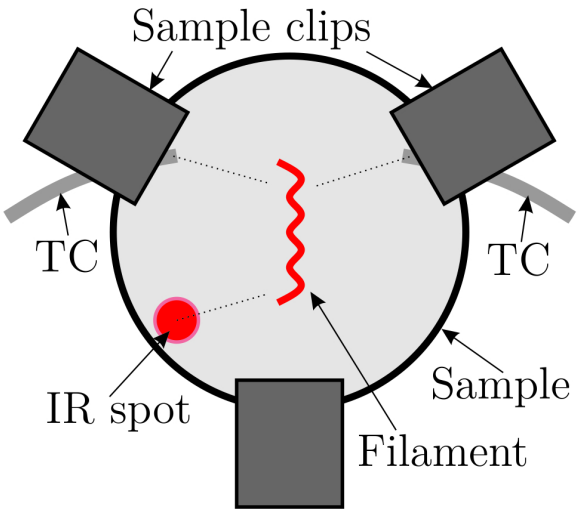

Figure 4.10. Calibrating the emissivity for the IR pyrometer. Showing the positions of the two thermocouples (TC) and IR spot, in an attempt to be equidistant from the filament.

Upon recording the temperatures a code was created which analysed the data. The code relies on using Planck's law, given by,

$$B = \frac{2hc^2}{\lambda^5}\left(\frac{1}{\exp\left(\frac{hc}{\lambda k_B T}\right) - 1}\right) \tag{4.6}$$

where B_0 is the spectral radiance per unit wavelength emitted from a body, h is the Planck constant, c is the speed of light, λ is the wavelength of the light used, k_B is the Boltzmann constant, and T is the temperature of the body. The measured irradiance, I, of the sample, is given by,

$$I = \epsilon\tau B \tag{4.7}$$

where ϵ is the emissivity, and τ the transmittance. For the first instance, T_{IR}, the temperature recorded by the IR pyrometer, is substituted into equation 4.6, and I is simply calculated from equation 4.7 with ϵ and τ as set (0.7 and 0.8, respectively).

Now, since $B = I/\epsilon\tau$, substituting this into equation 4.6, and re-arranging for T gives,

$$T = \frac{hc}{\lambda k_B}\left[\frac{1}{\ln\left(\frac{2hc^2\epsilon\tau}{I\lambda^5} + 1\right)}\right] \tag{4.8}$$

Given I, just calculated, and keeping $\tau = 0.8$, the code finds the value of ϵ in equation 4.8 that gives the desired T. The desired T could either be the value of the primary TC, T_p, the value of the secondary TC, T_s, or the average of the two, T_{avg}.

In practice, T_p and T_s often differed by several degrees, with a larger gap with higher temperatures. This is partly due to the lack of uniformity in the home-made filaments, hence causing un-even sample heating. This could also be due to errors apparent in TCs

due to them receiving current due to the heating method used. Regardless of the cause of the error, their maximum difference was no more than 50 degrees, and if the error was greater than this, then the data was not used, and new TCs made.

The results from the code may appear confusing, but it basically shows the ideal emissivity values as a function of temperature. For each sample, the ideal value for ϵ was calculated for the desired temperature of T_{p}, T_{s}, and T_{avg}. The results are shown in figure 4.11. For example, for sample C, when the secondary thermocouple read 509 °C, an emissivity of 0.186 in the IR pyrometer would have given the same temperature. A line of best fit through all the data is shown by the pink line, giving a value of the emissivity for the samples in the present work as 0.26±0.02. In actual practice the emissivity was calculated as a function of temperature, and changed depending on the desired temperature. At any given temperature, using the chosen emissivity value, the maximum error for any temperature measured by a thermocouple in figure 4.11 is 33 degrees. Therefore this will provide the error on the temperature readings.

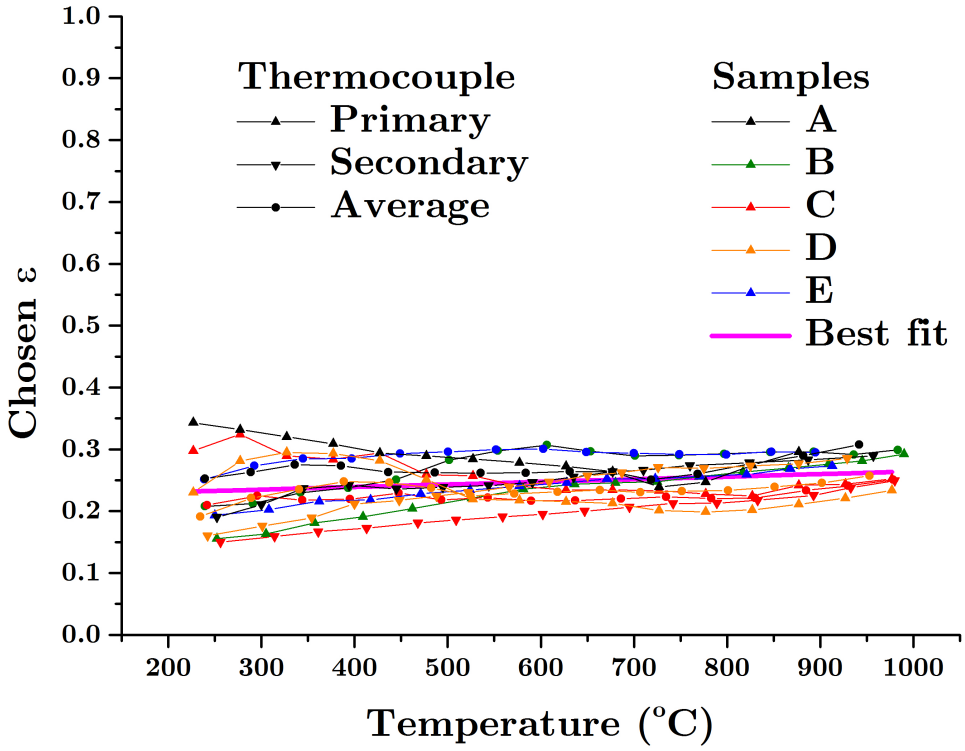

Figure 4.11. The chosen emissivity for each sample as a function of the temperature. The results of the code for choosing the optimal value for the emissivity. For each thermocouple reading, the emissivity value that would make the IR temperature display the same as the thermocouple is plotted.

4.5 Mass spectrometry

The mass spectrometer was used to get a picture of the gasses present in the chamber under operation. The mass spectrometer was placed on the axis of the target, but at a distance of ~380 mm from the target, due to the restricted geometry of the mass spectrometer. These data are therefore not representative of the conditions at the sample position necessarily, but can give, hopefully, a broader picture of the operation of the rig.

Initially a residual gas analysis (RGA) was performed, to see what was in the chamber before and after He gas flow was introduced. The base pressure was ~10×10^{-4} Pa and the He gas pressure was 5.3 Pa. The RGA is shown in figure 4.12. There was no recorded counts after a mass of 80 amu. One can see that there are significant background gases present in the chamber, however, with the addition of He, this seems like a very pure gas (it is 99.9995% purity) as there is no real change between the two spectra apart from the addition of He.

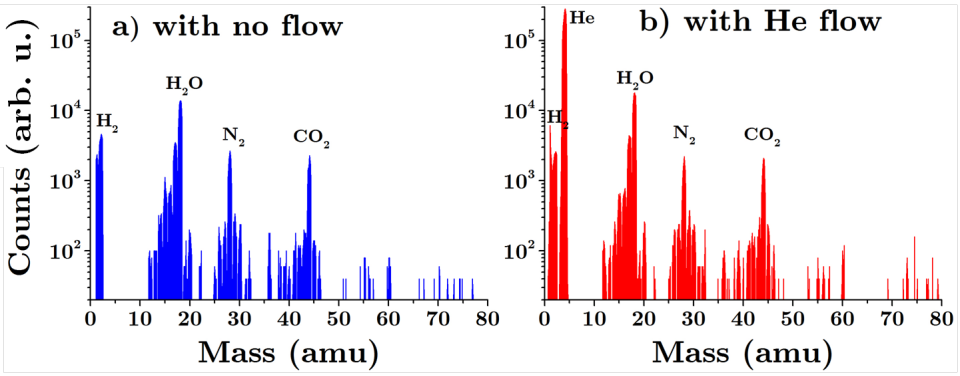

Figure 4.12. The residual gas analysis (RGA) performed, a) with no gas flow, and b) with He gas flow.

Next a full range mass spectrum was recorded whilst the plasma was in operation. The spectrum is shown in figure 4.13. Tungsten ions can be seen above 180 amu here, as well as tungsten oxides. It is interesting that there is almost as much H_2O as there is He collected. This hints at the rig being rather contaminated, and could prevent issues for fuzz growth. The low population of W ions is good in the sense of minimal deposition is wanted whilst growing fuzz. However, this does not account for neutral W atoms, and magnetrons are known to have low metal ionisation fractions, so this is not an accurate portrayal of deposition, but is an indication.

Lastly, the energies of He and W ions were analysed by keeping the mass constant, at 4 and 183.8 amu, respectively. These are shown in figure 4.14. The He ion energy presents itself with quite a wide range of energies, from 0 to 5 eV. The negative energies are likely an artefact of He ions being generated inside the mass spectrometer itself, due to the very small size of He atoms easily getting into the mass spectrometer. The W ion energies are between 2 and 5 eV.

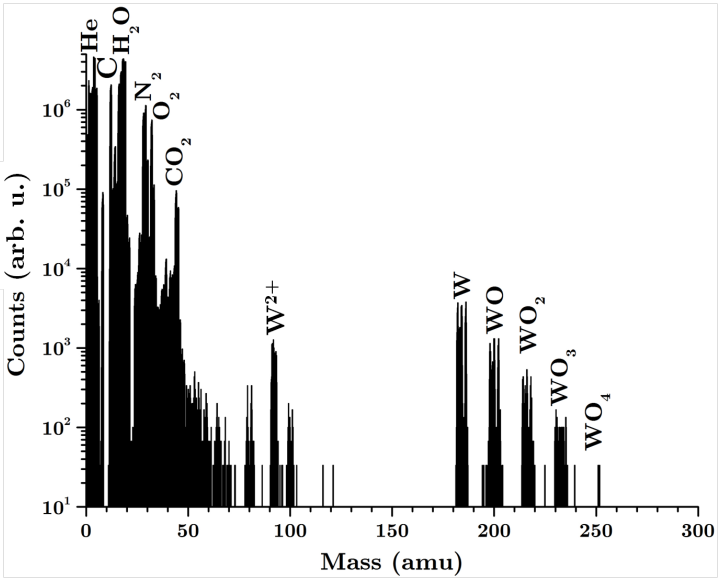

Figure 4.13. The full mass spectrum produced under plasma operation at 700 W and 40 mTorr He gas pressure.

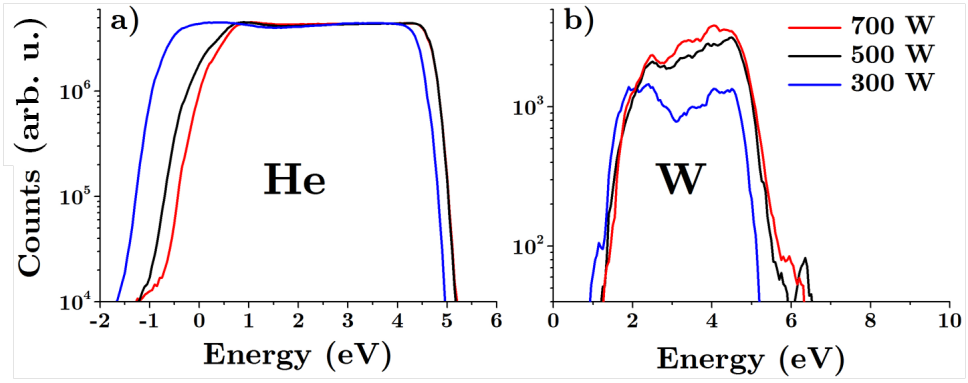

Figure 4.14. The mass spectrometer energy analyses of a) the He ions, and b) the W ions, performed at 300, 500, and 700 W.

4.6 Thermal probe

The active thermal probe (ATP) was placed in the magnetron and exposed to a plasma whilst sweeping various parameters. The parameters swept were the same as for the Langmuir probe sweeps performed in section 4.1, being the distance to the target, the power applied to the target, and the He gas pressure. The results are compiled in figure 4.15. The chosen parameters for fuzz growth, based on the Langmuir probe data, are a distance of 93 mm from the target, 700 W plasma power, and a He gas pressure of 40 mTorr. The closest position with the ATP is at 95 mm from the target, and the energy influx here is 9.4±0.1 MW m^{-2}. This is in line with measurements of the energy influx in similar devices. Ruben Wiese, the inventor of this probe, recorded energy influxes in excess of 8 MW m^{-2} in a RF inductively coupled plasma operating at 700 W [113]. Separately, in an RF magnetron device, with 3 targets operating at 100 W each, a calorimetric probe

was placed 50 mm from the centre of the targets, the probe recorded energies of the order of MW m^{-2} [121].

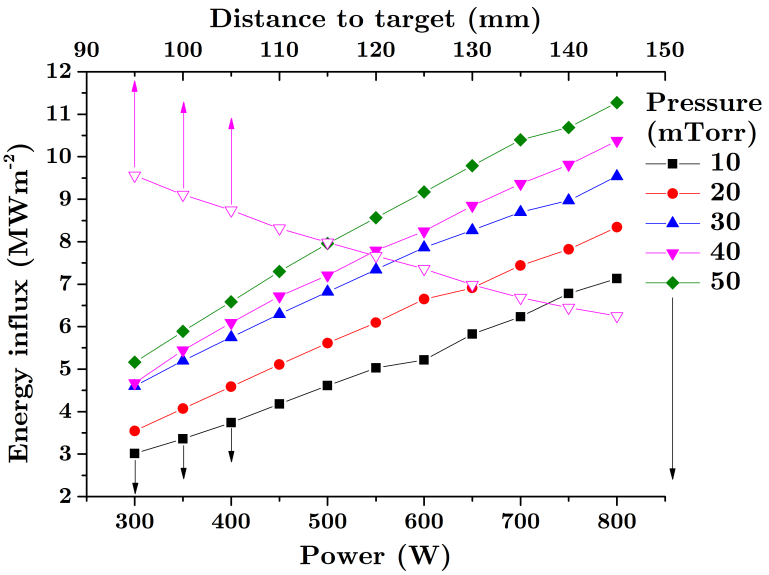

Figure 4.15. The energy influx measured at various parameters using the ATP. The closed symbols are for the bottom x axis, and were the sweeps of power performed at different gas pressures (10 - 50 mTorr) at a fixed distance from the target (95 mm), whilst the open symbols are for the top x axis, being a position sweep with fixed power and pressure of 700 W and 40 mTorr, respectively.

It must be noted that the ATP was not bias-able, and as such the results in figure 4.15 are at floating potential, and therefore do not give an accurate portrayal of the conditions that a sample growing fuzz will be under. As such, a passive thermal probe (PTP) was used, which was bias-able, and placed at the same location as the ATP, 95 mm from the target. This probe was calibrated by the ATP, by taking measurements with the PTP at potentials from -80 to -30, and then at ground, allowing an extrapolation to be made to the floating potential, at this point the PTP is calibrated to be the same as the ATP. The results for the PTP are shown in figure 4.16. The value of the energy influx for a growing sample at -53 V bias is therefore measured to be 9.5±0.5 MW m^{-2}. The same value as was measured using the ATP at floating potential.

4.7 Deposition

The deposition rate was monitored using a quartz crystal microbalance (QCM), as described in section 3.2.5. The deposition rate monitor was placed both facing the target and perpendicular to it, and at two different He gas pressures, of 30 and 40 mTorr. The QCM's results were not too unified, exhibiting quite a variety of rates each time the plasma was turned on, the reason for this is unknown. The QCM measures the thickness over time, and this is plotted in figure 4.17. One can see that there is no apparent differ-

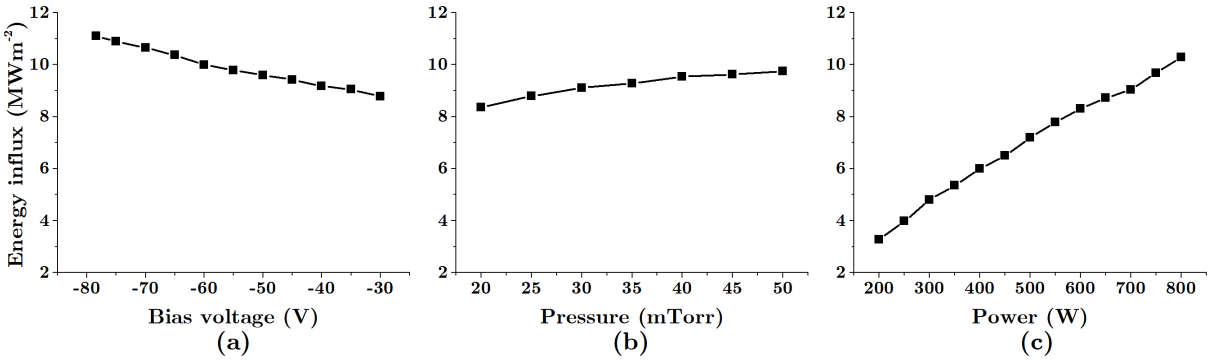

Figure 4.16. The energy influx as measured by the PTP, with (a) varying the bias at 700 W, and 40 mTorr, (b), varying the pressure at -53.5 V and 700 W, and (c) varying the power at -53.5 V and 40 mTorr.

ence in changing the pressure, although one might have expected a lower deposition rate given the decreased mean free path with higher pressures, but this is perhaps offset by the increase in flux of He ions impinging on the target, and hence increased sputtering. There is a large spread in the data obtained, this may be due to the measurements occurring at the limit of the QCMs detection capabilities or due to the inherent random nature of the plasma.

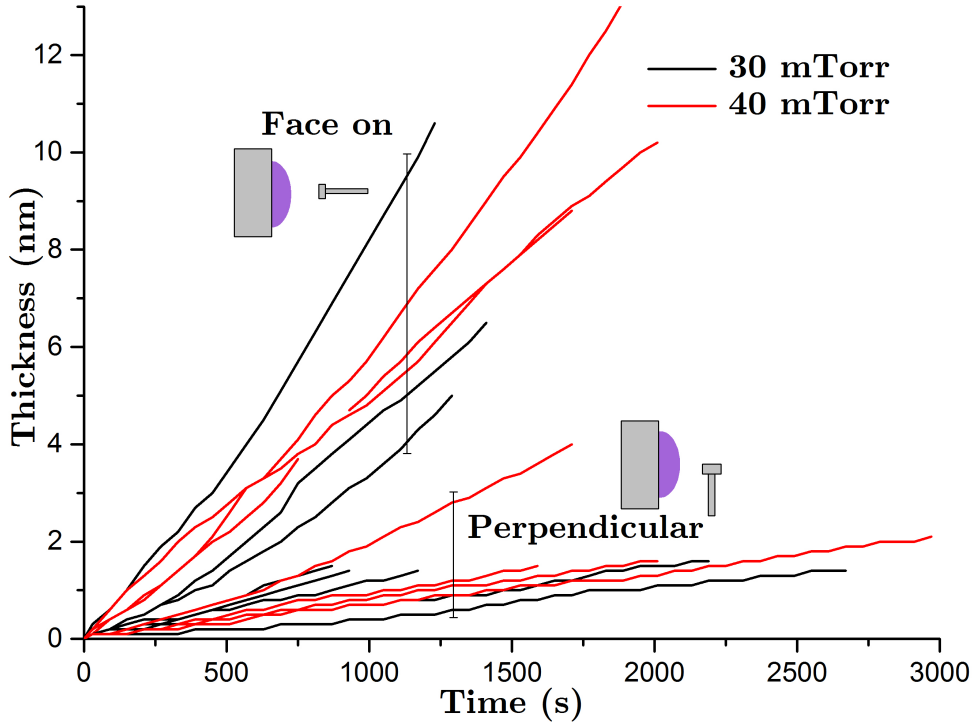

Figure 4.17. The thickness as measured by the QCM, shown for the QCM facing the target and facing perpendicular, at He gas pressures of 30 and 40 mTorr.

The QCM was placed at a distance of 150 mm from the target, as opposed to the usual position of previous probes being where the sample will be placed. This was due to the lack of ports that could support such a probe. This therefore may give an underestimate

on the deposition rate, as it is further away from the target, and depositing particles could be scattered away, and also less particles coming at an angle to the QCM will be collected. By differentiating the recorded thicknesses with time, the deposition rates can be calculated. The results are shown in table 4.1. Due to the long time required to gather the data, no further measurements were taken, which would have improved the error. The main value of interest is the 40 mTorr case facing the target, of 5.34 ± 2.32 pm s^{-1}, being the best estimate of the situation the sample growing fuzz will be under.

	Position	
Pressure	Facing	Perp.
30 mTorr	5.68 ± 5.09	1.37 ± 1.34
40 mTorr	5.34 ± 2.32	1.33 ± 1.59

Table 4.1. The deposition rates measured in pm s^{-1}, as measured by the QCM, both facing the target, and perpendicular to it, with He gas pressures of 30 and 40 mTorr.

The reason for the perpendicular measurements, both here and with the dummy probe was an attempt to see what the situation would be if the sample was placed perpendicular to the target, to reduce deposition, and if the reduction in deposition is worth the reduction in He ion flux. Taking the flux measurements from the dummy probe in figure 4.6, using the maximum flux for both the facing and perpendicular situation (at 40 mTorr), the flux is reduced from 1.07×10^{20} m^{-2} s^{-1} to 7.39×10^{19} m^{-2} s^{-1}, i.e. the flux perpendicular is 69% of the flux facing. The deposition, on the other hand, given in table 4.1, is reduced from 5.34 pm s^{-1} to 1.33 pm s^{-1}, i.e. the deposition rate perpendicular is 25% the rate facing. Therefore one could argue that it is worthwhile attempting to grow fuzz facing perpendicular to the target, given the deposition rate is reduced much more than the flux. However, more accurate measurements of the deposition rate should be performed first, to confirm this.

4.8 Thickness measurements

4.8.1 SEM

The conventional method used in the literature is to break the sample in half and image the cross-section in an SEM. An example of such an image is shown in figure 3.16.

Attempts were made to break a sample in half, however, due to the small size of samples used in the magnetron (10 mm), compared with the samples used at the PISCES laboratory (25 mm), it was difficult to achieve a fine break. As such, attempts to get a thickness from these images were difficult. An attempt to make thickness measurements by cross-sectional SEM can be seen in figure 4.18. The difficulty in deciding where to measure the thickness is apparent, as well as the very unclean cut, as can be seen in

figure 4.18. In the bottom two larger images of fig. 4.18, blue lines show where attempts to measure the thickness were done. From the image on the left, from left to right the thicknesses measured were 341, 399, and 417 nm, and for the image on the right, 187, 246, and 351 nm. This gives an average thickness of 323 nm ± 140 nm.

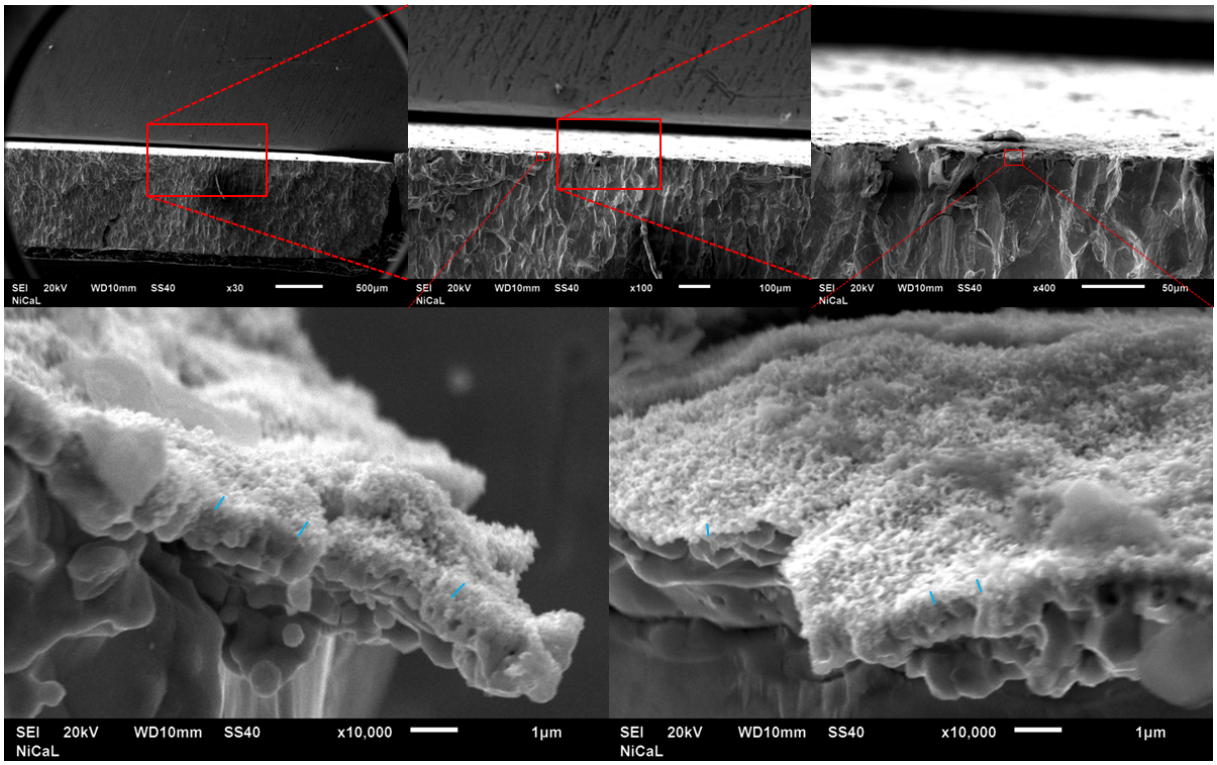

Figure 4.18. An SEM image of an attempt to get thickness measurements from a sample broken in half. Blue lines indicate attempts to measure the thicknesses in the bottom two images.

The SEM was also used with a different approach, by first scratching the sample, and then attempting to view the trench at an angle, thus hoping to see the trench wall, and hence get a value of the thickness of the fuzz layer. However, it was very difficult to define where the trench wall was in the images, and hence where the 'bottom' of the fuzz was. These tilted SEM images can be seen in figure 4.19.

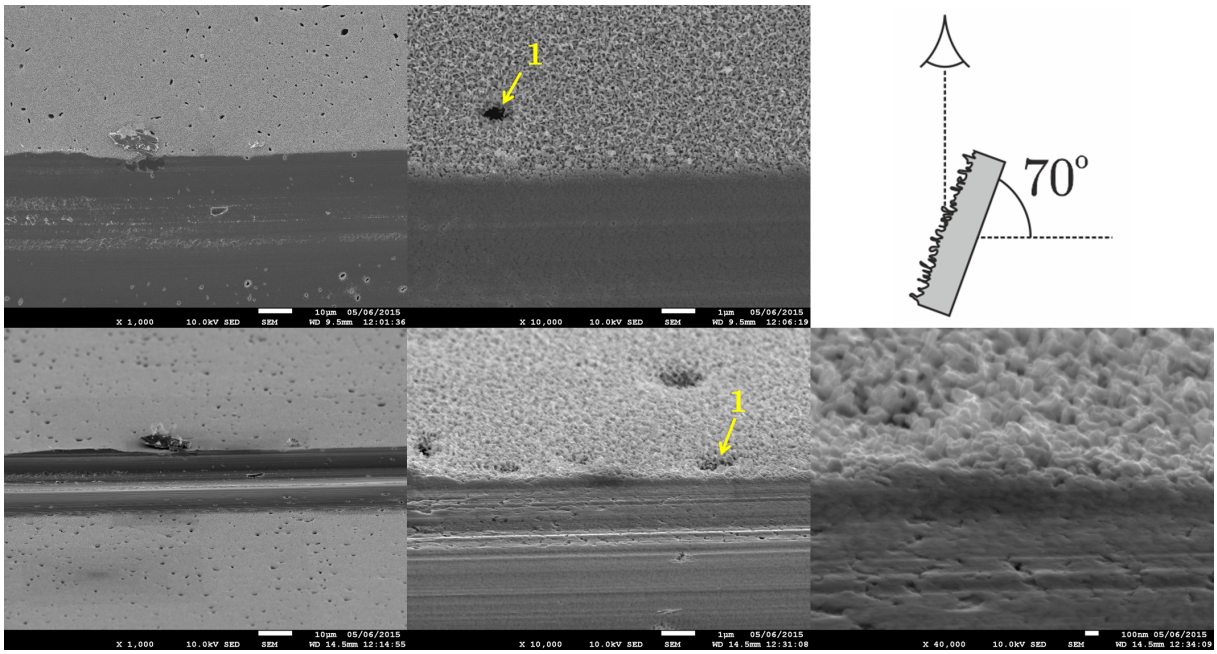

Figure 4.19. An SEM image of an attempt to get the fuzz layer thickness by making a scratch into the samples, thereby removing some fuzz, then viewing the scratch at an angle. The images on the top are taken perpendicular to the plane of the sample, whereas the images on the bottom image are taken with the sample tilted 70° away from the original position, as shown in the diagram in the top right. The number marker is there to point out a feature that appears in two of the images.

4.8.2 CFM

The confocal microscope (CFM) was first used at UC San Diego on the samples created there, and discussed in chapter 5. An example of a scratch imaged in the CFM is shown in figure 4.20. The thickness measured in this sample was 960 ± 90 nm. This method proved very easy for thick samples such as that in figure 4.20, but even for samples with very little fuzz, such as that shown in figure 4.21, it was possible to get a measurement. Although the area inside the scratch of the sample in figure 4.21 is very non-uniform, there is a region near the top right where a clear step profile can be seen, and hence a measurement can be taken, in this case being 50 ± 30 nm.

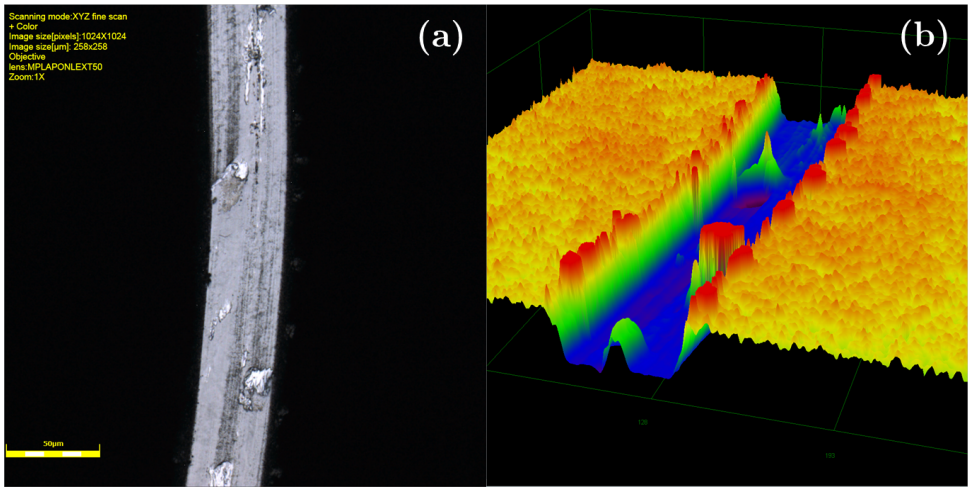

Figure 4.20. A result from the CFM used at UC San Diego. In (a) an optical image of the area scanned is shown, with (b) being the profile reproduced in the CFM giving the height information. The profile in (b) has been smoothed and stretched for ease of measurement. The scale bar in (a) is 50 μm. The thickness of this sample was measured to be 960 ± 90 nm.

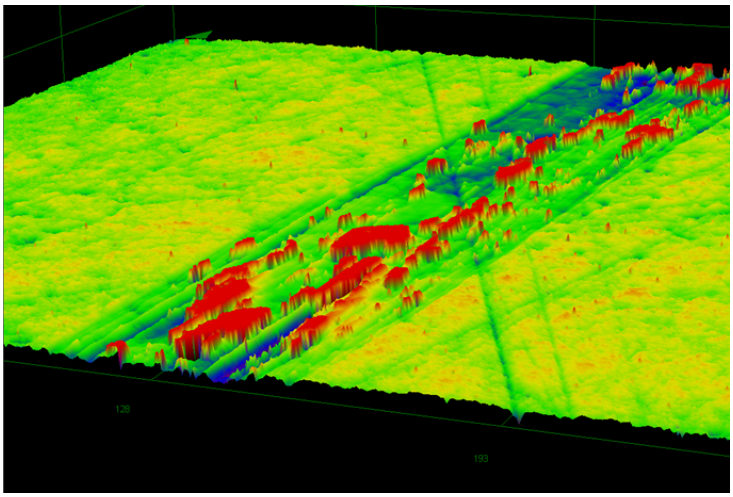

Figure 4.21. A result from the CFM at UC San Diego used on a thin sample. The thickness here was measured to be 50 ± 30 nm.

Attempts were done of the samples created at Liverpool in a CFM at the University

of Manchester. However, the results were not so fruitful, it appeared as if the scratching into the surface was making a cut deeper into the samples, as the depths of the scratches were on the order of microns, even for samples with very little exposure time. An example of this can be seen in figure 4.22. However, an obvious transition region from an area of fuzz to an area that has been scratched off is apparent, as such, a thickness could be attempted to be measured on the left hand-side of the scratch shown in figure 4.22. A profile of this sample is shown in figure 4.23. It can be seen that the scratch depth is over 2 μm's thick, and the area on the left of the scratch still presents difficulties for where to measure the fuzz layer from and to. An estimate of the layer thickness using figure 4.23b could be either 144, 210, or 287 nm (± 36 nm), depending on where the measurement was made from. The sample shown in this figure is actually the same sample imaged in the SEM in figure 4.19.

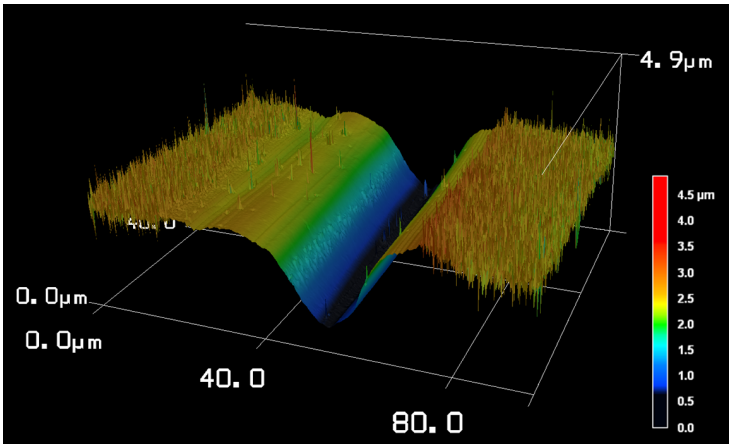

Figure 4.22. An attempt to use the CFM on a sample created at Liverpool. The scratch has seemingly made a very deep cut into the sample.

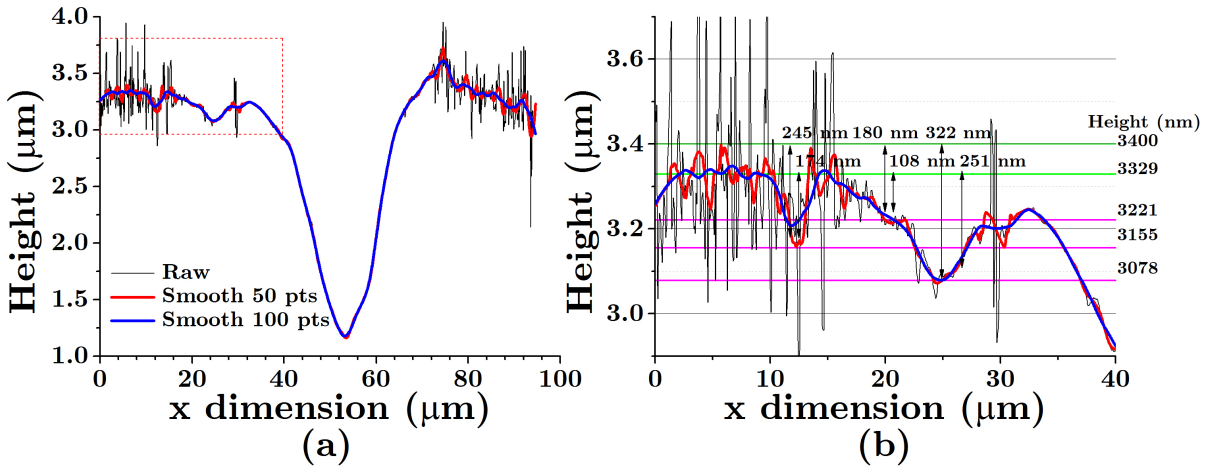

Figure 4.23. The profile of the CFM shown in figure 4.22, with (a) being the full profile, and (b) the zoomed-in area as highlighted in (a) by the red box. In (b) the tops of the estimated peaks are highlighted by the green horizontal lines, and the bottom of the troughs highlighted by pink lines. In both images the red and blue lines represent smoothed profiles of the data.

The variability shown in figure 4.23 is apparent in all of the samples. With the scratch depth being inconsistent, such that it could not be systematically accounted for. Also, as can be seen on the right-hand side of the profile in figure 4.23a, the profile appears to be decreasing here. This non-uniformity, across the whole sample, was seen in most samples, such that it appears as if the uniformity of the samples used at Liverpool were not as uniform as the samples used at UC San Diego. This is most likely due to the different methods for creating the mirror finish, with samples at UC San Diego using mechanical polishing for several hours in a lapping machine, whereas samples at Liverpool were electro-polished, which may have preferential treatment, and lead to non-uniformity of the sample finish. Also samples created at UC San Diego were scratched with metal tweezers, whereas the samples created at Liverpool were scratched using a fine razor blade.

In conclusion, the samples imaged in the CFM at Liverpool are too erroneous to obtain values from, however, the CFM technique used at UC San Diego proved very useful. An investigation should be undertaken into the different scratch techniques, and ideally a suitable machined scratch should be made, such that it can be guaranteed to be the same pressure applied each time.

4.8.3 AFM

The AFM also proved unable to create good images of fuzz. An example of what was often seen is shown in figure 4.24. This particular image shown is actually the same sample used in the CFM as shown in figure 4.22, again showing the deep trench made by the scratch. This time the fuzz is too small to be imaged at this scale, and possibly at this scan rate. AFM is a very time consuming method, and slower scan speeds provide better information, however, for the required measurement, it was deemed too slow to be worthwhile, and provided similar information to the CFM technique which was drastically quicker.

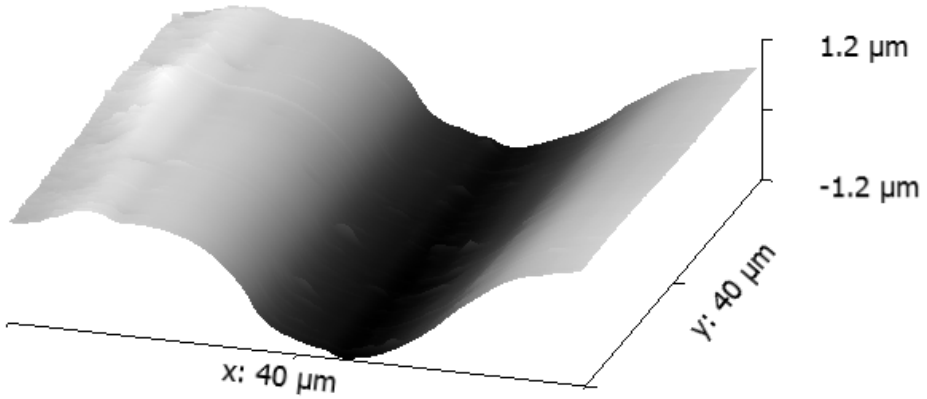

Figure 4.24. An AFM scan of a scratch made on the surface of a fuzz sample. This is the same scratch as that imaged by the CFM in figure 4.22.

4.8.4 Profilometer

The profilometer was attempted to be used on fuzz samples. However, the stylus pressing down on the sample then moving across simply scratched off the surface as the fuzz is too easily removed. This method could not be used to measure fuzz unless the fuzz was somehow protected, perhaps by depositing a metal film on it in order to protect it. However, this device could be used perhaps to make a uniform scratch before being imaged in a CFM.

4.8.5 Interferometer

The interferometer proved also inadequate for measuring fuzz layers due to reflectivity issues. For the samples that had very thick fuzz, the area where fuzz was is very optically black, with very little reflection, in fact, the reflectivity was too low that the interferometer picked up next-to-no signal from the area where fuzz was formed. However, with samples where the reflectivity was low enough, the fuzz was so thin that it was too hard to achieve measurable results at these heights.

4.8.6 FIB

The technique for getting thickness measurements via FIB milling out a trench and observing the cross-section proved the most successful of any technique used on the samples created at Liverpool. This technique provided the most definite distinction of where to measure the thickness from and to, with a very clear line of tendril generation and end. An example of a result is shown in figure 4.25, it can be clearly seen where to measure the fuzz from. The thickness of this sample was recorded at many different points along the x-dimension, giving a result of 330 ± 180 nm. For a method comparison, the sample imaged using this technique was the same sample imaged in the SEM in figure 4.19 and in the CFM in figure 4.23. The measured thicknesses are within the error provided by the CFM for the 210 and the 287 nm results. However, the issues still remain with the CFM technique over where to measure the thickness from.

Due to the certainty with measurements using this technique it was also used on the sample that thickness measurements were first attempted in the SEM via snapping in half and observing the cross section, as shown in figure 4.18. This sample had a very rough surface, as there was very little sample preparation, as this was the first sample. However, using this FIB milling technique the thickness is still very easily attainable even given the roughness of the surface, as can be seen in figure 4.26. The measurement using the FIB gives 480 ± 160 nm, whereas using the cross-sectional break method in section 4.8.1, the thickness was recorded to be 323 ± 140 nm. Although there is some overlap in the measurements, the FIB results are much more reliable.

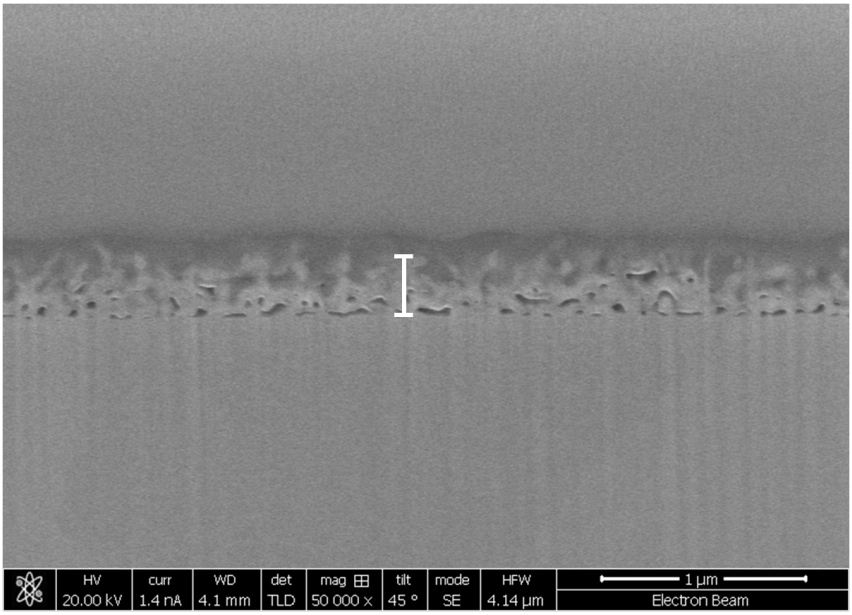

Figure 4.25. An SEM image of the result of the FIB milling technique used on the same sample as was used for the CFM and AFM. An example of one measurement is shown, 50-100 of these were made along the length and the mean value was used for the thickness. The scale is shown in the bottom right. The sample is tilted 45° in this image, therefore any apparent lengths must be multiplied by sin(45°).

4.9 Conclusions

Various diagnostic techniques have been applied to the magnetron setup in order to better understand the situation surrounding the samples whilst fuzz is growing. This Chapter mostly has significance for the work conducted in chapter 6, however, the discussion of the thickness measurements is also relevant to chapter 5.

Measurements using a cylindrical Langmuir probe were used to gather the starting conditions to grow fuzz at. These measurements were later updated by using a dummy probe, and then a sample probe. The sample probe provided the most accurate measurements of the situation for a growing fuzz sample, and provided the values for the He ion fluxes used in chapter 6. The calibration of the IR pyrometer is described, requiring measurements of the emissivity of the samples to be attained. Mass spectra of the plasma were acquired and a residual gas analysis was also performed on the chamber. Thermal probes were used to get estimates of the heat influx to the sample. A QCM was used to measure the deposition rate of tungsten atoms occurring throughout the growth. Lastly the various attempts to get the thickness measurements of the fuzz layers are described and compared. The most accurate and consistent technique proved to be the use of a FIB and SEM cross-sectional images.

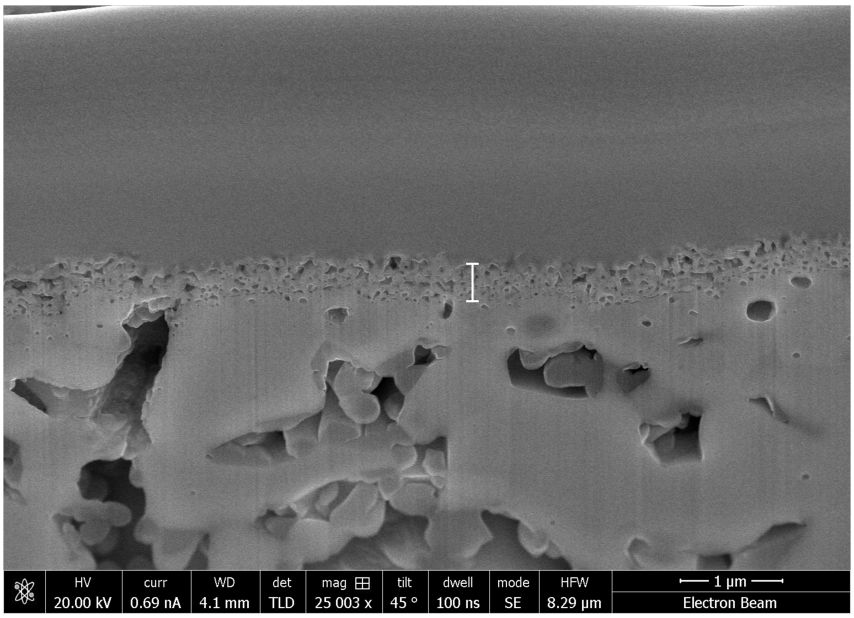

Figure 4.26. An SEM image of the FIB milling technique as used on a sample with a very rough surface finish, the same sample attempted to be measured in figure 4.18. An example of one measurement is shown, 50-100 of these were made along the length and the mean value was used for the thickness. The scale is shown in the bottom right. The sample is tilted 45° in this image, therefore any apparent lengths must be multiplied by sin(45°).

Chapter 5

Development of the Growth Equation

This chapter will show work on compiling data from many devices to look at fuzz growth in the bigger picture, not just that created in a magnetron sputtering device as is the case in chapter 6, with the aim to developing the growth equation as introduced in section 2.1.3. This section largely builds upon a collaboration with the UC San Diego, in particular with Dr. Matthew Baldwin of the Center for Energy Research. As has been previously pointed out, there are three main parameters which govern the growth of fuzzy tungsten: temperature, He ion energy, and fluence. This chapter looks at thicknesses of fuzz layers across a range of fluence, using data from the literature and data acquired from the magnetron sputtering device of chapter 6, as well as several devices at UC San Diego (described in this chapter). The aim is to see if there is a trend across the range, and attempt to build upon and develop the equations and mechanisms governing the growth of fuzz.

5.1 Introduction

The dependence of the fuzz layer thickness on plasma exposure time t, has been explored previously and determined to be more or less dependent on $t^{1/2}$ [20], as is discussed in section 2.1. However, in that work the incident He ion flux was a constant, being $5{\times}10^{22}$ $m^{-2}\,s^{-1}$ throughout the experiments. Later work [38, 122] shows that the same $t^{1/2}$ rate of growth is not maintained if the incident He ion flux is significantly less. In that case, many hours of plasma exposure under lower flux conditions are necessary to match layer thickness results taken at higher flux over just tens of minutes. This directly points to the additional importance of considering the total He ion fluence in addition to observation of exposure time. In the original paper suggesting a $t^{1/2}$ fit [20], as the flux was constant, a $t^{1/2}$ fit is directly proportional to a $\Phi^{1/2}$ fit, as $\Phi = \Gamma t$, where Φ is the fluence, and Γ is

the flux.

Looking further into the fluence dependence, in [20] the quoted growth of the layer begins at $t = 0$, the instant the plasma is initiated. Later work suggests [19], and hints in experiment [104], that an amount of time is necessary for the He bubbles to form and accumulate before the fuzz can begin to grow. This essentially amounts to an 'incubation' time or fluence, and is consistent with current hypotheses on the nature of fuzz growth [19,52] that emphasize near surface He bubble formation as underpinning the fuzz growth process.

To reconcile prior issues surrounding fluence, flux, and time, an expanded set of fuzz layer growth data have been taken at ~1120 K to complement the results in [20], which first demonstrated the $t^{1/2}$ nature of fuzz growth. The expanded set covers 4 orders of magnitude of He ion flux and fluence. The acquisition of these data required the use of many plasma devices of differing plasma density and flux. Included are the magnetron device [122] at the University of Liverpool (UoL) as explained in section 3.1.1, an inductively coupled RF plasma device PISCES-E [116] and the linear plasma devices PISCES-A [91] and PISCES-B [92] located at UC San Diego, and explained in section 5.2. The new data obtained, as well as data taken from the literature under similar conditions, collectively give rise to a more general fluence dependent growth expression, which reduces to the $t^{1/2}$ dependent form of [20] for the special case of constant He ion flux and zero surface erosion.

In erosive regimes, this new general expression is easily incorporated into the growth-erosion equilibria problem of [11, 43]. This problem is solved mathematically to give an expression for defining the thickness of the tungsten fuzz layer under the competing processes of growth and erosion by sputtering. A further outcome, in considering limits of this expression, is that simple analytical equations can be derived that give the approximate He ion fluence that satisfies the equilibria condition, and the equilibrium fuzz thickness, in an erosive regime. The validity of these simple expressions is explored by way of comparison to growth-erosion equilibrium results available in the literature and good agreement is observed.

5.2 Experimental method

Four increasingly powerful plasma devices, each with successively overlapping parameter space, were used to examine the growth of tungsten fuzz over a wide range of He ion flux and fluence spanning four orders of magnitude. A comparative summary of the operational parameters is given in table 5.1. Full descriptions of each device can be found in the literature [91,92,116,122], but a brief summary is provided here.

The lowest He ion flux and fluence conditions were produced by the magnetron sputtering device at the UoL. The device is described in section 3.1.1, and the two samples

		UoL Mag.	PISCES-E RF	PISCES-A LPD	PISCES-B LPD
$P_{\text{disch.}}$ *	(kW)	0.7	1.3	1.5	3.0
Γ	(10^{22} m^{-2} s^{-1})	0.001-0.01	0.01-0.5	0.5-8	5-20
Φ†	(10^{26} m^{-2})	0.01-0.1	0.1-5	5-80	50-200
T_e	(eV)	~7	~4	~6	~6
n_e	(10^{18} m^{-3})	~0.01	~0.5	~5	~10

Table 5.1. He plasma parameter spaces for the devices used in this study. *Values of $P_{\text{disch.}}$ pertain to maximum Γ. Values of T_e and n_e are conditions at mid-range Γ. †Calculated from ~27 h (10^5 s) of exposure time.

used for this experiment were prepared by polishing with wet and dry sandpaper, as detailed in section 3.3.1, and by electro-polishing, as described in section 3.3.2. The former sample was heated using the original PTS-1200 EB (Henniker Scientific) heater as described in section 3.1.2, and the second using the custom-built heater as described in section 3.1.3. The tungsten sample temperature was held at a constant temperature measured via type-k thermocouples or an IR pyrometer. A constant negative bias was applied to the samples, resulting in an average ion energy as displayed in table 5.2 by comparison to the plasma potential which was separately measured in section 4.1. The thicknesses of the samples were determined by SEM inspection by FIB milling out a trench and tilting the sample as described in section 3.6.6.

Samples prepared at UC San Diego were produced on tungsten sample discs cut from rods of 20 mm diameter for use in PISCES-E and PISCES-A, and 25 mm diameter for use in PISCES-B, supplied by Goodfellows. The tungsten was of 99.95% purity and all samples were 1.5 mm thick. Prior to plasma exposure, each was mechanically polished to a mirror finish down to a final lap with 3 μm diamond paste to produce a surface of average roughness better than 50 nm, as measured by a profilometer (Tencor Alpha-Step). Three plasma devices were used at UC San Diego. These are the RF inductively coupled plasma source PISCES-E [116], and the two DC reflex arc sources PISCES-A [91] and PISCES-B [92]. In succession, these devices bridge the gap from the UoL magnetron device to fusion-edge-plasma relevant regimes, and thereby also provide the necessary connection between prior UoL [122] and UC San Diego [20] work.

PISCES-E is described in detail in section 3.8.1. In experiments the samples were heated to ~1050 K before the plasma was turned on, at which point the temperature readings became erroneous. It is assumed that the plasma heated the sample a small amount, at the end of the exposure when the plasma was turned off the temperature reading became reliable again, typical values were ~1150 K. Because of this, the temperature of the sample was put at 1100±50 K throughout plasma exposure. He ion bombardment was achieved by biasing the sample and heater stage to -65 V using a variable power supply. The plasma potential measured from the retractable Langmuir probe was 15±5 V, giving

the average energy of the bombarding He ions as ~80 eV. The He ion flux was measured to be $2\pm0.4\times10^{21}$ m^{-2} s^{-1} throughout the experiments.

With the high density devices PISCES-A and PISCES-B as described in section 3.8.2 and 3.8.3, respectively, samples were heated by exposure to the plasma and the temperature was controlled by adjusting the flow rate of forced air cooling behind the sample. The temperature was measured by a thermocouple in contact with the back of the sample and kept fixed at ~1140 K for each exposure. As the samples were heated by the plasma, exposure time was taken to begin when the sample temperature passes 1073 K, at which point cooling is increased until the temperature stabilizes at ~1140 K. It is important to point out that the time taken to get from 973 K to 1073 K was 40±5 s, as fuzz is known to begin to grow around 900-950 K [33, 104] this 40 s is therefore used to establish a minimum error for the exposure fluence under low fluence operations, but is negligible for high fluence experiments in general. During exposure, samples were biased to -80 V, and a cylindrical reciprocating Langmuir probe was momentarily inserted into the plasma in order to determine the He ion flux and plasma potential. The plasma potential was noted to be -6±1 V, thus giving an incident ion energy of ~75 eV.

Subsequent to plasma exposure, the thicknesses of the fuzz layers were determined by cross-sectional SEM and CFM. Descriptions and comparisons of the two methods are provided in section 3.6.

Images from the literature of fuzzy samples were also used to contribute to the dataset. Thicknesses were taken from published SEM cross-sectional images from many sources and analysed using the ImageJ software. For each cross-section image, slices of the layers were used to measure the layer thickness. In choosing the slices, the line where fuzz was deemed to begin was chosen where the structure changes morphology, in most cases this was obvious as the structure changes colour as well as morphology; in a few cases this was less obvious, and this has been taken into account in the error bars. The top of the layer was chosen to be the maximum distance of the tendrils along the slice, and perpendicular to the sample plane, not accounting for the tendrils curling back on themselves. For each image, 5 slices were used to get an average value for the thicknesses, taking into account areas where the layer thickness could be said to be thicker and areas where it could be thinner in order to provide the error margins.

5.3 Results

Fifteen samples of tungsten were exposed to He plasmas in the various devices described. A listing of the plasma exposure conditions and the measured fuzz layer thicknesses for each sample is given in table 5.2. In addition to these data, a selection of tungsten fuzz results taken from the literature are listed in table 5.3, and are compiled to establish a database of available tungsten fuzz growth data at ~1100±100 K, given that this was the

temperature range used for the new samples. During the literature search, it was noted that many of the samples made in the NAGDIS devices (Nagoya University in Japan, see section 2.1.11) were performed at a higher temperature of 1400 K [19,33,123]. These were considered for inclusion, however, at higher temperatures the competition between growth and annealing out must be considered. This competition has been discussed in section 2.1.13. Therefore for a compilation to be done, and to not include the effect of annealing out due to high temperatures, samples could only be compiled at similar temperatures. Hence the chosen range of temperature is ~1100±100 K, in agreement with the range of temperatures in the experiments performed.

Device	Φ (10^{26} m^{-2})	Γ (10^{22} m^{-2} s^{-1})	T (K)	E_i (eV)	x (μm)
UoL Mag.	0.024±0.0002	0.01±0.0005	1000±50	56.5	0.3±0.1 (0.17±0.1)*
	0.038±0.0002	0.012±0.0002	1100±50	59.5	0.33±0.18 (0.16±0.07)*
PISCES-E	0.04±0.02	0.20±0.04	1100±50	80	0.04±0.03
	0.10±0.02	0.19±0.04	1100±50	80	0.25±0.04
	0.10±0.02	0.19±0.04	1100±50	80	0.38±0.03
	0.10±0.02	0.19±0.04	1100±50	80	0.44±0.05
	0.10±0.02	0.19±0.04	1100±50	80	0.71±0.06
PISCES-A	0.015±0.006	1.4±0.04	1140±20	75	0.05±0.03
	0.028±0.006	1.4±0.04	1140±20	75	0.05±0.03
	0.047±0.005	1.7±0.40	1140±20	75	0.12±0.04
	0.075±0.007	1.5±0.04	1140±20	75	0.41±0.08
	0.20±0.01	1.4±0.04	1140±20	75	0.27±0.05
	0.52±0.02	1.0±0.04	1140±20	75	0.96±0.09
	1.81±0.21	2.0±0.24	1140±20	75	3.87±0.16
	2.03±0.12	1.9±0.12	1140±20	75	2.90±0.20
PISCES-B	110.0±10	11.00±1	1120±30	75	6.5±0.8 $\left(14.2\pm^{10.4}_{2.8}\right)$*

Table 5.2. Plasma exposure conditions and corresponding sample fuzz layer thicknesses in this study. *Bracketed values are corrected for either mass gain or loss during plasma exposure as described in section 5.4.

The compiled dataset is shown in figure 5.1, with each device being represented by a different symbol. Figure 5.1 also shows a straight line fit (dotted line) to the data. This line is related to the $t^{1/2}$ growth dependence given by Baldwin and Doerner [20], extrapolated over the expanded range of fuzz layer thickness data explored in this study. Originally, this dependence was stated as proportional to $t^{1/2}$ for the case of constant He ion flux, and given by

$$x = (2Dt)^{\frac{1}{2}} \tag{5.1}$$

where x is the thickness of the fuzz layer, D is the effective diffusion coefficient, and t is time. The transformation to fluence is straightforward [122], and carried out in figure 5.1 to facilitate comparison to layer thickness results at different ion fluxes. By replacing

Ref.	Fig.	Device	$\Phi^{\dagger}$ (10^{26} m^{-2})	Γ (10^{22} m^{-2} s^{-1})	T (K)	E_i (eV)	x (μm)
[20]	3a	PISCES-B	0.15±0.03	5.0	1120	60	0.26±0.1
	3b		1.0±0.18	5.0	1120	60	1.70±0.1
	3c		2.2±0.36	5.0	1120	60	2.64±0.1
	3d		4.5±0.75	5.0	1120	60	3.25±0.1
	3e		11.0±1.8	5.0	1120	60	5.26±0.1
[18]	2b	PISCES-B	1.8	5.0	1120	60	3.35±0.45
	5a		1.8	5.0	1120	40	2.85±0.17
	5c		1.8	5.0	1120	40	2.26±0.24
[15]	2b	NAGDIS	0.14	1.0	1070	50	0.48±0.06
[124]	6a	NAGDIS-II	0.15	0.8	~1200	50	0.54±0.06

Table 5.3. Literature fuzz layer thicknesses for below sputter threshold He plasma exposure in the temperature range of 1000 – 1200 K. †Where provided, uncertainties are taken from listed Ref..

$t = \Phi/\Gamma$, where Φ is the fluence, and Γ is the flux, and redefining the growth parameter of D as $C = 2D/\Gamma$, the formula can be put in terms of fluence alone as

$$x = (C\Phi)^{\frac{1}{2}} \tag{5.2}$$

From the values in [20], it is determined that at 1120 K (with a flux of 5×10^{22} m^{-2} s^{-1}), $C = 2.64\times10^{-38}$ m^{4}.

5.4 Discussion

Looking at figure 5.1, a general positive correlation can be seen. The original $\Phi^{1/2}$ fit fits fairly well in the middle of the fluence range, but is lacking in the low fluence range, below ~4×10^{25} m^{-2}. The original data points from which the $\Phi^{1/2}$ fit was developed are the PISCES-B data points lying around $10^{26} - 10^{27}$ m^{-2} [20], hence the fit agreeing with the data so well in this region. In the low fluence region, the data points are seeming to drop off from the fit, being a bit lower than is predicted. Lastly, the highest fluence sample was created in the PISCES-B device, with a fluence of 1.1×10^{28} m^{-2}, being the longest fluence sample of fuzzy tungsten ever produced, taking 5 days operation to produce. This data point is sitting quite below the predicted $\Phi^{1/2}$ trend.

5.4.1 Corrections

Corrections can be applied to two of the current data points created in the present study. At low fluence, the data point produced in the magnetron device is revised lower in light of a measured mass gain caused by tungsten atom deposition [122] from the magnetron source. As was discussed in section 4.7, due to the nature of the device, there is an inherent

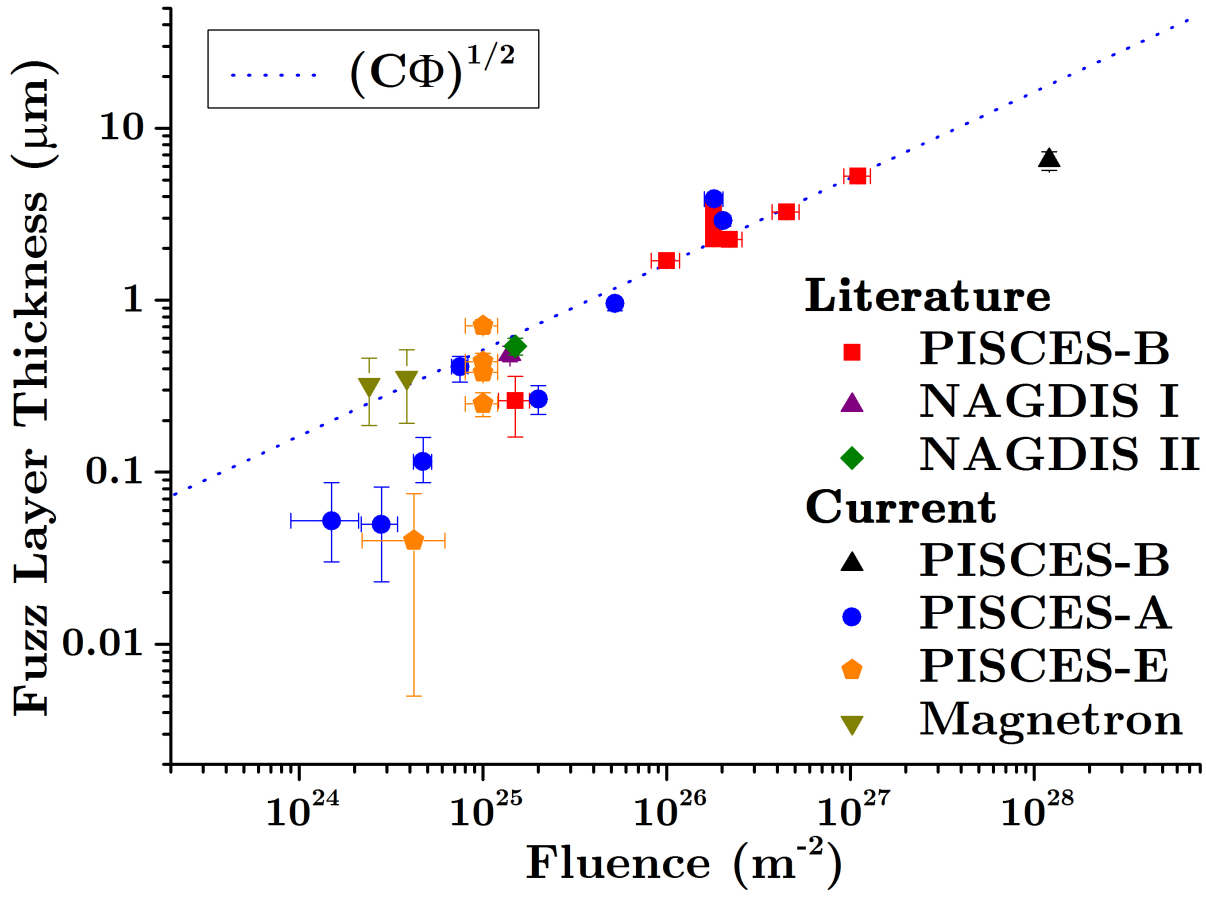

Figure 5.1. The compiled dataset showing both literature measurements and current measurements created on the devices as explained in this chapter for the current investigation. The original $t^{1/2}$ fit from [20] has been converted into a fluence fit and is shown overlaid as blue the dotted line.

deposition flux on to the sample throughout the exposure. While the measured fuzz layer thickness was 300 nm, there was a recorded 130 nm mass equivalent of tungsten fuzz deposited onto the growing fuzz layer. Since SEM observation of the fuzz morphology is similar to fuzz created by other means, it is assumed that the deposited tungsten incorporates into the growing fuzz layer in a manner similar to that described by tungsten atom movement along tendrils, as proposed in [52] (see section 2.1.5). The revision, which removes the influence of the deposition, places this data point closer to other nearby data at similar fluences that are produced in a plasma exposure without an incident tungsten atom flux (see figure 5.6). The significance of this correction is quite interesting. The uncorrected result is evidence that tungsten atom deposition leads to a potential enhancement of fuzz growth relative to non-deposition regimes, and as such, warrants further investigation. Implications, for an all tungsten metal reactor scenario are that tungsten may be deposited on various sites around the vessel, and thus fuzz could form at an enhanced rate, provided a sufficient surface temperature and He ion flux are also present.

The second revised data point is that taken at the highest He ion fluence (up to now) of

$\Phi = 1.1\times10^{28}$ m^{-2} in PISCES-B. The measured fuzz layer thickness on this sample of ~6.5 μm is depicted in figure 5.2, showing both the confocal microscope and SEM cross-section of this image. However this measurement is much lower than expected, noting that it sits quite below the line in figure 5.1. It has been shown previously that fuzzy samples grown in an erosive regime will be thinner than expected [11, 43]. This gives reason to suspect erosion in this case. The mass of the sample was weighed before and after exposure and a mass loss of 2.01±0.01 mg was recorded, giving evidence that material has been lost in some way. However, the energy of the bombarding He ions (~75 eV) is below the sputter threshold energy to cause erosion (~100 eV) [125].

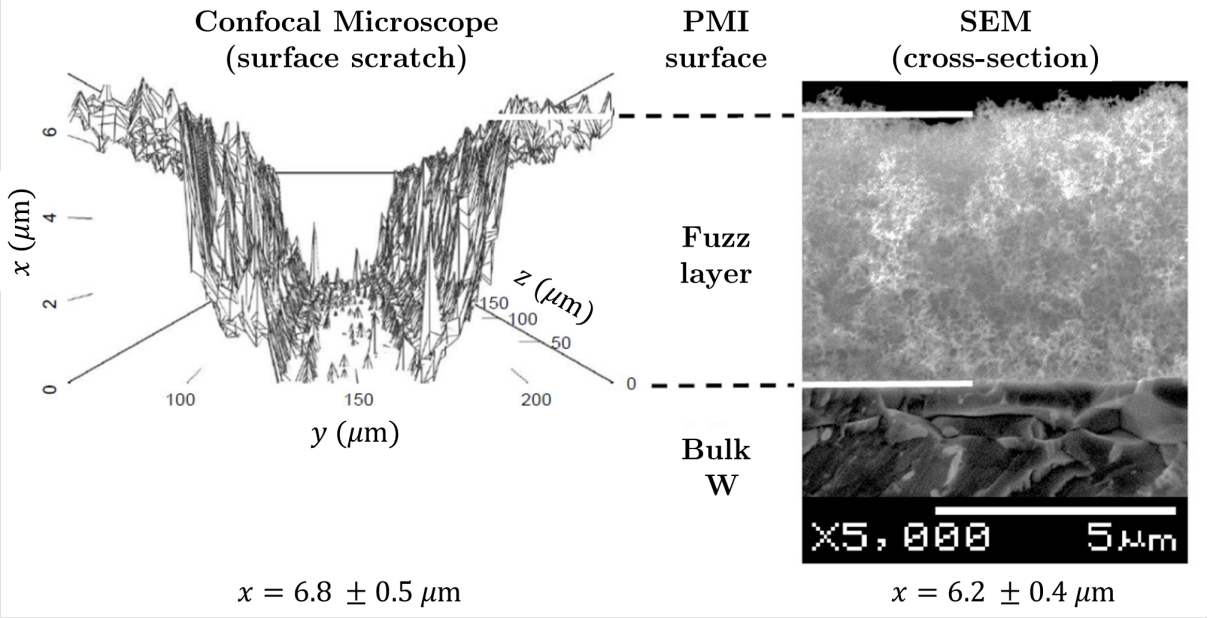

Figure 5.2. The thickness measurement of the longest fluence sample created to date, using PISCES-B with a fluence of 1.1×10^{28} m^{-2}. The thickness was measured using CFM and SEM giving an average of the two measurements as 6.5 ± 0.8 μm.

From this mass loss an equivalent layer of fuzz can be determined from a formula by Nishijima *et al.* [16],

$$p_f = 1 - \frac{\Delta m}{V \rho_b} \tag{5.3}$$

where p_f is the porosity of the fuzz, Δm is the mass loss, V is the volume of the eroded fuzz, and ρ_b is the density of the bulk tungsten. Letting $V = Ax_e$ in equation (5.3), where A is the area of the growing fuzz, and x_e is the eroded fuzz layer thickness. Re-arranging the equation for x_e gives us,

$$x_e = \frac{\Delta m}{\rho_b A(1 - p_f)} \tag{5.4}$$

For the values of the constants, $\rho_b = 19300$ kg m^{-3} [125] and $A = 3.8\times10^{-4}$ m^{-2} is the exposed area of the sample. The porosity can be measured by removing a defined portion of the fuzz on the sample by simply wiping it off. If the mass is measured before and after

	E_{th} (eV)	Y
N	45	5.00×10^{-3}
O	40	1.89×10^{-2}
W	11.75	2.10×10^{-3}
	Y_{tot}	2.60×10^{-2}

Table 5.4. Sputter threshold energy, E_{th}, values and sputter yields, Y, for trace impurities bombarding the long fluence PISCES-B sample, with E_i ~75 eV. Also shown is the total sputtering yield, Y_{tot} which is the total of the individual yields.

the wipe, equation (5.3) can be used, as knowing that $V = A_w x$, A_w in this case will be the area wiped off and x is 6.5±0.8 (as was measured). This leads to $p_f = 0.965\pm0.020$. Given all the values, $x_e = 7.79^{+10.4}_{-2.8}$ μm, adding this onto the measured value of ~6.5 μm gives a corrected value of $14.3^{+10.4}_{-2.8}$ μm. The large error on this corrected value comes from the error on the porosity.

The erosion could be accountable by trace impurities in the chamber throughout exposure. Possible trace impurities (<0.1 %) could be in the form of N_2, O_2, and W. The sputter threshold energy for ions impinging on tungsten can be calculated via:

$$E_{th} = \frac{(M_i + M_t)^2}{4M_i M_t} E_s \tag{5.5}$$

where E_{th} is the minimum energy for sputtering to occur, i.e. the threshold energy, M_i and M_t are the masses of the incident ion and the target ion, respectively, and E_s is the surface binding energy, which for W is 8.68 eV [126]. Values of E_{th} are shown in table 5.4, as well as the sputter yield values, Y, extrapolated from values in [127]. Summing these individual Y give the total sputtering yield of $Y_{tot} = 2.6\times10^{-2}$. The flux of sputtered atoms, Γ_{sp}, can be calculated as,

$$Y_{tot}\Gamma_{imp} = \Gamma_{sp} \tag{5.6}$$

The flux can also be changed into an erosion rate as $\Gamma = nv$, where n is the number density, and v is a velocity. For the case of a sputtered flux, this can be changed to be in terms of the density, and an erosion rate, E, as $\Gamma_{sp} = n_f E$, where n_f is the density of tungsten atoms in the fuzz, given by ρ_f/m_W, where, ρ_f is the density of the fuzz and m_W = the mass of a tungsten atom, therefore giving,

$$Y_{tot}\Gamma_{imp} = \frac{\rho_f E}{m_W} \tag{5.7}$$

Porosity can be defined as [128]:

$$p_f = 1 - \frac{\rho_f}{\rho_b} \tag{5.8}$$

This can be re-arranged in terms of ρ_f as,

$$\rho_f = (1 - p_f)\rho_b \tag{5.9}$$

Re-arranging equation (5.7) for E and substituting in equation (5.9) gives,

$$E = \frac{m_W Y_{tot} \Gamma_{imp}}{\rho_b (1 - p_f)} \tag{5.10}$$

For the values in equation (5.10), m_W = 183.84 u, Y_{tot} was calculated as in table 5.4 to be 2.6×10^{-2}. Assuming 0.01% of the total He ion flux, Γ_{He} (1.1×10^{23} m^{-2} s^{-1}) was from trace impurities, this gives the trace impurity flux Γ_{imp} = 1.1×10^{19} m^{-2} s^{-1}. The density ρ_b = 19300 kg m^{-3}, and p_f was measured to be 0.965. Substituting these values all into equation (5.10) gives E = 1.3×10^{-10} m s^{-1}. Applying this over the ~30 hours (1.1×10^{5} s) of exposure gives an eroded thickness of ~14 μm. Although this is just a back-of-the-envelope calculation, it shows that impurities could give rise to a similar order of erosion to that measured.

5.4.2 Incubation fluence

In figure 5.1 it is noted that the fuzz layer thickness increases rapidly to meet the fit at low fluence. In prior work it has been suggested that a certain amount of time is necessary before fuzz layer growth can commence [19]. In early works looking at the thickness of fuzz versus fluence, Kajita *et al.* noted a potential minimum fluence at ~4×10^{24} m^{-2}, as is shown in figure 5.3. In their work they used this to speculate that there is a necessary time before fuzz can form. This is due to the necessity of He ions being implanted into the surface causing nanobubbles to form, that in turn drive the onset and growth of the fuzz surface modification effect. This minimum fluence, or 'incubation fluence', is consistent with the current theories of fuzz formation (see section 2.1.5), which require He ions to gather into bubbles before fuzz can form [19,52]. On this basis the observed rapidly rising trend in fuzz layer growth is seemingly in agreement with the notion of an incubation fluence.

The incubation effect is also noted in other works examining He in tungsten phenomena. For example, in [124], reduced optical properties of a polished tungsten surface exposed at >1000 K to He plasma in NAGDIS-II was correlated with the formation of tungsten fuzz, as is shown in figure 5.4. As is discussed in section 4.4, the emissivity is a measure of the efficiency of thermal radiation, and depends on the surface finish. As fuzz grows, it would be expected that the emissivity should also change. In [124] they measured the surface temperature both by keeping a constant emissivity value (of 0.23 μm), and by simultaneously measuring the emissivity and measuring the temperature change with a varying emissivity value. Interestingly, no change was noted in the first few minutes

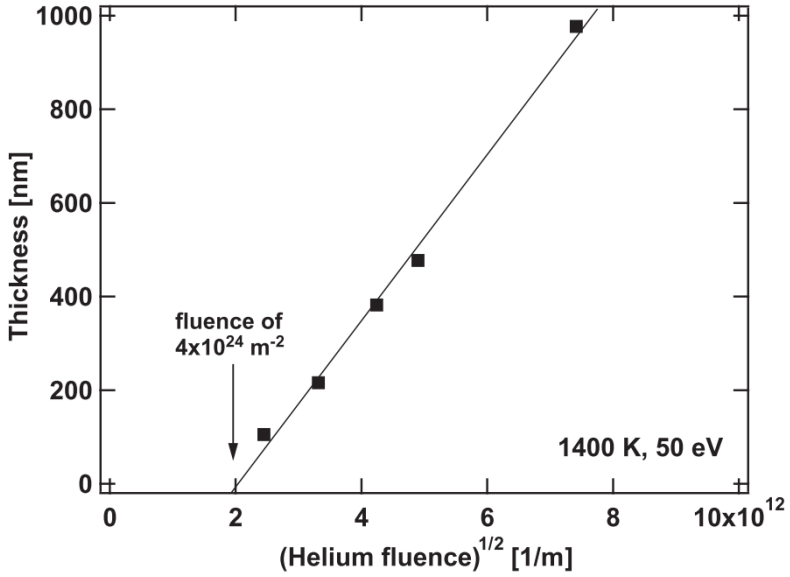

Figure 5.3. Thicknesses of samples exposed at 1400 K are plotted with the x-axis as $\Phi^{1/2}$ and the y-axis as thickness in nm. A minimum fluence of $4{\times}10^{24}$ m^{-2} was noted. Taken from [19].

of exposure, until ~ 4 minutes, when the measured emissivity drops. Equating this to a fluence gives ~ $2.4{\times}10^{24}$ m^{-2}. At lower He fluence, up to 10^{23} m^{-2}, El-Atwani *et al.* showed that no fuzz had yet formed, as is shown in figure 5.5 [140]. It is also worth mentioning that in [62], individual W samples were exposed to a He ion fluence of $1.5{\times}10^{24}$ m^{-2}, and $7.0{\times}10^{24}$ m^{-2}, following He exposure, samples were exposed to a fluence of D ions. After both exposures TDS was performed showing that $2.2{\times}10^{21}$ m^{-2} and $6.6{\times}10^{19}$ m^{-2} of D were retained, respectively. This shows that 2 orders of magnitude less D was retained at $7.0{\times}10^{24}$ m^{-2} as opposed to $1.5{\times}10^{24}$ m^{-2}. Fuzz layers have been shown to reduce D retention (see section 2.1.7), thus it seems there is a critical fluence causing this between 1.5 - $7.0{\times}10^{24}$ m^{-2}.

Including the effect of an incubation fluence, equation (5.2) can be rewritten as

$$x(\Phi) = (C(\Phi - \Phi_0))^{\alpha}\,, \tag{5.11}$$

defined for $x\,(\Phi) : \Phi > \Phi_0$, and where $\alpha = \frac{1}{2}$ and Φ_0 is the minimum (incubation) He fluence required for fuzz morphology to be observed. Equation (5.11) is depicted in figure 5.6 by the black dashed line for the case of $\Phi_0 = 2.5{\times}10^{24}$ m^{-2}. Also in figure 5.6 are the corrected data points as just discussed in section 5.4.1. This incubation fluence accommodates the trend in the lower fluence rather well.

The parameters in equation (5.11) are investigated by performing a constrained error analysis. Each parameter in turn is varied to the point where the quality of the fit becomes poor while the remaining parameters are held constant, allowing measures of uncertainties to be obtained. This is shown in figure 5.7. Figure 5.7a shows the effect of varying α.

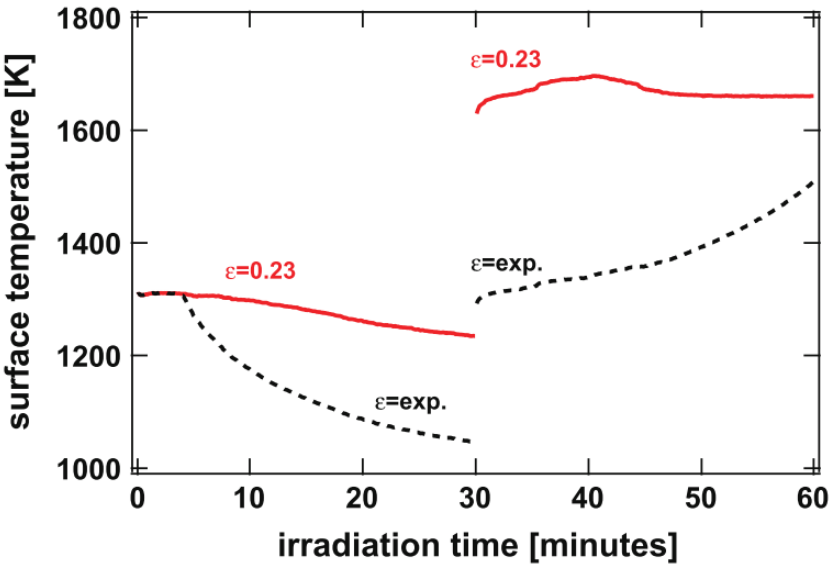

Figure 5.4. The time evolution of the surface temperature at a fixed emittance of 0.23 (in red), and a varying measured emittance (in black), measured at 1.6 μm. During the first 30 minutes fuzz was grown, in the second 30 minutes it was annealed off. Taken from [124].

While it remains unclear as to precisely why α should be equal to 0.5 from a physics point of view, it remains the case that the data are best described by this value, within a $\pm 10\%$ variation. Based on this, the correctness of this value is therefore assumed in the absence of any physical model proposing an alternative form. In the remainder of figure 5.7, the other parameters are optimised while keeping $\alpha = 0.5$ fixed, leading to the following fit values $C = 2.36^{+1.54}_{-0.56} \times 10^{-38}$ m^4 and $\Phi_0 = 2.5^{+1.5}_{-1.0} \times 10^{24}$ m^{-2}.

5.4.3 Erosion

Examining further the highest fluence data point, the lower than expected fuzz layer thickness is speculated to arise from low level impurity sputtering, which is consistent with the amount of measured mass loss. Yet while the precise nature of the loss remains unclear, the measured mass reduction gives an effective fuzz erosion yield by the He plasma in spite of the below sputter threshold plasma regime. This yield can be used to compare the measured thickness against previous growth erosion equilibrium studies. Fuzz growth-erosion equilibrium has been studied by Doerner *et al.* [11] and more recently by Noiri *et al.* [43]. Doerner *et al.* first looked at growing fuzz in erosive regimes, by biasing the W samples beyond the sputter threshold energy of He impinging on tungsten they were able to get a direct predictable sputter yield from Eckstein [127]. They proposed taking the original formula of equation $x = (2Dt)^{1/2}$ (equation (5.1)) in the differential form of,

$$\frac{\mathrm{d}x}{\mathrm{d}t} = \left(\frac{D}{2t}\right)^{\frac{1}{2}} \tag{5.12}$$

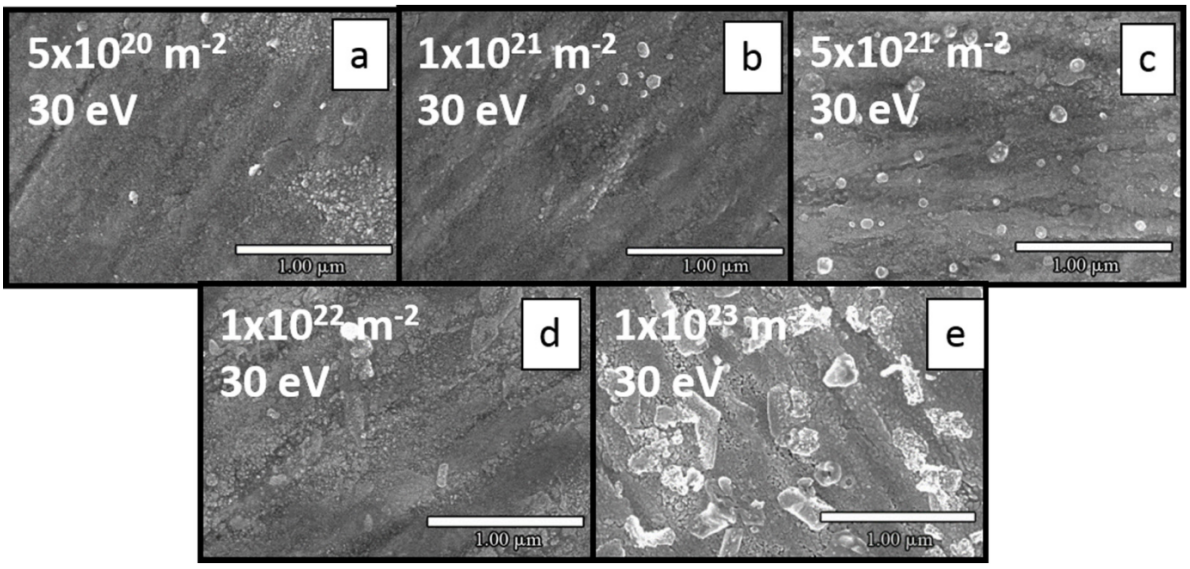

Figure 5.5. Low fluence He ion bombarding tungsten samples, showing that no fuzz is formed at fluences lower than ~10^{24} m^{-2}. Image taken from [140].

then introducing an erosion term by bringing in the net sputtering yield, Y_{net} as,

$$\frac{\mathrm{d}x}{\mathrm{d}t} = \left(\frac{D}{2t}\right)^{\frac{1}{2}} - Y_{\text{net}} \tag{5.13}$$

The idea behind the equation is that the growth rate of fuzz in an erosive regime depends on a growth term $(D/2t)^{1/2}$ and an erosion term Y_{net}. As time progresses the growth term continues to reduce, whilst the erosion term remains constant, and as such, a critical time will occur, t_c, at which point the growth term and the erosion term will balance out, and the fuzz will reach an equilibrium thickness, x_c. This is all fine in theory, and is what is seen in experiments, however, this equation does not produce that effect. As $t \to \infty$, the growth term $\to 0$ whilst the erosion term remains constant. This implies that for $t > t_c$, $\mathrm{d}x/\mathrm{d}t < 0$, and the fuzz will be eroded away, and as $t \to \infty$, $x \to -\infty$. This is not seen in practice, rather, fuzz does seem to reach an equilibrium thickness as the growth balances out with the erosion and stays at that point.

Noiri *et al.*'s attempt [43] took an alternative approach, noticing that there was an obvious issue with the previous erosion formula of equation (5.13). They proposed that the problem with the previous equation was that the growth rate solely relied on the time since growth began; whereas a more accurate approach is that the growth rate should depend on the amount of fuzz currently grown. Their approach led to the equation below,

$$\frac{\mathrm{d}x}{\mathrm{d}t} = \frac{D}{x} - E \tag{5.14}$$

where E represents the erosion rate in ms^{-1}. The underlying principal is the same, in the sense that after a critical time, t_c, the growth term D/x is equal to the erosion term E.

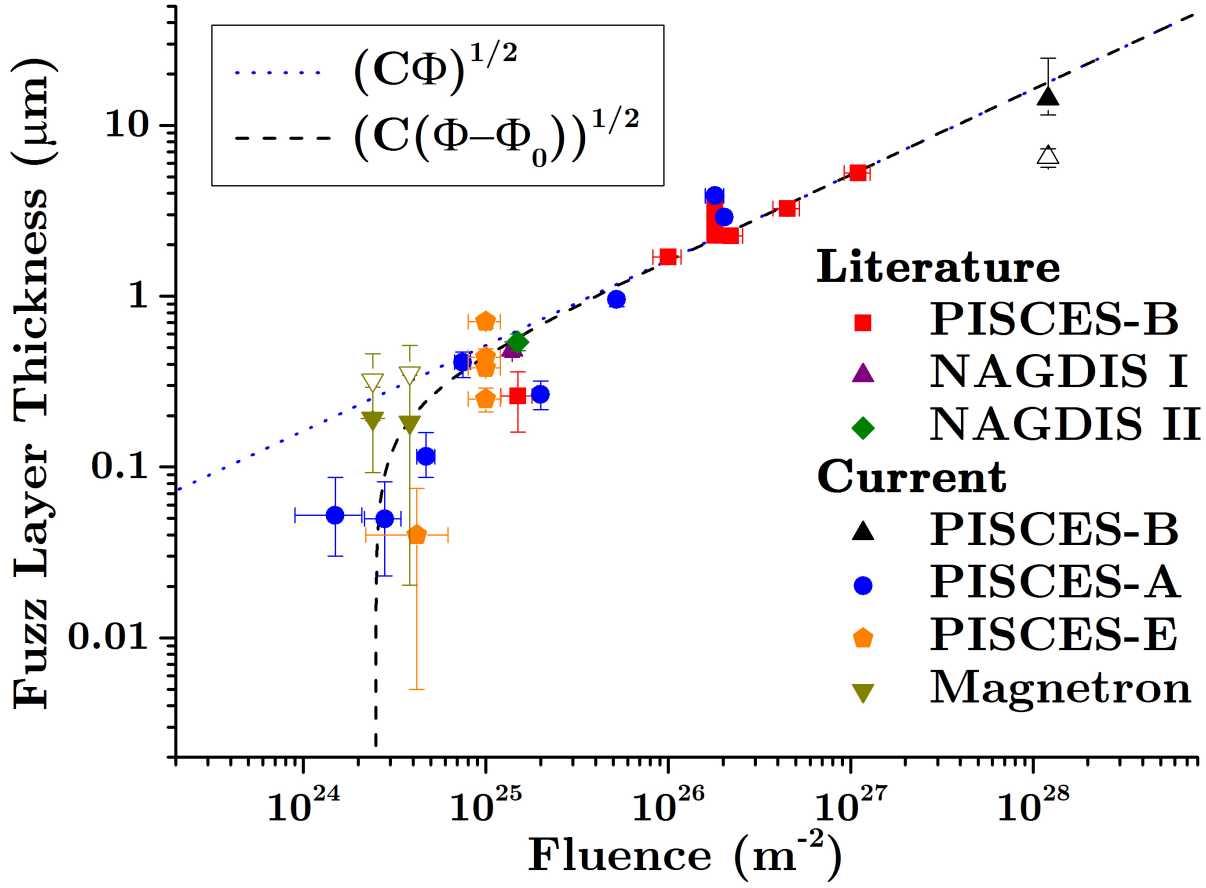

Figure 5.6. Compilation of literature and new results of fuzz thickness versus fluence. The blue dotted line is the original $\Phi^{1/2}$ fit from [20], the black dashed line is the new fit which includes the incubation fluence. Corrected data points have replaced the open symbols in the same colour and shape (at the same fluence), for the magnetron points and the long fluence PISCES-B point.

Only in Noiri *et al.*'s equation at t_c, $x = x_c$, and the growth term remains constant. Hence as $t \to \infty$, $x \to x_c$.

In Noiri *et al.*'s paper [43], they solved equation (5.14) for x numerically, with the results fitting fairly well with measured thicknesses of samples growing in erosive regimes. However, proposed here is an analytical solution for x. Before doing so, to be in line with the rest of this chapter, equation (5.14) can be changed to be in terms of Φ rather than t, as

$$\frac{\mathrm{d}x}{\mathrm{d}\Phi} = \frac{C}{2x} - \epsilon_f \tag{5.15}$$

where $C = 2D/\Gamma$ as before, and $\epsilon_f = E/\Gamma$ is the newly defined erosion parameter, which is derived in appendix A.1. Mathematically, there is a general solution to the differential problem of equation (5.15), which by direct integration using *Wolfram* [129], is given as,

$$x(\Phi) = \frac{C}{2\epsilon_f}\left(W\left[-\frac{1}{C}\exp\left(\frac{-2\epsilon_f^2}{C}(\Phi + A) - 1\right)\right] + 1\right) \tag{5.16}$$

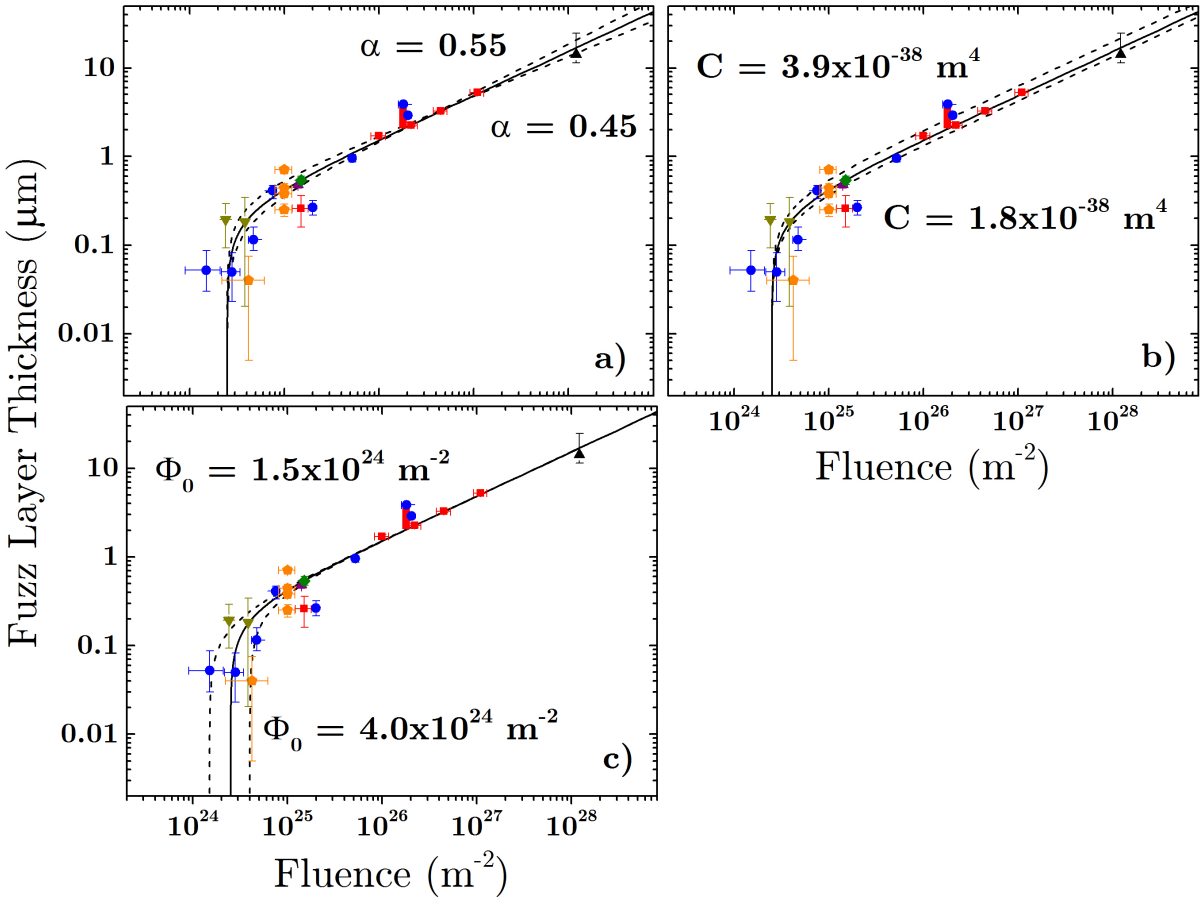

Figure 5.7. Optimising equation (5.11) by varying the parameters with a) varying α (and C) and keeping Φ_0 fixed, b) varying just C, and keeping α and Φ_0 fixed, and c) varying Φ_0 whilst keeping α and C fixed. The full line is the optimised case where α = 0.5, Φ_0 = 2.5×10^{24} m^{-2}, and C = 2.36×10^{-38} m^4. Dashed lines are the indicated parameter variations.

where A is the integration constant, and the function $W[z]$ acting on the real or complex argument is the Lambert W or product-log function, which is well described in [130]. In brief, $W[z]$ is defined to be the function satisfying,

$$z = W[z]e^{W[z]} \tag{5.17}$$

for any complex number z. The function is multi-valued unless the complex variable z is replaced by the real variable x, and defined only for $x \geq -1/e$. The intricacies of the Lambert function will be left to the reference of [130], however, the results of the solution will be pursued here. The integration constant A can be found by applying the boundary condition that the fuzz does not grow until the incubation fluence is exceeded, i.e. $\Phi > \Phi_0$, giving the boundary condition $x(\Phi_0) = 0$. The math for this can be found in appendix A.2, and gives the general solution of,

$$x(\Phi) = \frac{C}{2\epsilon_f}\left(W\left[-\exp\left(\frac{-2\epsilon_f^2}{C}(\Phi - \Phi_0) - 1\right)\right] + 1\right) \tag{5.18}$$

which gives the thickness of a fuzzy tungsten layer in an erosive regime, characterised by ϵ_f, as a function of the He ion fluence. There are several interesting features to be noted in the general solution. First, in the limit of $\Phi \to \infty$, the exponential term tends to 0, and another definition of the Lambert W function is $W[0] = 0$, hence $x(\Phi) \to C/2\epsilon_f$. That is, $x(\Phi)$ approaches a constant equilibrium thickness, defined by just the growth parameter C, and the erosion parameter ϵ_f, neither of which depend on the flux. This provides a simple solution for predicting the equilibrium thickness of fuzz in an erosive regime, a result that was not apparent in the two prior works on this topic [11, 43]. As with the original incubation fluence fit of equation (5.11), the new equation of (5.18) only gives real solutions for $\Phi > \Phi_0$.

Another interesting feature of the general solution is in the seemingly indeterminate nature of the solution when the erosion parameter is set to zero due to the $C/2\epsilon_f$ term at the beginning. One would have expected that if $\epsilon_f = 0$, the original equation of (5.11) should be attained. However, with some math tricks it can be shown that as $\epsilon_f \to 0$, the general solution of (5.18) converges to the non-erosive form of (5.11). The math for this is provided in appendix A.3. The new equation of (5.18) has been plotted in figure 5.8 alongside the non-erosive case of (5.11).

The erosion constant ϵ_f is derived in appendix A.1, given as,

$$\epsilon_f = \frac{Y}{(1 - p_f)} \frac{V_{mol}}{N_A} \tag{5.19}$$

The equilibrium thickness $x_{eq} = C/2\epsilon_f$ can therefore be written as,

$$x_{eq} = \frac{C}{2} \frac{(1 - p_f)}{Y} \frac{N_A}{V_{mol}} \tag{5.20}$$

An approximation for the equilibrium fluence, Φ_{eq}, the fluence necessary to approach the equilibrium thickness, can be found from equation (5.11) setting $x(\Phi_{eq}) = x_{eq}$,

$$\Phi_{eq} = \frac{x_{eq}^2}{C} + \Phi_0 \tag{5.21}$$

and using x_{eq} as just defined gives,

$$\Phi_{eq} = C \left(\frac{1}{2} \frac{(1 - p_f)}{Y} \frac{N_A}{V_{mol}} \right)^2 + \Phi_0 \tag{5.22}$$

Both x_{eq} and Φ_{eq} are shown geometrically in figure 5.8. Equations (5.20) and (5.22) are useful 'rule of thumb' expressions for determining the equilibrium fluence and thickness for fuzz layers in erosion regimes.

In the literature there are two papers that have reported growing fuzz in erosive regimes [11, 43]. The equations just derived are applied to the literature values and

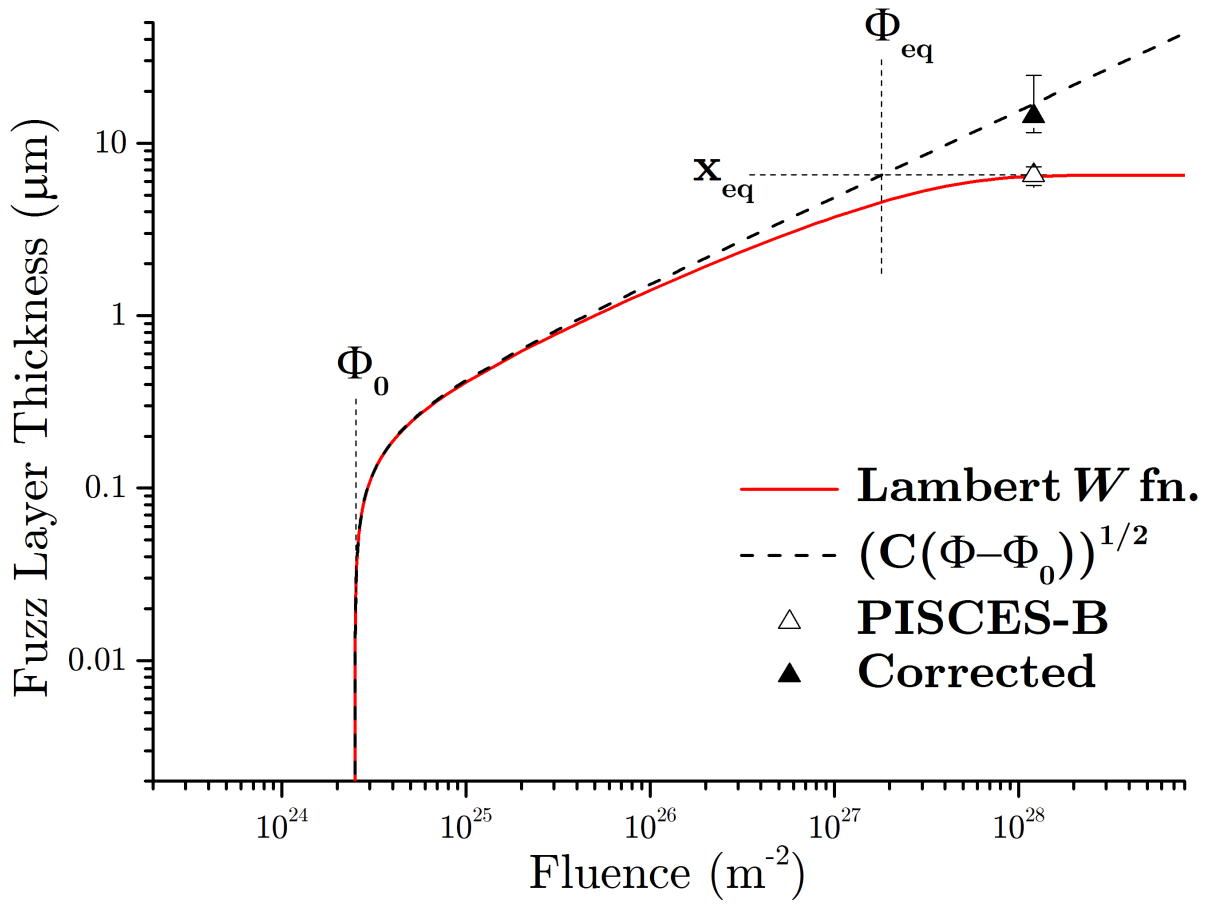

Figure 5.8. Fuzz layer thickness versus fluence in under erosive conditions. Showing a comparison of the new general solution of equation (5.18) involving erosion. The full red line is the new Lambert function of equation (5.18) and the dashed black line is the fit original equation without erosion (equation (5.11)). In calculations, $C = 2.36\times10^{-38}$ m^4 and $\epsilon_f = 1.51\times10^{-33}$ m^3, determined as explained in the text. In this figure x_{eq}, Φ_{eq}, and Φ_0 are indicated, as described in the text.

provided in table 5.5, which also shows the current PISCES-B sample. Predicted values are in reasonable agreement over a wide range of He ion fluence, ion impact energy, and exposure temperature. Although, by inspection of the measured values of x against the calculated values of $x(\Phi)$, it is clear that accuracy is favoured by avoiding the use of measured fuzz yields, and thus the need to account for porosity, which introduces a large uncertainty in calculated results for only slight variations. Better agreement seems apparent for the use of bulk yields, however, the yield values of [127] used in table 5.5 were systematically reduced by a further factor of 5 in calculations to achieve such agreement. This was done in accordance with the apparent discrepancy that exists between sputter yields obtained in high flux plasma experiments and calculations whenever low mass projectile species (D, He) are involved [131–133]. It is interesting to note that although in table 5.5, for the values from [43], where the predicted x values do not match up well with the measured values, the measured value in fact lines-up better with the predicted x_{eq}.

Ref.	Φ	T^*	E_{ion}	Y_{fuzz} (meas.)	$Y^\dagger_{bulk}$ [127]	p [16]	x (meas.)	$x(\Phi)$ Eqn.(5.18)	x_{eq} Eqn.(5.20)	Φ_{eq} Eqn.(5.22)
	(10^{26} m^{-2})	(K)	(eV)	(10^{-3})	(10^{-3})		(μm)	(μm)	(μm)	(10^{26} m^{-2})
	110	1140	75	0.0016	–	0.945 – 0.985	6.5±0.8	6.8 – 12.9	7.0 – 25.6	21 – 280
[11]	3.6	1120	200	–	2.3	–	2.0±0.5	1.5	1.6	1.1
[11]	3.6	1120	200	0.15	–	0.85 – 0.95	2.0±0.5	0.2 – 0.7	0.2 – 0.7	0.05 – 0.26
[11]	3.6	1120	250	–	5.4	–	0.9±0.3	0.7	0.7	0.2
[11]	3.6	1120	250	0.34	–	0.75 – 0.90	0.9±0.3	0.2 – 0.5	0.2 – 0.5	0.05 – 0.15
[43]	0.3	1300	250	–	5.4	–	2.0±0.5	1.0	1.9	0.6
[43]	0.03‡	1300	400	–	15	–	0.7±0.2	0.3	0.7	0.09
[43]	0.2	1300	400	–	15	–	0.7±0.2	0.6	0.7	0.1
[43]	0.02‡	1300	500	–	20	–	0.4±0.1	0.2	0.5	0.05
[43]	0.3	1300	500	–	20	–	0.3±0.1	0.5	0.5	0.06

Table 5.5. Comparison of current and literature fuzz layer thickness results grown in erosive regimes.

*C is taken to be 2.36×10^{-38} m^4 at 1120 K (present study). To accommodate exposure temperature other than the present study, the temperature dependence in [20] is used to adjust C.

†In equations (5.18) (5.20) and (5.22) when yield values of [127] are used, Y_{bulk} is reduced by a factor of 5 as described in the text. In these cases the porosity is set to 0.

‡For these low fluence cases Φ_0 was taken to be the minimum at 1.5×10^{24} m^{-2}. For all other cases Φ_0 was taken as 2.5×10^{24} m^{-2}.

To get Y_{fuzz} a simple sequence had to be followed. First a mass loss is measured, for the case of the current PISCES-B sample this was 2.01 mg. We can equate equation (5.10) for the erosion rate with $E = x_e/t$, giving,

$$E = \frac{x_e}{t} = \frac{m_W Y \Gamma}{\rho_b (1 - p_f)} \tag{5.23}$$

substituting in the equation for x_e from equation (5.4) gives,

$$\frac{\Delta m}{\rho_b A (1 - p_f) t} = \frac{m_W Y \Gamma}{\rho_b (1 - p_f)} \tag{5.24}$$

re-arranging for Y gives,

$$Y = \frac{\Delta m}{A \Gamma m_W t} \tag{5.25}$$

Giving a formula for Y without the need of p_f, purely from the mass loss, flux, and time of exposure (1.1×10^5 s), all easily measurable values with little error (unlike p_f).

Substituting in the values for the PISCES-B case gives a value of $Y_{fuzz} = 1.4\times10^{-6}$. Next, ϵ_f can be calculated from equation (5.19), however, it is noted that for the small range of values of the porosity (0.945 - 0.985), the Lambert function varies strongly in the high fluence region. The best fit result was achieved using a porosity of 0.985, as is displayed in figure 5.8. This results in a value of $\epsilon_f = 1.51\times10^{-33}$ m^3. A best fit for ϵ_f from the data gives $\epsilon_f = 1.78\times10^{-33}$ m^3, from this, keeping $Y_{fuzz} = 1.4\times10^{-6}$, to give the measured mass loss, would require $p_f = 0.9969$, quite larger than measured.

It is natural to try to use the new growth equation of (5.18) to predict the outcomes of the future tokamaks, ITER and DEMO. According to Roth *et al.* [9], the net ITER

tungsten fuzz erosion rate is predicted to be ~3×10^{-10} m s^{-1} which is closely similar to the highest fluence case in PISCES-B reported here (see section 5.4.1). The equilibrium thickness, x_{eq}, can be estimated by $x_{eq} = C/2\epsilon_f$, with $\epsilon_f = E/\Gamma$. Brooks *et al.* [51] predict the D-T flux in the divertor region to be ~4×10^{23} m^{-2} s^{-1}, of this flux 5% is He, hence Γ_{He} is ~2×10^{22} m^{-2} s^{-1}. Keeping to the fuzz created in a similar temperature window as the PISCES-B sample here, i.e. C = 2.36×10^{-38} m^4, which is a fair assumption given the hottest parts of the W divertor region are expected to be 1000 - 1400 K [46], this gives x_{eq} = 0.8 μm. This is much lower than in PISCES-B due to an order of magnitude lower He ion flux but a similar erosion rate, hence equilibrium will be reached at lower thickness. In terms of time necessary for such a thickness to be reached, using equation (5.21), Φ_{eq} = 2.9×10^{25} m^{-2}. Given Γ_{He} = 2×10^{22} m^{-2} s^{-1}, this would be achieved in 1400 s. As the shot duration of ITER is 400 s [7], this would be achieved within 4 shots (10 shots are planned a day [7]).

Extrapolating to DEMO is harder due to the nature of DEMO being quite open at this point in time. However, Bolt *et al.* propose Γ_{He} of ~ 2×10^{23} m^{-2} s^{-1} [134]. If the region of interest is kept to the region of the divertor with surface temperatures around ~1100 K, this will lead to a similar C value as before. In the absence of predicted erosion rates for a divertor region in DEMO, it could be assumed that the erosion parameter ϵ_f, being independent of flux, is the same for DEMO as it was for ITER. This, of course, implies that x_{eq} is again 0.8 μm, due to the increased flux, this would imply both increased growth rate, and increased erosion, balancing out to give the same x_{eq}. However, as Φ_{eq} will also not be affected, x_{eq} will be attained quicker, due to the increased flux. Given Φ_{eq} = 2.9×10^{25} m^{-2}, this would be expected to be reached within a mere 145 s. However in DEMO there is the added effect of potential W from the main wall armour being deposited onto the divertor. As the magnetron result hints, this deposited tungsten can be caught up in the growth of the fuzz and add to the overall thickness of the fuzz. This implies that the fuzz could continue to grow a little further, as the original growth rate formula is potentially instead given by,

$$\frac{dx}{dt} = \frac{D}{x} + S_W - E \tag{5.26}$$

where S_W is the rate of deposited tungsten (caused by sputtering of the tungsten target, not the sample). This implies that equilibrium is not reached until

$$\frac{D}{x_{eq}} + S_W = E \tag{5.27}$$

Implying that x_{eq} is now given by,

$$x_{eq} = \frac{E - S_W}{D} \tag{5.28}$$

or in terms of C and ϵ_f,

$$x_{eq} = \frac{2}{C}\left(\epsilon_f - \frac{S_W}{\Gamma}\right) \tag{5.29}$$

The flux cannot be removed from this equation entirely as S_W is not necessarily dependant on flux, as it has it's own separate source. Of course, in the magnetron case, the generation of the He flux also generates the deposited flux, so they are relatable. These new equations could not be used to predict an equilibrium thickness in the magnetron rig if the erosion was assumed to be due to impurities as in the PISCES-B case. This is because $S_W > E$, i.e. the rate of tungsten atoms being deposited to the growing sample is greater the erosion rate. Which does imply that, in theory, if $S_W > E$, then one could grow fuzz indefinitely, or at least discover new limiting factors.

5.5 Conclusions

The thickness of tungsten fuzz layers has been measured for four orders of magnitude of He ion fluence and flux under below threshold sputtering conditions in the temperature range of $1000-1140$ K and compared to a compilation of previously published data. Considering the growth of the layer as a function of the He ion fluence (rather than time) reveals a more general form of the growth dependence than was originally given in [20]. This new equation also reconciles different rates of growth observed at different fluxes. The current analysis shows that the dependence in [20] is a special case of the more general growth expression of equation (5.11), which also accommodates the observation of a rapid onset of early stage growth by the inclusion of an incubation fluence. Arguments are made that the incubation fluence is almost certain to be associated with the set up formation of He bubbles within the near surface. The general growth expression is easily incorporated into the growth-erosion equilibrium problem of [11, 43] to give an analytical solution based on the Lambert W function, and for which simple 'rule of thumb' limit expressions can be derived to determine the equilibrium thickness and approximate equilibrium fluence from a specified erosion yield.

Chapter 6

Magnetron Grown Fuzzy Tungsten

This chapter presents the results of experiments growing fuzz in the magnetron sputtering device at the University of Liverpool, as described in section 3.1.1.

6.1 Introduction

As fuzz could potentially occur in ITER, it is an area of active research. However, it has been showing some promise outside of the realm of fusion power. Recently it has been used in the splitting of water molecules [70], and many authors expect that it's high surface area could be harnessed as a catalyst [32, 71]. Also, due to it's very low reflectivity, it could prove useful in the solar cell industry [69]. There has previously been some research studying the formation conditions of fuzz, with samples being created over a wide range of parameter space. However, as was shown in the last chapter, there exists an area with little work on fuzz generation, being the low fluence work, $<10^{25}$ m^{-2}. This region is important to investigate as it contains the proposed incubation fluence, as introduced in section 5.4.2.

The fuzz created here is on the low scale of fluence, at $\sim10^{24}$ m^{-2}. Typically, fuzz made in the literature uses linear plasma devices (LPDs) with an exposure fluence of 10^{25}-10^{27} m^{-2}. In LPDs (those introduced in section 2.1.11), the fluxes are typically on the order of 10^{22}-10^{24} $m^{-2}\,s^{-1}$, two orders greater than in a magnetron. As such, to attain the fluences as presented here of $\sim10^{24}$ m^{-2}, LPDs would require only 1-100 seconds. In such devices, this is on the scale of the error in time, whereas in a low flux device like a magnetron, this can take several hours. As most experiments are orders higher fluence, this error is not an issue, however at the low fluence end of the scale, when it could take ~40 s to change temperature by 100 K (see section 5.2), depending on the flux, this fluence error could be as large as 10^{25} m^{-2}. As such, large scale LPDs are not appropriate for studying fluences of the order of 10^{24} m^{-2} and below. These should be studied on alternative devices.

Also, LPDs provide a high flux of ions to the sample, and as a by-product of this high flux, the sample is heated to the temperatures necessary for fuzz to form, with active

cooling installed to keep the temperature at the specified point. Therefore the temperature is coupled to the plasma parameters, making it difficult to change the temperature without changing the He ion energy or the He ion flux to the sample. Magnetrons do not generate enough heating by the plasma alone to get the sample to the temperatures required for fuzz generation. Therefore a separate heating method is installed, thereby decoupling the sample temperature from the plasma conditions. This allows greater precision over the temperature. Additionally, magnetrons permit having the sample held at a target temperature before the plasma exposure begins, thus being more certain on the exposure start time.

Magnetrons also present a significant difference to other low flux devices in that deposition is occurring onto the growing fuzz sample throughout the exposure. This presents a unique situation of growing fuzz whilst having W deposited on top of it, potentially emulating the situation in DEMO, the future fusion power plant.

If magnetrons can be used to create fuzz, compared to LPDs, these are very cheap, simple devices, already common in many laboratories worldwide, therefore opening up fuzz research to a much wider community. Also, magnetrons exist in industry already, so if a potential industrial aspect could be shown, this could be more easily scaled up.

The work here studies the formation conditions of fuzz generation in a magnetron device. There are three main parameters which control fuzz formation, being the He ion fluence to the sample throughout the exposure, the He ion energy, and the sample surface temperature. These have been investigated in the literature in section 2.1.3, however, they have not been studied vigorously. Each parameter is swept in the magnetron revealing new insights into the formation conditions. These conditions are compared to previous work in the literature and discrepancies are discussed. In this chapter, the experimental method used to generate the samples as well as the results is explained, then the results from each technique is presented, followed by an in-depth discussion of the results, finishing with a conclusion.

6.2 Experimental method

The device used for plasma exposure was a magnetron sputtering device, as described in section 3.1.1. The samples were held by a substrate holder facing the target and positioned along its axis at a distance of 93 mm. To heat the sample a custom-built heater was used which involved a tungsten filament just behind the sample. A current was passed through the filament causing electrons to be emitted, then the filament was raised to ~-100 V in order to accelerate the electrons to the back of the W sample, thereby heating it. A thorough description of the heater unit is described in section 3.1.3. The heating filament was powered by a PTS-1200 electron beam heater (Henniker Scientific), as described in section 3.1.2. The sample temperature was monitored throughout exposure by an IR

pyrometer, as described in section 3.1.4.2. The heater unit and the IR pyrometer were connected in a feedback loop to keep the temperature constant throughout exposure. The samples were biased by a power supply connected to the sample by a cable insulated with Kapton tape.

The vacuum chamber was pumped down with a rotary and turbo pump working in series to a base pressure of the order of 10^{-4} Pa. The chamber was then filled with He gas of 99.9995% purity to a pressure of 5.3 Pa. The magnetron target was operated at 700 W for each exposure.

In order to measure the plasma diagnostics, a special sample was made of steel which was insulated from the sample holder clips, but had an insulated cable attached to it to enable it to be connected to a Langmuir probe acquisition box. This probe is described in detail in section 3.2.2. Operating at 700 W with 5.3 Pa He gas pressure, the plasma potential was measured at -3.2±1 eV, and the He ion flux which varied depending on the bias of the sample [119, 120], was of the order of $1{\times}10^{20}$ m^{-2} s^{-1}.

The samples used in this study were 99.95% tungsten discs (Future Alloys) of 10 mm diameter and 1 mm thickness. They were prepared by first polishing by hand to as good as a finish as possible using wet and dry sandpaper sequentially through grades P400, 360, 240, and 150. After this, samples were electro-polished for ~15 minutes to a mirror finish. This technique is described in detail in section 3.3.2. The emissivity of the samples was separately determined to be 0.26±0.02 as is described in section 4.4.

The operating procedure was to first get the sample to the desired temperature with He gas present (but with the plasma off at this stage). This typically took ~15 minutes, depending on the temperature. Once the temperature was attained the plasma was powered on at 300 W and ramped up 200 W every minute to 700 W. After one minute at 700 W, the sample bias power supply was switched on, at which point the time of exposure was deemed to begin.

Throughout exposure, due to the nature of the magnetron device, sputtered W atoms from the target were deposited on the growing samples. Using a quartz crystal microbalance, this deposition rate was separately measured to be 5.3±2.3 pm s^{-1}, as is described in section 4.7.

After exposure, samples were analysed using a variety of techniques. They were each imaged with an SEM (JEOL 7001) in order to provide images of the surface structure. The reflectivity of each sample was measured using a USB2000+ spectrometer connected by fibre optic cable to a DH-2000-BAL deuterium and halogen light source (Ocean Optics), as described in section 3.5. The surface roughness of each sample was measured using a VK-X210 confocal microscope (CFM) (Keyence), as is described in section 3.7. Lastly, the thickness of the fuzz layer of the samples were measured by using a focused ion beam (FIB) of gallium ions to mill out a trench, the fuzz cross-section could then be observed by tilting the sample in an SEM, as is described in section 3.6.6. For each image of

the cross-section it could be clearly seen where the fuzz deformation started and ended, and this thickness was measured at approximately 100 different points along the image, providing the mean value and error bars from 2× the standard deviation.

6.3 Results

There are 3 main parameters concerning the formation of fuzz, these being fluence, temperature, and He ion energy. Samples of fuzz were grown under a sweep of each of these parameters. First a sweep of time was performed, with exposure durations of 1h-9h in steps of 1h, whilst keeping the He ion energy fixed at 40 eV and the surface temperature at 1100 K. Next the sample bias was swept, hence sweeping the bombarding He ion energies, this was done from 25-70 eV in steps of 5 eV, each sample was exposed for 9h and at 1100 K. Lastly, the sample temperature was swept from 900-1200 K in 50 K steps, exposed for 9h with He ions of 60 eV.

6.3.1 SEM images

The SEM images of the time sweep are shown in figure 6.1. An unexposed sample following the same cleaning procedure as the exposed samples is shown in figure 6.1a for comparison. Each of these experiments were performed with a constant He ion flux of 9.4×10^{19} m^{-2} s^{-1}, at 40 eV, and the surface temperature was kept constant at 1100 K. It can be seen that even after 1h exposure there is already significant difference from a clean sample. Orientation preference due to grain direction is clearly observed in the early stages up to 3h (1×10^{24} m^{-2}), and there seems to be a preferred orientation still at 6h (2×10^{24} m^{-2}) (observable at lower magnification than in fig. 6.1g). However, from 7h (2.4×10^{24} m^{-2}) upwards this seems to no longer exist, and the orientation is random. Only at >8h (2.7×10^{24} m^{-2}) could the structure be comparable to low fluence fuzz created on other devices, with longer tendrils beginning to show. Consistent in each image beyond 3h (1×10^{24} m^{-2}) is the existence of 'globules', or 'bubbles'. These appear to remain at the same size until about 7h (2.4×10^{24} m^{-2}) when they appear to become elongated.

The SEM images of the energy sweep are provided next, shown in figure 6.2. An important point must be made for the energy sweep; as the bias is increased negatively, the ion current does not saturate (as can be seen in figure 3.7). The ion current continues to increase as the bias increases. This is due to the expanding sheath [111]. Therefore each energy step is actually a step in fluence too (see figure 4.8). The exact fluences for each sample are marked on each image in figure 6.2. For a true representation of the impact of sweeping the energy, the time of exposure for each sample should have been adjusted to keep the fluence constant. However, some comparisons can be made between figure 6.1 and 6.2. By comparing samples with similar fluence, an impact of the energy

can be implied. A comparison can be made between fig. 6.2a and fig. 6.1d, having 0.9 and 1.0×10^{24} m^{-2} and 25 and 40 eV, respectively. One could argue that at 25 eV, even at slightly lower fluence the protrusions look more pronounced than at 40 eV. For samples ≥50 eV there seems to be little difference in the morphology, all exhibiting quite random structure as seen in fuzz created in other devices.

The SEM images for the temperature sweep are shown in figure 6.3. Since this sweep was performed after the energy sweep, it was deemed that the fuzz most resembling fuzz found in the literature was at 60 eV, and hence the temperature sweep was performed at 60 eV. The temperature is the parameter that seems to have the biggest impact on the structure formed. One can see that there is quite a big jump between 1050 and 1100 K, where at 1050 K there are still only the globules seen at lower fluences, however at 1100 K there are larger protrusions and early forms of tendrils. From 1100 K to 1200 K it appears as if the tendrils get thinner.

Fuzz formation has rarely been observed at an angle, with authors preferring to look either face-down or at the cross-section, however, by tilting the samples in the SEM device, a more 3D picture can be achieved. This was done for the temperature sweep and is presented in figure 6.4. These are the exact same samples as imaged in figure 6.3, and provide an interesting alternate view on the structure. One can see that as the temperature increases these protrusions grow upwards from the surface, it appears as if these are pictures in time, however, the fluence was kept exactly the same for each exposure. Clearly the temperature has a significant impact on the fuzz formation. In fig. 6.4h it appears as if some melting has occurred, as bands of structure appear rather than just tendrils. Note that any apparent height observed in these images must be multiplied by $\sin(70^\circ)$ in order to correct for tilt.

6.3.2 Thickness

The thicknesses of the fuzz layers were measured using the FIB milling technique. The SEM images from these are quite interesting and have been provided in appendix B. However, the measurements of the thickness are provided here in figure 6.5. It can be seen that there is a general increase with fluence, with samples sitting generally above the line, apart from the one outlier at 4h, they all seem to nicely follow a trend.

6.3.3 Roughness

The roughness of every sample shown in the SEM images is presented in figure 6.6. The vertical scale is kept the same in each image to allow for easy comparison amongst parameters. Roughness can be simply associated with fuzz formation, the thicker the fuzz, generally the rougher the surface, due to the nature of the fuzz structure. Looking solely at the roughness, it can be seen that for the time of exposure there is no apparent change

until 8h, when the roughness rises significantly. Comparing this to the corresponding SEM images of figure 6.1 it can be seen to correlate with the apparent change from just globules to streaks/tendrils as seen from ≥7h, however, at 8h the features seem more protruded, whereas 7h still appears fairly flat.

For the energy sweep, bearing in mind again that there is an inherent fluence sweep as a by-product of changing the energy, there is an apparent general increase up to 60 eV, then a decrease. Again, this could just be associated with the increased fluence, and could in fact not imply an energy dependence.

Looking at the temperature sweep one can see the most drastic change in roughness with a large jump from 1050 to 1100 K, and the roughness continuing to increase substantially as the temperature is increased. The difference of 50 K affects the roughness much more than any of the other parameter sweeps. This observation is also seen in the SEM images of figure 6.3 and 6.4.

6.3.4 Reflectivity

The reflectivity of each sample was also measured, and the results are shown in figure 6.7. The reflectivity of each sample increases with wavelength. The wavelength chosen for the following figures was 632.8 nm, fitting with work on reflectivity values by other authors, as will be discussed later. It can be seen that these in some way depict the same information as the roughness curves in figure 6.6. In figure 6.7a, a clean sample is shown at 0h exposure, with a reflectivity at 632.8 nm of 81%. In the time sweep the reflectivity gradually descends over time and appears to be plateauing at around 9h. In the energy sweep, the reflectivity is generally low throughout, again with the lowest reflectivity reported at 3% for 60 eV, and slightly increasing in reflectivity at higher energies. For the temperature sweep, as was seen for the roughness curves, this shows the most drastic drop from 1050 to 1100 K, as well as the lowest value of 0.8% for the 1200 K case.

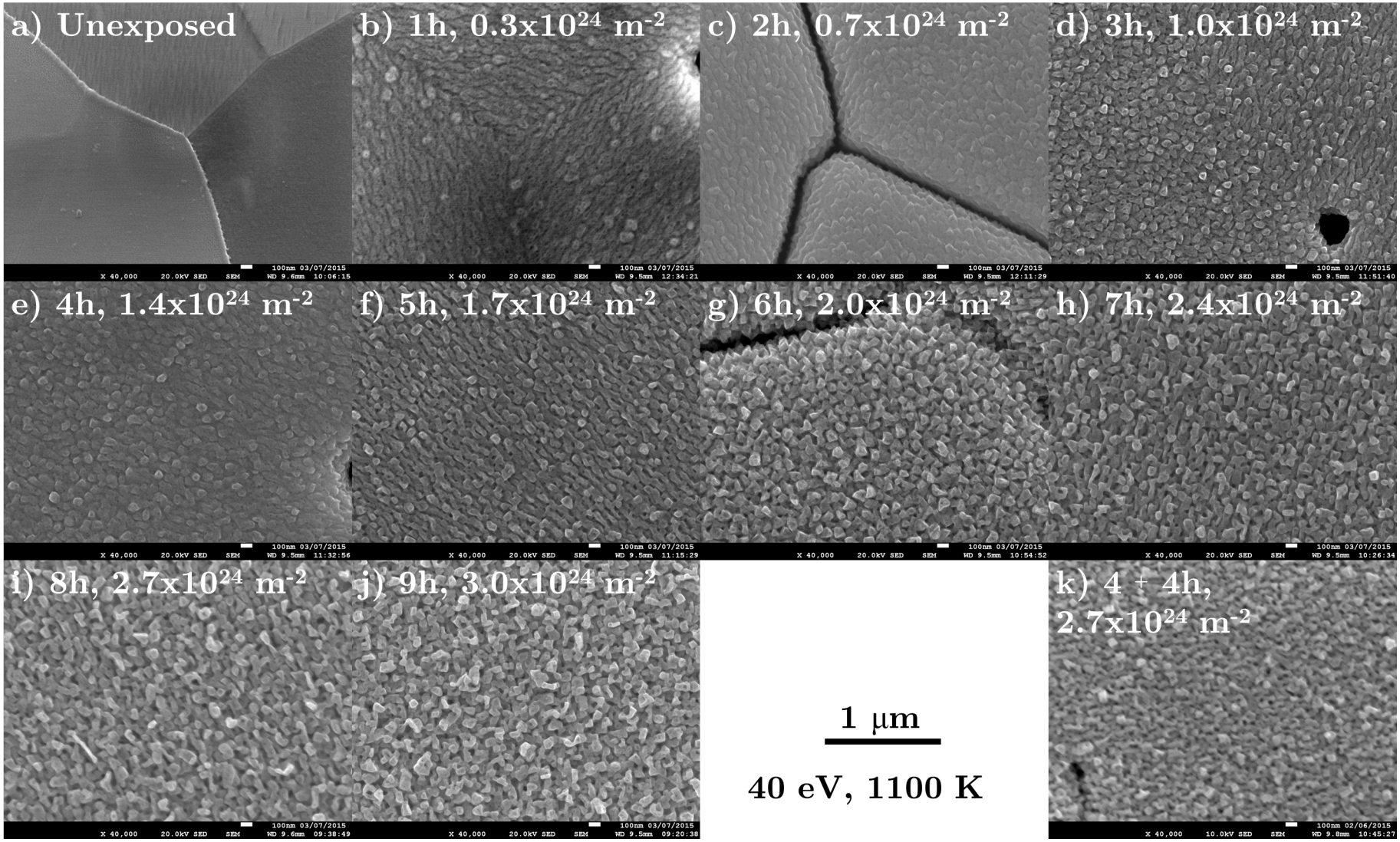

Figure 6.1. SEM images of the time (and hence fluence) sweep. The other conditions, of 40 eV He ion energy, and 1100 K surface temperature, were kept constant throughout exposure. An unexposed sample is shown in a) for comparison. The image shown in k) is discussed in section 6.4. Each image is taken at 40,000× magnification, and the scale bar is shown in gap between imgaes j) and k).

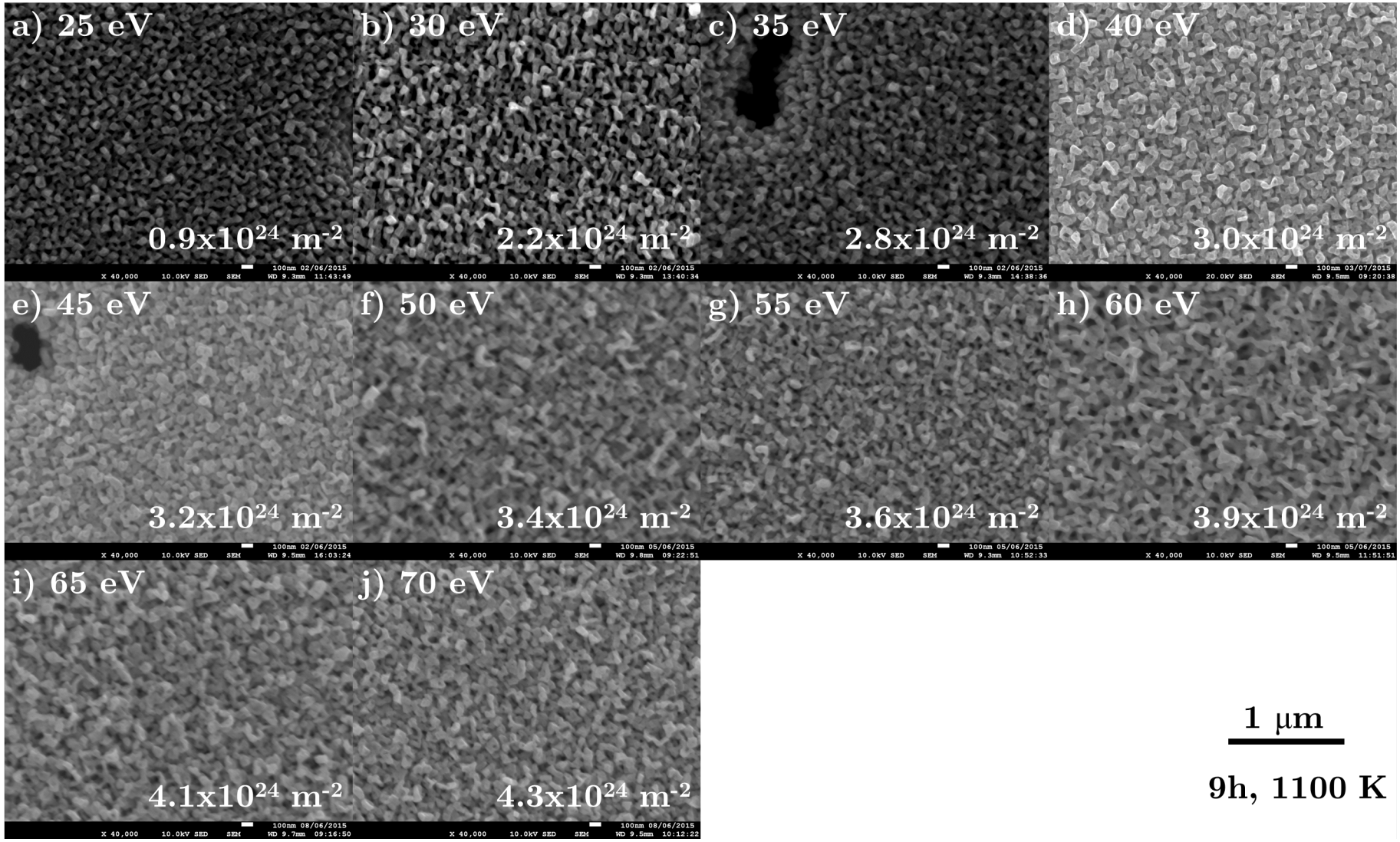

Figure 6.2. SEM images of the energy (and hence fluence as a by-product) sweep. The other conditions, of 9h exposure, and 1100 K surface temperature, were kept constant throughout exposure. Each image is taken at 40,000× magnification, and the scale bar is shown in the bottom right. The actual fluence for each sample is shown in the bottom right of each image.

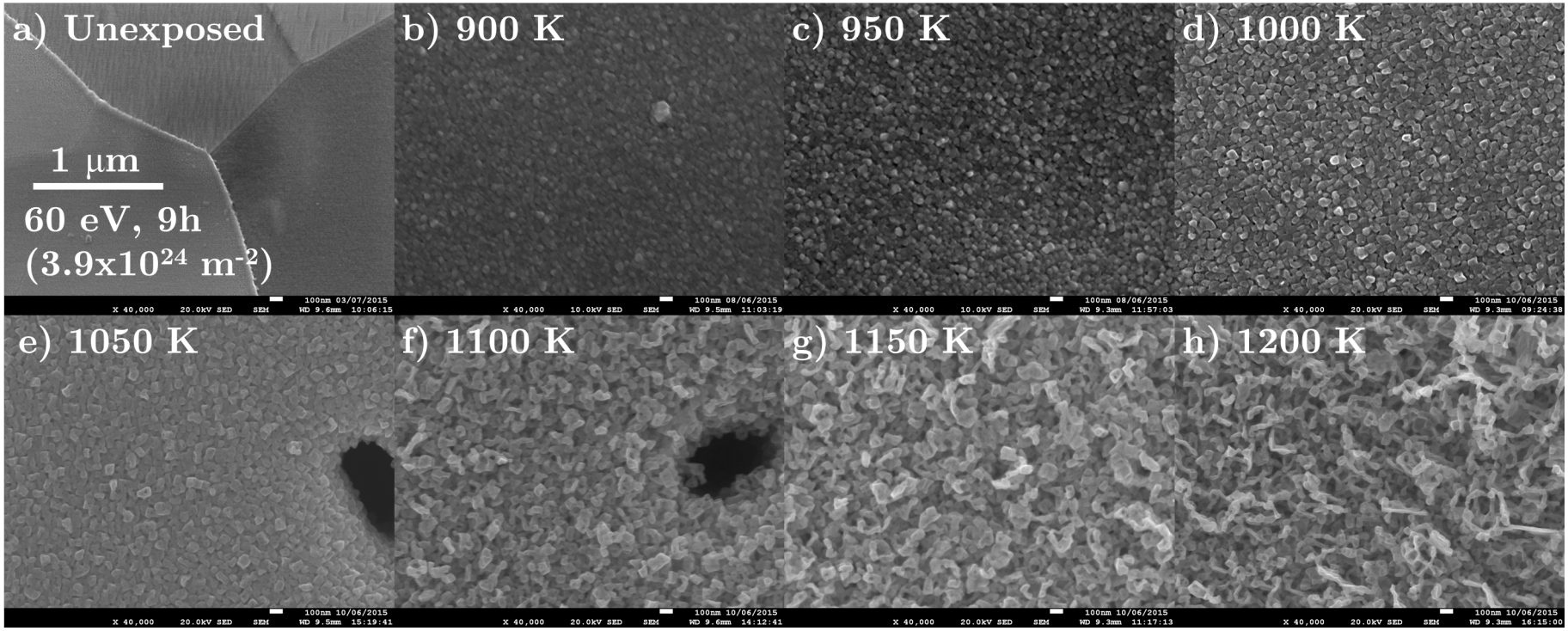

Figure 6.3. SEM images of the temperature sweep. The other conditions, of 60 eV He ion energy, and 9h ($3.9{\times}10^{34}$ m^{-2}) exposure, were kept constant for each sample. An unexposed sample is shown in a) for comparison. Each image is taken at 40,000× magnification, and the scale bar is shown in image a).

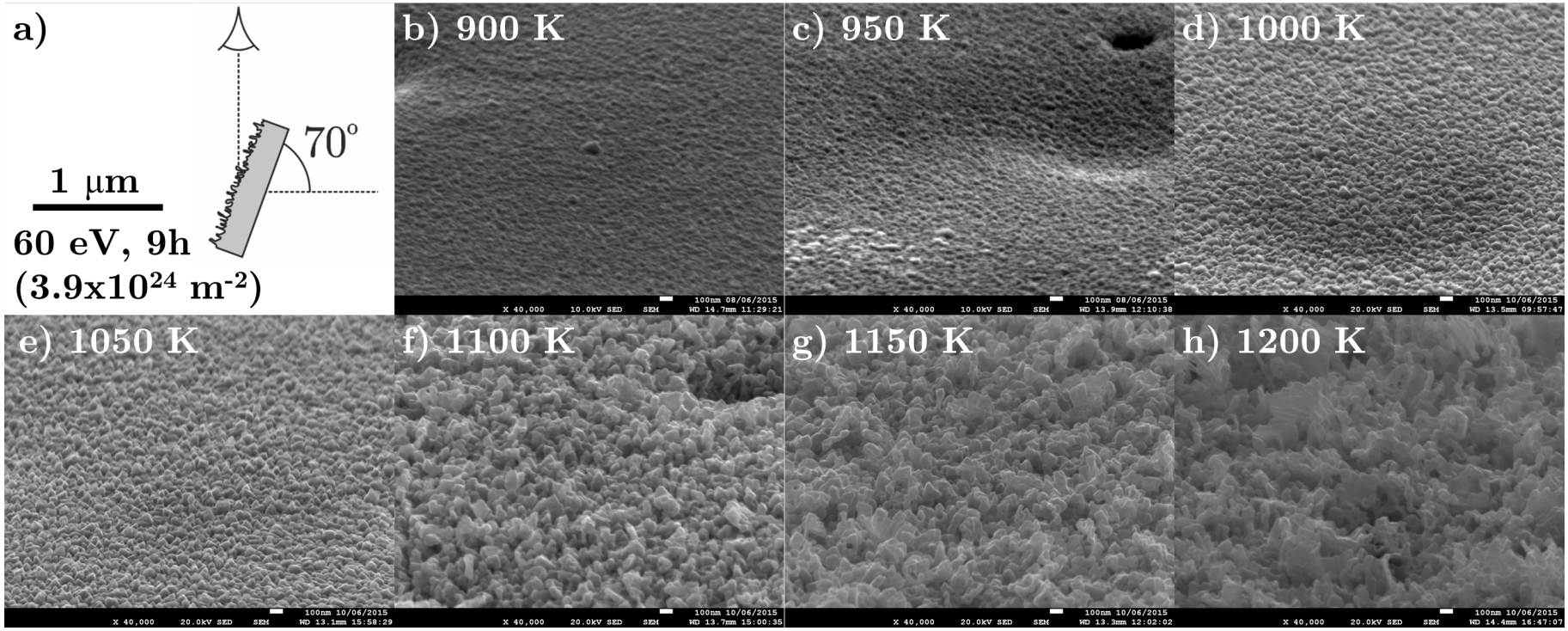

Figure 6.4. SEM images of the temperature sweep taken with the samples tilted 70° to the norm, as shown in the top left. These images are the same samples imaged in figure 6.3. The other conditions, of 60 eV He ion energy, and 9h ($3.9{\times}10^{34}$ m^{-2}) exposure, were kept constant for each sample. A diagram of the imaging position in the SEM is shown in a). Each image is taken at 40,000× magnification, and the scale bar is shown in image a). Note that any apparent height observed in these images must be multiplied by sin(70°) in order to correct for tilt.

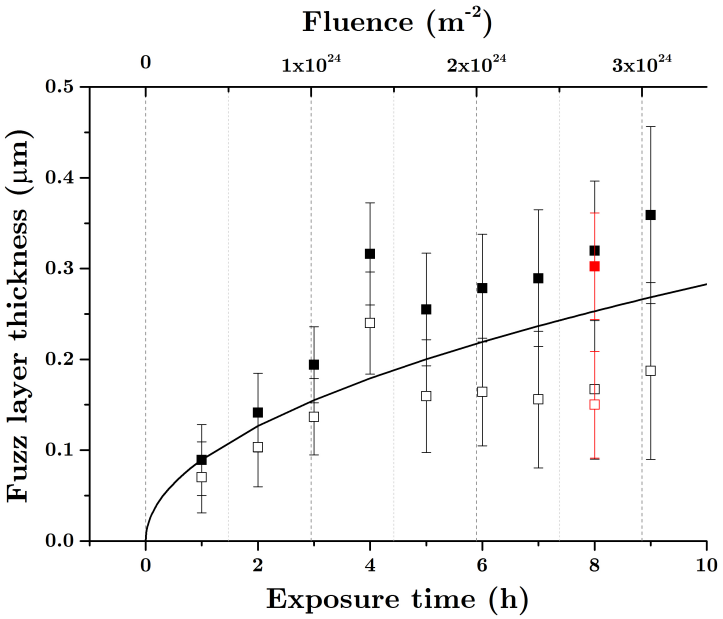

Figure 6.5. Measurements of the fuzz layer thickness using the FIB milling technique for the fluence sweep. The time in hours is shown on the bottom axis, and the equivalent fluence is shown on the top axis. The filled-in squares represent the measurements from the SEM images of figure B.1, the open symbols have the deposition subtracted from the measurement. The red symbols represents the 4+4h exposure (see section 6.4.7). The line shown is the fit of $x = (C\Phi)^{1/2}$.

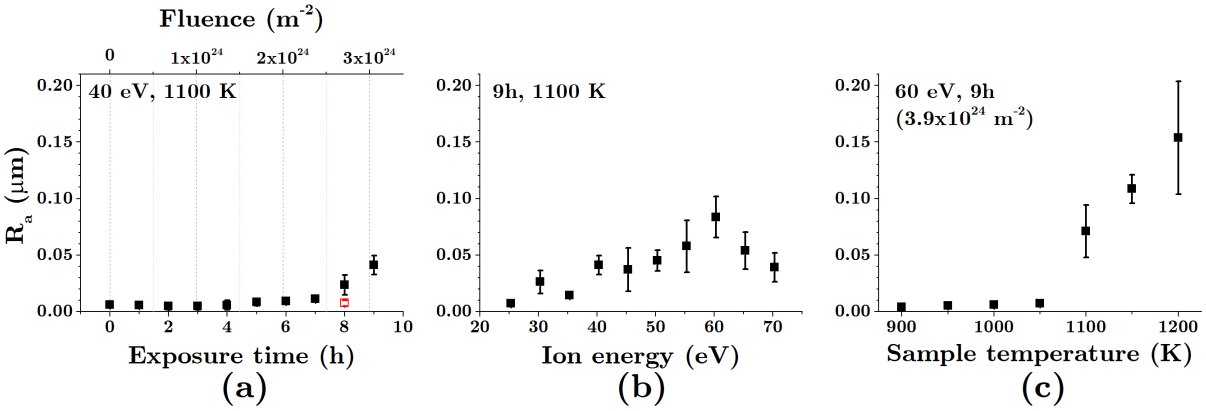

Figure 6.6. The roughness values shown for each parameter sweep. The vertical scale is the same in each figure. In a) is the time sweep, showing the fluence on the top axis. In b) is the energy sweep, and in c) the temperature sweep. For each sweep, the conditions kept constant are displayed in the top left. The red open square in a) represents the 4+4h exposure (see section 6.4.7).

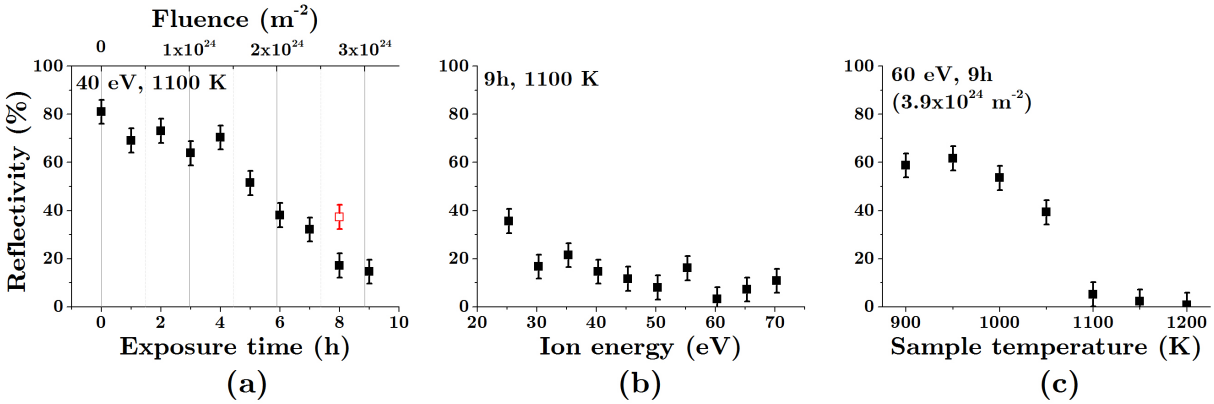

Figure 6.7. The reflectivity values shown for each parameter sweep. The vertical scale is the same in each figure. In a) is the time sweep, showing the fluence on the top axis. In b) is the energy sweep, and in c) the temperature sweep. For each sweep, the conditions kept constant are displayed in the top left. The open symbols in a) represent the 4+4h exposure (see section 6.4.7).

6.4 Discussion

The morphology of the fuzz created here, particularly the higher fluence samples, resemble the structure seen on fuzz created by other devices [12, 33, 38, 135]. Tendrils, 50-100 nm wide, are seen protruding from the surface and with random orientation. Since they are made under similar conditions it is fair to compare the results here with those from other devices.

6.4.1 Boundary conditions for fuzz formation

The boundary conditions for fuzz to form has been studied before in the literature. In section 2.1.3 the conditions are discussed. In terms of fluence, a minimum fluence has been hinted at in experiments, with Kajita *et al.* proposed a minimum fluence of $4{\times}10^{24}$ m^{-2} [19]. Regarding the samples presented in the fluence sweep of figure 6.1, the issue of defining when fuzz exists and when it does not is now apparent. There is no strict definition of fuzz, yet authors tend to agree that it is tendril/coral/branch-like formation with random orientation. Even in computer simulations and theoretical models of the growth mechanisms they do not define a 'pre-fuzz' and then at a later time 'fully formed fuzz'. In such models [19, 52, 84], the early stages of fuzz are represented by blobs and protrusions, as seen in the early fluence samples of figure 6.1. Therefore, one could define the structure as seen in fig. 6.1d at $1{\times}10^{24}$ m^{-2} as fuzz, despite the fact that it is not very fuzzy, in the usual sense of the word.

An attempt is made to define a 'pre-fuzz', as opposed to regular/fully-formed fuzz, commonly seen at fluences $>10^{25}$ m^{-2}. As fuzz is defined with random orientation, it would be fair to define pre-fuzz as having non-random orientation, i.e. showing dependence on the underlying grain direction, as can be seen in fig. 6.1b-g (in fig. 6.1g it is barely visible in the top right of the image, however a lower magnification image of this sample is provided in figure 6.8 in which non-random orientation can be seen). Such grain preference at low fluences has been seen before by several authors [136–138]. As the fluence increases, the underlying orientation bias begins to disappear as it becomes more random, by $3{\times}10^{24}$ m^{-2} (fig. 6.1j) the orientation has no observable bias. This is presumably due to the tendrils growing upwards from the surface and beginning to bend in random directions, as is more observable with fig. 6.3f for example.

The second definition of fuzz is the tendril-like structure, therefore a fitting definition for pre-fuzz would be not exhibiting tendril-like structure. The difference between the globules and the tendrils can be seen by comparing figures 6.3e and 6.3f. In e, the globules appear to be of a regular dimension, with mostly hard edges, as seen especially in fig. 6.8, as opposed to being circular in shape. They also tend to have 3-5 sides to the shape, as seen from top-down. However, as is the case in fig. 6.3f, there is no more uniformity of the shapes and it certainly appears to be more coral/tendril-like.

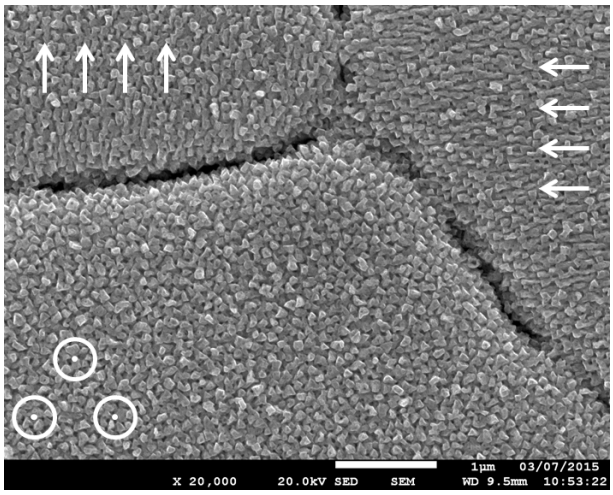

Figure 6.8. Structure orientation can be seen in the 6h (2×10^{24} m^{-2}) exposure. This sample is the same image as fig. 6.1g taken at 20,000× magnification rather than 40,000×. The structure can be seen to have different, yet subtle, orientation at different grain locations, as divided clearly by a grain boundary.

Using these two definitions of pre-fuzz, one can make claims about boundary conditions from when pre-fuzz becomes fuzz. Looking first to fluence, as shown in fig. 6.1, a preferred orientation is barely observable at 2.4×10^{24} m^{-2} (from South-southwest to North-northeast, however this is no longer seen at 2.7×10^{24} m^{-2}. This hints at a cross-over point at $2.4\pm0.4\times10^{24}$ m^{-2}. The minimum fluence prediction by Kajita *et al.* of 4×10^{24} m^{-2} is an extrapolation from thicker fuzz samples [19], and is not far off the value presented here. The incubation fluence, as predicted in the previous chapter (chapter 5), was given at $2.5\pm1.5\times10^{24}$ m^{-2}, which fits nicely with the defined cross-over point from pre-fuzz to fuzz.

Looking to the energy sweep, one could certainly argue that globules exist at 25 eV, whereas at 30 eV tendrils exist. However, due to the previously pointed out fluence dependence by-product, this should not be taken as a fuzz formation condition. Previous work in the literature has noted a range of minimum energies for fuzz to form. As detailed in section 2.1.3, the lowest energy leading to fuzz formation was at 12 eV [12], however, Baldwin *et al.* found no change at 20 or 27 eV [38]. Kajita *et al.* also stated they found a minimum energy of 20 eV [33]. The present theory is that fluence needs to be taken into account when comparing different energies. The SEM images of the energy sweep do not present any apparent cross-over point, this is most likely at ≤20 eV, as other authors have reported.

Regarding the temperature, it is clear already from the SEM images, that pre-fuzz becomes fuzz between 1050 and 1100 K. The error on the temperature readings in the present experiments were due to the difference in emissivity between samples, and was deemed to be a maximum of 30 K (see section 4.4). Therefore, the widest gap possible is 1020-1130 K giving the boundary condition for temperature at 1080±60 K (rounded to

the nearest 10 K). The minimum temperature was first shown by Sakaguchi *et al.* in [34]. They created samples at 900, 1130, 1400, 1750, and 2040 K. At 900 K there is no fuzz, however there is surface structure in the form of what appears to be ripples. Their 900 K samples was created under a fluence of 4.5×10^{24} m^{-2}, very close to the 900 K sample shown in fig. 6.3 b, with 3.9×10^{24} m^{-2}. However the structures do not look similar, with no ripples apparent in the magnetron sample. This could perhaps be due to the different sample preparation methods, or due to the existence of deposition in the magnetron, as will be discussed in section 6.4.3. At 1130 K there is definite fuzz growth, implying the cross-over point is somewhere in between, and therefore their measured minimum temperature for fuzz formation is 1020±120 K, overlapping the results presented here. When authors state the minimum temperature for fuzz to form, they mostly cite the seminal work of Kajita *et al.* in [33]. Kajita *et al.* compiled many experiments with He ions bombarding heated W samples and noted whether fuzz formed or not (see fig. 2.7). Purely from this compilation, a broad region can be seen where fuzz formation takes over, from the chart it can be said that there is fuzz at ~1100 K, but not at ~900 K. This gives a broad cross-over region of 1000±100 K, again fitting with the results shown here. A recent study by Miyamato *et al.* involving fluences of 10^{23}-10^{26} m^{-2}, at 50 eV, showing no fuzz formation even at 973 K [35]. They did not go to higher temperatures, but this does place a lower limit on the temperature range. The different ranges have been presented diagrammatically in figure 6.9. However, it must be noted that only the present experiments have error bars on the temperature readings, and as such, the ranges represented by the other authors should be even wider. The range presented here is the smallest range yet.

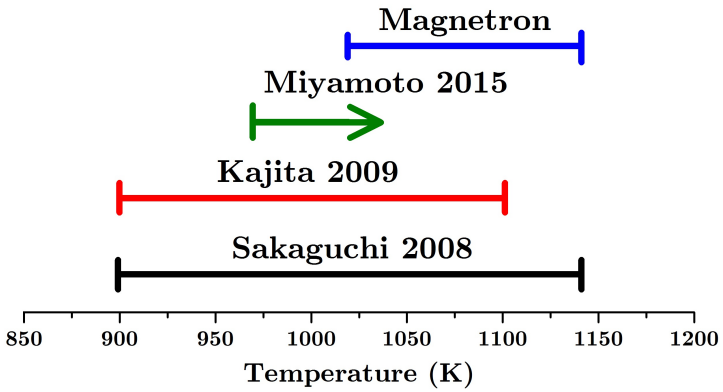

Figure 6.9. The various minimum temperatures for fuzz to form that have been thus far predicted by Sakaguchi *et al.* in [34], by Kajita *et al.* in [33], by Miyamoto *et al.* in [35], and by the present results as shown in figure 6.3.

6.4.2 Competition of growth and annealing out of fuzz

It has been shown, by several authors, that higher surface temperatures begin to anneal out the surface [18, 102, 103] (see section 2.1.13). Kajita *et al.* in [102] showed that an-

nealing of the fuzz can be significant even at 1400 K, with almost all the fuzz removed after 10 mins of pure annealing. Clearly, then, whilst growing fuzz at elevated temperatures, there is a competition between growth of fuzz and annealing out of fuzz. Recent work by Meyer showed that after annealing for 30 mins at 1300 K the fuzz was almost entirely re-integrated back into the bulk [103]. This hints that even at 1300 K fuzz can be re-integrated, just at a slower rate. Perhaps this is also true at even lower temperatures, simply requiring more time to re-integrate the fuzz. Therefore there must be a temperature dependence of the annealing out factor, which must be compared against the growth rate of the fuzz (the He ion flux) in order to see if fuzz will form or annealing will dominate. Several authors have cited a critical flux of ~10^{21} $m^{-2}\,s^{-1}$ for fuzz formation [102, 104], however, one could argue that at lower fluxes, the annealing dominates, and hence less fuzz is seen. As the present work indicates, fuzz can be made at lower fluxes, even an order of magnitude less, but they must be operated at lower temperatures, to reduce the effect of annealing.

Clearly in the high flux LPDs, the flux is so high that the growth factor is dominant over annealing, such that one can only see the re-integration of fuzz when the plasma is switched off. Whereas at lower fluxes, such as the present situation, the flux is so low that annealing out could become a significant effect during growth. Looking to the highest temperature sample here, shown in figure 6.3h and particularly 6.4h, one can see that there is some apparent melting of the fuzz, as the tendrils are forming strange structures, and seemingly joining together, implying that the temperature is beginning to be detrimental to the fuzz growth. In the temperature study by Sakaguchi *et al.* in [34], they also show that with increasing temperature (up to 2040 K) the features get thicker. De Temmerman *et al.* also show this quite clearly, evidently some form of melting occurs between these tendrils even though the melting point of W is ~3700 K [136]. An image from De Temmerman *et al.*'s paper demonstrating this is shown in figure 6.10.

These hint that at even higher temperatures the fuzz would begin to be less apparent, due to the annealing dominating over the low growth rate. This does therefore potentially imply that for low flux studies, there is a much smaller temperature window for fuzz to occur in, and perhaps the upper boundary on temperature is not 2000 K as reported [11, 33], but is dependant on the flux (the growth rate). One might expect to see fuzz at higher temperatures than 2000 K given higher available fluxes in the future, possibly with the upcoming results from the newly refurbished Magnum-PSI at DIFFER capable of producing fluxes of the order of 10^{24} $m^{-2}\,s^{-1}$. Unfortunately due to the construction of the sample holder used in the magnetron device, higher temperatures could not be attained in this study, however, this could be looked into for future studies.

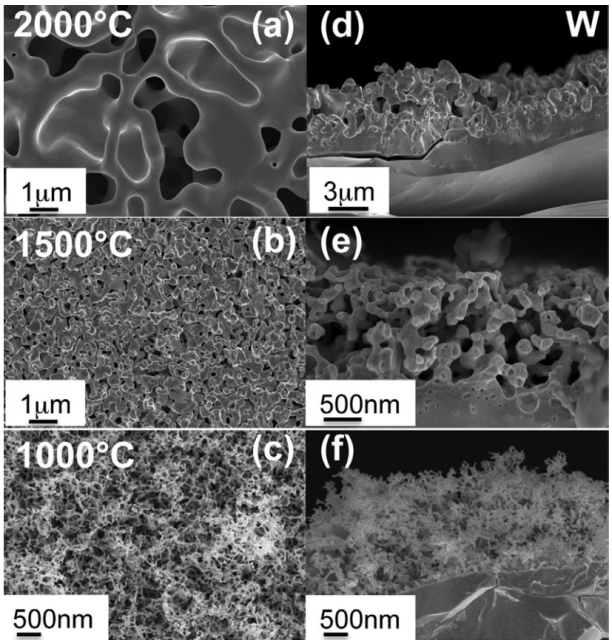

Figure 6.10. The competition between growth and annealing out of fuzz is shown with this wide temperature sweep by De Temmerman *et al.*. The temperatures are displayed in the top-left of each row. For each temperature, the top view is shown on the left and the cross-section on the right. Image taken from [136].

6.4.3 Deposition in a magnetron device

Creating fuzz in a magnetron sputtering device posed several challenges. Deposition being one of the main constituents of this. Due to the inherent nature of the device, sputtering of the target will occur, leading to the target atoms being deposited onto the growing fuzzy sample. Hence, the target was chosen to be W. Thus, the deposition would be W onto W, and not present any new species to develop on the growing sample. Additionally, W has a particularly low sputter yield, reducing the amount of deposition compared to using a conventional target. There is a concern that some of the pre-fuzz presented here is actually just caused by the deposition of tungsten, and the images seen are just that. SEM images of W deposited by a magnetron device onto a silicon substrate is presented in [139]. They present SEM images of a 206 nm thick W film deposited onto silicon wafers in a He atmosphere, shown here in figure 6.11. It can be seen that the structure presented there does not feature any of the globules or protrusions presented here, and clearly the He has a significant effect at elevated temperatures, and all of the images here are not just brought about by the depositing W.

The deposition rate in the present work was measured using a quartz crystal microbalance to be 5.3±2.2 $\mathrm{pm\,s^{-1}}$, as discussed in section 4.7. Over a 9h exposure, this would lead to ~170 nm of deposited W. This is a significant layer of deposition considering that the thicknesses being dealt with in the magnetron are ~300 nm. Despite this level of deposition, the fuzz morphology appears the same as fuzz made in devices where there is no deposition. This implies that the deposited W atoms do not simply produce a film

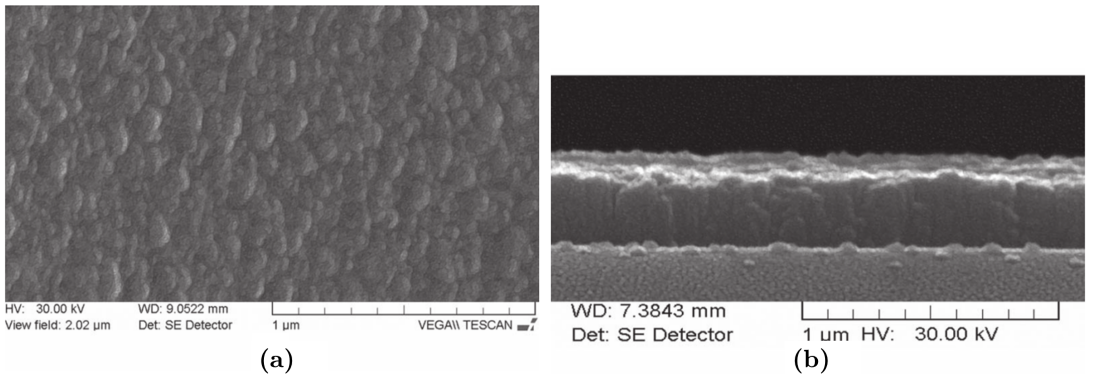

(a) (b)

Figure 6.11. SEM images of W deposited onto a Si wafer in a He atmosphere. In (a) the top surface can be seen, and in (b) the cross-section. Image reproduced from [139].

over the growing structures. This is in part due to the nature of this deposition occurring simultaneously with the growth such that it is fully integrated with the fuzz growth. Perhaps the depositing atoms become integrated with the surface W atoms. One of the theories for the mechanism of fuzz growth presented by Krasheninnikov proposes that the growth of fuzz could be due to the viscoelastic flow of W particles around the He bubbles [52]. Perhaps the deposited W atoms can be caught up in this flow and not prevent fuzz growth but actually enhance it.

6.4.4 Comparison to other devices

PISCES-A

In the previous chapter, whilst at UC San Diego, three samples were created on the PISCES-A device at fluences so low that they could be achievable in the magnetron at Liverpool. The experimental conditions for these were a He ion energy of 75 eV, and a surface temperature of 1140±20 K, the flux and fluence varied slightly between samples as is displayed in table 6.1. The experimental procedure is explained in the previous chapter in section 5.2. An important thing to note is the error on the time of exposure of 40 s. At such short exposures, this leads to a significant error on the fluence. SEM images were taken of the samples, using the same methods as used for the magnetron samples. These images are shown in figure 6.12.

Φ (10^{24} m^{-2})	Time (s)	Γ (10^{22} m^{-2} s^{-1})	T (K)	E_i (eV)
1.5±0.6	107	1.4±0.04	1140±20	75
2.8±0.6	200	1.4±0.04	1140±20	75
4.7±0.5	286	1.7±0.4	1140±20	75

Table 6.1. Plasma conditions for the PISCES-A samples at low fluence.

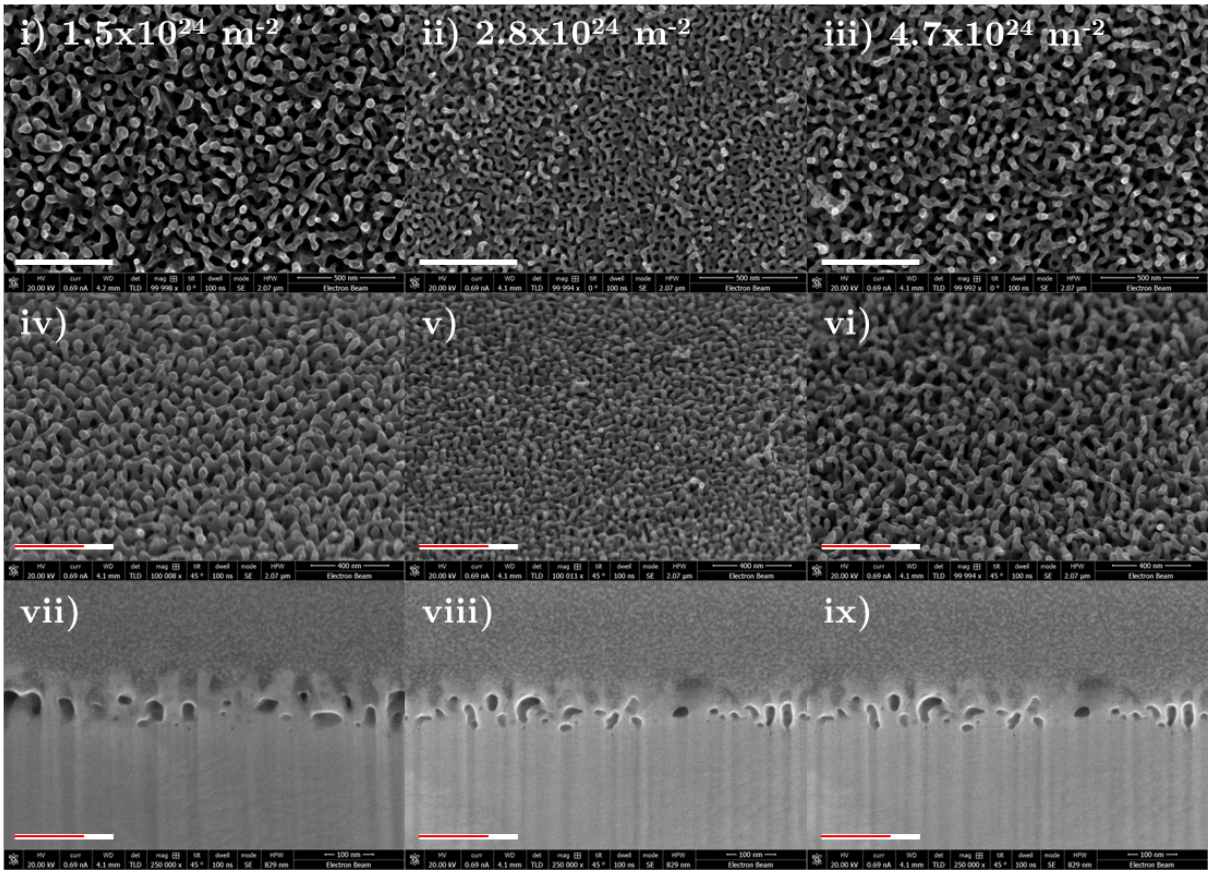

Figure 6.12. SEM images of low fluence samples created in PISCES-A for comparison to the samples made in a magnetron. Each column is a different sample, with the fluence noted in the top row. The top row is surface images, the middle row is surface images taken at a tilt of 45°, and the bottom row is the cross-section after FIB milling. A white scale bar for each image is in the bottom-left corner representing 500 nm. In order to correct for the tilt in the bottom two rows, measurements must be multiplied by $\sqrt{2}$; this has been accounted for by the red scale bars, representing 500 nm after accounting for tilt.

Looking at the SEM images one can tell instantly that they are quite distinct from the samples made in a magnetron. The tendrils are very distinct, as is the random orientation. These would certainly all be defined as fuzz, rather than pre-fuzz. These samples were all taken at 75 eV, the highest energy investigated in the magnetron was 70 eV, but as the energy sweep shows, there is no observable difference between ~50-70 eV. Given the error on the fluence measurements, the PISCES-A samples could cover fluences from 9×10^{23} - 5.2×10^{24} m^{-2}; this would cover almost all the samples created in the magnetrons. Yet there is a fundamental difference between the samples created in each device. The closest looking image of a sample created in the magnetron is shown side-by-side to a PISCES-A sample in figure 6.13 in order to show the difference in surface structure. In PISCES-A the structure, not the orientation, is uniform, with very clear tendrils appearing and no sign of globules. In the magnetron, there is a wide range of structures sizes, as discussed later in section 6.4.9. However, the tendrils seen in PISCES-A are much smaller than those seen in any magnetron sample. These were measured to be ~28 nm, as opposed to

~50 nm in a magnetron.

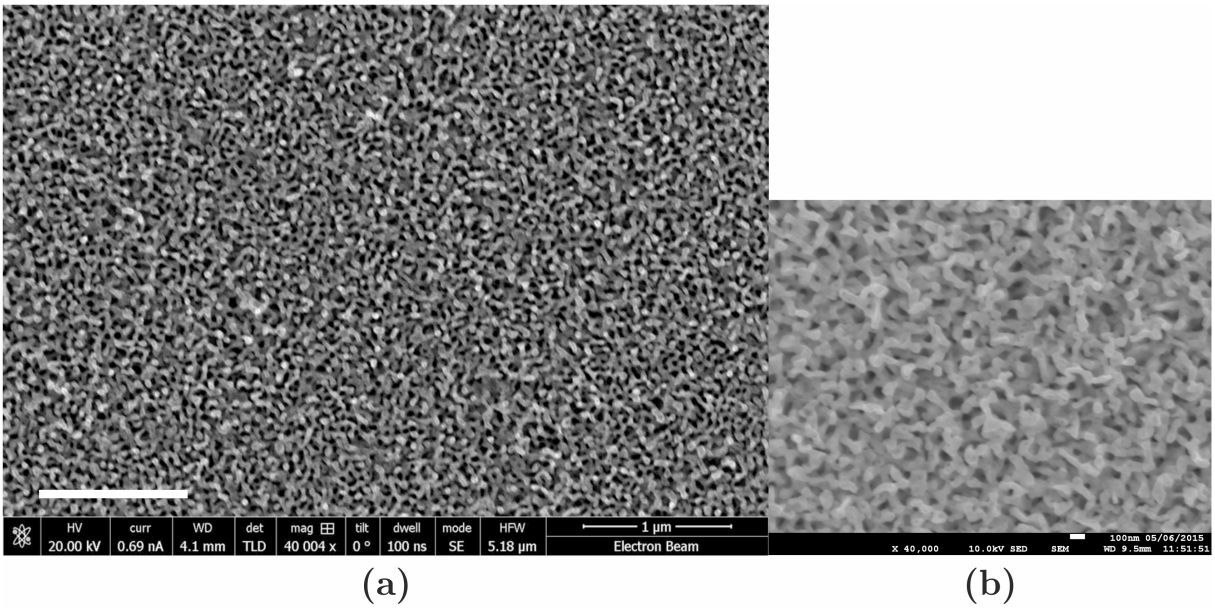

(a) (b)

Figure 6.13. SEM images providing a comparison of a sample created in (a), PISCES-A, to a sample created in (b), the magnetron device. Both images are at the same scale which is shown in the bottom left of image (a), representing 1 μm.

Regarding the existence of the tendrils in PISCES-A, this would lead one to think that the fuzz is more developed than that created in a magnetron. However, when looking at the thicknesses, a different picture is shown. The PISCES-A samples were originally measured in the previous chapter using the CFM technique, however, in order to be a fair comparison to the magnetron samples, these PISCES-A samples were measured again using the same FIB milling technique used for the magnetron samples. The thicknesses of both devices are shown in figure 6.14. The PISCES-A samples can be seen to be universally lower than the magnetron samples, even when the deposition layer is subtracted. This is most likely due to the difference in time-scales between the two devices, being of two orders of magnitude different. This implies that flux and time are important factors to consider between devices, and perhaps one cannot just regard the fluence alone.

It is quite plausible that the deposition in the magnetron is what gives it the non-uniform structure. The samples grown in PISCES-A and in other devices in the literature, do not have to contend with deposition. Depositing over the growing tendrils would occur at random intervals, and at random orientations to the growing tendrils, sometimes landing on the tops of the tendrils, other times on the sides. This would also explain the bigger structure widths seen in the magnetron compared to those seen in PISCES-A, and the more random structure.

As an aside note, the CFM and the FIB technique can be directly compared as they have both been used to measure the PISCES-A samples. Both measurements are shown in figure 6.14. The CFM technique used in UC San Diego apparently slightly underestimates

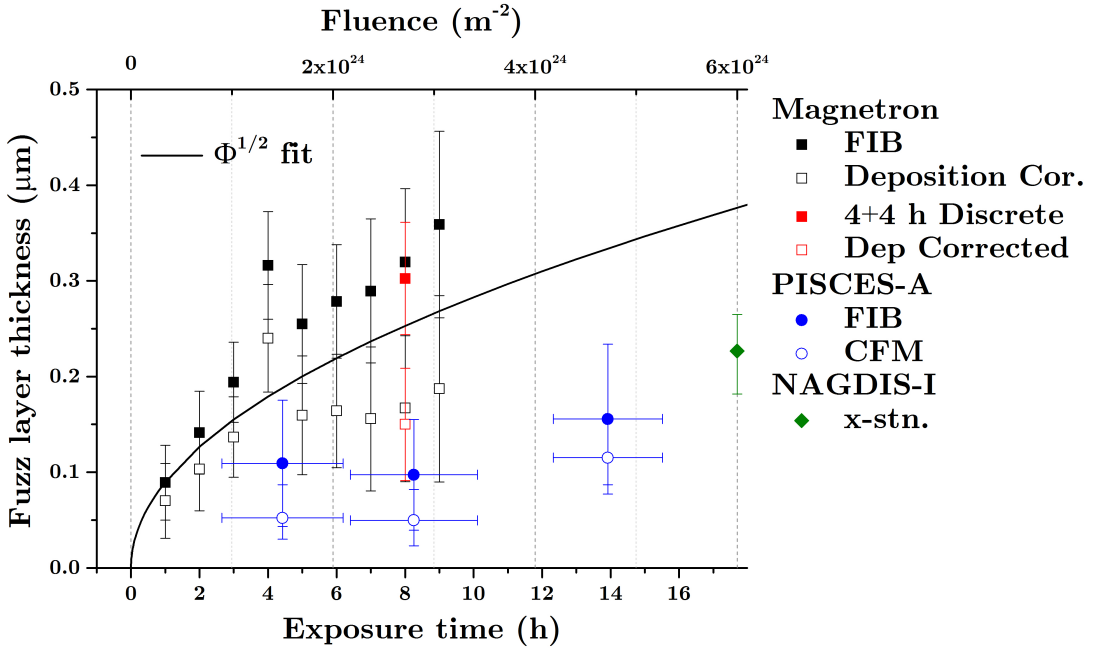

Figure 6.14. Thicknesses of the magnetron samples compared to those created in other devices. The bottom axis, is only relevant for the magnetron points, whereas the top axis is relevant for all devices. The magnetron measurements are represented by squares. The filled-in squares are the FIB measurements, the open squares are with the deposition rate accounted for. The red squares are the discrete exposure, as discussed in section 6.4.7. The blue circles are the samples created in PISCES-A, with the filled-in circles being the new FIB measurements, and the open circles the previous CFM measurements. The green diamond is the sample created in NAGDIS-I measured by cross-section SEM imaging.

the FIB measurements by ~50 nm. This is contrary to what was seen when using the CFM at the University of Manchester, as is shown in section 4.8. This is again most likely due to the scratching technique used, and shows the flaw of the CFM technique. In UC San Diego the samples were scratched with metal tweezers, not particularly sharp. In Manchester, they were scratched with razor blades. It appears as if the tweezers did not go all the way to the bulk, whereas the razor blades penetrated deeper into the bulk. Another way of looking at this is that with the FIB technique, where one defines the start of fuzz is slightly lower than what may be called the start of the fuzz using other techniques, as it allows one to see lower depths than usual. Unfortunately this technique cannot be compared to conventional cross-sectional SEM images, as that technique was not successfully conducted at Liverpool, as discussed in section 4.8.

Nano-PSI

Some low fluence work has been done by El-Atwani *et al.* on He ions bombarding W samples at elevated temperatures in an 'expanding thermal plasma device' called Nano-PSI, at DIFFER [140]. Their conditions were a surface temperature of 1270 K, He ion energies of 30 eV, the fluxes were ~9×10^{19}-2×10^{20} m^{-2} s^{-1}, and fluences from 5×10^{20}-1×10^{23}

m^{-2}. Images of their samples have already been shown in the previous chapter in figure 5.5. The energy is slightly on the low side, but as shown in the present energy sweep, surface structure still appears. The temperature is slightly beyond the capabilities here, but structure certainly appears at such levels. The flux is the same as the flux of the magnetron device. The lowest fluence sample created in the present work in the magnetron was 3.4×10^{23} m^{-2}, >3× higher than the longest fluence sample in El-Atwani *et al.*'s work. Even at their highest fluence it is not comparable to what is seen in the magnetron. They see small stone-shaped structures, comparable perhaps to the globules seen in the present work, however, as their fluence increases, the structure looks much more affected, but in a strange manner. The sample looks as if it is contaminated, however, there is only W present. Perhaps the existence of these globules early on is brought about by the elevated temperatures. As the present temperature sweep shows, a difference of 100 K can make a significant change, perhaps at 1270 K, and at such low fluxes, the globules can appear more readily, first appearing at 1×10^{21} m^{-2} in their work. The main conclusion from their work is that at fluences $\leq1\times10^{23}$ m^{-2}, fuzz is certainly not seen, which is definitely in-line with the results of the present work.

NAGDIS-I

The lowest fluence samples ever created by the NAGDIS team in Japan, were made at a fluence of 6×10^{24} m^{-2} by Kajita *et al.* [33]. The experimental conditions were a surface temperature of ~1400 K, He ion energies of 50 eV, 375 s of exposure, and a flux of 1.6×10^{22} $m^{-2}\,s^{-1}$. The main differences to note, are obviously the much higher surface temperature and flux. The flux here is comparable to that used in PISCES-A. SEM images of their lowest fluence sample is shown in figure 6.15. The surface structure looks like nothing made in either PISCES-A or the magnetron, implying further that at elevated surface temperatures the structures form together, as has been previously discussed in section 6.4.2. The cross-section image, however, shows one similar aspect to those created in a magnetron, in that globules appear with $\lesssim$100 nm diameter. The thickness of their sample is measured to be 230±40 nm. This is plotted alongside the other low fluence work in figure 6.14, as represented by the green diamond. it can be seen that this thickness, along with the PISCES-A is less than the thickness of the layers measured by the magnetron. Again, this is speculated to be due to the much higher surface temperature causing the structure to be partially annealed back into the bulk, and the existence of deposition in the magnetron.

DIONISOS

Another device has been used to create some low fluence samples, by Woller *et al.*, being a helicon plasma source called DIONISOS, a more powerful version of PISCES-E described

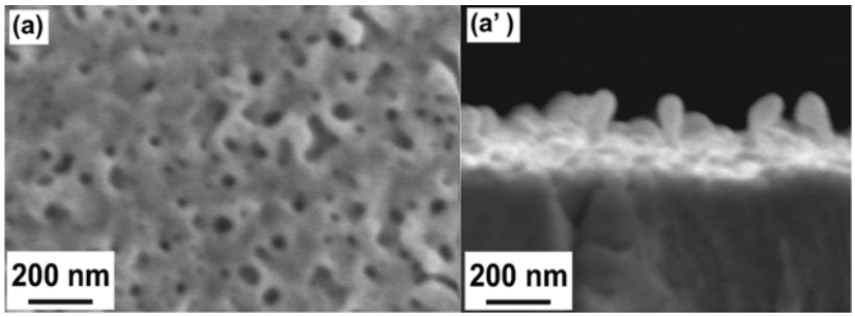

Figure 6.15. SEM images of the lowest fluence sample created in NAGDIS-I, with a fluence of 6×10^{24} m^{-2}. Figure (a) is the surface image, and (a') is the cross-section. Image taken from [33].

in section 3.8.1, based at MIT, Massachusetts, USA [141]. Of their samples, two are of relevance here, being created at 1057 and 1103 K and at fluences of 2.6×10^{23} and 4.9×10^{24} m^{-2}, respectively. In both cases the He ion energy was 60 eV, and the fluxes were 2.1×10^{20} and 5.6×10^{21} $m^{-2}\,s^{-1}$, respectively. These conditions are summarised in table 6.16, corresponding to the SEM images shown in figure 6.16.

Image	T (K)	Γ (10^{20} $m^{-2}\,s^{-1}$)	time (s)	Φ (10^{23} m^{-2})
a)	1057	2.5	1040	2.6
b)	1103	56	875	49

Table 6.2. Plasma conditions for the DIONISOS samples shown in figure 6.16. Values taken from [141].

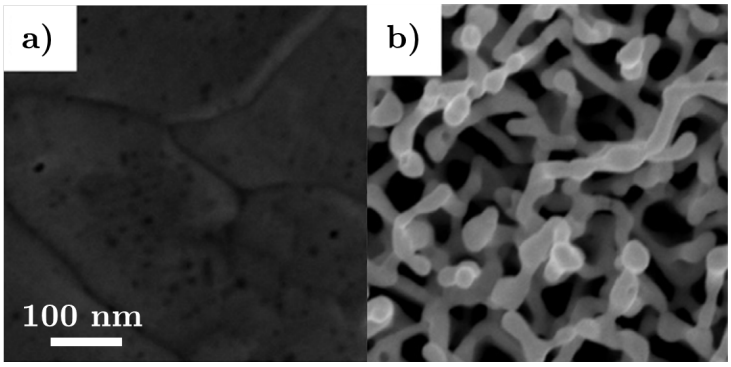

Figure 6.16. Two relevant samples created in DIONISOS. The scale bar for both images is shown in the bottom right, representing 100 nm. The exposure conditions for these two images are shown in table 6.2. Images reproduced from [141].

The lower flux sample, shown in fig. 6.16a was created at a fluence of 2.6×10^{23} m^{-2}, this is comparable to the lowest fluence sample created in the magnetron shown in figure 6.1b, with a fluence of 3.4×10^{23} m^{-2}. In both cases, very little surface structure exists. However, for their high fluence case, of fig. 6.16b, the fluence here is 4.9×10^{24} m^{-2}, this certainly exhibits fuzz. The most comparable sample created in a magnetron is the one

created at 70 eV in the energy sweep, having a fluence of $4.3{\times}10^{24}$ m^{-2}. The features are quite similar, although, much like the situation in PISCES-A, the sample created by DIONISOS is much more uniform than the sample created in the magnetron. The two main differences are the existence of deposition in the magnetron, and the order of magnitude difference in the flux. Both these factors seem possible for the difference in the structure formation.

6.4.5 Extension of the growth model

The original fuzz growth model, as discussed in section 5.4, was given by Baldwin and Doerner in [20], and is easily converted into fluence as $x = (C\Phi)^{1/2}$, where x is the fuzz layer thickness, C the growth constant, and Φ the fluence. This fit is overlaid in the thickness measurements of figures 6.5 and 6.14. One can see that the magnetron data follows the trend but is generally sitting above it. This could imply an enhanced growth for fuzz created in a magnetron as opposed to fuzz created by other devices. This provides hints that if fuzz is grown in a depositing regime, then enhanced fuzz growth can occur. This could possibly be the case in DEMO, the future concept fusion reactor after ITER. DEMO is envisioned to likely have all of its plasma facing components as W. Erosion at the first wall will lead to deposition in the divertor region, the region where fuzz is expected to grow. This could therefore lead to thicker fuzz than is predicted by current trends. For predictions in DEMO, it would probably be a good idea to include the expected deposition rate along with the expected thickness of the fuzz layers to provide a potentially higher estimate. At the moment, DEMO is too far from being a reality to have figures to begin to estimate thicknesses. However, this is provided as a point to take into account as figures do begin to emerge as DEMO becomes closer to a reality.

In the previous chapter a compilation of fuzz thickness created by different devices was charted in terms of fluence versus thickness. A simplified version of that fit is presented in figure 6.17. The magnetron results plotted here are the measurements without correcting for deposition, as was done in the previous chapter. It can be seen that the new measurements closely follow the original $\Phi^{1/2}$ fit. However, to say that a magnetron produces enhanced fuzz for the same equivalent fluence in other devices can be seen to be not significantly so. If the magnetron data is extrapolated to higher fluences, it can be seen to join the other data at higher fluences, albeit still sitting slightly above the trend, this is within the spread of the data around the fit already apparent.

There now appears to be a conflict between which fit is appropriate. In the previous chapter it was discussed how the incubation fluence fit more accurately portrays the low fluence fuzz. However, the lower fluence magnetron data shows that the original non-incubation fluence fit is appropriate. Thereby presenting a conflict. This can be alleviated by comparing the cross-over point of pre-fuzz to fuzz, as just introduced, to the incubation

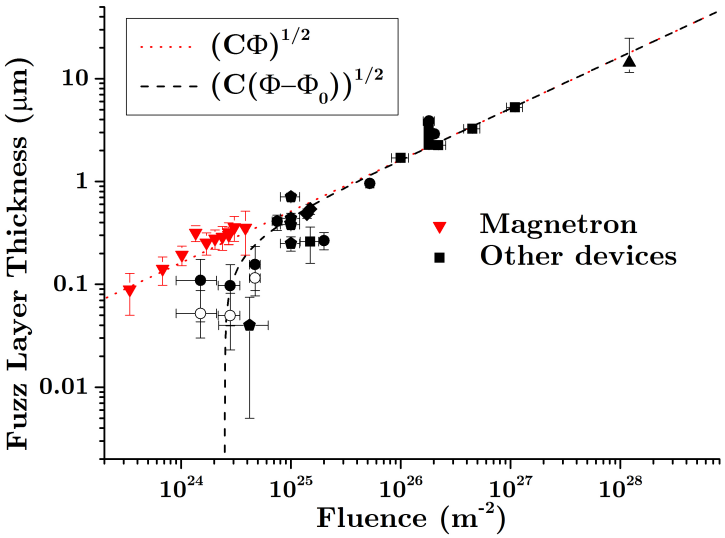

Figure 6.17. Thicknesses of fuzz created in other devices compared with the magnetron device. The compilation chart was made in the last chapter, and is taken from figure 5.6, only with the magnetron results marked in red, and all the other devices marked in black. The open circles represent the previous PISCES-A measurements using the CFM. The new measurements using the FIB are plotted slightly above these as full circles. Shown overlaid are two fits, the original $\Phi^{1/2}$ fit with a red dotted line, and the proposed fit that includes incubation fluence shown in the black dashed line.

fluence. One could easily argue that the samples presented in the fluence sweep in this chapter, before the cross-over point, are not fuzz. However, low fluence samples created in PISCES-A definitely do exhibit fuzz like tendencies.

Zooming into the low fluence region of the compilation chart can reveal more of what is going on in this region. This is provided in figure 6.18. In this chart, the samples that created in the magnetron that have been deemed fuzz have been marked separately as stars, whereas the samples that are deemed pre-fuzz are marked as triangles. By doing so, it can be seen that when corrected for the deposition, the magnetron fuzz samples sit closely to the incubation fluence fit, alongside the PISCES-A samples as measured by the FIB technique. It appears as if there are two routes to create fuzz, the slow route, as provided by the magnetron (shown by the red dotted line), created with long exposures at low flux, or the fast route, provided by high fluxes and short times (shown by the black dashed line).

6.4.6 Comparison to other magnetron attempts

The only other attempt to make fuzz in a magnetron device was conducted by Iyyakkunnel *et al.* in [142], a team at the University of Basel, Switzerland. However, their results differ to the results presented here. They follow the same incentives in trying to create fuzz in a cheaper less complex way than using the traditional LPDs used for the majority of fuzz research. Their device was a 3.5 inch (88.9 mm) wide target, as opposed to a 150 mm wide

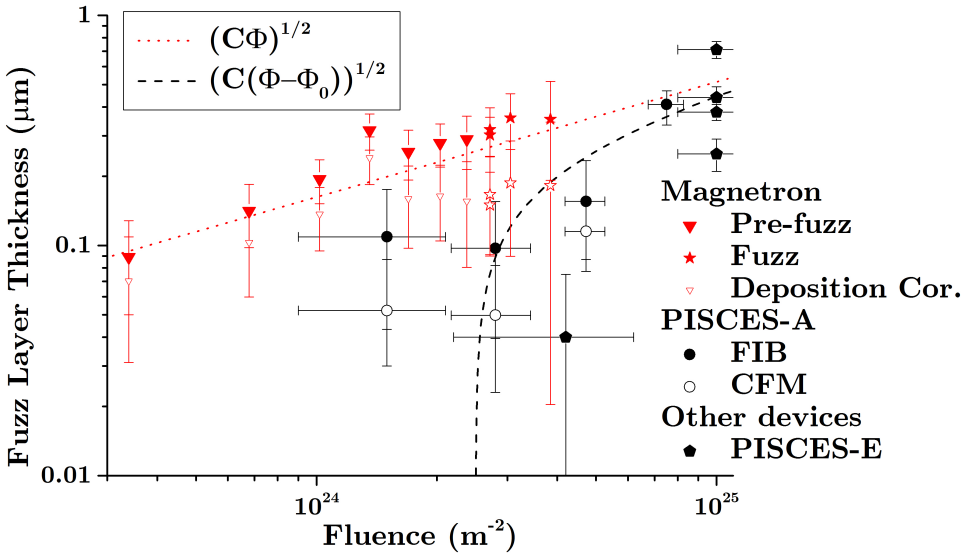

Figure 6.18. The low fluence region of the compilation chart. Here, the magnetron points are separated between those defined as fuzz as stars, and those as pre-fuzz as triangles. For the magnetron points, filled-in symbols represent the original measurements, whereas open symbols have the deposition subtracted.

one used here. They operated in pulsed DC mode, which can reduce the deposition [143], whilst increasing the ion currents compared with continuous DC operation [144]. The present work, however, used continuous DC operation. They operated with Ar present in the gas (as well as He), which would lead to enhanced deposition of the W target. The samples produced in their devices are presented in figure 6.19. It is difficult to know the exact He fluence for their samples, however, they quote an ion flux measured by a Langmuir probe to be ~5×10^{19} m^{-2} s^{-1}, about half the fluxes presented in the present work. The samples shown in figure 6.19 were exposed for 2h, thereby giving a fluence of 3.6×10^{23} m^{-2}. The difference between the two images is that in fig. 6.19a a He ion fluence of ~3.3×10^{23} m^{-2} is shown, with the presence of Ar ions during growth, whereas fig. 6.19b refers to pure He. The surface temperature was 1000 K for both samples, and their He ion energy was calculated to be ~100 eV.

The images in figure 6.19 look almost exactly like those of fig. 6.3c and d, taken at 950 and 1000 K, respectively, and 3.9×10^{24} m^{-2}. Although these images both have the same temperature, the present samples had a fluence 10× that of theirs. This implies that either one of the works has an incorrectly calculated fluence, or the fuzz changes very little at 1000 K from ~3×10^{23} to 3×10^{24} m^{-2}. A sample in the magnetron with the same fluence is shown in fig. 6.1b, with a fluence of 3×10^{23} m^{-2}, taken at 1100 K (as opposed to 1000 K). These samples look very different, with very few globules existing in the present work at that fluence. Assuming that both measurements of the fluence are correct, then the differences between the two devices must be highlighted. Their samples are created with almost double the energy of the He ions, however, as shown by the energy sweep in figure 6.2, this probably produces little difference, still being below the sputter threshold energy

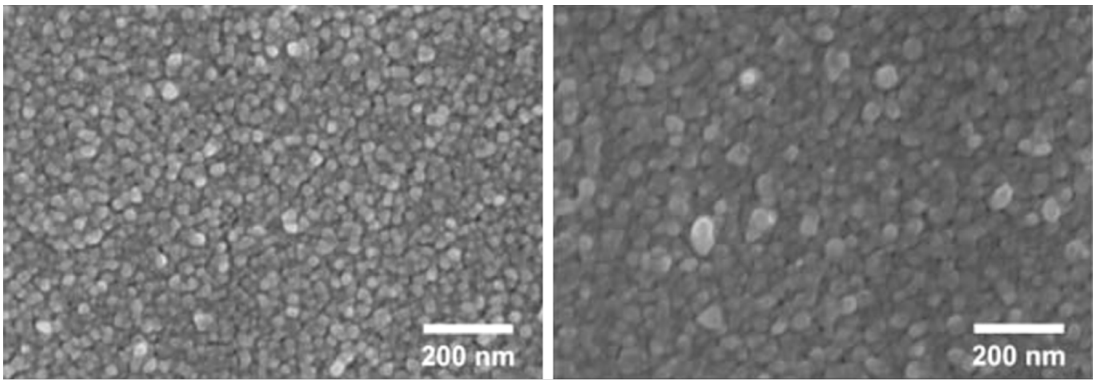

Figure 6.19. The surface structure created by Iyyakkunnel *et al.* by their magnetrons sputtering device. Image (a) was prepared with a 92% He gas (8% Ar), and (b) with 100% He. Images taken from [142].

for He. Comparing samples of the same fluence, i.e. fig. 6.1b to fig. 6.19, the difference in temperature is 100 K. As shown in the temperature sweep of figure 6.3, the difference between 1000 and 1100 K is drastic. This could explain why fig. 6.1b appears quite different from their samples. This would imply that at the higher temperature of 1100 K, the existence of the globules and protrusions seen in fig. 6.19 is delayed, potentially due to the competition of the annealing out versus growth as previously discussed.

6.4.7 Discrete exposure time

The limit of the time of exposure in the present experiments was a result of what could be performed in a working day, due to not wanting to leave the exposure unattended. However, is it the case that discrete exposures, without breaking the vacuum, are equivalent to one long exposure? Discrete exposures have already been done before for very long fluence samples [32], but a comparison between discrete and continuous exposure has not been performed. A sample was prepared in the same manner as all the others, then exposed for 4h, at which point the plasma and the heating were simultaneously switched off, and the exposure time paused. The sample was left in the vacuum chamber overnight without breaking the vacuum. The following day the sample was treated as if new, and following the exact same procedure used before, the sample was exposed for another 4h. The other conditions for the exposure was exactly the same as the 8h exposure. Thus they were both at 1100 K, and with 40 eV He ions. The two samples to compare are shown in the SEM pictures of fig. 6.1i and k. Better SEM images are presented in figure 6.20. The thickness of the discrete sample was measured along with the other samples, and is shown by the red symbols in figure 6.5. The roughness of the surface and the reflectivity has also been measured and is presented in figures 6.6a and 6.7a, respectively, represented by the open symbols in each case.

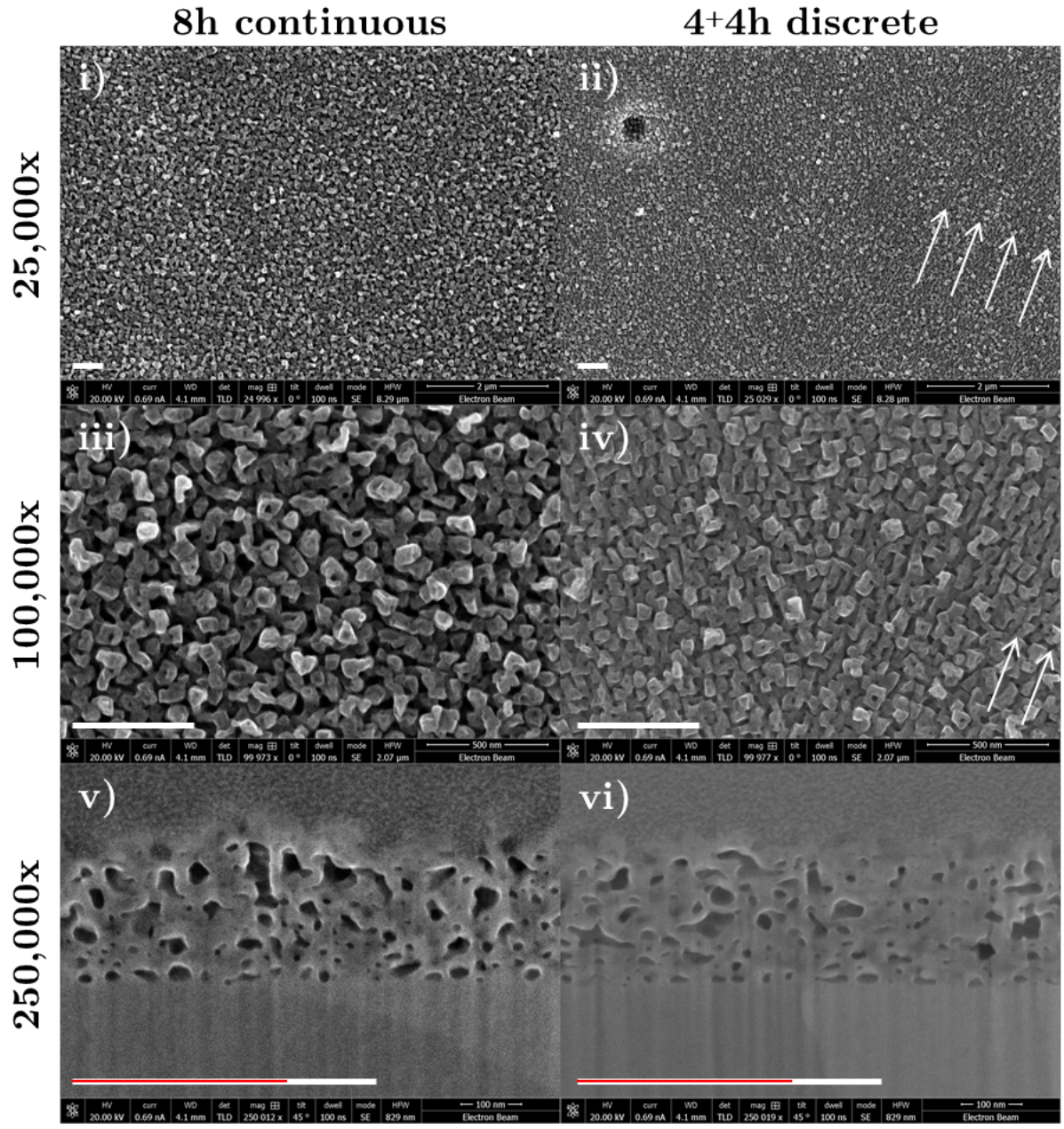

Figure 6.20. SEM images showing the comparison between continuous and discrete fuzz growth. Both samples were exposed for a total fluence of $2.7{\times}10^{24}$ m^{-2}. The images on the left are samples created in one continuous 8h exposure, whereas the images on the right are created in two 4h exposures, left overnight in between. The top row shows surface images taken at 25,000× magnification, the middle row is taken at 100,000×, whereas the bottom row is the cross-section after FIB milling, and is taken at 250,000× magnification. A scale bar is provided in the bottom left of each image, representing 500 nm in each case. Care must be taken for the bottom two images, as they were taken at a tilt of 45°, therefore any measurement made in those images should be multiplied by $\sin(45^\circ)$ $(= \sqrt{2})$. This correction factor is portrayed by the shorter red line, representing 500 nm after accounting for the tilt.

By comparing the two samples side by side, some interesting features can be seen. Firstly, regarding just the SEM images of the surface, they do appear distinct. The continuous exposure seems more developed, whereas the discrete exposure appears behind, still exhibiting some directionality (as shown by the white arrows overlaid in fig. 6.20), there are less protrusions, and the globules are smaller. The images of the surface of the discrete sample are more comparable to the 6h or 7h exposure at 2.0 and 2.4×10^{24} m^{-2}, respectively. Looking at the roughness of the two surfaces, as presented in figure 6.6a, these were measured to be 23±9 nm and 7±3 nm, for the continuous and discrete exposures, respectively. It can be seen that for the discrete case the roughness is ~1/3 of the continuous case, fitting more in-line with the roughness values between 4 - 6h. For the reflectivity values, as presented in figure 6.7a, these were measured to be 17%, and 37% for the continuous and discrete cases, respectively. The discrete measurement is more in-line with the measurements for the 6 - 7h exposures, fitting well with what is observed in the SEM images. So the SEM surface images, the roughness values, and the reflectivity values, all would suggest that the discrete sample is not as fully developed as the continuous sample. However, looking to the thickness measurements, the most important of all values for fuzz, as presented in figure 6.5, one can see that the thickness for the discrete exposure is only slightly less than the continuous, and sits in-between the 7 and the 8h exposures. For the continuous sample the thickness is measured to be 320±80 nm, whereas for the discrete sample it is measured to be 300±60 nm. Looking to the SEM images of the cross-section, as provided on the bottom row of figure 6.20, the two images actually look very alike from this point of view, with very similar heights. Although, the continuous sample appears to have more gaps, implying again that it is more tendril-like.

There are some possible causes of differences between the exposures. For fuzz to form, it is pretty certain that He bubbles need to penetrate into the surface, and to coalesce as bubbles which leads to surface modification (see section 2.1.5). As such, it is possible that while the discrete sample is being left over night, He can escape the surface, slowing down the onset of the fuzz growth. There is a theory that for fuzz to grow, the surface needs to be saturated with He bubbles [84, 145], therefore when the discrete sample starts the exposure again the following day, before fuzz can grow this saturation needs to take place, hence slowing the growth down. On top of that, following the work of thermal desorption spectroscopy (TDS)[1] by Baldwin *et al.* in [62], they show that a sample with fuzz grown on it at 1120 K, after being placed in the TDS device, showed some He ejection below 1000 K. On the 2nd exposure of the discrete sample, as the sample is being heated to the target temperature before exposure begins, some He will therefore escape. This will again cause stunted growth, hence explaining why the discrete exposure does not look as

[1] TDS is a technique whereby a sample is heated up and the levels of He are recorded by a residual gas analyser.

fully formed as the continuous.

Another theory is that at the end of the first exposure, the 4h level is attained, then perhaps, during the 2nd exposure, a new layer grows on top of this one. This would imply the layer having the structure of a ~4h exposure, but be much thicker. However, if this were the case, then due to the decreasing growth rate with time, one would expect a discrete exposure to be thicker than an 8h, and be 2× the thickness of the 4h. Looking to the thickness chart of figure 6.5, although unfortunately the one 4h exposure is clearly presenting itself as an anomaly, one can judge from the other samples where the expected measurement ought to be. The thickness for the 4h ought to be at 230 nm, so twice this is 460 nm, much thicker than the discrete case.

Deposition for the discrete case is the same as in the continuous case, being a predicted deposition layer of 150 nm. After accounting for deposition, as shown by the open symbols in figure 6.5, it can be seen that the amount grown not by deposition is 150 nm for the discrete case. This is actually below the corrected cases for the 5-7h samples too. It is, however, very close to where the expected 4h should be (after correction). This has been shown diagrammatically in figure 6.21. This implies that if one is considering the deposition to be caught up in the growth in magnetrons, then the actual thickness caused by He ions, rather than W deposition is much more in line with that expected for the 4h case. However, this would mean that the discrete sample only 'grew' for 4h. Possibly implying that for the discrete case, the first exposure got re-integrated into the original surface. Thus, before the 2nd exposure began, the thickness was only the original surface layer + the W deposited during the 1st exposure. Then, in the 2nd exposure, there was 4h worth of growth, and another 4h worth of W deposition. Is this possible? From what is known about annealing out, in other studies, the lowest temperature annealing out of fuzz occurred at 1300 K by Meyer *et al.* [103]; after 30 mins the layer was restored to the original level. That does not necessarily imply that 10 minutes is required to anneal out a surface, perhaps given the small thicknesses apparent in the present work, such a small layer could be annealed out in less time, and at lower temperatures. However, there is not an obviously large annealing period. After the 1st exposure, the plasma and heating are turned off at the same time, the IR pyrometer still reads the temperature on the sample during this cooling period. Although these values were not recorded, it is observed that the temperature initially drops very quickly, down to ~600 K in <30 s. However, before the 2nd exposure is counted to begin, the heating up is quite gradual, at a rate of 1 $K\,s^{-1}$. The temperature is brought to 1100 K, therefore existing above 900 K for 200 s, and then the plasma is ramped up to 700 W. From the time the sample passes 900 K, to the time that the bias is turned on, this is about 8 minutes. For >1000 K, this is about 6 minutes, and 1100 K for 4 minutes. To know if annealing did actually cause the difference, a dedicated annealing study should be conducted.

That all said, although the difference of the thicknesses between the discrete sample

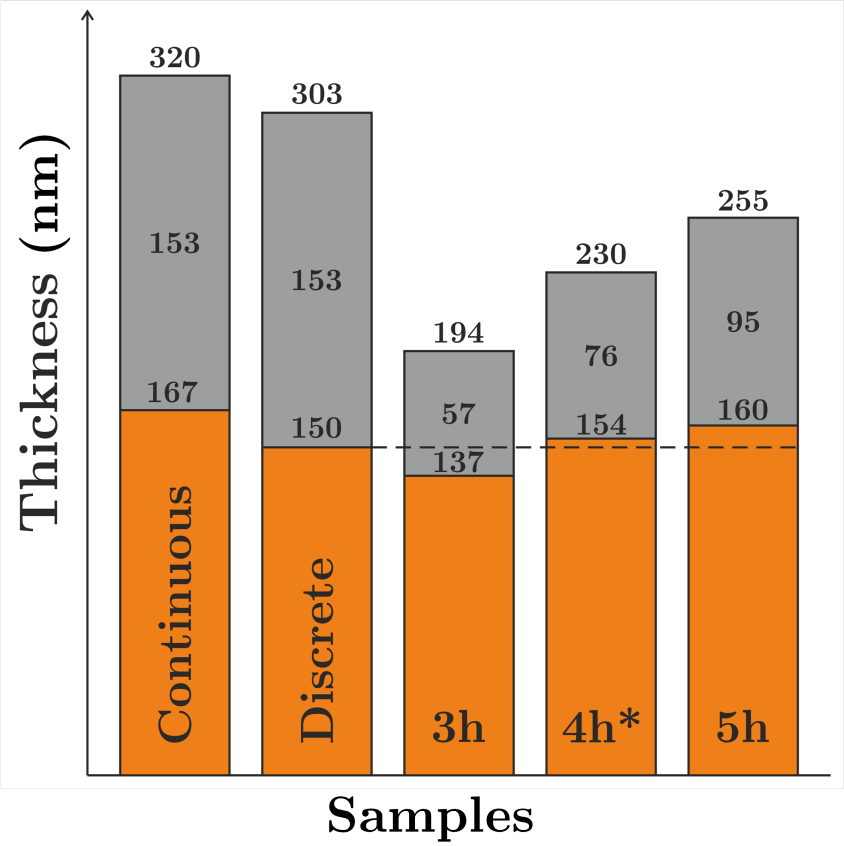

Figure 6.21. Comparison of the thicknesses of a few samples, with the amount possibly caused by deposition highlighted in gray, and the part not caused by deposition in orange. *The values for the 4h exposure were extrapolated from the trend of figure 6.5 rather than the measured value.

and the continuous sample is only 17 nm, this is within the margin of error. However, the reflectivity and roughness measurements are certainly outside the error, and are apparent in the top down SEM images. Even so, this is only one sample, and as the single 4h exposure shows, anomalies can exist in a magnetron, so in order to take anything substantial from this much more data is required. That said, at low fluences, there is cause to suspect differences may occur operating in discrete exposure, however, for high flux devices, with high fluence exposures, these differences are probably negligible.

6.4.8 Reflectivity and roughness

The reflectivity measurements presented here can be compared to reflectivity measurements performed in the literature. Sakaguchi *et al.* in [34] looked at the reflectivity of W samples exposed at different sample temperatures. They observed the reflectivity of several fuzzy samples using a He-Ne laser at 632.8 nm, hence 632.8 nm was chosen as the wavelength in figure 6.7. They show that the reduction in reflectivity is greater at higher surface temperatures, as is also apparent here. They also show that the reflectivity of fully formed fuzzy surfaces is $\lesssim$1%. Further work by Sakaguchi *et al.* reported also seeing

that the reflectivity is reduced more at lower wavelengths than at higher [146]. Work by Kajita *et al.* also reports on the reflectivity decreasing with increasing fluences to nearly 1%.

The roughness values presented here in figure 6.6 are in line with values of roughnesses measured by other authors. Kajita *et al.* mentioned the roughness of fuzzy samples was measured to be ~100 nm's. Their samples being much thicker and more developed than the present samples, this fits well with the rougher surfaces measured here, for example at 1200 K at ~160 nm (see fig. 6.6c).

Both roughness and reflectivity can be indicators for fuzz growth, and are intrinsically related to one another, with fuzzier samples exhibiting rougher surfaces and less reflectivity. Gathering all the samples created here, and plotting them on a chart of reflectivity versus roughness reveals how interconnected they are. This is shown in figure 6.22. This is an obvious trend, as when the surface roughness increases, more light is scattered away and hence the measured reflectance is lower [147]. It has been speculated that roughness values can be used to infer the reflectivity, and perhaps with thicker fuzz samples the surface roughness can be measured to give an indication of the reflectivity [148].

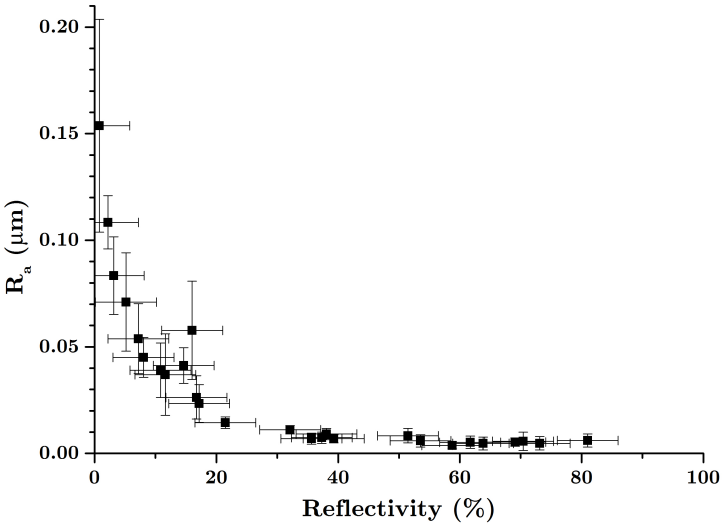

Figure 6.22. A comparison between the reflectivity and the surface roughness for all the samples created in the magnetron. The one outlier is the sample created in the energy sweep at 55 eV.

Another interesting trend can be noted when plotting the reflectivity and the roughness against the thickness of each sample, as has been done in figure 6.23. It can be seen that the reflectivity and the roughness values follow S-curves with the surface roughness, changing very little for the first ~200 nm, before changing rapidly between 200-350 nm, then saturating at thicker values.

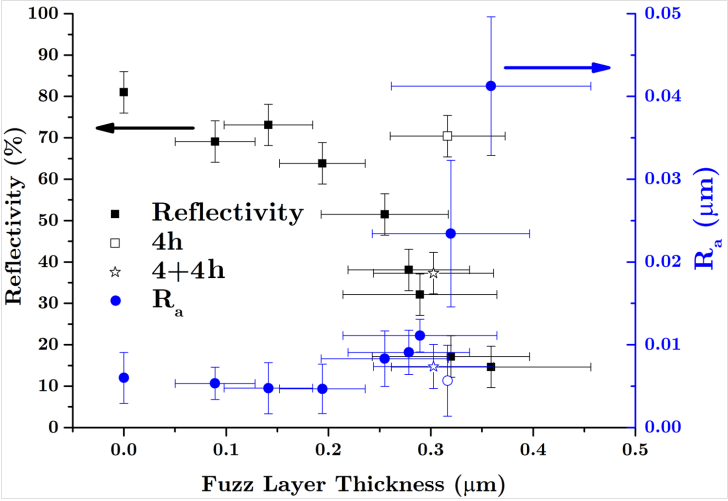

Figure 6.23. A comparison of reflectivity and surface roughness with the fuzz layer thickness. The reflectivity values on the left-hand axis are shown in black squares, and the roughness values on the right-hand axis are shown in blue circles.

6.4.9 Structure width

Another measurement worth taking on fuzz samples is usually the tendril width, however, many of the samples here do not exhibit tendrils. A better measurement would be the structure widths, but this requires some defining. Using the SEM images as presented in figures 6.1-6.3 the widths of the structures were measured using ImageJ. In the lower fluence samples, where the streaks or ripples appear, the width of these ripples was measured. Also the globules widths were measured, though when it was not possible to define a width, the length across the whole globule was measured, often from a few directions, to get an average structure size. Where tendrils appeared the widths were measured, but not the lengths. For each sample, 100-280 structures were measured and an average taken with 2× the standard deviation used for the error bars. An example of a measurement of an image is shown in figure 6.24, with the individual measurements shown by the yellow lines. These should rather be called 'apparent structure widths' as it is only taken from the top-down images and cannot take into account the 3D geometry of the structures. This method is not recommended, as it is very time consuming. To get the results it took over 4500 individual measurements.

The measurements for each sample in the parameter sweeps are shown in figure 6.25. It can be seen that across all three parameter sweeps there is very little change. The samples are more than within each other's error bars, showing that there is a very wide variety in each sample. However, there are a few points to emphasise from the results. In the fluence sweep, this is the only one that shows a potential trend, with the widths slightly decreasing with increasing fluence. This is also echoed in the work of Kajita *et al.* in [19]. They look at the widths of structures over a much larger range of fluence, from 6×10^{24} - 5.5×10^{25} m^{-2}, bearing in mind that the surface temperature was 1400 K (and 50 eV He ions). They

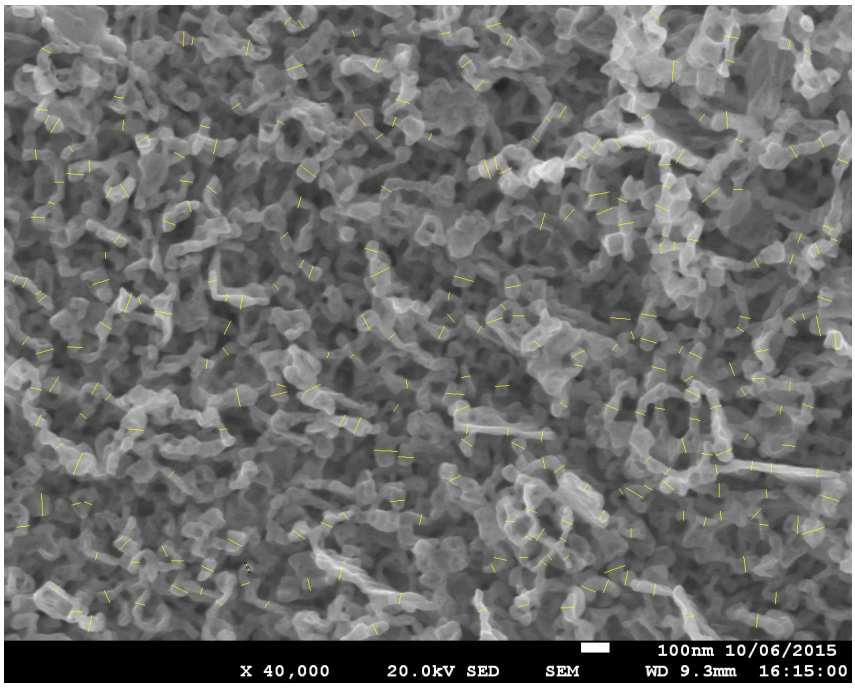

Figure 6.24. An example image of the measurements of the widths of the structures. Shown on this image are 280 measurements, represented by the yellow lines, which were averaged to get the value plotted in figure 6.25. This particular sample is the 1200 K exposure shown in figure 6.3h.

measured the width of structures using an entirely different method, via 'slice analysis', which is beneficial in that it removes the bias of selecting which structures to measure, but only counts the top most structures, whereas the present technique includes structures lower down, as long as they are observable. At $6{\times}10^{24}$ m^{-2} they measure the widths to be 110±30 nm, decreasing to 47±7 nm by $2.4{\times}10^{24}$ m^{-2}. Whereas here, the widths of the structures in the magnetron only just reached 100 nm at the maximum error bar in a few cases, with a width of 53±36 nm for a fluence of $3{\times}10^{24}$ m^{-2}. This difference could be due to the work of Kajita *et al.* being at much higher temperatures, partially annealing the structures, and hence them coming together to form larger structures, as has been seen in other works at higher temperatures than present [34, 136]. Or, this may be due to the deposition occurring in the magnetron as discussed in section 6.4.4.

It is interesting to note that the discrete sample is notably lower than the continuous sample, as shown by the red open square in figure 6.25. This is reassuring to the technique used to get such measurements, as by comparing the two SEM images, as is done in figure 6.20, the difference in structure widths is evident. However, the reasoning for this is not clear, as the discrete measurement is a bit lower than all the other exposures, and if any trend is seen, it implies that the features are smaller with increasing fluence. Rather, one might have expected to see the discrete sample sitting above the continuous in this figure.

If one wanted to make a general statement about the structure widths made in the present work, this could be done by comparing all the measurements made during the

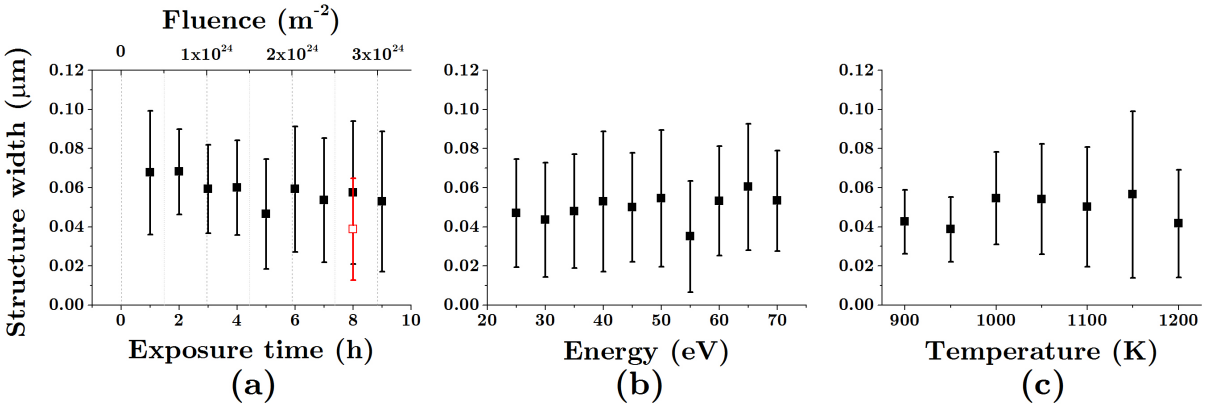

Figure 6.25. Measurements of the structure widths for the various parameter sweeps, with (a) showing the time (and hence fluence sweep), (b) the energy sweep, and (c) the temperature sweep. In (a) the red open square represents the 4+4 h discrete growth sample.

energy sweep and the temperature sweep, as these two sweeps show no apparent trend. Doing so would bring together over 2900 measurements made via this technique, and a histogram is shown in figure 6.26. This gives an average structure width of 50±31 nm.

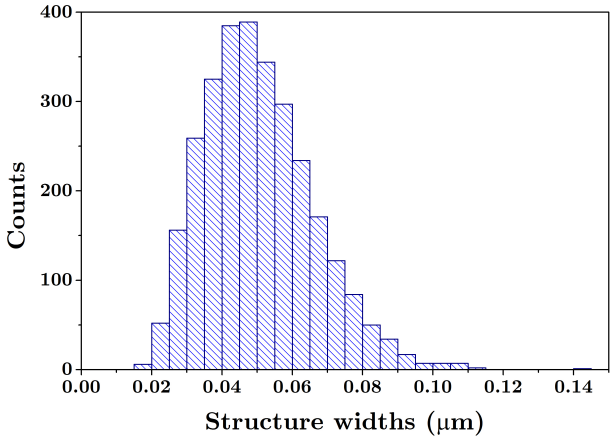

Figure 6.26. A histogram combining all the measurements from the energy and temperature sweep, with a bin size of 5 nm. This gives an average structure width of 50±31 nm.

The problem with this technique is that it takes in all the widths, both of the bigger structures, and the smaller ones, such that the average is still in the middle, but the spread gets larger. This is perhaps seen in the temperature sweep, where the spread at 1150 K is much bigger than at 900 K, with much bigger features existing, and slightly smaller structures too. A roughness profile could perhaps be used instead to perform a slice analysis, the technique used by other authors. However, the CFM used in the present work had a minimum step size of 46 nm, just about the size of the structures here.

6.4.10 Emissivity concern

As the surface structure changes, the emissivity could be assumed to change too. Lots of fuzz created in the literature uses IR pyrometers to monitor the temperature of the samples

during growth. The general consensus is to ignore any change in emissivity that may occur during fuzz growth, due to the complexity of trying to integrate it into the IR pyrometer during growth [15, 19, 33, 42, 59, 64, 142, 149–151]. However, the emissivity is inferred to increase as fuzz grows, due to the blackening of the surface. As the actual emissivity of the sample rises the emissivity set in the IR pyrometer will be an underestimate. This would imply that the temperature reading will be an overestimate, and the actual surface temperature will be less than is being measured. This has been seen in one experiment by Kajita *et al.* whereby they used two IR pyrometers, one as usual, with a set emissivity value, and the other has the emissivity varied based on live measurements during growth [124]. They show how as fuzz develops, with constant heat input, the emissivity rises, causing the actual temperature to drop. Their measured temperature difference is 250 K. This is quite a substantial difference if one considers that the temperature sweep performed here is implying that 50 K can make a substantial difference. Hence, the temperature sweep is therefore potentially untrustworthy. The temperature of fuzz growing samples should instead be more appropriately referred to as the 'initial temperature'.

Recent work by Takamura investigated this change in emissivity, and using two methods recorded the emissivity of a sample as fuzz grew [67]. Using one method Takamura measured the emissivity of the fuzz to be ~0.5; using another method it was calculated to be nearly 1.0, that of a black body. They write that the 0.5 was most likely an underestimate, and conclude that an emissivity of 1.0 is more likely the case. Using Planck's formula for radiation, as was used in the calibration chapter for the emissivity (see section 4.4), one can calculate the temperature of the sample for other emissivities. If the sample was recorded to have a temperature of 1100 K, and the emissivity was set to 0.266, then if the emissivity was changed to 0.5, the temperature would have read 990 K. If the emissivity was instead set to 1.0, then the temperature would have read 890 K. This is a substantial temperature drop. However, this is a gradual drop, changing as the fuzz grows. Other authors have measured the emissivity of a fuzzy sample, Kajita *et al.* also measure it to be ~1.0 [152], whilst De Temmerman reports this as 0.8 [153].

In the temperature ranges presented by other authors shown in figure 6.9, both Sakaguchi *et al.* and Kajita *et al.* use IR pyrometers, without evidence for calibrating the emissivity during growth [33, 34], whereas Miyamoto *et al.* used a thermocouple placed behind the sample [35]. Authors who use thermocouples placed behind the sample have the sample heated by the plasma exposure. The heating method in the magnetron has samples heated from the back, so thermocouples here could interfere with the heating method, and give an overestimate of the plasma facing surface temperature.

This is clearly an issue that needs to be addressed for future fuzz experiments. This would imply that using IR pyrometers should not be recommended, however, experience using thermocouples in the present experiments proved to be very difficult (see section 3.1.4.1). Ways around this could involve measuring the emissivity during exposure, though

this is no easy task, and requires extra equipment and setup, but this was what some authors did [124]. Thermocouples seem the best option, placing them behind the sample, and not exposed to the plasma, as is done in the PISCES devices.

6.5 Conclusions

Three parameter sweeps have been performed in a magnetron device, the He ion fluence to the sample, the He ion energy, and the sample surface temperature. A cross-over point from pre-fuzz to fully formed fuzz has been found in section 6.4.1, with a fluence of $2.4\pm0.4\times10^{24}$ m^{-2}, closely overlapping with the incubation fluence discovered in the previous chapter at $2.5\pm1.5\times10^{24}$ m^{-2}. There has been no apparent cross-over point in the energy range from 25-70 eV. Regarding the temperature, a clear cross-over point is seen at 1080±60 K. From the parameter sweeps it was found that the best conditions for making fuzz in magnetrons is a fluence of $\geq2.4\times10^{24}$ m^{-2}, a He ion energy of 60 eV, and a surface temperature of 1100 K. The competition between annealing out of fuzz and growth of fuzz has been discussed in section 6.4.2, hinting that annealing could occur at lower temperatures (~1200 K) than previously seen (≥1300 K), presenting a potential issue for high-temperature low-flux experiments. In section 6.4.3, the issue of deposition occurring in magnetrons is discussed.

The fuzz created in the magnetron is compared to low fluence experiments conducted in PISCES-A in section 6.4.4, as well as low fluence experiments in other devices in the literature. It is found that the fuzz created by higher flux devices provides much more uniform structure, whereas magnetron fuzz is much more random. The structure widths are also much thinner in other devices. Both these effects are most likely due to the deposition occurring in a magnetron, causing random and thicker structures.

The growth model created in the previous chapter is discussed with the addition of the new magnetron thicknesses in section 6.4.5. It is found that the thicknesses of samples created in a magnetron follow the original $\Phi^{1/2}$ relation, as opposed to the new incubation fluence relation. This is discussed in light of only the highest fluence samples in the magnetron exhibiting fuzz like tendencies, as samples created with similar fluences in higher flux devices show fuzz formation at much thinner thicknesses than present, possibly again due to the deposition occurring in the magnetron.

In section 6.4.6, fuzz attempts in a magnetron in the literature have been discussed and the results compared. In the work of Iyyakkunnel *et al.*, their fluences were much lower than the present cases, however, their samples exhibit similar features to the lower fluence samples presented here.

A sample created with discrete exposure is compared to the same fluence in one continuous exposure in section 6.4.7. There are several interesting differences between the samples, with features appearing smaller in the discrete sample. However, the overall

layer thickness is very similar for the two cases.

The reflectivity and roughness measurements are compared to literature values, to one-another, and to the fuzz layer thickness in section 6.4.8. The roughness and reflectivity are clearly intrinsically linked, and both of them change quickly as the thickness changes from 200-350 nm, before saturating out. The structure widths of the samples created in the magnetron are measured, showing a small decrease with the fluence, but no apparent trend in the energy or temperature sweeps was observed. The average structure width was measured to be 50±31 nm. Lastly the problems of using IR pyrometers to measure the surface temperature are discussed in section 6.4.10, proposing that this should be investigated in future studies.

To summarise, fuzz can be readily and repeatedly created in a magnetron device. The structures differs slightly from that of higher flux devices, most likely owing to the deposition occurring. However, they can certainly provide a method for creating and studying fuzz, and more research should be done on them.

Chapter 7

Conclusions

7.1 Summary

This thesis presents new results for the field of fuzzy tungsten research. An extensive literature search has been performed, bringing together for the first time works from over 100 papers on the area. The various characteristics associated with fuzz have been presented and the current work on the formation conditions shown. The potential for fuzz to occur in ITER has been discussed as well as positive and negative aspects of fuzz occurring. The various proposed growth mechanisms presented in the literature have been introduced and a brief summary of the current work on simulating fuzz has been provided. Fuzz appearing on other metals has been shown, being found so far on Mo, Ni, Fe, and Ti. An introduction to key devices for making fuzz is given, and evidence for creating fuzz in a tokamak shown. Methods for removing fuzz and mitigating it's effects found in the literature are presented. Lastly, a brief introduction to some relevant plasma physics necessary for the present work is provided.

The experimental procedure detailed the apparatus and experimental setup used to obtain the data in the later chapters. The magnetron rig used at the Liverpool University is detailed, including the sample holder and heater that was developed in order to create fuzz. The diagnostic equipment are described with many pictures and schematics given to help explain how they work. The plasma devices used at UC San Diego are also briefly introduced. The preceding chapter outlines the initial calibration of the experimental setup, beginning with Langmuir probe data on the plasma properties, to custom probe designs which portray more accurately the situation for a growing fuzz sample in a magnetron. Other preliminary work is shown on calibrating the IR pyrometer, mass spectrometry data, results from a thermal probe, and deposition measurements. This chapter finishes with various attempts to get the thickness of fuzz layers.

The next two chapters are the results chapters, presenting new findings in the field. The first chapter is centred on a collaboration with Dr. Matthew Baldwin of UC San

Diego. Prior to doing some experimental work on their large scale high power plasma devices, a compilation of many fuzz samples in the literature was undertaken. This brought together many fuzz samples covering four orders of magnitude of fluence, for the first time the bigger picture of fuzz thickness versus fluence could be seen. To compliment this dataset, new samples were created using three devices at UC San Diego and the magnetron at Liverpool, covering the current range of fluence, and extending it even further at either end. A sample was created with the longest fluence to date, taking 5 days of operation on one of the most powerful linear plasma devices in the world, PISCES-B[1]. The results of this compilation shed some new light on the underlying fuzz growth equations. Firstly an incubation fluence is noted in the data as well as hints in the literature. This is a fluence necessary before fuzz develops, owing to the time needed for the He bubbles to develop before tendril formation can begin. This brought about a small correction to the previously accepted growth formula to account for this incubation fluence. The highest fluence data point warranted investigation on growing fuzz in erosive regimes. In doing so, a new equation was presented which combines growth and erosion, and makes some interesting predictions for fuzz growth in such regimes, fitting fairly well with results in the literature.

The second results chapter presents outcomes from samples created in the magnetron device at the University of Liverpool. This constitutes the bulk of the work performed throughout the PhD in developing this technique. Magnetrons have not traditionally been used to create fuzz, with large scale, complex, expensive devices being the norm. However, an experimental technique was developed showing that the magnetron can be used to create and study fuzz. Three parameter sweeps were undertaken, being the three main parameters for fuzz formation of He ion fluence, bombarding He ion energy, and sample surface temperature. A thorough discussion of the results is given. To begin with, the boundary conditions for fuzz formation are re-examined, showing a smaller temperature window for fuzz to occur and little dependency on the energy of the He ions above 25 eV. The low fluence work shows a form of pre-fuzz, which is defined in a separate light to fully formed fuzz. The existence of this pre-fuzz encourages the introduction of a cross-over fluence from pre-fuzz to full fuzz. This cross-over point coincides with the incubation fluence from the previous chapter. The competition of growth of fuzz versus the annealing out of fuzz seen at higher fluences is discussed in light of apparent melting occurring in the highest temperature sample created in the magnetron. Results hint that lower flux devices will see annealing out happening at lower temperatures due to the lower growth rate. The results from the magnetron differ from fuzz created in other devices at similar fluences, appearing much more random in structure. This is most likely to be a result

[1]PISCES-B can be considered the 3rd most powerful, in terms of maximum flux, with the top 2 being at DIFFER, with PILOT-PSI as the 2nd most powerful, and MAGNUM-PSI the most powerful. However MAGNUM-PSI is not yet fully operational, and PILOT-PSI has to operate in pulses due to the intense heating achieved.

of the existence of the deposition occurring simultaneously during growth. Attempts to grow fuzz in a magnetron by other authors is presented and differences discussed. A one-off sample was made in two consecutive exposures, left to rest over night, the difference between such a sample and a sample grown under one continuous exposure is shown. The reflectivity and the roughness measurements performed on each sample are discussed with regard to literature values and some trends were seen in the parameter sweeps. The widths of the structures are measured and they are noted to be on average larger than structures created in other devices at similar fluences. Lastly some possible concern over the emissivity value of fuzz samples changing with time is discussed.

Overall, the aim of the present work was to develop a method for creating fuzz on a cheap and small scale. This has been achieved and the device has been shown to find new insights in the field. This has paved the way for future work to be undertaken on the rig, suggestions of which will be provided in the next section. The hope is that many laboratories world-wide can use a similar low-flux setup to research fuzz, and hopefully some novel uses for fuzz will arise outside of fusion research, making use of its unique properties.

7.2 Future work

There are many avenues for future work on the magnetron as it is a newly developed technique for making fuzz with a lot of potential. Firstly, the unique feature of magnetrons over other plasma devices for studying fuzz is the existence of deposition occurring throughout growth. Dedicated studies on this should be done involving growing fuzz under various different deposition rates. However, a challenge lies therein as the deposition rate is linked to many other parameters. By varying the plasma power the deposition rate is easily changed, however, this will also affect the He ion flux to the sample, hence affecting the fluence. Varying the gas pressure will also affect the deposition rate and the flux. Introducing a trace amount of argon may provide a good source of enhanced deposition whilst not varying the He ion flux to the sample. Simply facing the sample perpendicular to the target will greatly reduce the deposition; results in chapter 4 show that the deposition will be reduced by 75% with the flux only being reduced by 31%. Also a shield could be employed, however this may reduce the flux too much. At any rate, the part that deposition plays on growing fuzz samples should be investigated.

The energy sweep presented on the magnetron was also a fluence sweep, a dedicated energy sweep accounting for the change in flux at different biases should be conducted. This will give a fairer picture of the effect of changing the energy on the structure.

The competition of annealing versus growth is an interesting topic, and it has been hinted that annealing can occur at lower temperatures than 1300 K. This could be studied in the magnetron. Ideally the temperature capacity of the sample heater should be

improved beyond 1200 K such that higher temperatures could be investigated in order to overlap with other annealing studies done at 1300 and 1400 K.

At the end of the last chapter, the problem with emissivity was discussed, ideally this should be addressed. Possible solutions include using thermocouples that are unexposed to the plasma, perhaps in a hole in the side of the samples or behind them. An alternative approach is to continue using the IR pyrometer but to adjust the emissivity during growth. To do this would require a dedicated study to find how the emissivity changes over time. As a side note, the emissivity of the fuzz samples created in the magnetron should also be measured, however, this is difficult using current contact methods (thermocouples touching the surface) as the fuzz structure is so fragile.

It has been noted that in pre-fuzz the orientation of the structures is grain dependant, this should warrant overlapping the observed orientation with the underlying grain orientation to see if an obvious pattern exists. Grain orientations were never measured on the samples created in the magnetron, however they are of the right fluence to investigate any patterns.

There was an idea to attempt to make fuzz on the magnetron target itself by removing the target from the cooling, allowing the surface to reach sufficient temperatures for fuzz to form. The benefits of such a technique, if proved successful, could be easy mass production of fuzz. All fuzz made in the literature is created on small discs of diameters 10-25 mm or so. If a potential industrial application is found, the manufacturing of large samples of fuzz would be highly sought after. Of course, complications will quickly become apparent, the foremost is that the fuzz grown on a target will be in a complicated erosive regime due to sputtering and deposition regime due to prompt re-deposition of sputtered particles.

Other metals have been found to show fuzz; these could be investigated in a magnetron. However, due to the nature of the device, if deposition cannot be prevented then the target would have to be replaced to make sure the growing fuzz is of the desired material, and not just fuzzy tungsten. Other targets will have much higher sputter yields and hence much more deposition will occur. This may not be detrimental to the growing of fuzz, as demonstrated here, but it clearly has some effect. Perhaps if a detailed deposition study was done first, it could help direct a study on different metals.

There is a question that has not been addressed yet, being what is the thinnest layer of tungsten necessary to form fuzz? Perhaps only a few nm's are necessary for fuzz to form. This would have relevance in tokamaks where fuzz could grow at W deposition sites. Magnetron devices can easily create very thin tungsten films, complementing such a study. It is probable that W fuzz could be grown in the current setup using any material as the sample, as W could be deposited on the surface and then fuzz grow out of the deposited material.

The potential use of fuzzy W so far investigated in the literature has first made fuzz and then oxidised it afterwards, as tungsten oxide is more readily useful as a material

than pure tungsten. Perhaps, by seeding oxygen into the vacuum chamber whilst growing fuzz, the samples could be oxidised *in situ*, thereby creating a whole process in one of making fuzz and having it ready for application.

There is still the idea that fuzz could be used as a catalyst due to its high surface area. A collaboration with some departments well versed in catalysts would be great to develop these ideas. If not W, then an oxide thereof, or maybe another material that fuzz can be made on should be investigated.

If time was given on the PISCES devices again, there are several things that would be worth investigating. Firstly, it would be beneficial to add even more data to the compilation chart, encompassing the whole fluence range, and filling-in more of the gaps. More samples created at the extreme long fluences would also be of interest to confirm the results of the lone sample there. Equally, more experiments at low fluence should be sought after to confirm the existence of the incubation fluence. More data of fuzz grown in an erosive regime could complement the proposed erosion/growth equation. An important study is the competition of growth versus annealing. This could be attempted on a magnetron, but devices with higher fluxes allow a better study of this, as higher temperatures can be achieved and without the issue of deposition occurring. A study on the issues surrounding emissivity could be undertaken as their current setup uses thermocouples quite confidently. If an IR pyrometer was added, the changes of the reading on the pyrometer could be seen as the fuzz develops. Lastly, a study could be done looking at the differences between samples created in discrete exposures and those created in continuous exposures. This could complement such a study done on a magnetron, seeing if the differences still exist at higher fluences and fluxes.

Bibliography

[1] McCracken, G. and Scott, P. (2012) *Fusion: The Energy of the Universe*. Elsevier Science.

[2] The Jet Team (1992) Fusion energy production from a deuterium-tritium plasma in the JET tokamak. *Nuclear Fusion*, **32**, 187–203.

[3] Pitts, R., et al. (2011) Physics basis and design of the ITER plasma-facing components. *Journal of Nuclear Materials*, **415**, S957–S964.

[4] Chen, F. F. (2011) *An Indispensable Truth*. Springer.

[5] Guern, F. L. and Ciattaglia, S. (2011) R&D on in-Vessel Dust and Tritium Management in ITER. *2011 IEEE/NPSS 24th Symposium on Fusion Engineering*, pp. 1–5.

[6] Paméla, J., Matthews, G., Philipps, V., and Kamendje, R. (2007) An ITER-like wall for JET. *Journal of Nuclear Materials*, **363-365**, 1–11.

[7] Federici, G., Skinner, C., and Brooks, J. (2001) Plasma-material interactions in current tokamaks and their implications for next step fusion reactors. *Nuclear Fusion*, **41**, 1967.

[8] Nygren, R., Raffray, R., Whyte, D., Urickson, M., Baldwin, M., and Snead, L. (2011) Making tungsten work ICFRM-14 session T26 paper 501 Nygren et al. making tungsten work. *Journal of Nuclear Materials*, **417**, 451–456.

[9] Roth, J., Tsitrone, E., and Loarte, A. (2009) Recent analysis of key plasma wall interactions issues for ITER. *Journal of Nuclear Materials*, **390-391**, 1–9.

[10] Ihli, T., et al. (2008) Review of blanket designs for advanced fusion reactors. *Fusion Engineering and Design*, **83**, 912–919.

[11] Doerner, R., Baldwin, M., and Stangeby, P. (2011) An equilibrium model for tungsten fuzz in an eroding plasma environment. *Nuclear Fusion*, **51**, 043001.

[12] Takamura, S., Ohno, N., Nishijima, D., and Kajita, S. (2006) Formation of Nanostructured Tungsten with Arborescent Shape due to Helium Plasma Irradiation. *Plasma and Fusion Research*, **1**, 051.

[13] Zenobia, S. (2010) *Effects of helium ion implantation on the surface morphology of tungsten at high temperature for the first wall armor and divertor plates of fusion reactors*. Ph.D. thesis, The University of Wisconsin - Madison.

[14] Ueda, Y., Peng, H. Y., Lee, H. T., Ohno, N., Kajita, S., Yoshida, N., Doerner, R., De Temmerman, G., Alimov, V., and Wright, G. (2013) Helium effects on tungsten surface morphology and deuterium retention. *Journal of Nuclear Materials*, **442**, S267–S272.

[15] Ueda, Y., et al. (2011) Exposure of tungsten nano-structure to TEXTOR edge plasma. *Journal of Nuclear Materials*, **415**, S92–S95.

[16] Nishijima, D., Baldwin, M., Doerner, R., and Yu, J. (2011) Sputtering properties of tungsten fuzzy surfaces. *Journal of Nuclear Materials*, **415**, S96–S99.

[17] Kajita, S., Yokochi, T., Ohno, N., and Kumano, T. (2012) Near Infrared Radiation from Heated Nanostructured Tungsten. *Japanese Journal of Applied Physics*, **51**, 01AJ03.

[18] Baldwin, M. and Doerner, R. (2010) Formation of helium induced nanostructure fuzz on various tungsten grades. *Journal of Nuclear Materials*, **404**, 165–173.

[19] Kajita, S., Yoshida, N., Yoshihara, R., Ohno, N., and Yamagiwa, M. (2011) TEM observation of the growth process of helium nanobubbles on tungsten: Nanostructure formation mechanism. *Journal of Nuclear Materials*, **418**, 152–158.

[20] Baldwin, M. and Doerner, R. (2008) Helium induced nanoscopic morphology on tungsten under fusion relevant plasma conditions. *Nuclear Fusion*, **48**, 035001.

[21] Federici, G., Brooks, J., Coster, D., Janeschitz, G., Kukuskhin, A., Loarte, A., Pacher, H., Stober, J., and Wu, C. (2001) Assessment of erosion and tritium codeposition in ITER-FEAT. *Journal of Nuclear Materials*, **290-293**, 260–265.

[22] Haasz, A., Poon, M., and Davis, J. (1999) The effect of ion damage on deuterium trapping in tungsten. *Journal of nuclear materials*, **269**, 520–525.

[23] Preininger, D. and Ehrlich, K. (1981) The influence of helium bubble migration on the creep rupture behavior of first wall materials under thermal transients. *Journal of Nuclear Materials*, **104**, 91–95.

[24] Niwase, K., Ezawa, T., Tanabe, T., Kiritani, M., and Fujita, F. (1993) Dislocation loops and their depth profiles in He^+ and D^+ ion irradiated nickel. *Journal of Nuclear Materials*, **203**, 56–66.

[25] Ezawa, T., Sugimoto, M., Niwase, K., Sasaki, S., Iwase, A., Iwata, T., and Fujita, F. (1991) Depth distribution of damage in helium-ion and proton irradiated nickel. *Journal of Nuclear Materials*, **179-181**, 974–977.

[26] Gruber, E. E. (1967) Calculated size distributions for gas bubble migration and coalescence in solids. *Journal of Applied Physics*, **38**, 243–250.

[27] Ye, M. Y., Takamura, S., and Ohno, N. (1997) Study of hot tungsten emissive plate in high heat flux plasma on NAGDIS-I. *Journal of Nuclear Materials*, **241-243**, 1243–1247.

[28] Nishijima, D., Ye, M., Ohno, N., and Takamura, S. (2004) Formation mechanism of bubbles and holes on tungsten surface with low-energy and high-flux helium plasma irradiation in NAGDIS-II. *Journal of Nuclear Materials*, **329-333**, 1029–1033.

[29] Iwakiri, H., Yasunaga, K., Morishita, K., and Yoshida, N. (2000) Microstructure evolution in tungsten during low-energy helium ion irradiation. *Journal of Nuclear Materials*, **283-287**, 1134–1138.

[30] Ye, M., Fukuta, S., Ohno, N., Takamura, S., Tokunaga, K., and Yoshida, N. (2000) ; Modifications of Tungsten Irradiated by Low Energy and High Flux Helium Plasma. *Journal of Plasma Fusion Research*, **3**, 265–269.

[31] Tokunaga, K., Doerner, R., Seraydarian, R., Noda, N., Kubota, Y., Yoshida, N., Sogabe, T., Kato, T., and Schedler, B. (2003) Surface morphology and helium retention on tungsten exposed to low energy and high flux helium plasma. *Journal of Nuclear Materials*, **313-316**, 92–96.

[32] Baldwin, M. (2014). Personal communciation.

[33] Kajita, S., Sakaguchi, W., Ohno, N., Yoshida, N., and Saeki, T. (2009) Formation process of tungsten nanostructure by the exposure to helium plasma under fusion relevant plasma conditions. *Nuclear Fusion*, **49**, 095005.

[34] Sakaguchi, W., Kajita, S., Ohno, N., Takagi, M., and Kurishita, H. (2008) Formation condition of fiberform nanostructured tungsten by helium plasma exposure. *Proceedings of ITC18*, pp. 246–249.

[35] Miyamoto, M., Mikami, S., Nagashima, H., Iijima, N., Nishijima, D., Doerner, R., Yoshida, N., Watanabe, H., Ueda, Y., and Sagara, A. (2015) Systematic investigation of the formation behavior of helium bubbles in tungsten. *Journal of Nuclear Materials*, **463**, 333–336.

[36] Nishijima, D., Ye, M., Ohno, N., and Takamura, S. (2003) Incident ion energy dependence of bubble formation on tungsten surface with low energy and high flux helium plasma irradiation. *Journal of Nuclear Materials*, **313-316**, 97–101.

[37] Tokunaga, K., Tamura, S., Yoshida, N., Ezato, K., Taniguchi, M., Sato, K., Suzuki, S., and Akiba, M. (2004) Synergistic effects of high heat loading and helium irradiation of tungsten. *Journal of Nuclear Materials*, **329-333**, 757–760.

[38] Baldwin, M., Lynch, T., Doerner, R., and Yu, J. (2011) Nanostructure formation on tungsten exposed to low-pressure rf helium plasmas: A study of ion energy threshold and early stage growth. *Journal of Nuclear Materials*, **415**, S104–S107.

[39] Meyer, F. W., Hijazi, H., Bannister, M. E., Krstic, P. S., Dadras, J., Meyer, H. M., and Parish, C. M. (2014) He-ion and self-atom induced damage and surface-morphology changes of a hot W target. *Physica Scripta*, **T159**, 014029.

[40] Zenobia, S. J., Garrison, L. M., and Kulcinski, G. L. (2012) The response of polycrystalline tungsten to 30keV helium ion implantation at normal incidence and high temperatures. *Journal of Nuclear Materials*, **425**, 83–92.

[41] Lasa, A., Henriksson, K. O. E., and Nordlund, K. (2013) MD simulations of onset of tungsten fuzz formation under helium irradiation. *Nuclear Instruments and Methods in Physics Research Section B: Beam Interactions with Materials and Atoms*, **303**, 156–161.

[42] Kajita, S., Yoshida, N., Ohno, N., and Tsuji, Y. Growth of multifractal tungsten nanostructure by He bubble induced directional swelling. *New Journal of Physics*, **17**, 43038.

[43] Noiri, Y., Kajita, S., and Ohno, N. (2015) Nanostructure growth by helium plasma irradiation to tungsten in sputtering regime. *Journal of Nuclear Materials*, **463**, 285–288.

[44] Martynenko, Y. V. and Nagel, M. Y. (2012) Model of fuzz formation on a tungsten surface. *Plasma Physics Reports*, **38**, 996–999.

[45] Lasa, A., Tähtinen, S. K., and Nordlund, K. (2014) Loop punching and bubble rupture causing surface roughening A model for W fuzz growth. *EPL (Europhysics Letters)*, **105**, 25002.

[46] Pitts, R., et al. (2013) A full tungsten divertor for ITER: Physics issues and design status. *Journal of Nuclear Materials*, **438**, S48–S56.

[47] Dolan, T. (2014) *Magnetic Fusion Technology*. Lecture Notes in Energy, Springer.

[48] Wampler, W. R., Whyte, D. G., Wong, C. P. C., and West, W. P. (2001) Suppression of net erosion in the DIII-D divertor with detached plasmas. *Journal of Nuclear Materials*, **290-293**, 346–351.

[49] Ueda, Y., Coenen, J., De Temmerman, G., Doerner, R., Linke, J., Philipps, V., and Tsitrone, E. (2014) Research status and issues of tungsten plasma facing materials for ITER and beyond. *Fusion Engineering and Design*, **89**, 901–906.

[50] Brooks, J., Causey, R., Federici, G., and Ruzic, D. (1997) Assessment of erosion and surface tritium inventory issues for the ITER divertor. *Journal of Nuclear Materials*, **241-243**, 294–298.

[51] Brooks, J., Allain, J., Doerner, R., Hassanein, A., Nygren, R., Rognlien, T., and Whyte, D. (2009) Plasma–surface interaction issues of an all-metal ITER. *Nuclear Fusion*, **49**, 035007.

[52] Krasheninnikov, S. I. (2011) Viscoelastic model of tungsten fuzz growth. *Physica Scripta*, **T145**, 014040.

[53] Connor, J. W., Kirk, A., Wilson, H. R., and Benkadda, S. (2008) Edge localised modes (ELMs): Experiments and theory. *AIP Conferenc Proceedings*, vol. 174, pp. 174–190.

[54] Zohm, H. (1996) Edge localized modes (ELMs). *Plasma Physics and Controlled Fusion*, **38**, 105–128.

[55] Kajita, S., Takamura, S., Ohno, N., Nishijima, D., Iwakiri, H., and Yoshida, N. (2007) Sub-ms laser pulse irradiation on tungsten target damaged by exposure to helium plasma. *Nuclear Fusion*, **47**, 1358–1366.

[56] Kajita, S., De Temmerman, G., Morgan, T., Van Eden, S., de Kruif, T., and Ohno, N. (2014) Thermal response of nanostructured tungsten. *Nuclear Fusion*, **54**, 033005.

[57] Kajita, S., Kitaoka, D., Ohno, N., Yoshihara, R., Yoshida, N., and Yoshida, T. (2014) Surface modification of titanium using He plasma. *Applied Surface Science*, **303**, 438–445.

[58] Kajita, S., Takamura, S., and Ohno, N. (2009) Prompt ignition of a unipolar arc on helium irradiated tungsten. *Nuclear Fusion*, **49**, 032002.

[59] Tokitani, M., Kajita, S., Masuzaki, S., Hirahata, Y., Ohno, N., and Tanabe, T. (2011) Exfoliation of the tungsten fibreform nanostructure by unipolar arcing in the LHD divertor plasma. *Nuclear Fusion*, **51**, 102001.

[60] Kajita, S., Ohno, N., and Takamura, S. (2011) Tungsten blow-off in response to the ignition of arcing: Revival of arcing issue in future fusion devices. *Journal of Nuclear Materials*, **415**, S42–S45.

[61] Aussems, D., Nishijima, D., Brandt, C., Van Der Meiden, H., Vilémová, M., Matějíček, J., De Temmerman, G., Doerner, R., and Lopes Cardozo, N. (2015) The occurrence and damage of unipolar arcing on fuzzy tungsten. *Journal of Nuclear Materials*, **463**, 2–6.

[62] Baldwin, M., Doerner, R., Wampler, W., Nishijima, D., Lynch, T., and Miyamato, M. (2011) Effect of He on D retention in W exposed to low-energy, high-fluence (D, He, Ar) mixture plasmas. *Nuclear Fusion*, **51**, 103021.

[63] Nishijima, D., Sugimoto, T., Iwakiri, H., Ye, M. Y., Ohno, N., Yoshida, N., and Takamura, S. (2005) Characteristic changes of deuterium retention on tungsten surfaces due to low-energy helium plasma pre-exposure. *Journal of Nuclear Materials*, **337-339**, 927–931.

[64] Takamura, S., Miyamoto, T., and Ohno, N. (2012) Effects of fibre-form nanostructures on particle emissions from a tungsten surface in plasmas. *Nuclear Fusion*, **52**, 123001.

[65] Nishijima, D., Kikuchi, Y., Nakatsuka, M., Baldwin, M., Doerner, R., Nagata, M., and Ueda, Y. (2011) Effects of Pre-Plasma Exposure on Tungsten Surface Cracking Due to ELM-like Pulsed Plasma Bombardment D. Nishijima. *Fusion Science and Technology*, **60**, 1447.

[66] Takamura, S., Miyamoto, T., Tomida, Y., Minagawa, T., and Ohno, N. (2011) Investigation on the effect of temperature excursion on the helium defects of tungsten surface by using compact plasma device. *Journal of Nuclear Materials*, **415**, S100–S103.

[67] Takamura, S. (2015) Radiative Cooling Properties of He-Defected Tungsten with Fiber-Form Nanostructured Surface. *Journal of Nuclear Materials*, **466**, 239–242.

[68] Takamura, S., Miyamoto, T., and Ohno, N. (2010) Deepening of Floating Potential for Tungsten Target Plate on the way to Nanostructure Formation. *Plasma and Fusion Research*, **5**, 039.

[69] Kajita, S., Saeki, T., Yoshida, N., Ohno, N., and Iwamae, A. (2010) Nanostructured Black Metal: Novel Fabrication Method by Use of Self-Growing Helium Bubbles. *Applied Physics Express*, **3**, 085204.

[70] De Respinis, M., De Temmerman, G., Tanyeli, I., Van De Sanden, M. C. M., Doerner, R. P., Baldwin, M. J., and Van De Krol, R. (2013) Efficient plasma route to nanostructure materials: case study on the use of m-WO3 for solar water splitting. *ACS applied materials & interfaces*, **5**, 7621–7625.

[71] Kajita, S., Yoshida, T., Kitaoka, D., Etoh, R., Yajima, M., Ohno, N., Yoshida, H., Yoshida, N., and Terao, Y. (2013) Helium plasma implantation on metals: Nanostructure formation and visible-light photocatalytic response. *Journal of Applied Physics*, **113**, 134301.

[72] Sefta, F., Hammond, K. D., Juslin, N., and Wirth, B. D. (2013) Tungsten surface evolution by helium bubble nucleation, growth and rupture. *Nuclear Fusion*, **53**, 073015.

[73] Smirnov, R. and Krasheninnikov, S. (2013) On the shear strength of tungsten nanostructures with embedded helium. *Nuclear Fusion*, **53**, 082002.

[74] Ito, A. M., Yoshimoto, Y., Saito, S., Takayama, A., and Nakamura, H. (2014) Molecular dynamics simulation of a helium bubble bursting on tungsten surfaces. *Physica Scripta*, **T159**, 014062.

[75] Hu, L., Hammond, K. D., Wirth, B. D., and Maroudas, D. (2014) Dynamics of Small Mobile Helium Clusters near Tungsten Surfaces. *Surface Science*, **626**, L21–L25.

[76] Li, X.-C., Shu, X., Tao, P., Yu, Y., Niu, G.-J., Xu, Y., Gao, F., and Luo, G.-N. (2014) Molecular dynamics simulation of helium cluster diffusion and bubble formation in bulk tungsten. *Journal of Nuclear Materials*, **455**, 544–548.

[77] Ferroni, F., Hammond, K. D., and Wirth, B. D. (2015) Sputtering yields of pure and helium-implanted tungsten under fusion-relevant conditions calculated using molecular dynamics. *Journal of Nuclear Materials*, **458**, 419–424.

[78] Kobayashi, R., Hattori, T., Tamura, T., and Ogata, S. (2015) A molecular dynamics study on bubble growth in tungsten under helium irradiation. *Journal of Nuclear Materials*, **463**, 1071–1074.

[79] Smirnov, R., Krasheninnikov, S., and Guterl, J. (2015) Atomistic modeling of growth and coalescence of helium nano-bubbles in tungsten. *Journal of Nuclear Materials*, **463**, 359–362.

[80] Takayama, A., Ito, A. M., Seiki, S., Ohno, N., and Nakamura, H. (2013) First-Principles Investigation on Trapping of Multiple Helium Atoms within a Tungsten Monovacancy First-Principles Investigation on Trapping of Multiple Helium Atoms within a Tungsten Monovacancy. *Japanese Journal of Applied Physics*, **52**, 01AL03.

[81] Takayama, A., Ito, A., Oda, Y., and Nakamura, H. (205) First principles investigation of cluster consisting of hydrogenhelium atoms interstitially-trapped in tungsten. *Journal of Nuclear Materials*, **463**, 355–358.

[82] Saito, S., Takayama, A., Ito, A. M., and Nakamura, H. (2013) Binary-collision-approximation-based simulation of noble gas irradiation to tungsten materials. *Journal of Nuclear Materials*, **438**, S895–S898.

[83] Henriksson, K. O. E., Nordlund, K., Krasheninnikov, A., and Keinonen, J. (2005) Difference in formation of hydrogen and helium clusters in tungsten. *Applied Physics Letters*, **87**, 1–3.

[84] Ito, A., et al. (2015) Molecular dynamics and Monte Carlo hybrid simulation for fuzzy tungsten nanostructure formation. *Nuclear Fusion*, **55**, 073013.

[85] Takamura, S. (2014) Initial Stage of Fiber-Form Nanostructure Growth on Refractory Metal Surfaces with Helium Plasma Irradiation. *Plasma and Fusion Research: Letters*, **9**, 1302007.

[86] Tanyeli, I., Marot, L., Van De Sanden, M. C. M., and De Temmerman, G. (2014) Nanostructuring of iron surfaces by low-energy helium ions. *ACS applied materials & interfaces*, **6**, 3462–3468.

[87] Mantenieks, M. A. (1999) Sputtering Threshold Energies of Heavy Ions. *NASA technical memorandum*, p. 209273.

[88] Hotston, E. (1975) Threshold energies for sputtering. *Nuclear Fusion*, **15**, 544–547.

[89] Tanyeli, I., Marot, L., Mathys, D., Van De Sanden, M. C. M., and De Temmerman, G. (2015) Surface Modifications Induced by High Fluxes of Low Energy Helium Ions. *Scientific Reports*, **5**, 9779.

[90] Kajita, S., Saeki, T., Ohno, N., Tokitani, M., Hatae, T., and Sakaguchi, W. (2011) Degradation of optical reflectivity of in-vessel mirror materials by helium bombardment. *Journal of Nuclear Materials*, **417**, 838–841.

[91] Goebel, D., Campbell, G., and Conn, R. (1984) Plasma surface interaction experimental facility (PISCES) for materials and edge physics studies. *Journal of Nuclear Materials*, **121**, 277–282.

[92] Hirooka, Y. (1990) A new plasma-surface interactions research facility: PISCES-B and first materials erosion experiments on bulk-boronized graphite. *Journal of Vacuum Science & Technology A: Vacuum, Surfaces, and Films*, **8**, 1790.

[93] Ohno, N., et al. (2001) Static and dynamic behaviour of plasma detachment in the divertor simulator experiment NAGDIS-II. *Nuclear Fusion*, **41**, 1055–1065.

[94] Van Rooij, G. J., et al. (2007) Extreme hydrogen plasma densities achieved in a linear plasma generator. *Applied Physics Letters*, **90**, 121501.

[95] De Groot, B., Ahmad, Z., Dahiya, R. P., Engeln, R., Goedheer, W. J., Lopes Cardozo, N. J., and Veremiyenko, V. (2003) Magnum-psi, a new linear plasma generator for plasma-surface interaction studies in ITER relevant conditions. *Fusion Engineering and Design*, **66-68**, 413–417.

[96] Clement, S., Chankin, A., Ciric, D., Coad, J. P., Falter, J., Gauthier, E., Lingertat, J., and Puppin, S. (1999) Power deposition in the JET divertor during ELMs. *Journal of Nuclear Materials*, **266-269**, 285–290.

[97] Andrew, P., Coad, J., Corre, Y., Eich, T., Herrmann, A., Matthews, G., Paley, J., Pickworth, L., Pitts, R., and Stamp, M. (2005) Outer divertor target deposited layers during reversed magnetic field operation in JET. *Journal of Nuclear Materials*, **337-339**, 99–103.

[98] Gentile, C. A., et al. (1997) The operation of the TFTR tritium system. *Fusion Engineering, 1997. 17th IEEE/NPSS Symposium*, pp. 283–285.

[99] Wright, G., Brunner, D., Baldwin, M., Doerner, R., Labombard, B., Lipschultz, B., Terry, J., and Whyte, D. (2012) Tungsten nano-tendril growth in the Alcator C-Mod divertor. *Nuclear Fusion*, **52**, 042003.

[100] Marmar, E. S. and the Alcator C-Mod team (2007) The Alcator C-Mod Program. *Fusion Science and Technology*, **51**, 261–265.

[101] Wong, C. P. C. (2013), Exposure of W-fuzz to Vertical Displacement Events in DIII-D. Presentation at the 14th PFMC conference in Jülich, Germany.

[102] Kajita, S., Ohno, N., Yajima, M., and Kato, J. (2013) Growth annealing equilibrium of tungsten nanostructures by helium plasma irradiation in non-eroding regimes. *Journal of Nuclear Materials*, **440**, 55–62.

[103] Meyer, F. W., Hijazi, B. M. E., H, Unocic, K. A., Garrison, L. M., and Parish, C. M. (2015), Flux threshold measurements of He-ion beam induced nano-fuzz formation on hot tungsten surfaces. presentation at the 15th PFMC conference in Aix-en-provence, France.

[104] Baldwin, M., Doerner, R., Nishijima, D., Tokunaga, K., and Ueda, Y. (2009) The effects of high fluence mixed-species (deuterium, helium, beryllium) plasma interactions with tungsten. *Journal of Nuclear Materials*, **390-391**, 886–890.

[105] Miyamoto, M., Nishijima, D., Baldwin, M., Doerner, R., Ueda, Y., and Sagara, A. (2013) Influence of Be seeding on microstructures of tungsten exposed to D-He mixture plasmas in PISCES and its impacts on retention properties. *Journal of Nuclear Materials*, **438**, 979–982.

[106] Al-Ajlony, A., Tripathi, J. K., and Hassanein, A. (2015) Role of carbon impurities on the surface morphology evolution of tungsten under high dose helium ion irradiation. *Journal of Nuclear Materials*, **466**, 569–575.

[107] Chen, F. F. (2010) *Introduction to Plasma Physics and Controlled Fusion*. Springer.

[108] Yamamura, Y. and Tawara, H. (1996) Energy dependence of ion-induced sputtering yields from monatomic solids at normal incidence. *Atomic Data and Nuclear Data Tables*, **62**, 149–253.

[109] Kelly, P. and Arnell, R. (2000) Magnetron sputtering: a review of recent developments and applications. *Vacuum*, **56**, 159–172.

[110] Mott-Smith, H. M. and Langmuir, I. (1926) The theory of collectors in gaseous discharges. *Physical Review*, **28**, 727–763.

[111] Merlino, R. L. (2007) Understanding Langmuir probe current-voltage characteristics. *American Journal of Physics*, **75**, 1078.

[112] Lieberman, M. and Lichtenberg, A. (2005) *Principle of Plasma Discharges and Materials Processing*. Wiley.

[113] Wiese, R., Kersten, H., Wiese, G., and Bartsch, R. (2015) Energy influx measurements with an active thermal probe in plasma-technological processes. *EPJ Techniques and Instrumentation*, **2**, 2.

[114] Lee, S., Chen, Y., and Hung, j. . I. p. . . t. . T. u. . h. v. . . y. . ., J.-C. .

[115] Reyntjens, S. and Puers, R. (2000) Focused ion beam induced deposition: fabrication of three-dimensional microstructures and young's modulus of the deposited material. *Journal of Micromechanics and Microengineering*, **10**, 181.

[116] Taylor, K. J., Yun, S., and Tynan, G. R. (2004) Control of plasma parameters by using noble gas admixtures. *Journal of Vacuum Science & Technology A: Vacuum, Surfaces, and Films*, **22**, 2131.

[117] Yun, S., Taylor, K., and Tynan, G. R. (2000) Measurement of radial neutral pressure and plasma density profiles in various plasma conditions in large-area high-density plasma sources. *Physics of Plasmas*, **7**, 3448.

[118] Tynan, G. R. (1997) Characterization of an azimuthally symmetric helicon wave high density plasma source. *Journal of Vacuum Science & Technology A: Vacuum, Surfaces, and Films*, **15**, 2885.

[119] Virostko, P., Tichý, M., Hunicka, Z., and Adámek, P. (2007) Measuring the Ion Current to the Substrate During Deposition of Thin Films by Hollow Cathode Plasma Jet. *WDS'07 Proceedings of Contributed Papers, Part II*, pp. 212–217.

[120] Pauleau, Y. and Barna, P. (1996) *Protective Coatings and Thin Films: Synthesis, Characterization, and Applications*. NATO ASI series 3, Springer Netherlands.

[121] Bornholdt, S., Itagaki, N., Kuwahara, K., Wulff, H., Shiratani, M., and Kersten, H. (2013) Characterization of the energy flux toward the substrate during magnetron sputter deposition of ZnO thin films. *Plasma Sources Science and Technology*, **22**, 025019.

[122] Petty, T. J. and Bradley, J. W. (2014) Tungsten nanostructure formation in a magnetron sputtering device. *Journal of Nuclear Materials*, **453**, 320–322.

[123] Kajita, S., Saeki, T., Hirahata, Y., Yajima, M., Ohno, N., Yoshihara, R., and Yoshida, N. (2011) Development of Nanostructured Black Metal by Self-Growing Helium Bubbles for Optical Application. *Japanese Journal of Applied Physics*, **50**, 08JG01.

[124] Kajita, S., Yoshida, N., Yoshihara, R., Ohno, N., Yokochi, T., Tokitani, M., and Takamura, S. (2012) TEM analysis of high temperature annealed W nanostructure surfaces. *Journal of Nuclear Materials*, **421**, 22–27.

[125] Langley, R., Bohdansky, J., Eckstein, W., Mioduszewski, P., Roth, J., Taglauer, E., Thomas, E., Verbeek, H., and Wilson, K. (1984) Data Compendium for Plasma-Surface Interactions. *Nuclear Fusion*, **24**, S9–S117.

[126] Kudriavtsev, Y., Villegas, A., Godines, A., and Asomoza, R. (2005) Calculation of the surface binding energy for ion sputtered particles. *Applied Surface Science*, **239**, 273–278.

[127] Eckstein, W. (2002) *Calculated Sputtering, Reflection and Range Values*. Max-Planck-Institut für Plasmaphysik.

[128] Danielson, R. and Sutherland, P. (1986) *Methods of Soil Analysis: Part 1 - Physical and Mineralogical Methods*. Soil Science Society of America, American Society of Agronomy.

[129] Wolfram Research, Inc. (2015) *Mathematica 10.1*. Wolfram Research, Inc.

[130] Corless, R. M., Gonnet, G. H., Hare, D. E. G., Jeffrey, D. J., and Knuth, D. E. (1996) On the Lambert W function. *Advances in Computational Mathematics*, **5**, 329–359.

[131] Nishijima, D., Doerner, R. P., Baldwin, M. J., and De Temmerman, G. (2009) Erosion yields of deposited beryllium layers. *Journal of Nuclear Materials*, **390-391**, 132–135.

[132] Doerner, R. P., Björkas, C., Nishijima, D., and Schwarz-Selinger, T. (2013) Erosion of beryllium under high-flux plasma impact. *Journal of Nuclear Materials*, **438**, S272–S275.

[133] Doerner, R., Grossman, A., Luckhardt, S., Seraydarian, R., Sze, F., Whyte, D., and Conn, R. (1998) Response of beryllium to deuterium plasma bombardment. *Journal of Nuclear Materials*, **257**, 51–58.

[134] Bolt, H., Barabash, V., Krauss, W., Linke, J., Neu, R., Suzuki, S., and Yoshida, N. (2004) Materials for the plasma-facing components of fusion reactors. *Journal of Nuclear Materials*, **329-333**, 66–73.

[135] Wright, G., et al. (2013) Comparison of tungsten nano-tendrils grown in Alcator C-Mod and linear plasma devices. *Journal of Nuclear Materials*, **438**, S84–S89.

[136] De Temmerman, G., Bystrov, K., Zielinski, J. J., Balden, M., Matern, G., Arnas, C., and Marot, L. (2012) Nanostructuring of molybdenum and tungsten surfaces by low-energy helium ions. *Journal of Vacuum Science & Technology A: Vacuum, Surfaces, and Films*, **30**, 041306.

[137] El-Atwani, O., Hattar, K., Hinks, J., Greaves, G., Harilal, S., and Hassanein, A. (2015) Helium bubble formation in ultrafine and nanocrystalline tungsten under different extreme conditions. *Journal of Nuclear Materials*, **458**, 216–223.

[138] Fan, H., Yang, Q., Li, X., Ni, W., Niu, J., and Liu, D. (2015) Microscopic Damage of Tungsten and Molybdenum Exposed to Low-Energy Helium Ions. *Plasma Science and Technology*, **17**, 331–336.

[139] Tiron, V., Andrei, C., Nastuta, A., Rusu, G., Vitelaru, C., and Popa, G. (2009) Carbon and Tungsten Sputtering in a Helium Magnetron Discharge. *IEEE Transactions on Plasma Science*, **37**, 1581–1585.

[140] El-Atwani, O., Gonderman, S., Suslov, S., Efe, M., Temmerman, G. D., Morgan, T., Bystrov, K., Hattar, K., and Allain, J. P. (2015) Early stage damage of ultrafine-grained tungsten materials exposed to low energy helium ion irradiation. *Fusion Engineering and Design*, **93**, 9–14.

[141] Woller, K., Whyte, D., and Wright, G. (2015) Dynamic measurement of the helium concentration of evolving tungsten nanostructures using Elastic Recoil Detection during plasma exposure. *Journal of Nuclear Materials*, **463**, 289–293.

[142] Iyyakkunnel, S., Marot, L., Eren, B., Steiner, R., Moser, L., Mathys, D., Düggelin, M., Chapon, P., and Meyer, E. (2014) Morphological changes of tungsten surfaces by low-flux helium plasma treatment and helium incorporation via magnetron sputtering. *ACS Applied Materials and Interfaces*, **6**, 11609–11616.

[143] Carter, D. and Walde, H. (2002) Parameter optimization in pulsed DC reactive sputter deposition of aluminum oxide. *45th Annual Technical Conferenc Proceedings. Society of Vacuum Coaters*, pp. 570–577.

[144] Bradley, J. W. and Welzel, T. (2009) Physics and phenomena in pulsed magnetrons: an overview. *Journal of Physics D: Applied Physics*, **42**, 093001.

[145] Stewart, D., Osetskiy, Y., and Stoller, R. (2011) Atomistic studies of formation and diffusion of helium clusters and bubbles in BCC iron. *Journal of Nuclear Materials*, **417**, 1110–1114.

[146] Sakaguchi, W., Kajita, S., Ohno, N., and Takagi, M. (2009) In situ reflectivity of tungsten mirrors under helium plasma exposure. *Journal of Nuclear Materials*, **390-391**, 1149–1152.

[147] Yonehara, M., Matsui, T., Kihara, K., Isono, H., Kijima, A., and Sugibayashi, T. (2004) Experimental Relationships between Surface Roughness, Glossiness and Color of Chromatic Colored Metals. *Materials Transactions*, **45**, 1027–1032.

[148] Bennet, H. and Porteus, J. (1961) Relation between surface roughness and specular reflectance at normal incidence. *Journal of the Optical Society of America*, **51**, 123–129.

[149] Kajita, S., Yoshida, N., Ohno, N., Hirahata, Y., and Yoshihara, R. (2014) Helium plasma irradiation on single crystal tungsten and undersized atom doped tungsten alloys. *Physica Scripta*, **89**, 025602.

[150] Kajita, S., Tokitani, M., Saeki, T., Ohno, N., and Yoshida, N. (2013) Low-energy helium irradiation on in-vessel mirror materials. *Journal of Nuclear Materials*, **442**, S515–S519.

[151] Komori, K., Yoshida, T., Yagi, S., Yoshida, H., Yajima, M., Kajita, S., and Ohno, N. (2014) Application of Nanostructured Tungsten Fabricated by Helium Plasma Irradiation for Photoinduced Decolorization of Methylene Blue. *e-Journal of Surface Science and Nanotechnology*, **12**, 343–348.

[152] Kajita, S., Ohno, N., Yokochi, T., Yoshida, N., Yoshihara, R., Takamura, S., and Hatae, T. (2012) Optical properties of nanostructured tungsten in near infrared range. *Plasma Physics and Controlled Fusion*, **54**, 105015.

[153] De Temmerman, G., Bystrov, K., Doerner, R., Marot, L., Wright, G., Woller, K., Whyte, D., and Zielinski, J. (2013) Helium effects on tungsten under fusion-relevant plasma loading conditions. *Journal of Nuclear Materials*, **438**, S78–S83.

Appendices

Appendix A

Solving the Lambert W Function

A.1 The erosion parameter ϵ_{f}

The rate of volume loss is given by,

$$\frac{\partial V}{\partial t} = -A\frac{\partial z}{\partial t} \tag{A.1}$$

where V is the volume, t is time, A is the surface area, and z is the thickness lost, with $\partial z/\partial t = E$, the erosion rate or velocity.

From the integral form of the continuity equation we have,

$$\frac{\partial}{\partial t}\iiint_{V} n_{\mathrm{f}}\mathrm{d}V = -\oiint_{S}\Gamma\mathrm{d}A \tag{A.2}$$

where V is the volume, n_{f} is the number density of a fuzzy layer, and S is the contour of the surface. The density is constant, so that can be brought outside the integral on the left-hand-side, and on the right-hand-side, the flux loss is constant over the area, giving,

$$n_{\mathrm{f}}\frac{\partial V}{\partial t} = -\Gamma A \tag{A.3}$$

Equating $\partial V/\partial T = -AE$ as in equation (A.1) with equation (A.3) gives,

$$-nAE = -\Gamma A \tag{A.4}$$

Re-arranging for Γ, we have,

$$\Gamma = n_{\mathrm{f}}E \tag{A.5}$$

As was discussed in section 5.4.1, equation (5.6) relates the bombarding flux to the sputtered flux, reproduced below for convenience,

$$Y\Gamma_{\mathrm{in}} = \Gamma_{\mathrm{out}} \tag{A.6}$$

where Y is the sputter yield, Γ_{in} is the incoming flux of He ions onto the sample, and Γ_{out} is the flux of W atoms being sputtered out.

Flux can be written as $\Gamma = nv$, in this case the velocity v can be replaced by E, giving,

$$Y\Gamma_{\text{in}} = n_{\text{f}}E \tag{A.7}$$

Re-arranging for E/Γ we have,

$$\frac{E}{\Gamma} = \frac{Y}{n_{\text{f}}} \tag{A.8}$$

the bulk number density, n_{b} is equal to the number of atoms in a mole, N_{A}, divided by the volume of a mole, V_{mol}, i.e.

$$n_{\text{b}} = \frac{N_{\text{A}}}{V_{\text{mol}}} \tag{A.9}$$

As porosity can be defined as [128]:

$$p_{\text{f}} = 1 - \frac{n_{\text{f}}}{n_{\text{b}}} \tag{A.10}$$

where p_{f} is the porosity of a fuzzy layer, n_{f} is the number density of a fuzzy layer. This can be re-arranged for n_{f} as,

$$n_{\text{f}} = (1 - p_{\text{f}})n_{\text{b}} \tag{A.11}$$

By subbing equation (A.9) into (A.11), n_{f} can be given as,

$$n_{\text{f}} = (1 - p_{\text{f}})\frac{N_{\text{A}}}{V_{\text{mol}}} \tag{A.12}$$

Subbing this back into (A.8) gives,

$$\frac{E}{\Gamma} = \frac{Y}{(1 - p_{\text{f}})}\frac{V_{\text{mol}}}{N_{\text{A}}} \tag{A.13}$$

As $\epsilon_{\text{f}} = E/\Gamma$ by definition, this gives,

$$\epsilon_{\text{f}} = \frac{Y}{(1 - p_{\text{f}})}\frac{V_{\text{mol}}}{N_{\text{A}}} \tag{A.14}$$

A.2 Solving the integration

The integration constant A can be found by applying boundary condition that the fuzz does not grow until the incubation fluence is exceeded, i.e. $\Phi > \Phi_0$, giving the boundary condition $x(\Phi_0) = 0$. Setting this in equation (5.16), gives,

$$x(\Phi_0) = \frac{C}{2\epsilon_{\text{f}}}\left(W\left[-\frac{1}{C}\exp\left(\frac{-2\epsilon_{\text{f}}^2}{C}(\Phi_0 + \text{A}) - 1\right)\right] + 1\right) = 0 \tag{A.15}$$

This is satisfied if $W[z] = -1$, with z being the function inside the Lambert W function. This actually is a special case for the Lambert W function, as by definition,

$$W[-e^{-1}] = -1 \tag{A.16}$$

Hence we setting $z = -e^{-1}$ gives $W[z] = -1$.

$$-\frac{1}{C}\exp\left(\frac{-2\epsilon_f^2}{C}(\Phi_0 + A) - 1\right) = -e^{-1} \tag{A.17}$$

Solving this for A can be done via the following steps,

$$\begin{aligned}
\exp\left(\frac{-2\epsilon_f^2}{C}(\Phi_0 + A) - 1\right) &= Ce^{-1} \\
\frac{-2\epsilon_f^2}{C}(\Phi_0 + A) - 1 &= \ln(Ce^{-1}) \\
\frac{-2\epsilon_f^2}{C}(\Phi_0 + A) - 1 &= \ln C - \ln e \\
-2\epsilon_f^2(\Phi_0 + A) - C &= C\ln C - C \\
-2\epsilon_f^2\Phi_0 - 2\epsilon_f^2 A &= C\ln C \\
2\epsilon_f^2 A &= -2\epsilon_f^2\Phi_0 - C\ln C \\
A &= -\Phi_0 - \frac{C\ln C}{2\epsilon_f^2}
\end{aligned}$$

Substituting A back into the general solution of equation (5.16) gives,

$$\begin{aligned}
x(\Phi_0) &= \frac{C}{2\epsilon_f}\left(W\left[-\frac{1}{C}\exp\left(\frac{-2\epsilon_f^2}{C}(\Phi - \Phi_0 - \frac{C\ln C}{2\epsilon_f^2}) - 1\right)\right] + 1\right) \\
&= \frac{C}{2\epsilon_f}\left(W\left[-\frac{1}{C}\exp\left(\frac{-2\epsilon_f^2}{C}(\Phi - \Phi_0) + \ln C - 1\right)\right] + 1\right) \\
&= \frac{C}{2\epsilon_f}\left(W\left[-\frac{1}{C}\exp(\ln C)\exp\left(\frac{-2\epsilon_f^2}{C}(\Phi - \Phi_0) - 1\right)\right] + 1\right)
\end{aligned}$$

Giving the general solution as,

$$x(\Phi_0) = \frac{C}{2\epsilon_f}\left(W\left[-\exp\left(\frac{-2\epsilon_f^2}{C}(\Phi - \Phi_0) - 1\right)\right] + 1\right) \tag{A.18}$$

A.3 When $\epsilon_f = 0$

Beginning where appendix A left off with equation (A.18), for ease let β be defined as,

$$\beta = \exp\left(\frac{-2\epsilon_f^2}{C}(\Phi - \Phi_0)\right) \tag{A.19}$$

such that the Lambert W function part of equation (A.18) can be written as,

$$W\left[-\exp\left(\frac{-2\epsilon_f^2}{C}(\Phi - \Phi_0)\right)e^{-1}\right] = W[-\beta e^{-1}] \tag{A.20}$$

Following the methodology in [130], the Lambert W function can be expanded by a power series to give,

$$W[-\beta e^{-1}] = -1 + \sqrt{2(1-\beta)} - \frac{2}{3}(1-\beta) + \ldots \tag{A.21}$$

As the series expands, the factor $(1-\beta)$ increases in power by a factor of $\frac{1}{2}$ for each additional term, but as $\epsilon_f \to 0$, $\beta \to 1$, meaning that higher order terms become increasingly small. Therefore the expression is truncated to the first two terms. In a similar fashion, a Taylor series expansion can be performed on β as,

$$\beta = 1 - \frac{2\epsilon_f^2}{C}(\Phi - \Phi_0) + \left(\frac{2\epsilon_f^2}{C}(\Phi - \Phi_0)\right)^2 - \ldots \tag{A.22}$$

where again, as $\epsilon_f \to 0$, the higher order terms are increasingly small. Taking only the first two terms of (A.22), and substituting this expression into (A.21) gives (for small $\epsilon_f \to 0$),

$$\begin{aligned} W[-\beta e^{-1}] &\approx -1 + \left[2\left(1 - 1 + \frac{2\epsilon_f^2}{C}(\Phi - \Phi_0)\right)\right]^{\frac{1}{2}} \\ W[-\beta e^{-1}] &\approx -1 + \left(\frac{4\epsilon_f^2}{C}(\Phi - \Phi_0)\right)^{\frac{1}{2}} \end{aligned} \tag{A.23}$$

Substituting the result of equation (A.23) into (A.18) results in,

$$\begin{aligned} x(\Phi) &\approx \frac{C}{2\epsilon_f}\left(-1 + \left(\frac{4\epsilon_f^2}{C}(\Phi - \Phi_0)\right)^{\frac{1}{2}} + 1\right) \\ &\approx \frac{C}{2\epsilon_f}\left(\frac{4\epsilon_f^2}{C}(\Phi - \Phi_0)\right)^{\frac{1}{2}} \\ &\approx (C(\Phi - \Phi_0))^{\frac{1}{2}} \end{aligned} \tag{A.24}$$

Thus, as $\epsilon_f \to 0$, equation (A.24) is obtained, or the approximation of equation (5.11).

Appendix B

SEM Images of the Cross-Section of Fuzz

SEM images were taken of the cross-sections of the fuzz layers after milling out a trench as described in section 3.6.6. The images were taken of the three different parameter sweeps performed in chapter 6. In figure B.1 is the time sweep.

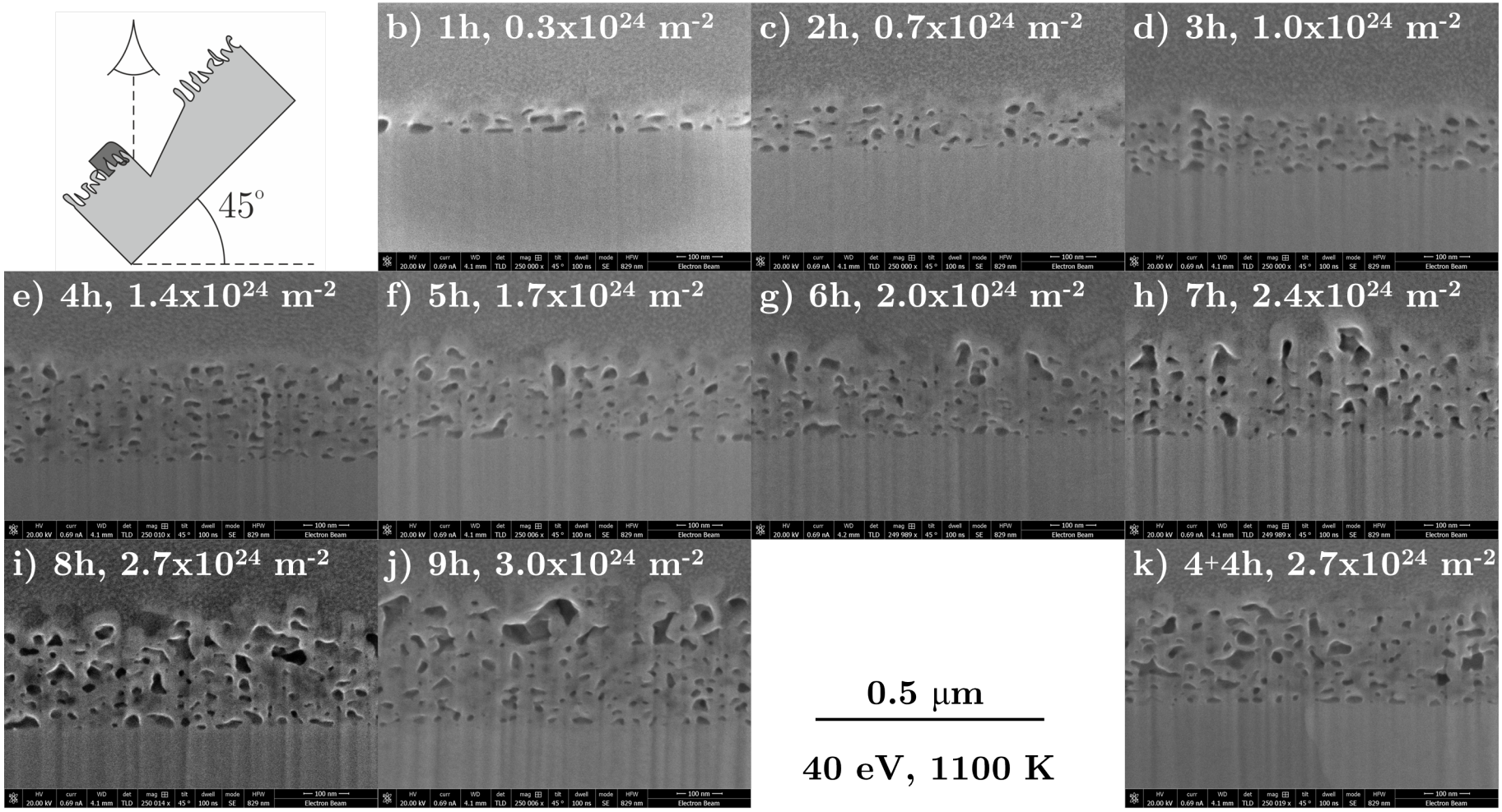

Figure B.1. SEM images of the cross-section of the fuzz layers after milling out a trench. The observation of the samples in the SEM is shown in the top left. The samples are tilted 45° so any measurements in these images should be multiplied by $\sqrt{2}$ to account for the tilting. Images are taken at 250,000× magnification and the scale bar is shown inbetween images j and k is almost the same in each sample.

Appendix C

Mean Free Path Versus Sheath Thickness

In this section the mean free path and the sheath thickness in the magnetron device are calculated and compared. This is important to be able to consider the sheath surrounding the samples as collison-less. Otherwise the energy of the He ions must be further investigated.

C.1 Mean free path

Introduced in section 2.2, equation (2.3) gives a simple expression for the mean free path, reproduced here,

$$\lambda_{\mathrm{m}} = \frac{1}{n_{\mathrm{n}}\sigma} \tag{C.1}$$

where λ_{m} is the mean free path, n_{n} is the density of neutral atoms per m^3, and σ is the cross-sectional area of the neutral atoms.

The gas pressure used for all the experiments in chapter 6 was maintained at 40 mTorr = 5.33 Pa. This can be converted to density via the ideal gas equation,

$$n_{\mathrm{n}} = \frac{P}{k_{\mathrm{B}}T} \tag{C.2}$$

where P is the pressure, k_{B} is the Boltzmann constant, and T is the temperature of the gas. Assuming the gas is at room temperature, this gives,

$$\begin{aligned} n_{\mathrm{n}} &= \frac{5.3}{1.38 \times 10^{-23} \cdot 300} \\ &= 1.28 \times 10^{21} \end{aligned}$$

A value of the cross-section can be simply estimated via,

$$\sigma = \pi r^2 \tag{C.3}$$

where r is the radius of the He atoms, being 31 pm, this gives $\sigma = 3.0{\times}10^{-21}$ m^2.

Substituting these values into the equation for the λ_m in (C.1) gives,

$$\begin{aligned}\lambda_m &= \frac{1}{1.28 \times 10^{21} \cdot 3.0 \times 10^{-21}} \\ &= 0.26 \text{ m}\end{aligned}$$

C.2 Sheath thickness

The Debye length gives an indication of the sheath thickness, introduced in section 2.2, and calculated via equation (2.5), reproduced below,

$$\lambda_{De} = \left(\frac{\epsilon_0 k_B T_e}{ne^2}\right)^{1/2} \tag{C.4}$$

where λ_{De} is the Debye length, ϵ_0 is the electric constant, T_e is the electron temperature, and n is the density of the bulk plasma.

From the preliminary results, in section 4.3, T_e is measured to be 7.6 eV, and n as 10^{15} m^{-3}. Substituting these into equation (C.4) gives,

$$\begin{aligned}\lambda_{De} &= \left(\frac{8.85 \times 10^{-12} \cdot 1.38 \times 10^{-23} \cdot 7.6}{10^{15} \cdot (1.6 \times 10^{-19})^2}\right)^{1/2} \\ &= 7.6 \times 10^{-6} \text{ m} = 7.6\ \mu\text{m}\end{aligned}$$

It can be seen that 0.26 m $\gg$ 7.6 μm, thus it is fair to assume a collision-less sheath.